Dissertation zur Erlangung des Doktorgrades

der Fakultät für Chemie und Pharmazie

der Ludwig-Maximilians-Universität München

On the way to non-toxic and highly stable perovskite-based optoelectronics

–

Synthesis and investigations of lead-free perovskites for photovoltaic applications

Enrico Greul

aus

Dresden, Deutschland

2019

Erklärung

Diese Dissertation wurde im Sinne von § 7 der Promotionsordnung vom 28. November 2011 von Herrn Prof. Dr. Thomas Bein betreut.

Eidesstattliche Versicherung

Diese Dissertation wurde eigenständig und ohne unerlaubte Hilfe bearbeitet.

München, 04. Februar 2019

Enrico Greul

Dissertation eingereicht am 08. Februar 2019

1. Gutachter: Prof. Dr. Thomas Bein

2. Gutachter: Prof. Dr. Achim Hartschuh

Mündliche Prüfung am 04. März 2019

Warte nicht bis der Sturm vorüberzieht,

sondern lerne, im Regen zu tanzen.

unbekannt

Danksagung

Zuerst einmal möchte ich mich bei meinem Doktorvater Prof. Dr. Thomas Bein für die wiederholte Aufnahme in seine Gruppe für F-Praktikum, Master- und Doktorarbeit bedanken. Er hat mir stets die Möglichkeit gegeben an sehr interessanten Forschungprojekten zu arbeiten und mir dabei geholfen mich frei zu entfalten. Des Weiteren möchte ich mich für seinen Zuspruch und seine Unterstützung bedanken, auch wenn die Ergebnisse mal nicht so kommen wollten wie erhofft.

Weiterhin möchte ich mich bei Dr. Pablo Docampo bedanken der stets reges Interesse an meinen Projekten zeigte und mir immer mit Rat und Tat zur Seite stand. Ohne seinen Input und seinem fast unbegrenzten Vorrat an Ideen wären einige meiner Projekte wohl nicht bis zur Veröffentlichung gekommen. Vor allem bedanke ich mich für seine aufmunternden und motivierenden Worte nach dem ich wieder einmal „gescoopt“ wurde und ich am liebsten wieder einmal die „Flinte ins Korn“ werfen wollte.

Ein besonderer Dank geht auch an die Photovoltaik Subgroup. Obwohl ich einige Doktoranden habe kommen und gehen sehen hatten wir immer sehr viel Spaß bei der Arbeit und unsere Diskussionen waren höchst produktiv. Vielen Dank an die ehemaligen und aktuellen Subgroup-Mitglieder Norma, Alesja, Ashkat, Flo, Fabi, Bini, Hongi, Nadja, Tina, Meltem, Michiel, Max und alle anderen die ich in dieser Aufzählung vergessen haben sollte. Insbesondere möchte ich Norma danken, da sie meine Betreuerin während meines F-Praktikums im AK Bein war und in mir ein sehr großes Interesse an der Materialwissenschaft und der Photovoltaik im Besonderen geweckt hat. Auch möchte ich mich speziell bei Michiel bedanken, der mir während meiner Doppelperovskit-Projekte tatkräftig zur Seite stand und mitgeholfen hat selbige zu einem guten Ende zu bringen.

Ein weiterer Dank geht auch an meine Kollaborationspartner und Praktikanten. Vor allem möchte ich mich bei Irene bedanken, die, trotz meiner nicht immer optimalen Proben, alles getan und nicht aufgegeben hat das Beste aus meinen Proben herauszuholen. Vielen Dank auch an meine Praktikanten und RISE-Studenten Christian, Sonja und Andrew für ihre tatkräftige Unterstützung.

Des Weiteren möchte ich mich bei Regina und Corinna bedanken die den Großteil des im Arbeitkreis anfallenden Papierkrams erledigen und mir mit allen bürokratischen Angelenheiten behilflich waren. Vor allem vor und nach Konferenzen bestand erhöhter

Redebedarf bezüglich Dienstreiseantrag und Reisekostenerstattung. Nochmals Vielen Dank für eure Hilfe.

Einen nicht unerheblichen Teil an dem Erfolg meiner Promotion hatte Tina, die als gute Fee des Arbeitskreises immer dafür gesorgt hat, dass wir all unsere Chemikalien zum Experimentieren zur Verfügung hatten. Vor allem möchte ich mich dafür bedanken, dass sie nie die Geduld verloren hat wenn ich sie zum x-tenmal gefragt habe ob denn meine Chemikalien schon da sind.

Auch möchte ich mich bei meinen ehemaligen Bürokollegen für die gute Atmosphäre und den Spaß den wir zusammen hatten bedanken. Vielen Dank an Joni, Derya, Lisa, Julian, Torben, Flo, Stefan, Christian, Laura, Alex, Mona und Maria. Natürlich möchte ich mich auch bei allen ehrenamtlichen Büromitgliedern bedanken, die immer einen Grund gefunden haben uns zu besuchen. Des Weiteren möchte ich mich bei allen Mitgliedern des AK Bein für das herzliche Willkommen heißen in der Gruppe und die sehr nette Atmosphäre bedanken.

Zuletzt möchte ich mich noch bei den Menschen bedanken die mir am nächsten stehen. Ein besonderer Dank geht an meine Mutter die es mir mit ihrer positiven Einstellung zu dem was ich tue erst ermöglicht hat ein Studium aufzunehmen und bis zur Promotion voranzutreiben. Im gleichen Maße möchte ich meiner Freundin Manuela danken, dass sie mich immer bedingungslos unterstützt und mir jederzeit den Rücken freigehalten hat, auch wenn wieder einmal eine Prüfung zu schreiben war oder wenn es mal wieder später geworden ist. Durch ihre aufmunterden Worte hat sich mich immer wieder aufs Neue motiviert, mich mit vollem Elan ins Labor zu stürzen, auch wenn es mal nicht so gut lief. Ein großer Dank geht auch an meine Tochter Alessia für die vielen schönen Stunden Spiel und Spaß zwischen der Arbeit.

Abstract

Our modern way of life is based on the consumption of energy, which is mainly provided by the burning of fossil fuels, such as natural gas, oil or coal. Since such resources are limited on earth, humankind will run out of them sooner or later, endangering the wealth and the living standard of the people all over the world. Furthermore, the extensive burning of fossil fuels causes a massive emission of so-called greenhouses gases leading to an effect called global warming, which finally ends up in a dramatic increase of severe weather phenomena, such as floods, droughts and storms. In order to ensure that future generations can be provided with sufficient energy and to prevent or at least slow down the global warming, a lot of effort has already been put into the development of possibilities to produce sustainable energy without the emission of greenhouse gases. Among others, the harvesting of sunlight to generate electrical energy has turned out to be very promising, since the annual energy provided by sunlight hitting the earth is far more than the global energy consumption. Although conventional state-of-the-art silicon-based photovoltaics can already convert sunlight into electrical power with an efficiency of about 25 %, their production consumes a significant amount of energy, hampering a rapid market penetration of solar cells. In order to make electrical power generated by solar energy more competitive to other energy sources, new photovoltaic concepts based on abundant materials that can be easily processed have to be developed.

Possible candidates for reaching this goal can be organic-inorganic lead halide perovskite-type materials, which show competitive efficiencies of more than 20 % for lead iodide based compounds. However, the toxicity of lead represents a major obstacle for the commercialization of this technology. A promising alternative to lead is given by tin based perovskites showing encouraging efficiencies of more than 6 %. However, the high sensitivity of the utilized Sn^{2+} cations towards moisture and oxygen makes the design of stable solar cells difficult.

In order to find new, more stable Sn^{2+} based perovskites suitable for optoelectronic applications, this thesis presents a comprehensive study of two different compounds, namely *n*-butylammonium tin iodide ($(BuA)_2SnI_4$) and phenylethylammonium tin iodide ($(PEA)_2SnI_4$) and their lead-based counterparts. Furthermore, their methylammonium-containing relative, methylammonium tin iodide ($MASnI_3$), was investigated. Optoelectronic investigations revealed that $(BuA)_2SnI_4$ and $(PEA)_2SnI_4$ feature excellent properties making them interesting for photovoltaic and light emitting applications. Furthermore, moisture

stability studies showed that the introduction of phenylethylammonium results in a drastic enhancement of the tin-based perovskite, most likely due to the large hydrophobic organic residue of the organic cation.

Besides the toxicity of lead, the hazardous nature of the organic solvents utilized for the formation of the perovskite films is one concern preventing metal halide perovskite based optoelectronics from their commercialization. Here, lead-free tin-based perovskite films have been prepared by replacing the commonly used solvents *N*,*N*-dimethylformamide and dimethylsulfoxide by a mixture of the less hazardous alternatives methanol and 1,4-dioxane. The films made by the less hazardous approach feature an excellent smooth and homogeneous morphology and solar cells comprising such films show moderate efficiencies of about one percent, which is most likely caused by the formation of Sn^{4+} due the facile oxidation of Sn^{2+}.

Due to the high sensitivity of Sn^{2+} towards moisture and oxygen, a new, more stable, lead-free class of materials, namely double perovskites has been investigated for optoelectronic applications. Due to its optoelectronic properties, $Cs_2AgBiBr_6$ is one of the most suitable double perovskites for photovoltaic applications. Here, a synthesis protocol for the formation of $Cs_2AgBiBr_6$ thin films was developed comprising a preheating and a hot annealing step. It turned out that preheating the substrate and the precursor solution increased the amount of material deposited on top of the substrate, which in turn enhances the optoelectronic properties of the resulting films. Hot annealing at temperatures of more than 250 °C is needed to convert side phases occurring during the spin-coating process into the desired double perovskite phase. Solar cells comprising such films exhibit promisingly high efficiencies of almost 2.5 % and high stability under working conditions.

Since the quality of the films of the photoactive material has a tremendous influence on device performance, a route for the preparation of high quality $Cs_2AgBiBr_6$ films has been developed. The photoactive layer is deposited via spin-coating with simultaneous precipitation of the double perovskite crystals by the addition of an antisolvent. Due to the different solubility properties of $Cs_2AgBiBr_6$ compared to lead and tin based perovskites, different organic solvents have been tested for their suitability to form homogeneous and smooth double perovskite films. It turned out that *iso*-propyl ether is an excellent antisolvent for the preparation of high quality $Cs_2AgBiBr_6$ films. Planar heterojunction solar cells comprising the newly developed films exhibited promising power conversion efficiencies of up to one percent.

Table of content

1 Introduction

In 2015, 196 countries subscribed to the so-called climate agreement of Paris, which was decided at the 21st world climate conference. A main goal of the supporters of the climate agreement was to reduce or prevent the climate change caused by the so-called global warming. Accordingly, the subscribers to the Paris climate agreement decided to try to limit the increase of the global average temperature to 2 °C with respect to preindustrial values.[1] The reduction of the emission of so-called green-house gases is considered to be one major issue to achieve this goal. Green-house gases reduce the amount of solar energy which gets reflected by the surface of the earth, leading to a heating up of the world´s atmosphere.[2] A large fraction of man-made green-house gas emissions is caused by the burning of fossil fuels, which is still the most important way to produce energy, see Figure 1-1.

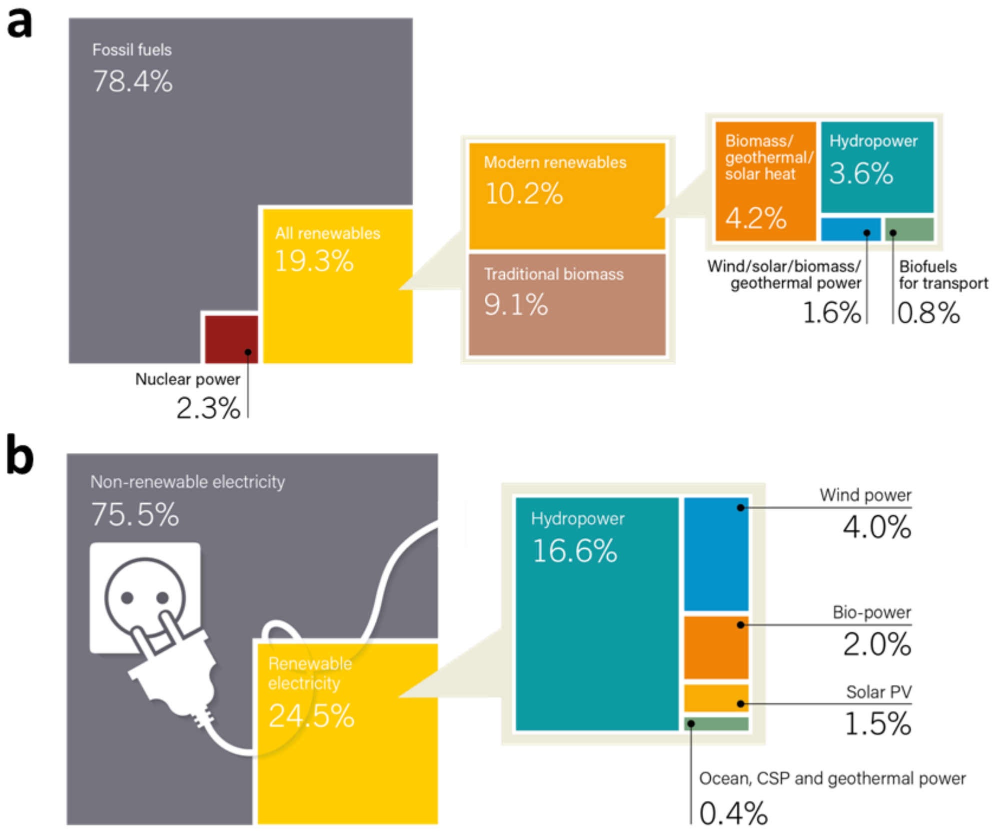

Figure 1: a) Estimated renewable energy share of total final energy consumption in 2015. b) Estimated renewable energy share of global electricity production by the end of 2016.[3]

The emission of green-house gases can be expected to rise rapidly during the next decades since the energy demand of countries that are outside the Organization for Economic Cooperation and Development (OECD) is permanently increasing (Figure 1-2a). In particular, the energy demand of Asian countries, including India and China, which currently represent one third of world´s population, is disproportionately rising, see Figure 1-2b.[4]

Figure 1-2: a) Development of the world´s energy consumption from the year 1990 until 2040. The plot is divided in countries which are a member of the Organization for Economic Cooperation and Development (OECD) and countries which are not a member of the OECD (non-OECD). b) Development of the energy consumption of selected parts of the world from the year 1990 until 2040.[4]

Besides the fact that the burning of fossil fuels increases the average temperature of the world´s atmosphere leading to catastrophic weather phenomena, like storms, droughts and floods, fossil fuels are also a limited resource. Considering that the formation of the nowadays used fossil fuels took millions of years, humankind will run out of them sooner or later.[5]

Accordingly, new sources for energy production have to be developed, which cover the world´s rising energy demand and simultaneously do not emit green-house gases.

An efficient way to produce electrical energy without emitting green-house gasses is the use of wind and water power.[6] Among the sources of renewable energy, wind and water power already represent by far the largest portion. In contrast, the contribution of solar energy to the world´s energy production is less than one percent.[7] Considering that 3.5 $\mathrm{x}10^{24}$ J of solar energy are reaching the earth every year, which is about 10000 times more than the annual human energy consumption, there is a huge potential to increase the impact of photovoltaics on the world´s energy production.[8]

Commonly used state-of-the-art silicon-based photovoltaics show power conversion efficiencies of more than 20 %. Although the cost for highly efficient silicon solar cells has been decreased significantly during the last decades, the processing of such photovoltaics is still relatively complex and consumes much energy, due to the need for highly phase pure single crystalline or polycrystalline silicon, limiting the throughput of such photovoltaics. In order to overcome this drawback, the processing of existing silicon-based photovoltaics has to be improved and novel approaches and materials have to be investigated for their applicability in photovoltaics. In particular, cheap and abundant materials, which can be easily processed by solution-based methods, are of special interest, due to the possibility to manufacture highly efficient photovoltaics by printing methods, which could lead to a dramatic increase of the production of solar cells. Such materials hold promise for cheap solar cells, which can be distributed rapidly all over the world, especially in threshold and developing countries. This would represent a huge step helping to achieve the goals decided in the climate agreement of Paris in sufficient time.

1.1 Basic Operation Principle of Photovoltaics

A solar cell is a device that generates electric power upon absorption of sunlight. All photovoltaics are based on semiconductors, which are materials featuring a forbidden energy gap between their electron filled valence band (VB) and their empty conduction band (CB). The forbidden energy gap is called band gap (BG). Without any external excitation source, semiconductors exhibit almost no free charge carries in the CB leading to a low conductivity, between that of conductors and insulators. Upon light absorption or the application of an external electric field, electrons can be excited into the CB and the semiconductor becomes conductive. It is important to notice that electrons can only be transferred into the CB if the energy, which is applied to the electrons, equals or exceeds the energy of the BG, see Figure 1-3 b.[9,10]

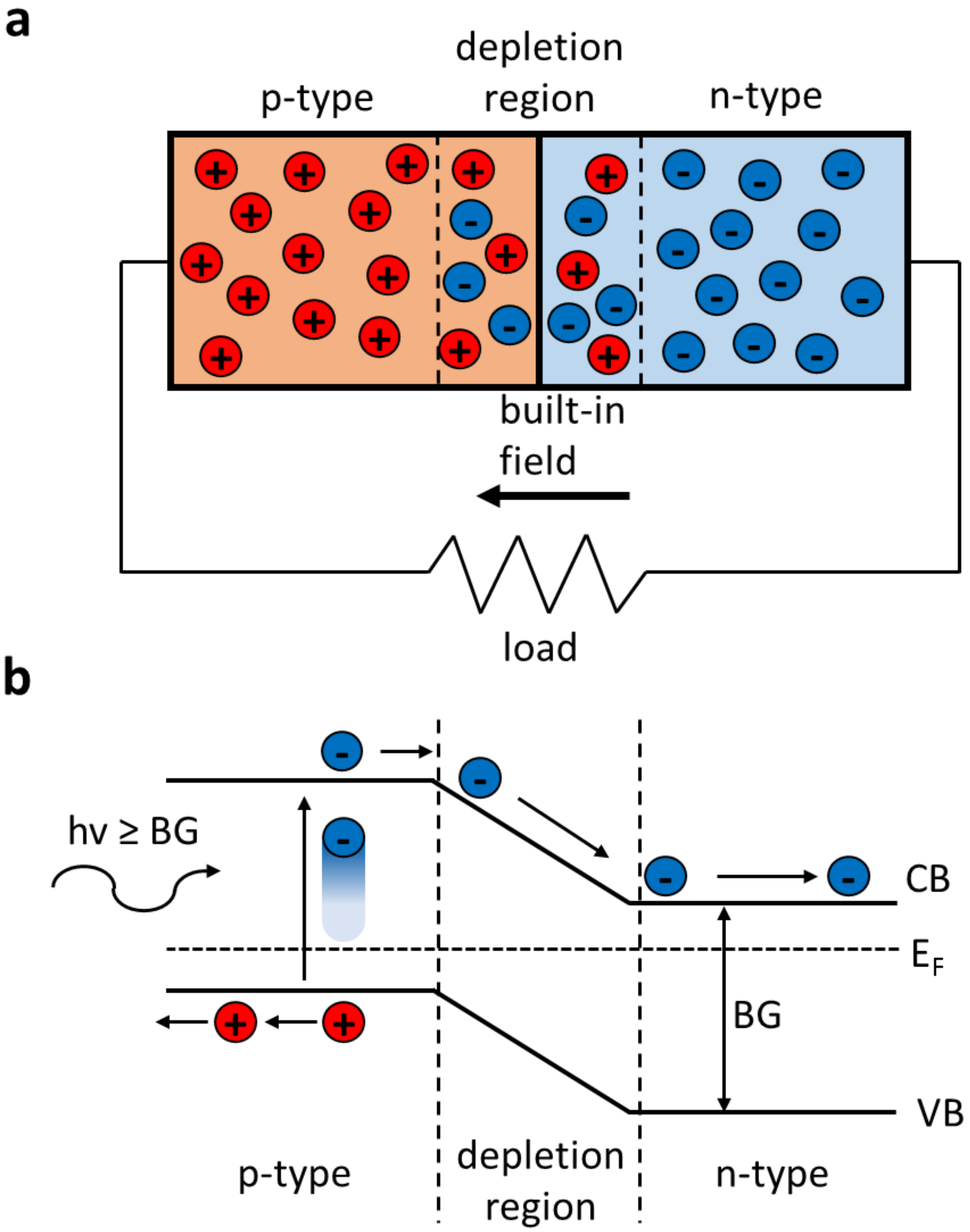

Figure 1-3:a) Simplified schematic of a p-n-junction based solar cell. b) Schematic of the band structure of the p-n-junction based solar cell depicted in Figure 1-3a showing the processes involved in the light absorption event. The blue circles represent electrons and the red circles represent holes. The wave-shaped arrow indicates a photon with a photon energy (hv) equal to or larger than the BG (3).

A classical semiconductor solar cell consists of an n-type and a p-type semiconductor which are in close contact with each other. Such an assembly is called p-n-junction. A simplified schematic of a p-n-junction based solar cell is given in Figure 1-3a. According to Figure 1-3a, a p-n-junction based solar cell basically consists of an n-type semiconductor (n-type) and a p-type semiconductor (p-type), which build the p-n-juction. The two semiconductors are connected to an exerternal circuit, which exctracts the generated charges out of the semiconductors. An n-type semiconductor features an excess of negatively charged electrons, wherein a p-type semiconductor features an excess of positively charge holes. If a p-type semiconductor is in close contact with an n-type semiconductor, the excess electrons of the n-type semiconductor and the excess holes of the n-type semiconductor diffuse towards either the p-type semiconductor or the n-type semiconductor, respectively, in order to compensate charges. Due to this charge carrier diffusion, a so-called depletion region forms in the region close to the interface between the two semiconductors. In the depletion region, the concentration of the negatively charged electrons in the n-type semiconductor is lower than that of the n-type semiconductor, which is not part of the depletion region. The distribution of the positively charged holes in the p-type semiconductor is similar to that described before for the elecrons in the n-type semiconductor. The distribution of the charge carriers within the depletion region creates a built-in field which counteracts the diffusion process of the electrons and the holes, limiting the size of the depletion region. Figure 1-3b shows a schematic of the band structure of the p-n-junction given in Figure 1-3a. Depending on the type of the semiconductor, the Fermi-energy E_F of the semiconductors is either shifted towards the CB (n-type) or towards the VB (p-type). Due to the differences in the E_F of the n-type and the p-type semiconductor, the CB and the VB in a p-n junction are bent in the region of the depletion region. In Figure 1-3b, a photon, with a photon energy equal to or larger than the BG is absorbed in the p-type semiconductor. This leads to the excitation of an electron from the VB to the CB of the p-type semiconductor. The excited electron creates a hole in the VB. Both the electron and the hole are free to move. After excitation, the electron diffuses towards the depletion region where it follows the course of the CB towards the n-type semiconductor. The electron and the hole, which was created by the excited electron, are then extracted by the external circuit (see Figure 1-3a)..[9,10]

As already mentioned, semiconductors are only able to absorb photons featuring an energy equal or exceeding the energy of the BG. Therefore, a semiconductor for photovoltaic applications must be able to absorb the majority of sun light hitting the earth. Figure 1-4a shows a so-called AM1.5 solar spectrum, which represents the sun light reaching the earth surface after passing through 1.5 times the earth atmosphere under a zenith angle of $z = 48.2°$. The AM1.5 spectrum is a widely used reference solar spectrum and represents the illumination conditions on a clear, sunny day in countries lying in mid-latitudes, like the United States of America, European countries, China and Northern India.[12] Accordingly, the BG of a semiconductor for photovoltaic applications should be small enough to absorb as much light as possible in the range where the illumination intensity of the AM1.5 spectrum is high. On the other hand, if the BG is too small a lot of energy gets lost due to thermalization (see Figure 1-4b).[13] In the early 1960s, W. Schockley and H. J. Queisser calculated for the first time the optimal BG for a single junction silicon-based solar cell to be between 1.1 eV and 1.5 eV, reflecting a wavelength cutoff between 825 nm and 1125 nm.[14] Since then, the maximum theoretical efficiency η_{max} of a single junction solar cell at a given BG is called the Schockley-Queisser limit.

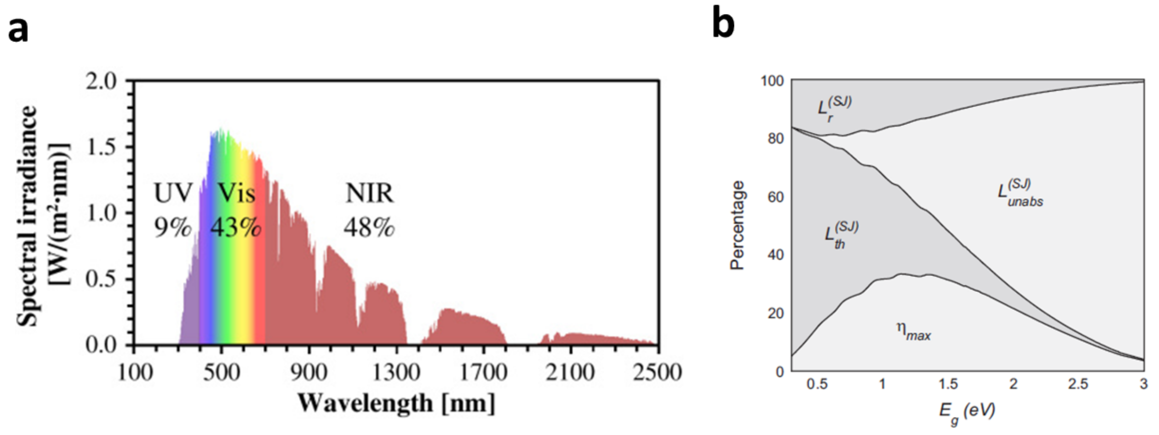

Figure 1-4: a) Depiction of an AM1.5 solar spectrum including the three spectral ranges ultraviolet (UV), visible (Vis) and near infrared (NIR).[11] b) Schematic illustration of the Schockley-Queisser limit showing different efficiency loss pathways, where L_{th} is the thermalization loss, L_{r} is the loss which occurs from partial reflection of the incident light, L_{unabs} is the loss caused be unabsorbed photons and η_{max} is the maximum efficiency.

In principle, a solar cell can be considered as a diode. Thus, the model electrical circuit given in Figure 1-5 consists of a diode with a current source (light current) connected in parallel. Without illumination, the solar cell behaves like a diode exhibiting an exponential increase in current flow under forward bias conditions and almost no current flow under reverse bias conditions. Under illumination, the current-voltage (J-V) curve depicted in Figure 1-5b is moving up along the y-axis indicating light driven current generation. According to Figure 1-5a, the efficiency of the solar cell is strongly influenced by several resistances, namely shunt resistance (R_{sh}) and series resistance (R_{s}). As given in the electrical model circuit in Figure 1-

5b, R_{sh} should be infinite and R_s should be zero in an ideal solar cell. Both resistances can be estimated from the shape of the *J-V* curve. In particular, the slopes of the *J-V* curve at the intersections of the curve with either the y-axis or the x-axis, representing the maximum obtainable current and voltage, respectively, of the solar cell are of special interest. A detailed explanation of the characteristic points of a *J-V* curve is given in the characterization section.

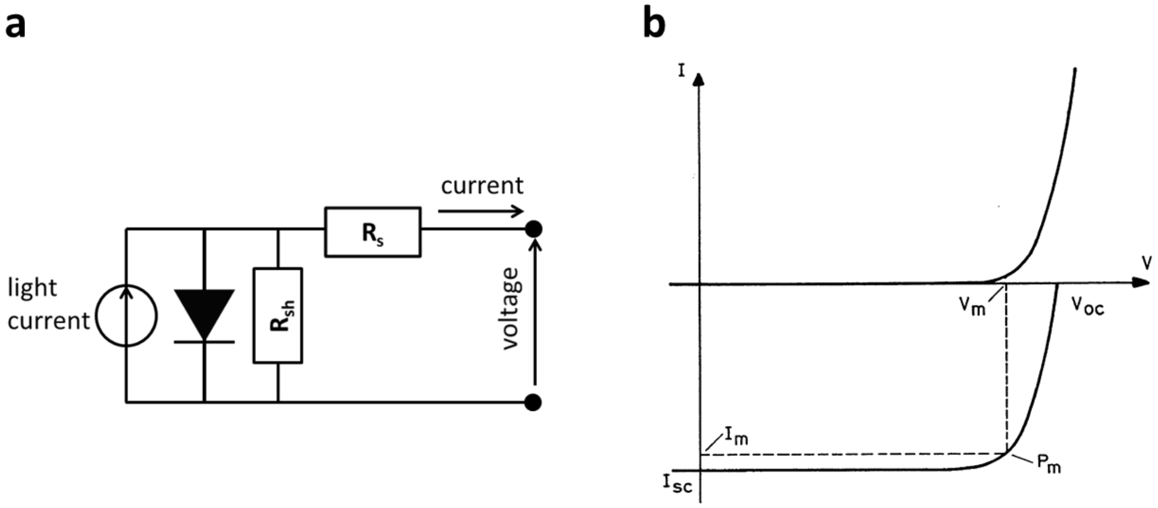

Figure 1-5: a) Model electrical circuit of a solar cell. b) Typical current-voltage (J-V) curve of a solar cell.[15]

Since their invention several decades ago, many different types of solar cells have been developed. During the quest for solar cells that are highly efficient, cheap and environmentally friendly, a large variety of materials have already been investigated for their applicability in photovoltaics. Furthermore, also the assembly of the solar cells has changed. The following section is giving a short overview over the evolution of solar cells during the last decades.

1.1.1 State of the Art Solar Cell Technologies

In the early 1950s, the first reasonably efficient solar cell, based on crystalline silicon (c-Si), was presented by researchers of the Bell Laboratories exhibiting a power conversion efficiency (PCE) of up to 6 %. After about 30 years of development, solar cells have reached PCEs of far more than 20 %. Considering the Schockley-Queisser limit of ~30 % for single junction solar cells, state-of-the-art c-Si based photovoltaics are already close to their theoretical maximum efficiency.[16] Despite the huge effort which has been put into the development of highly efficient solar cells during the last decades, the majority of commercially available photovoltaics is still based on the same basic principle from the early 1950s. A schematic of a typical c-Si solar cell comprising layers of n-type and p-type c-Si is depicted in Figure 1-6.[17,18] The interface between the p-type and n-type layer is called p-n-junction and is needed for charge separation.[18] According to Figure 1-6, the main part of such a solar cell is a c-Si wafer, which has to be single crystalline and highly phase pure, making the processing very costly, which made early solar cells very expensive.

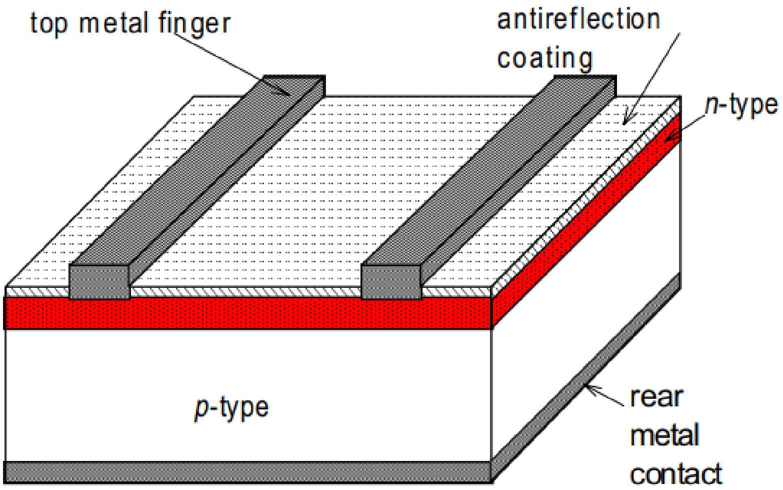

Figure 1-6: a) Basic assembly of a crystalline silicon based solar cell.[17]

In order to make the costs for solar cells more competitive to the costs of other energy sources, like coal and oil, new photovoltaic concepts have been invented. The so-called second generation solar cells are based on thin films of the photoabsorber material. For comparison, while the film thickness of the thin film based devices ranges from several hundred nanometer to a few tens of microns, due to the smaller absorption coefficient of Si (with indirect band gap) the film thickness typically used for c-Si solar cells is about 200 µm.[17,19] One of the first developed thin film solar cells was based on amorphous silicon (a-Si). a-Si is the non-crystalline form of silicon featuring several advantages, like a direct band gap with a high value for the optical absorption coefficient.[20] Due to the excellent optical properties of a-Si only a thin film (<300 nm) of the photo absorber is needed for a photovoltaic device. Together with the relatively simple processabilitiy of this material, by vapor deposition methods at low temperatures, a-Si is a promising candidate for low cost photovoltaics.[21] Since the electron mobility in a-Si is much lower than that in c-Si, a-Si based photovoltaics feature a p-i-n homojunction meaning that the p-i-n junction is created by the same material, see Figure 1-7a.[21] The p-i-n junction consist of an internal (i-a-Si:H) a-Si layer which acts as photoabsorber, sandwiched between a layer of n-type and p-type a-Si, labeled n-a-Si:H and p-a-Si:H, respectively. The n- and p-type layers create an internal electric field in the i-a-Si:H layer which helps to separate the charges generated in the absorber layer.[22] Since a-Si based solar cells show rather low PCEs below 10 %, and due to stability issues,[21,23] further thin film materials for applications in photovoltaics have been developed.[24]

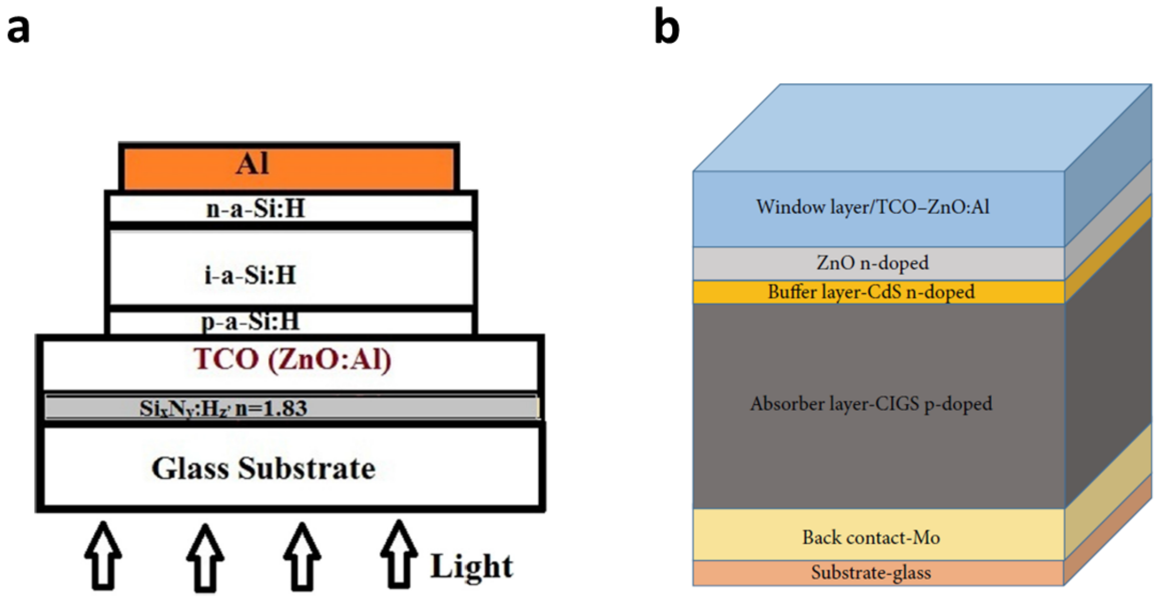

Figure 1-7: a) Schematic of the assembly of a typical a-Si based solar cell.[24] b) Schematic of the assembly of a typical CIGS based solar cell.[25]

Another approach for thin film photovoltaics is based on cadmium telluride (CdTe) or copper indium gallium selenide (CIGS) films serving as absorber layers. CdTe and CIGS are, similar to a-Si, easy to process and feature excellent band gap energies between 1 eV and 1.7 eV.[25,26] As depicted in Figure 1-7b, solar cells comprising either CIGS or CdTe absorber layers are based on a p-n junction of the p-type photoabsorber and a thin n-type cadmium sulfide (CdS) layer. In contrast to the p-i-n junction in an a-Si silicon based device, where the junction is created by the same material, the p-n junction of CIGS or CdTe based photovoltaics is formed by two different materials and therefore called heterojunction. Although CIGS and CdTe based photovoltaics show efficiencies of about 22 %, there are still issues concerning the stability against moisture and the toxicity of components of the devices.[27,28]

Although all solar cell technologies presented so far show reasonably good performance, they suffer from a number of problems, like the need for expensive vacuum or high temperature processing routes or the toxicity of their components. Accordingly, many other approaches to convert sun light into electricity have been developed.

A promising technology to produce low cost solar cells without the need of a vacuum process is the so-called organic photovoltaics (OPV).[29] As already indicated by the name, OPV relies on the use of organic semiconductors. A typical organic solar cell comprises a so-called bulk heterojunction, which is a blend of an organic electron donor, also acting as photoabsorber, and an organic electron acceptor. A suitable electron donor can be a small molecule or a polymer, while commonly used electron acceptors are fullerenes or quantum dots. The bulk heterojunction is sandwiched between a metal contact and a hole transporting layer/transparent contact, see Figure 1-8.[30]

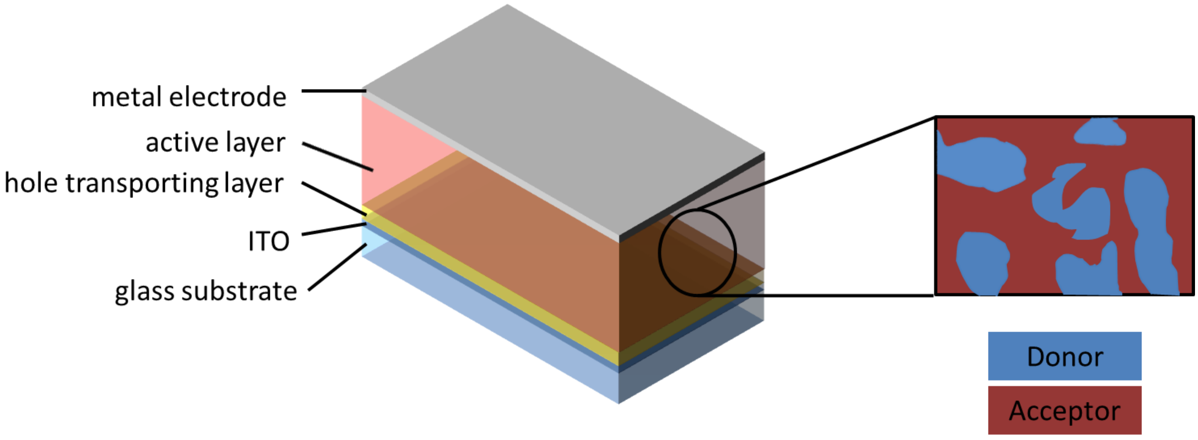

Figure 1-8: Schematic assembly of a bulk heterojunction organic solar cell including the distribution of the donor and acceptor phases within the active layer.

Although OPV does not reach PCEs similar to silicon-based photovoltaics, OPV features several advantages. For example, the band gap energy of the photoabsorber can be easily changed by just changing the structure of the organic absorber. Furthermore, organic photoabsorbers feature high optical absorption coefficients making it possible to use very thin films of the absorber material in solar cells. Additionally, in principle organic films can be processed by high-throughput and low-temperature roll-to-roll techniques, which allow for a cheap mass production of OPVs. Since OPVs are much lighter than silicon based solar panels and can be deposited on flexible substrates, OPVs can be easily integrated into already existing structures, like windows or building fronts.[31]

1.2 Hybrid Perovskite Solar Cells – A Game Changer in Photovoltaics

Although known and investigated for several decades, hybrid organic-inorganic lead iodide perovskites have attracted much attention in the photovoltaics community just a few years ago, after the report on hybrid inorganic-organic lead iodide based solar cells featuring promising PCEs exceeding 10 %, in 2012.[32] The term perovskite typically describes a class of metal oxide with the composition ABX$_3$ exhibiting the structure of CaTiO$_3$. A special class of perovskites are the hybrid organic-inorganic metal halide perovskites, where A can be a small organic cation, such as methylammonium (MA) or formamidinium (FA), B can be Sn^{2+} or Pb^{2+} and X can be Cl$^-$, Br$^-$ or I$^-$. In this case, the metal ion is octahedrally coordinated by six halide ions. The metal halide octahedra, in turn, are connected by their corners to each other forming a three-dimensional network. The organic cation is situated inside the voids created by the three dimensional network of metal halide octahedra, see Figure 1-13a.

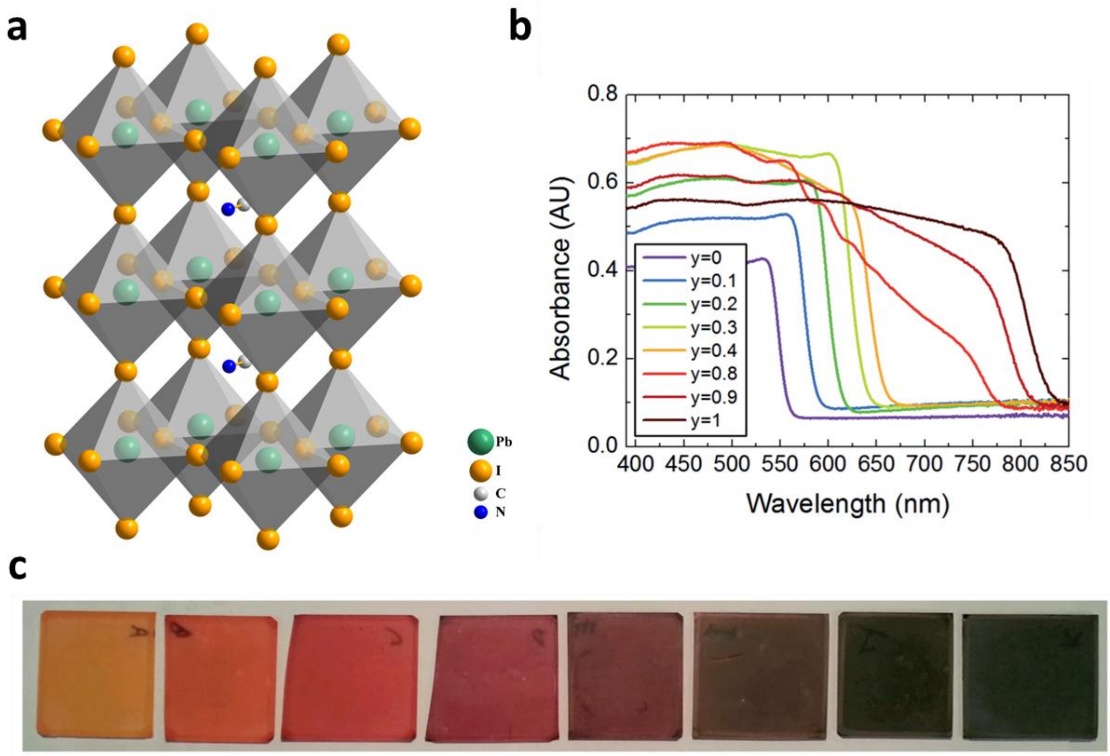

Figure 1-13: a) Crystal structure of methylammonium lead iodide (hydrogens omitted). b) Absorption spectra of formamidinium lead iodide and different mixtures of iodide and bromide. y = 0 refers to 100 % bromide and y = 1 to 100 % iodide. c) Images of films made of formamidinium lead halide featuring different bromide and iodide mixtures.[33]

In particular, lead based hybrid organic-inorganic halide perovskites are excellent materials for photovoltaic applications due to their outstanding properties, namely high absorption coefficients[34], long lifetimes of the photogenerated species[35] and the tunability of their BG just by replacing iodide by bromide, see Figure 1-13b & c.[36,37] Furthermore, the perovskite structure of such compounds features a high flexibility allowing for the incorporation of a varity of different metal cations, organic cations and anions.[33]

The first solar cells comprising hybrid organic-inorganic lead halide perovskites as absorber were still based on the widely used dye sensitized solar cell (DSSC) architecture featuring a liquid electrolyte.[38] Due to the corrosive nature of the electrolyte leading to the degradation of the absorber material, the manufactured solar cells showed only modest PCEs.[38,39] After the liquid electrolyte had been replaced by a solid state HTM, the efficiency of hybrid organic-inorganic lead iodide based solar cells could be rapidly increased to the already mentioned 10 %.

Furthermore, it could be shown that the kind of material utilized for the mesoporous scaffold did not matter. In particular, the performance of solar cells featuring a scaffold made of alumina, which is an insulator, was not worse than that of devices comprising a titania scaffold.[32] Subsequent studies on lead based hybrid perovskites revealed that the material itself shows excellent transport properties with electron-hole diffusion length exceeding one micron.[35] Accordingly, the several micron thick mesoporous titania layer could be replaced by a several nanometer thin, dense electron selective contact.[40] As result, device fabrication without a high temperature annealing step to sinter the TiO_2 nanoparticles together was possible, just by using preformed nanoparticles or electron selective organic molecules for the formation of the electron selective contact, which made it possible to assemble hybrid organic-inorganic lead halide perovskite based solar cells even on plastic substrates.[41,42]

On the other hand, the removal of a thick mesoporous layer creates the need for homogeneous, pin-hole free absorber layers to obtain good working devices. Therefore, many different methods to deposit high quality hybrid perovskite films have been developed and all aspects of the synthesis of such films, including the precursor solution,[43–49] the thermal annealing step,[50–53] the addition of additives to aid film formation and the treatment of substrate before film deposition have been optimized.[54–61] Due to the effort put into the development of high quality hybrid organic-inorganic lead halide perovskite films, state-of-the art solar cells now show efficiencies of more than 20 %.[62,63] The evolution of the device architecture which leads to such high-performing photovoltaics is given in Figure 1-14.

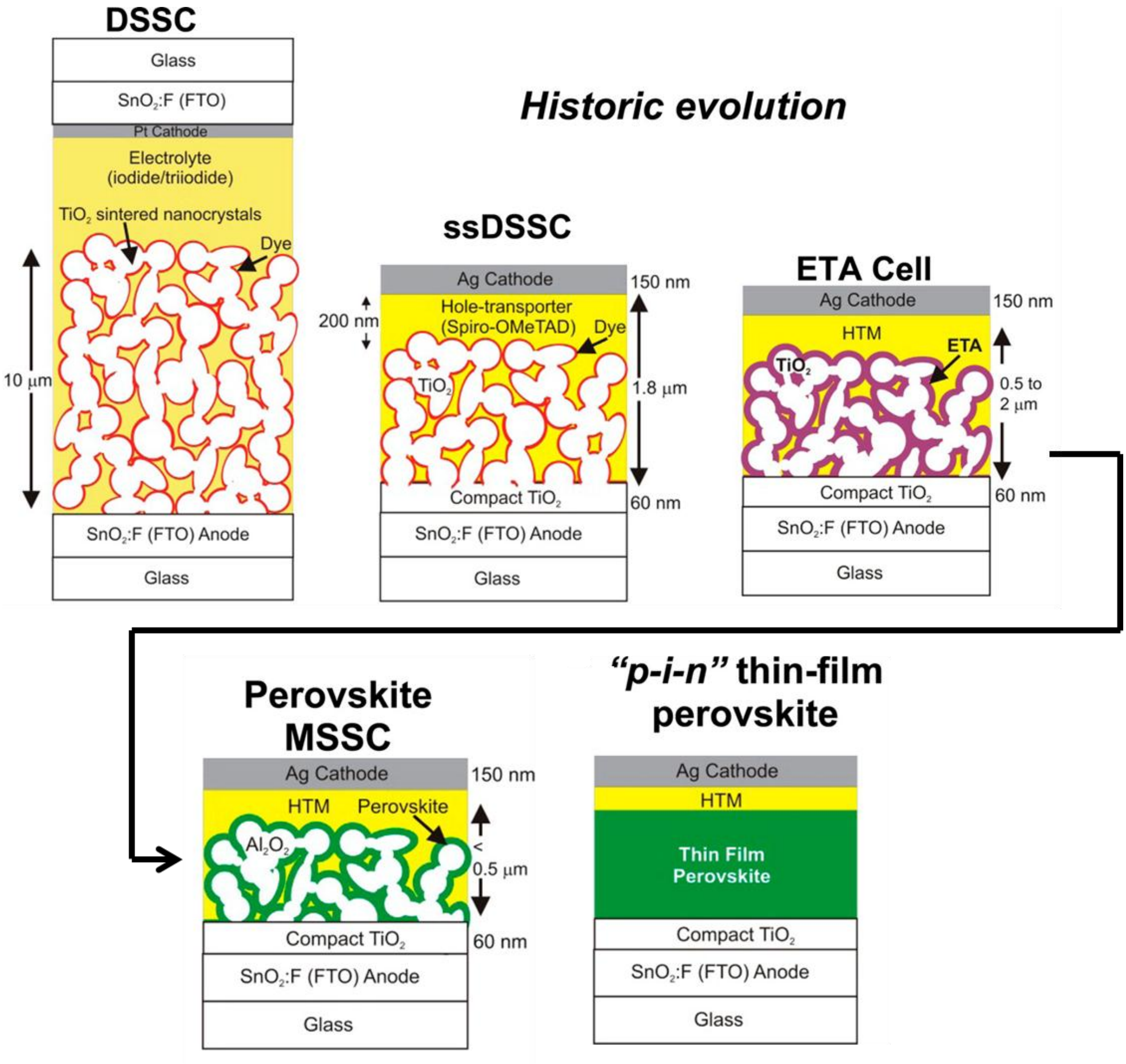

Figure 1-14: Historic evolution of the solar cell architecture starting from a classical dye sensitized solar cell featuring a mesoporous scaffold and finishing with a planar heterojunction hybrid perovskite solar cell.[64]

Despite the high performance of hybrid organic-inorganic lead halide perovskite based solar cells approaching already values of commercially available photovoltaics, such as GaAs or Si, several challenges have to be managed before their commercialization. One important issue, which has to be addressed, is related to stability problems of hybrid lead halide based perovskites. Thus, hybrid lead halide perovskites exhibit a high sensitivity towards moisture leading to the degradation of the hybrid perovskite even at relatively modest relative humidity values of about 50 % and higher.[65,66] Furthermore, hybrid lead halide perovskites show phase transitions and even degradation at solar cell operating temperatures.[67-69] Besides stability problems, one of the most important obstacles for the widespread application of hybrid lead halide based perovskites arises from the content of lead in this class of materials, which is hazardous to the environment and human health.[70,71] The following sections will review recent results addressing the above-mentioned aspects to illustrate the efforts that have already been put into the solution of these issues in order to make halide perovskites accessible for commercialization.

1.2.1 Stability

While silicon based photovoltaics feature almost constant PCEs for several years under operation conditions, non-encapsulated solar cells based on hybrid lead halide perovskites show a significant decrease of their performance on a much shorter time scale.[72] The much faster decrease of the device performance is associated with the degradation of the hybrid metal halide absorber layer upon exposure to light, oxygen, moisture and thermal stress.[73,74] In order to commercialize hybrid lead halide perovskite based photovoltaics, such devices have to show a reasonably constant power output for at least 10000 h.[75] Since state-of-the-art perovskite based solar cells exhibit a stable power output of only up to 2000 h, the stability of these devices under ambient conditions has to be significantly improved.[76,77] Therefore, it is also necessary to understand the pathways of how the hybrid lead halide perovskites degrade under the exposure of the distinct environmental conditions.

In order to illustrate possible degradation pathways of hybrid lead halide perovskites upon exposure to humidity, the degradation of one of the most widely used compounds, namely methylammonium lead iodide ($MAPbI_3$), is discussed below. In general, when $MAPbI_3$ is exposed to conditions where the water in the gas phase surrounding the perovskite is able to condense, $MAPbI_3$ decomposes irreversible into aqueous hydroiodic acid (HI), solid lead iodide (PbI_2) and MA which can be either released as gas (ammine) or dissolved in water, leading to a permanent loss of the device efficiency.[36,78]

However, when $MAPbI_3$ is exposed to conditions where the water is not allowed to condense, the water molecules can be slowly incorporated into the crystal lattice of $MAPbI_3$, resulting in a separation of the PbI_2 octahedra and leading to the formation of the dihydrate, $(MA)_4PbI_6 \bullet 2H_2O$.[65] The dihydrate formation is a two-step process. In the first step, the structure is saturated with one water molecule per formula unit giving the monohydrated species, $MAPbI_3 \bullet H_2O$. Upon longer exposure to humidity the reaction proceeds further and a second water molecule is incorporated into the structure, resulting in the final dihydrate. During this reaction, the favorable 3D arrangement of the PbI_6 octahedra in the non-hydrated compound undergoes a transition into a 1D network of double-chains of $MAPbI_3$ in the monohydrate, resulting in the final 0D structure of isolated PbI_6 octahedra in the dihydrate. A reaction scheme of the slow hydration of $MAPbI_3$ with the corresponding schematic crystal structures is given in Figure 1-15a.

$$4\,(MA)PbI_3 + 4\,H_2O \rightleftharpoons 4\,[(MA)PbI_3 \cdot H_2O] \rightleftharpoons [(MA)_4PbI_6 \cdot 2\,H_2O] + 2\,H_2O + 3\,PbI_2$$

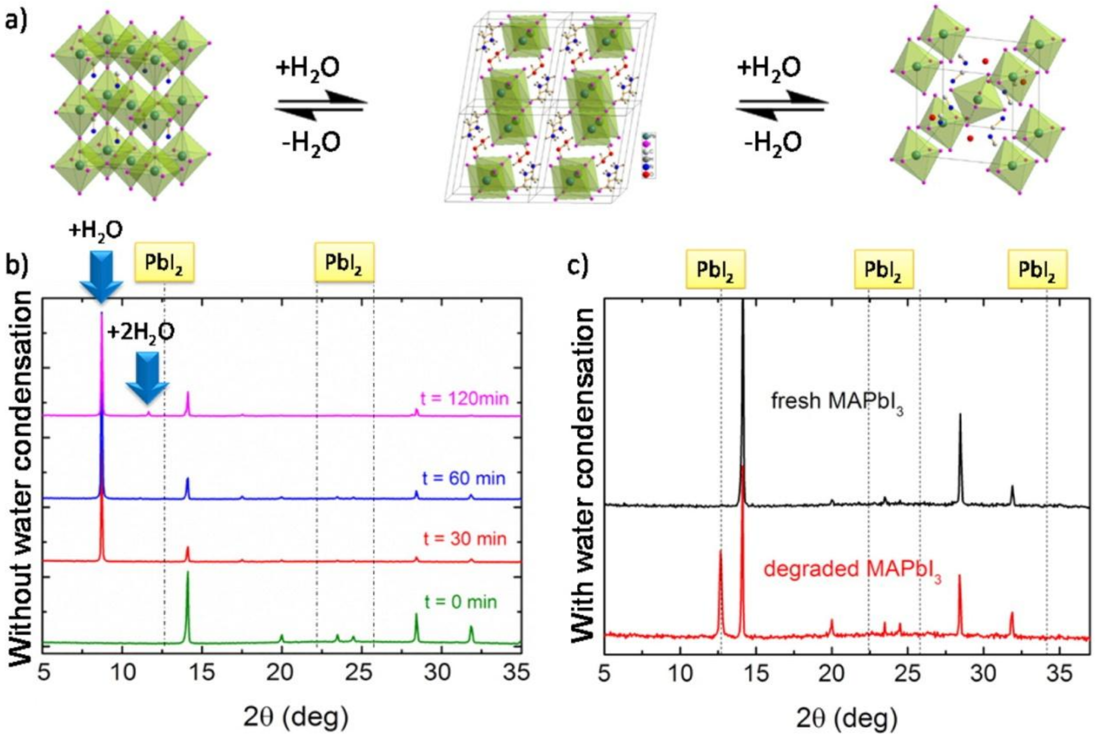

Figure 1-15: a) Hydration reaction scheme with the corresponding crystal structures. b) XRD patterns of $MAPbI_3$ thin films exposed to humidity conditions without water condensation. c) XRD patterns of $MAPbI_3$ thin films exposed to humidity conditions with water condensation.[65]

According to the reaction equation given in Figure 1-15a, the monohydrate is an intermediate product on the way to the dihydrate and can be easily converted back to the non-hydrated species.[79] Figure 1-15b shows XRD patterns of $MAPbI_3$ thin films which were exposed to slow hydration conditions for two hours. It can be clearly seen that the monohydrate forms first before the dihydrate appears, confirming that the formation of the dihydrate is a two-step process. However, the formation of the dihydrate is accompanied by the generation of PbI_2 and the release of water molecules. The released water can be used to convert remaining non-hydrated $MAPbI_3$ to the monohydrate. Similar to the formation of the monohydrate from the dry $MAPbI_3$, also the reaction from the monohydrate to the dihydrate is reversible but limited by the phase separation of the reaction products.[65] When $MAPbI_3$ is exposed to liquid water, e.g. due to condensation of air humidity, MA can be dissolved in it leading to a permanent removal of the organic cation, which results in an irreversible degradation of the hybrid perovskite as shown in Figure 1-15c. As long as $MAPbI_3$ is not irreversibly degraded, hydrated $MAPbI_3$ can be fully converted back into the non-hydrated form just by exposing it to relatively dry air (~ 30 %RH) for several hours.[65]

In order to improve the stability of $MAPbI_3$ against moisture, several approaches have been explored so far. Noh *et al*. showed that a partial substitution of iodide by bromide leads to more stable devices since the bromide analog of $MAPbI_3$ is in general more stable towards moisture than the pure iodide compound.[36,80] However most of the developed methods to make $MAPbI_3$ based photovoltaics less sensitive against moisture are based on the protection of the perovskite layer from direct contact with water, such as crystal crosslinking,[81] the adoption of protective transport layers or electrodes[82,83] and the use of hydrophobic materials.[84]

Besides humidity, other factors of importance during the operation of a solar cell can also lead to the degradation of the hybrid perovskite. Thus, considering the low thermal conductivity of $MAPbI_{3,}$ heat deposited by light cannot be distributed effectively. Considering that conventional solar panels based on silicon featuring a much higher thermal conductivity can heat up to more than 60 °C during summertime, the thermal stability of $MAPbI_3$ becomes a critical issue.[85–87] Studies by Juarez-Perez *et al.* revealed that $MAPbI_3$ starts to degrade already at relatively low temperatures of about 80 °C under ambient conditions.[88] Since the thermal degradation of $MAPbI_3$ at such low temperatures is characterized by a loss of the organic cation, a common method to increase the thermal stability of the perovskite is to replace the organic molecule by the inorganic cesium.[88,89] Also, doping of the perovskite with other metal cations, such as Mn^{2+} or Zn^{2+}, has been proposed to have a beneficial influence on the thermal stability of the compound.[90]

However, the substitution of the organic cation by Cs points to another common issue of lead halide perovskites, which is the presence of different structural modifications of the same compound. In the case of $CsPbI_3$, the desired black phase needed for optoelectronic applications is not stable at room temperature.[91,92] In order estimate the stability of ABX_3 perovskites, the so-called tolerance factor (*t)* can be used, which was introduced by

Goldschmidt in 1927.[93] In the case of an ABX_3 perovskite, *t* is depends on the radii *r* of the ions A, B and X and is defined as follows:

$$\boldsymbol{t = \frac{r_A + r_X}{\sqrt{2}\,(r_B + r_X)}} \tag{1-1}$$

In general, a *t* value between 0.9 and 1 leads to an ideal cubic structure while *t* values between 0.71 and 0.9 result in distorted perovskite structures with tilted octahedra. Values below 0.71 and above 1 do not lead to perovskite structures.[93] Accordingly, $MAPbI_3$ features a distorted perovskite structure due to its low *t* value of about 0.83. Despite the low *t* value, $MAPbI_3$ can undergo a phase transition to the cubic phase upon heating to at least 54 °C.[68,94] Since the phase transition of $MAPbI_3$ occurs in a temperature range which is typical for solar cell operation temperatures in summer, the transition can have negative effects on the device performance. For example, the permanent cycling between two crystal structures during day and night could lead to material fatigue and a reduced device lifetime.

In order to avoid a phase transition at solar cell operation conditions, MA can be replaced by FA, which leads to a perovskite phase transition at 125 °C.[95] Due to the large *t* value of more than 1, the desired photoactive α-phase of $FAPbI_3$ is not stable at room temperature. Instead the non-photoactive hexagonal δ-phase forms.[96] Figure 1-16a shows the crystal structures of PbI_2 and of resulting compounds when either MA or FA is incorporated, including the high temperature polymorphs.[67]

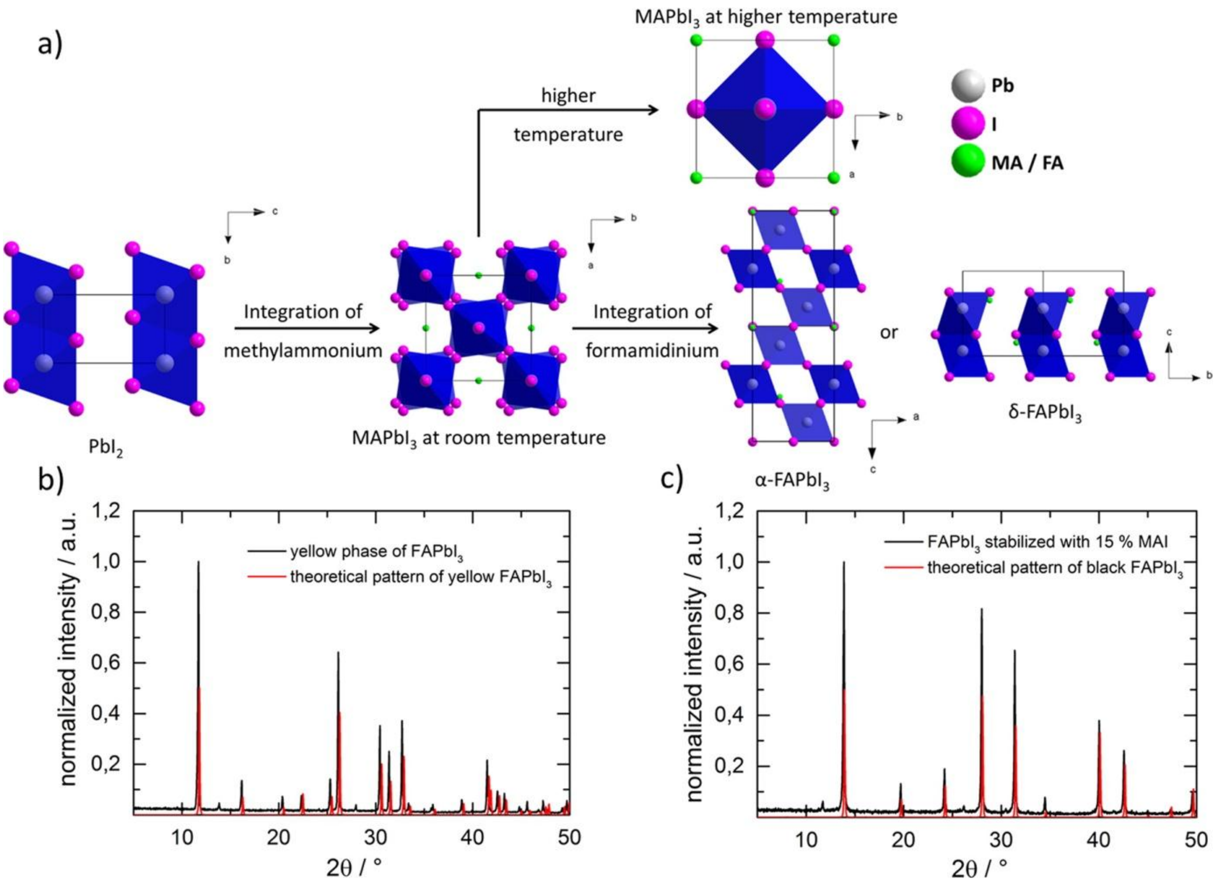

Figure 1-16: a) Crystal structures of PbI_2 and the resulting compounds when either MA or FA is incorporated, including the high temperature polymorphs. b) PXRD pattern of $FAPbI_3$. c) PXRD pattern of $FAPbI_3$ stabilized with 15 % MAI.[67]

According to Figure 1-16a, the thermodynamically more stable δ-$FAPbI_3$ phase consists of layers of face-sharing PbI_6 octahedra forming a 2D structure. Due to the lower dimensionality of the PbI_6 octahedra scaffold compared to the 3D assembly in the photoactive α-$FAPbI_3$ phase, the δ-$FAPbI_3$ phase exhibits an increased BG energy of 2.2 eV and compromised charge transport properties. A viable method to stabilize the α-$FAPbI_3$ phase is the partial substitution of FA by MA. The replacement of 15 % FA by MA completely suppresses the phase transition from the α to the δ phase in a temperature range from RT to 220 °C. Despite the incorporation of the smaller MA cation, PXRD measurements do not show any change in the lattice parameters between the pure α-$FAPbI_3$ phase and the MA/FA mixed phase, see Figure 1-16b & c. Furthermore, also the optoelectronic properties of the neat $FAPbI_3$ and the MA/FA mixed phase are very similar.[67] A possible explanation for the stabilization of α-$FAPbI_3$ by the partial substitution of FA by MA can be an increased overall hydrogen bonding strength between the organic cation and the iodide or an increase of the Madelung energy.

Also, a combination of both effects is conceivable. State-of-the-art solar cells comprising FA/MA mixed cation perovskite films achieve PCEs of more than 20 %.[97]

1.2.2 Toxicity

Previous studies on $MAPbI_3$ films that were exposed to simulated rain revealed that the lead, which is hazardous to the environment and human health, can be easily washed off the substrate due to the relatively high solubility of PbI_2 in water.[98-101] In particular, water-soluble lead salts can be easily absorbed by living organism, making lead very harmful. Although the acute toxicity of lead is relatively low, the long-term uptake of a small amount of 1 mg lead per day will lead to symptoms of a chronic lead poisoning, such as birth defects.[102–105] Similar to most of the other heavy metals, lead has a negative influence on many biological processes. Furthermore, it is harmful to many different tissues and organs, including heart, bones, kidneys, reproductive and nervous systems. Additionally, it affects the brain, which is the organ being the most sensitive to lead. Thus, lead poisoning can cause permanent learning and behavior disorders in children.[106]

Accordingly, the US Environmental Protection Agency (EPA) has restricted the maximum accepted lead levels in water and air to 15 and 0.15 µg/L, respectively and the Center for Disease Control (CDC) has set standards regarding elevated lead concentrations in the blood for adults to 10 µg/dL and for children to 5µg/dL.[107,108] Accordingly, the lead content in many different products, such as gasoline, ceramics, water pipe solder and paints has been limited and even dramatically reduced during the last decades. Considering the significant hazardousness of lead and the relatively high water solubility of lead salts, the lead content of lead halide perovskite based photovoltaics is considered to be a major obstacle for the commercialization of this technique.

Additionally, the processing of perovskite based photovoltaics can be quite harmful due to the need for hazardous solvents, such as *N*,*N*-dimethylformamide (DMF), dimethyl sulfoxide (DMSO) and *N*-methyl-2-pyrrolidone (NMP) to dissolve the perovskite. In particular DMF, which is the most common solvent for the preparation of perovskite films, is known to be hepatotoxic and is classified to be harmful for reproduction.[109-112] Accordingly, there is also an urgent need for replacing these solvents by less hazardous alternatives. However, since by far the most effort has been put into the search for less hazardous alternatives to lead, only the developments in the field of lead-free perovskites will be discussed in the following.

In order to find less hazardous alternatives to lead, many different lead-free perovskites have been investigated for their viability for photovoltaic applications. The most obvious alternatives are the elements tin (Sn) and germanium (Ge), which are also members of group 14 in the periodic table. But while lead is featuring a stable oxidation state 2+, the stability of this oxidation state drastically decreases when moving up the periodic table. However, photovoltaic devices comprising either Sn^{2+} or Ge^{2+} have been prepared. Tauc plots and current-voltage characteristics of different Ge^{2+} based perovskites are displayed in Figure 1-17a & b.

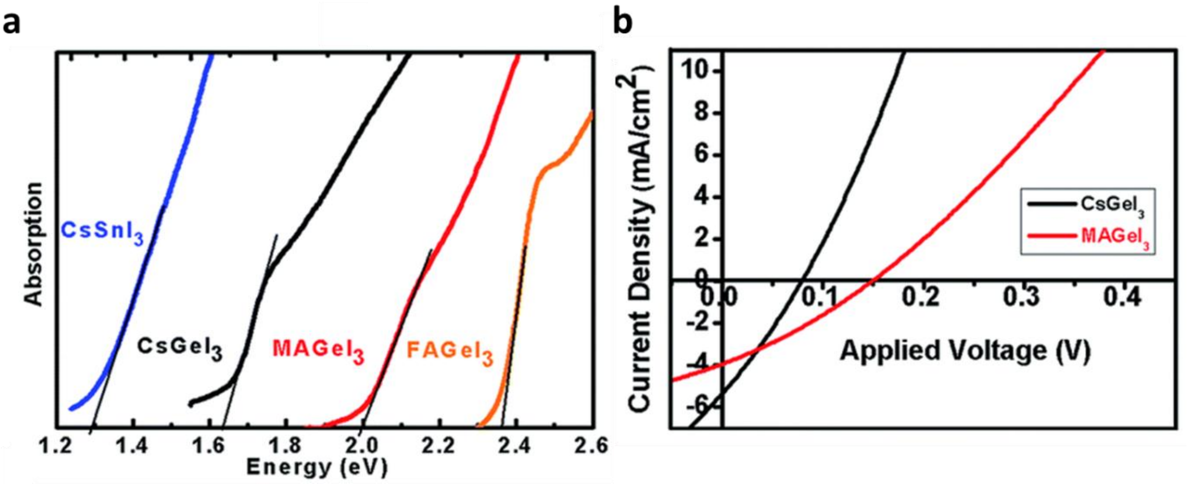

Figure 1-17 a) Tauc plots of $CsSnI_3$, $CsGeI_3$, $MAGeI_3$ and $FAGeI_3$. The Tauc plot of the tin based perovskite is given as reference. b) Current-voltage curves of solar cells with $CsGeI_3$ and $MAGeI_3$.[113]

According to Figure 1-17a, the BG energy of Ge based perovskites increases with increasing size of the A^+ cation, with $CsGeI_3$ featuring a BG energy close to the ideal BG given by the Schockley-Queisser limit.[14] However, Ge^{2+} perovskite based photovoltaics show very poor performance with a maximum PCE of 0.2 % for a $MAGeI_3$ based solar cell. The low performance of these devices is mainly attributed to the formation of Ge^{4+} due to oxidation.[113]

Hybrid perovskites based on the other group 14 element, Sn, have been extensively investigated during the last decade. They have shown good mobilities in transistors and they can become metallic depending of their composition.[114,115] In 2014, Noel *et al.* reported on $MASnI_3$ based solar cells with PCEs of more than 6 %.[116] Similar to $MAPbI_3$, $MASnI_3$

crystallizes in a tetragonal structure with similar lattice parameters as the Pb-based analog. Furthermore, $MASnI_3$ exhibits promising optoelectronic properties for photovoltaic applications. Thus, the optical absorption of $MASnI_3$ covers the whole visible and partially the near infrared starting from about 1000 nm. Similar to $MAPbI_3$, $MASnI_3$ features a strong photoluminescence signal at about 980 nm, being red-shifted compared to its Pb-based counterpart.[116] The crystal structure and the optoelectronic properties of $MASnI_3$ are given in Figure 1-18a & b.

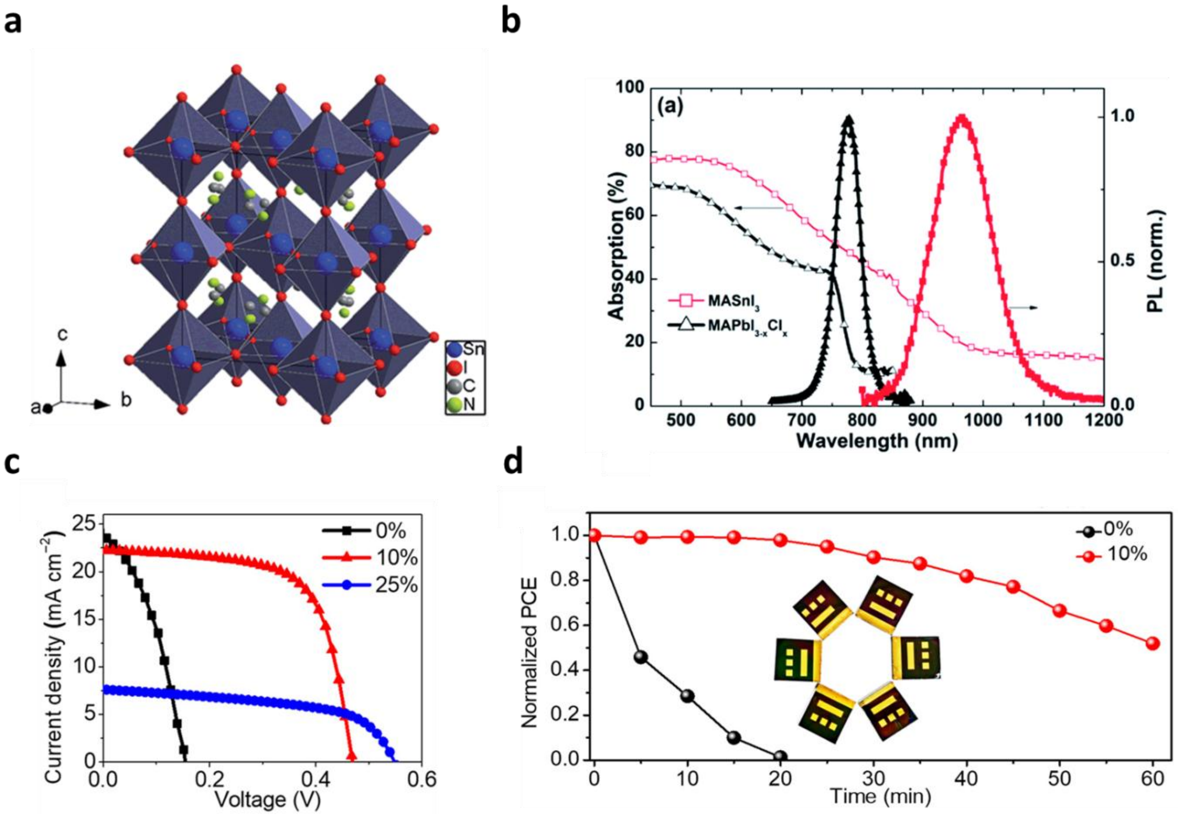

Figure 1-18 a) Crystal structure of $MASnI_3$ b) Absorption and photoluminescence spectra of $MAPbI_3$ and $MASnI_3$. The $MAPbI_3$ data are given as reference.[116] c) Current-voltage characteristics of $FASnI_3$ based solar cells where 0 %, 10 % or 25 % of the FA were replaced by ethylenediammonium (en). d) Evolution of the device performance of un-encapsulated $FASnI_3$ based solar cells with and without the addition of en.[117]

Since the first reports on Sn halide perovskite based solar cells, much effort has been put into the improvement of the device performance and stability, resulting in Sn perovskite based photovoltaics exhibiting a higher stability under ambient conditions with PCEs of more than 7 %, see Figure 1-18c & d.[117] However, despite this progress, Sn^{2+} based photovoltaics still suffer from a rapid degradation upon exposure to oxygen and moisture.

Extensive investigations have also been carried out with divalent transition metals in order to overcome the stability problems of Sn^{2+} based perovskites. In particular, copper (Cu) is considered to be possible substitute for lead. Initially, hybrid Cu halide compounds were studied mainly due to their interesting magnetic properties.[118,119] First investigations on hybrid Cu halide perovskites for the application in photovoltaics have been carried out by Cortecchia *et al.*, where they synthesized and characterized $(MA)_2CuCl_xBr_{4-x}$. However, due to the small ionic radius, Cu forms 2D layered structures even with the relatively small MA cation, see Figure 1-19a.[120]

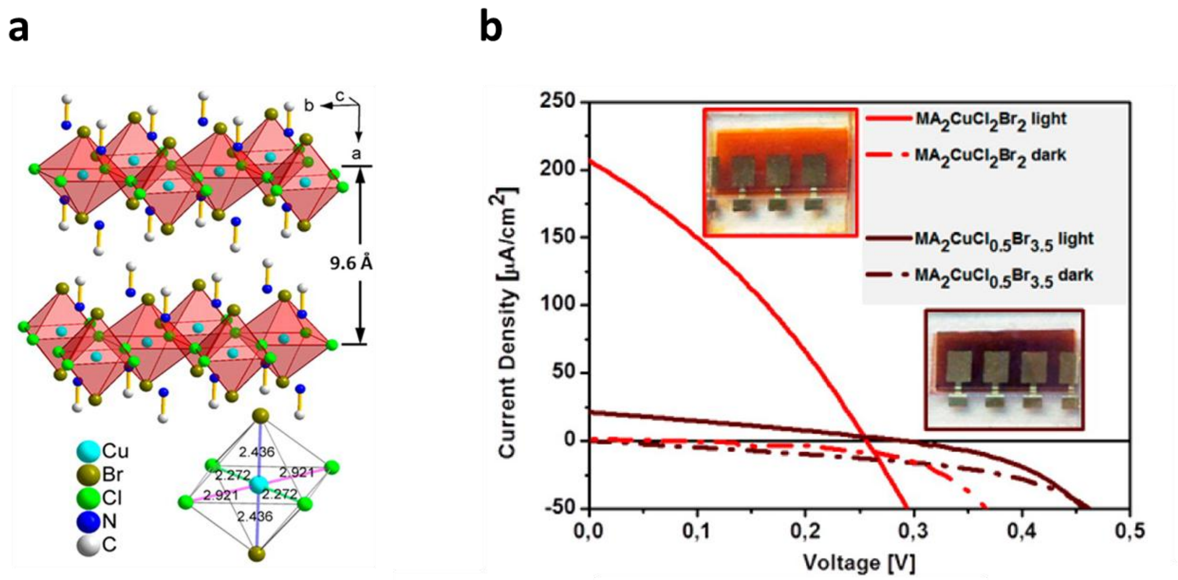

Figure 1-19 a) Crystal structure of $(MA)_2CuCl_xBr_{4-x}$ b) Current voltage characteristics of Cu based hybrid perovskites with different Cl/Br ratios.[120]

Regarding the optical properties, the absorption onset of the MACu halide based compound gets red-shifted with increasing bromide content covering nearly the full visible range. However, a pure bromide perovskite is not favorable since the Cu^{2+} gets reduced by the bromide. Therefore, the use of chloride is needed to stabilize the hybrid perovskite. Current-voltage curves of $(MA)_2CuCl_xBr_{4-x}$ based solar cells comprising two different Cl/Br ratios are depicted in Figure 1-19b. Although both materials show a very low performance, the much lower performance of the Br rich phase can be explained by trap states which are induced due to the reduction of copper. The low overall performance of $(MA)_2CuCl_xBr_{4-x}$ based solar cells is caused by a combination of a low absorption coefficient and a heavy mass for holes.[120]

Recent works on Cu perovskites featuring larger cations could strongly increase the device performance to more than 0.6 %.[121] This increase in efficiency holds promise for better working devices in the future.

Due to the stability issues of Sn^{2+} and the very low performance of Cu^{2+} based photovoltaics, elements that do not exhibit the oxidation state 2+ have also been investigated. The most obvious candidates are group 15 elements. These elements, generally, feature an ns^2np^3 valence shell configuration and can occur in the oxidation states 3-, 3+, 5+. Despite the different possible oxidation states of group 15 elements the oxidation state 3+ gets stabilized with increasing atomic mass due to the inert pair effect.[122] Accordingly, Bi^{3+} is the most stable cation of the heaviest group 15 element Bi. Combined with its low toxicity, Bi is a very promising candidate for lead free photovoltaics.[123]

First Bi perovskite based photovoltaics have been reported by Park *et al.*, utilizing $A_3Bi_2I_9$, where A can be Cs or MA, as photoactive layer. Such perovskites are built of bioctahedral $(Bi_2I_9)^{3-}$ clusters surrounded by the organic or inorganic cations. The crystal structure of $Cs_3Bi_2I_9$ is given in Figure 1-20a.[124]

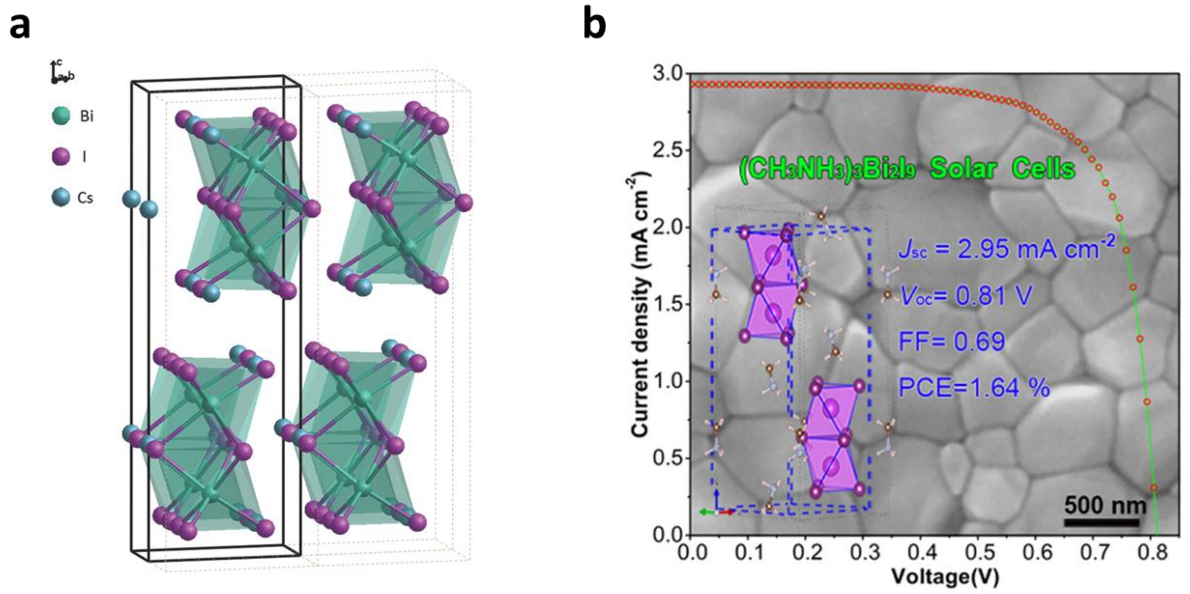

Figure 1-20 a) Crystal structure of $Cs_3Bi_2I_3$[124] b) Current-voltage characteristic of a $MA_3Bi_2I_9$ based solar cell featuring a high quality absorber layer.[125]

Both $Cs_3Bi_2I_9$ and $MA_3Bi_2I_9$ feature a BG energy of about 2.2 eV, but only the fully inorganic perovskite exhibits a relatively strong, broad photoluminescence signal with its maximum at about 650 nm. Solar cells comprising absorber layers of $MA_3Bi_2I_9$ or $Cs_3Bi_2I_9$ showed PCEs of 0.12 % and 1.09 %, respectively.[124] The rather low performance compared to $MAPbI_3$ based photovoltaics is attributed to the lower absorption coefficient of $A_3Bi_2I_9$ and the higher number of traps states within the Bi perovskite crystals. Furthermore, the poor film quality of the$A_3Bi_2I_9$ films is also considered to be a major issue impeding high PCEs. Accordingly, Zhang *et al.* developed a new synthesis route to obtain high quality $MA_3Bi_2I_9$ films resulting in devices showing more than 1.6 % PCE with high long-term stability, see Figure 1-20b.[125]

Another promising Bi-based materials class for photovoltaic applications is called Rudorffites and is derived from the $NaVO_3$ structure. Rudorffites feature the general formula $A_aB_bX_x$ ($x = a+3b$), where A: Ag, Cu; B: Bi, Sb; X: I, Br. This structure is based on edge-sharing AX_6 and BX_6 octahedra, which is different from the typical perovskite structure comprising corner-sharing metal halide octahedra, see Figure 1-21a.[126]

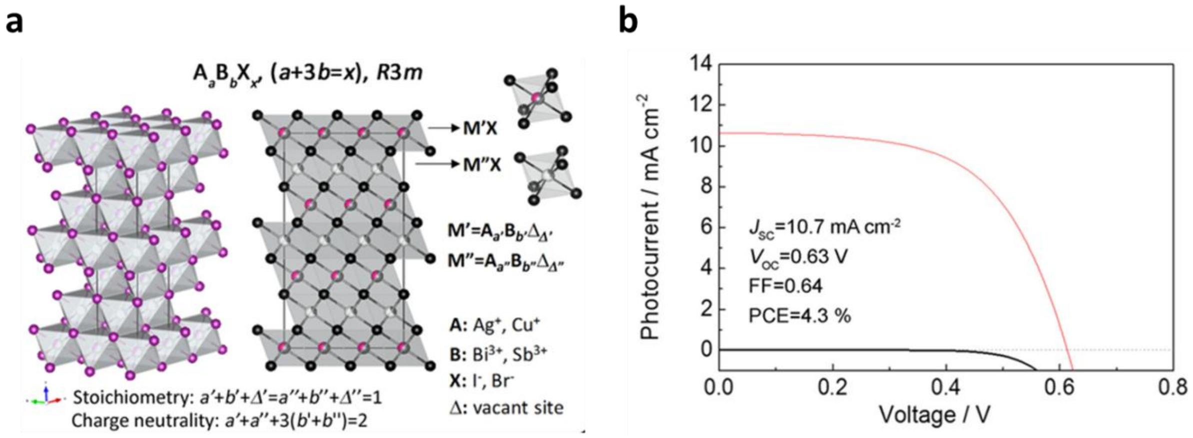

Figure 1-21 a) General crystal structure of Rudorffites b) Current-voltage characteristic of a Ag_3BiI_6 based solar cell.[126]

In contrast to the above-mentioned Cu and Bi based perovskites where structures of low dimensionality are formed, Rudorffites form a continuous 3D structure of connected metal halide octahedra, which holds promise for good charge transport properties. The most promising Rudorffites for photovoltaic applications are Ag-Bi based iodides due to their relatively small BG of about 1.8 eV. Accordingly, several groups have reported on solar cells based on Ag-Bi iodides with different composition, namely $AgBi_2I_7$, Ag_2BiI_5 and Ag_3BiI_6.[126–128] In particular, Ag_3BiI_6 based devices showed an impressively high PCE of more than 4 % pointing to the high potential of Bi based photovoltaics, see Figure 1-21b.

Besides Rudorffites, another class of Bi based materials, the so-called double perovskites, have attracted a lot of attention for the use in photovoltaics. Bismuth-based double perovskites, also called elpasolites, feature a highly symmetrical cubic structure with the general formula $A_2M^{1+}BiX_6$ consisting of a 3D network of corner-sharing metal halide octahedra. Although Bi-based double perovskites comprising A = Rb, Cs, CH_3NH_3; M^{1+} = Na, K, Tl and X = F, Cl, Br have been studied for several decades, they did not come into focus for photovoltaic applications due to their large BG of more than 3 eV or their toxicity in case of Tl.[129–134] This changed as several groups have reported on the synthesis of a Bi^{3+} based double perovskite with Ag^+ as monovalent cation featuring an BG of about 2 eV for the bromide based material, see Figure 1-22a, b & c.[135–140]

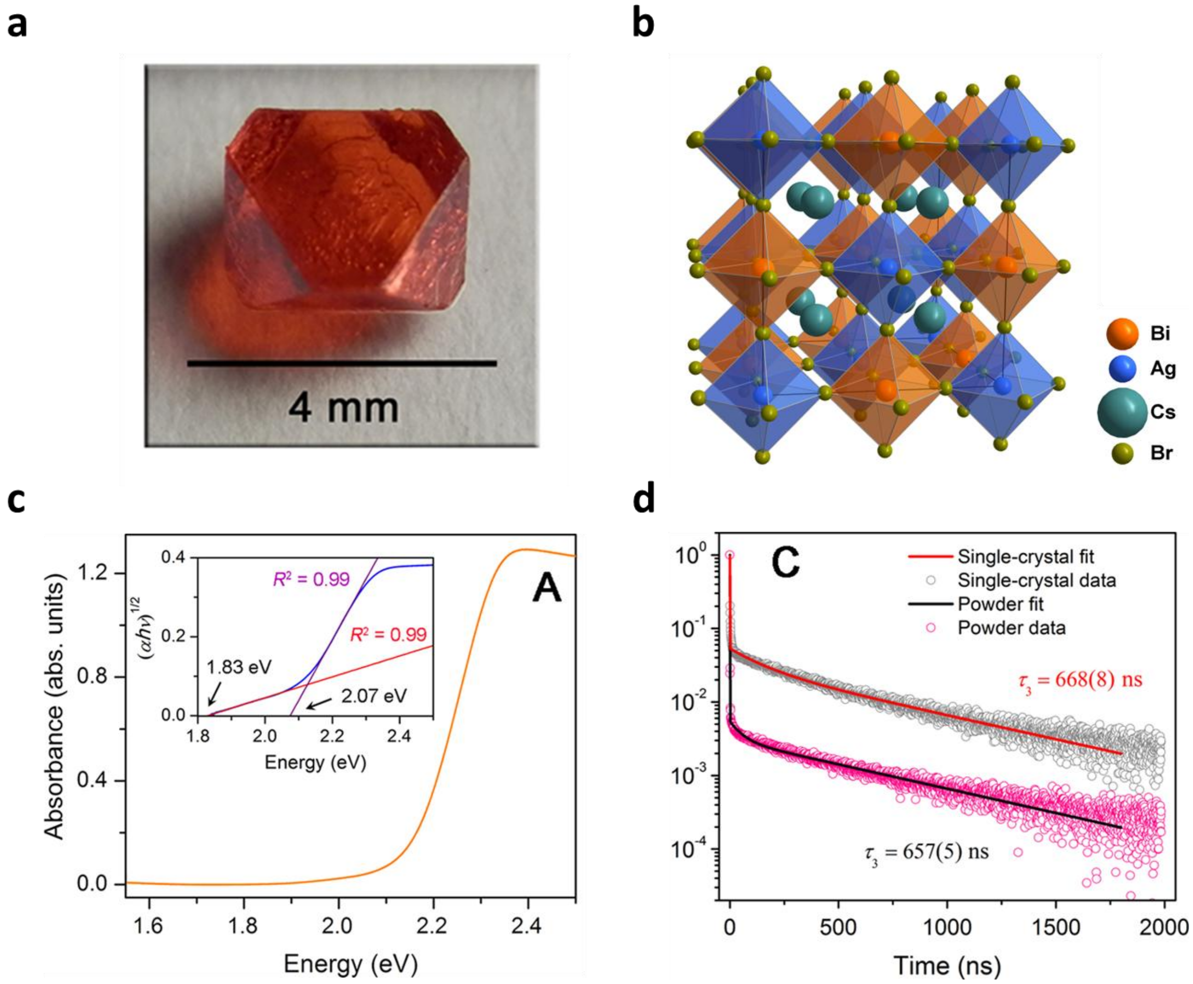

Figure 1-22 a) Image of a $Cs_2AgBiBr_6$ single crystal. b) Crystal structure of $Cs_2AgBiBr_6$. c) Absorbance spectrum and Tauc plot of a $Cs_2AgBiBr_6$ single crystal. d) Time-resolved photoluminescence decays of $Cs_2AgBiBr_6$ crystals and powders.

Together with the long photoluminescence lifetimes of several hundred nanoseconds (see Figure 1-22d) and calculated charge carrier effective masses close to those calculated for $MAPbI_3$, Ag-Bi based double perovskites are promising candidates for photovoltaic applications.[135–140] Recent studies on $Cs_2AgBiBr_6$ films for photovoltaic applications revealed encouraging PCEs of almost 2.5 % for devices comprising a mesoporous TiO_2 layer and 1.44 % for devices featuring a planar assembly.[141,142] Considering that these are the very first reported PCEs of double perovskite based solar cells, belonging to the highest of all reported lead-free perovskite solar cells (except Sn^{2+} based devices, which are fairly unstable), Bi halide double perovskites hold promise for non-toxic and stable photovoltaics, which may become competitive in comparison with Pb halide perovskite based solar cells.

1.3 Literature

[1] https://ec.europa.eu/clima/policies/international/negotiations/paris_de

[2] *Fundamentals of Materials for Energy and Environmental Sustainability*, Cambridge University Press, Cambridge, UK **2011**.

[3] http://www.ren21.net/status-of-renewables/global-status-report/

[4] https://www.eia.gov/outlooks/ieo/

[5] V. Scott, R. S. Haszeldine, S. F. B. Tett, A. Oschlies, *Nature Clim. Change* **2015**, *5*, 419.

[6] P. Denholm, G. L. Kulcinski, T. Holloway, *Environ. Sci. Technol.* **2005**, *39*, 1903.

[7] D. Di, K. P. Musselman, G. Li, A. Sadhanala, Y. Ievskaya, Q. Song, Z.-K. Tan, M. L. Lai, J. L. MacManus-Driscoll, N. C. Greenham, R. H. Friend, *J. Phys. Chem. Lett.* **2015**, *6*, 446.

[8] G. Xing, N. Mathews, S. S. Lim, N. Yantara, X. Liu, D. Sabba, M. Grätzel, S. Mhaisalkar, T. C. Sum, *Nat. Mater.* **2014**, *13*, 476.

[9] M. A. Green, A. Ho-Baillie, H. J. Snaith, *Nat. Photon.* 2014, 8, 506.

[10] P. Würfel, *Physics of Solar Cells: From Basic Principles to Advanced Concepts*, John Wiley & Sons, Weinheim **2009**.

[11] B. Cocilovo, A. Hashimura, D. J. Tweet, T. Voutsas, R. A. Norwood, *Appl. Opt.* **2015,** *54*(30), 8990.

[12] C. Gueymard, D. Myers, K. Emery, *Sol. Energy* **2002,** *73*(6), 443.

[13] F. H. Alharbi, S. Kais, *Renewable and Sustainable Energy Review* **2015,** *43*, 1073.

[14] W. Shockley, H. J. Queisser, *J. Appl. Phys.* **1961,** *32*(3), 510.

[15] A. Goetzberger, J. Knobloch, B. Voß, *Crystalline Silicon Solar Cells*, John Wiley & Sons, **1998**.

[16] M. A. Green, *Prog. Photovoltaics* **2012**, *20*, 472.

[17] M. A. Green, *Crystalline Silicon Solar Cells*, Ch 4 Green ed MA2.doc, **2001**.

[18] D. S. Ginley, D. Cahen, *Fundamentals of Materials for Energy and Environmental Sustainability*, Cambridge University Press, United Kingdom **2012**.

[19] A. Goodrich, P. Hacke, Q. Wang, B. Sopori, R. Margolis, T. L. James. M. Woodhouse, *Sol. Energ. Mat. Sol. Cells.* **2013,** *114*, 110.

[20] S. A. Ovshinsky, A. Madan, *Nature* **1978,** *276*, 482.

[21] A. G. Aberle, *Thin Solid Films*, **2009,** *501*, 4706.

[22] J. Cárabe, J. J. Gandia, *Opto-Electron. Rev.* **2004,** *12*(1), 1

[23] L. Staebler, C.R. Wronski, *Appl. Phys. Lett* **1977,** *31*, 292.

[24] C. B. Singh, S. Bhattacharya, V. Sing, P. B. Bhargav, S. Sarkar, V. Bhavanasi, N., Ahmad, *J. Renew. Sustain. Energy* **2013,** *5*, 031605.

[25] A. Parisi, R. Pernice, V. Rocca, L. Curcio, S. Stivala, A. C. Cino, G. Cipriani, V. Di Dio, G. R. Galuzzo, R. Miceli, A. C. Busacca, *Int. J. Photoenergy* **2015,** *2015*, 410549.

[26] J. N. Schulman, T.C. McGill, *Appl. Phys. Lett.* **1979,** *34*(10), 663.

[27] X. Wu, *Sol. Energy* **2004**, *77*, 803.

[28] M. A. Contreras, M. J. Romero, R. Noufi, *Thin Solid Films* **2006**, *511–512*, 51.

[29] S. E. Shaheen, D. S. Ginley, G. E. Jabbour, *MRS Bull.* **2005**, *30*, 10.

[30] M. C. Scharber, N. C. Sariciftci, *Prog. Polym. Sci.* **2013,** *38*, 1929.

[31] Y.-W. Su, S.-C. Lan, K.-H. Wie, *Mater. Today*, **2012,** 15(12), 554.

[32] M. M. Lee, Joël Teuscher, Tsutomu Miyasaka, Takurou N. Murakami, Henry J. Snaith, *Science* **2012,** *338*, 643.

[33] G. E. Eperon, S. D. Stranks, C. Menelaou, M. B. Johnston, L. M. Herz, H. J. Snaith, *Energy Environ. Sci*. **2014,** *7*, 982.

[34] S. De Wolf, J. Holovsky, S.-J. Moon, P. Löper, B. Niesen, M. Ledinsky, F.-J. Haug, J.-H. Yum, C. Ballif, *J. Phys. Chem. Lett.* **2014**, *5*, 1035.

[35] S. D. Stranks, G. E. Eperon, G. Grancini, C. Menelaou, M. J. P. Alcocer, T. Leijtens, L. M. Herz, A. Petrozza, H. J. Snaith, *Science* **2013**, *342*, 341.

[36] J. H. Noh, S. H. Im, J. H. Heo, T. N. Mandal, S. I. Seok, *Nano Lett.* **2013**, *13*, 1764.

[37] A. Sadhanala, F. Deschler, T. H. Thomas, S. E. Dutton, K. C. Goedel, F. C. Hanusch, M. L. Lai, U. Steiner, T. Bein, P. Docampo, D. Cahen, R. H. Friend, *J. Phys. Chem. Lett.* **2014**, *5*, 2501.

[38] A. Kojima, K. Teshima, Y. Shirai, T. Miyasaka, *J. Am. Chem. Soc.* **2009**, *131*, 6050.

[39] J. H. Im, C. R. Lee, J. W. Lee, S. W. Park, N. G. Park, *Nanoscale* **2011**, *3*, 4088.

[40] J. M. Ball, M. M. Lee, A. Hey, H. J. Snaith, *Energy Environ. Sci.* **2013**, *6*, 1739.

[41] D. Liu, T. L. Kelly, *Nat. Photon.* **2013**, *advance online publication*.

[42] P. Docampo, J. M. Ball, M. Darwich, G. E. Eperon, H. J. Snaith, *Nat. Commun.* **2013**, *4*, 2761.

[43] C.-Y. Chang, C.-Y. Chu, Y.-C. Huang, C.-W. Huang, S.-Y. Chang, C.-A. Chen, C.-Y. Chao, W.-F. Su, *ACS Appl. Mater. Interfaces* **2015**, *7*, 4955.

[44] C. Sun, Q. Xue, Z. Hu, Z. Chen, F. Huang, H.-L. Yip, Y. Cao, *Small* **2015**.

[45] X. Song, W. Wang, P. Sun, W. Ma, Z.-K. Chen, *Appl. Phys. Lett.* **2015**, *106*, 033901.

[46] S. Pang, H. Hu, J. Zhang, S. Lv, Y. Yu, F. Wei, T. Qin, H. Xu, Z. Liu, G. Cui, *Chem. Mater.* **2014**, *26*, 1485.

[47] W. Zhang, M. Saliba, D. T. Moore, S. K. Pathak, M. T. Hörantner, T. Stergiopoulos, S. D. Stranks, G. E. Eperon, J. A. Alexander-Webber, A. Abate, A. Sadhanala, S. Yao, Y. Chen, R. H. Friend, L. A. Estroff, U. Wiesner, H. J. Snaith, *Nat. Commun.* **2015**, *6*, 6142.

[48] F. Wang, H. Yu, H. Xu, N. Zhao, *Adv. Funct. Mater.* **2015**, *25*, 1120.

[49] T. Leijtens, B. Lauber, G. E. Eperon, S. D. Stranks, H. J. Snaith, *J. Phys. Chem. Lett.* **2014**, *5*, 1096.

[50] H.-L. Hsu, C.-P. Chen, J.-Y. Chang, Y.-Y. Yu, Y.-K. Shen, *Nanoscale* **2014**, *6*, 10281.

[51] J. Troughton, C. Charbonneau, M. J. Carnie, M. L. Davies, D. A. Worsley, T. M. Watson, *J. Mater. Chem. A* **2015**, *3*, 9123.

[52] M. Saliba, K. W. Tan, H. Sai, D. T. Moore, T. Scott, W. Zhang, L. A. Estroff, U. Wiesner, H. J. Snaith, *J. Phys. Chem. C* **2014**, *118*, 17171.

[53] A. Dualeh, N. Tétreault, T. Moehl, P. Gao, M. K. Nazeeruddin, M. Grätzel, *Adv. Funct. Mater.* **2014**, *24*, 3250.

[54] C.-Y. Chang, C.-Y. Chu, Y.-C. Huang, C.-W. Huang, S.-Y. Chang, C.-A. Chen, C.-Y. Chao, W.-F. Su, *ACS Appl. Mater. Interfaces* **2015**, *7*, 4955.

[55] C.-C. Chueh, C.-Y. Liao, F. Zuo, S. T. Williams, P.-W. Liang, A. K. Y. Jen, *J. Mater. Chem. A* **2015**, *3*, 9058.

[56] J. H. Heo, D. H. Song, S. H. Im, *Adv. Mater.* **2014**, *26*, 8179.

[57] C. Sun, Q. Xue, Z. Hu, Z. Chen, F. Huang, H.-L. Yip, Y. Cao, *Small* **2015**.

[58] Y. Chen, Y. Zhao, Z. Liang, *Chem. Mater.* **2015**, *27*, 1448.

[59] X. Song, W. Wang, P. Sun, W. Ma, Z.-K. Chen, *Appl. Phys. Lett.* **2015**, *106*, 033901.

[60] P.-W. Liang, C.-Y. Liao, C.-C. Chueh, F. Zuo, S. T. Williams, X.-K. Xin, J. Lin, A. K. Y. Jen, *Adv. Mater.* **2014**, *26*, 3748.

[61] C. Zuo, L. Ding, *Nanoscale* **2014**, *6*, 9935.

[62] W. S. Yang, J. H. Noh, N. J. Jeon, Y. C. Kim, S. Ryu, J. Seo, S. I. Seok, *Science* **2015**, *348*, 1234.

[63] http://www.nrel.gov/ncpv/images/efficiency_chart.jpg

[64] H. J. Snaith, *J. Phys. Chem. Lett.* **2013,** *4*(21), 3623.

[65] A. Leguy, Y. Hu, M. Campoy-Quiles, M. I. Alonso, O. J. Weber, P. Azarhoosh, M. van Schilfgaarde, M. T. Weller, T. Bein, J. Nelson, P. Docampo, P. R. F. Barnes, *Chem. Mater.* **2015**, *27*, 3397.

[66] J. A. Christians, P. A. Miranda Herrera, P. V. Kamat, *J. Am. Chem. Soc.* **2015**, *137*, 1530

[67] A. Binek, F. C. Hanusch, P. Docampo, T. Bein, *The Journal of Physical Chemistry Letters* **2015**, *6*, 1249.

[68] T. Baikie, Y. N. Fang, J. M. Kadro, M. Schreyer, F. X. Wei, S. G. Mhaisalkar, M. Graetzel, T. J. White, *J. Mater. Chem. A* **2013**, *1*, 5628.

[69] S. N. Habisreutinger, T. Leijtens, G. E. Eperon, S. D. Stranks, R. J. Nicholas, H. J. Snaith, *Nano Lett.* **2014**, *14*, 5561.

[70] L. Patrick, *Altern. Med. Rev.* **2006**, *11*, 2.

[71] I. R. Benmessaoud, A.-L. Mahul-Mellier, E. Horvath, B. Maco, M. Spina, H. Lashuel, L. Forro, *Toxicol. Res.* **2015**, *5*, 407.

[72] D. C. Jordan, S. R. Kurtz, *Prog.Photovolt:Res.Appl.* **2013,** *21*, 12.

[73] Y. Rong, L. Liu, A. Mei, X. Li, H. Han, *Adv. Energy Mater.* **2015**, *5*, 1.

[74] T. Leijtens, G. E. Eperon, N. K. Noel, S. N. Habisreutinger, A. Petrozza, H. J. Snaith, *Adv. Energy Mater.* **2015**, *5*, 1.

[75] P. Docampo, T. Bein, *Acc. Chem. Res.* **2016**, *49*, 339.

[76] F. Q. Zhang, X. C. Yang, H. X. Wang, M. Cheng, J. H. Zhao, L. C. Sun, L. C., *ACS Appl. Mater. Interfaces* **2014,** *6*, *16140*.

[77] H. W. Zhou, Y. T. Shi, Q. S. Dong, H. Zhang, Y. J. Xing, K. Wang, Y. Du, T. L. Ma, T. L., *J. Phys. Chem. Lett.* **2014,** *5*, 3241.

[78] J. M. Frost, K. T. Butler, F. Brivio, C. H. Hendon, M. van Schilfgaarde, A. Walsh, *Nano Lett.* **2014**, *15*, 2584.

[79] F. Hao, C. C. Stoumpos, R. P. H. Chang, M. G. Kanatzidis, *J. Am. Chem. Soc.* **2014**, *136,* 8094.

[80] Z. Cheng, J. Lin, *CrystEngComm.* **2010,** *12,* 2646.

[81] S. Luo, W. A. Daoud, *J. Mater. Chem. A* **2015**, *3,* 8992.

[82] J. H. Kim, P.-W. Liang, S. T. Williams, N. Cho, C.-C. Chueh, M. S. Glaz, D. S. Ginger, A. K. Y. Jen, *Adv. Mater.* **2015**, *27,* 695.

[83] Y. S. Kwon, J. Lim, H.-J. Yun, Y.-H. Kim, T. Park, *Energy & Environmental Science* **2014**, *7,* 1454.

[84] Y. Hu, J. Schlipf, M. Wussler, M. L. Petrus, W. Jaegermann, T. Bein, P. Müller-Buschbaum, P. Docampo, *ACS Nano* **2016**, *10,* 5999.

[85] A. Pisoni, J. Jaćimović, O. S. Barišić, M. Spina, R. Gaál, L. Forró, E. Horváth, *J. Phys. Chem. Lett.* **2014**, *5*, 2488.

[86] C. J. Glassbrenner, G. A. Slack, *Phys. Rev.* **1964,** *134*, A1058.

[87] M. Koehl, M. Heck, S. Wiesmeier, J. Wirth, *Sol. Energ. Mat. Sol. Cells.* **2011,** *95*, 1638.

[88] E. J. Juarez-Perez, Z. Hawash, S. R. Raga, L. K. Ono, Y. Qi, *Energy Environ. Sci.* **2016,** *9*, 3406.

[89] M. Kulbak, S. Gupta, N. Kedem, I. Levine, T. Bendikov, G. Hodes, D. Cahen,.

J. Phys. Chem. Lett. **2016,** *7,* 167.

[90] A. Swarnkar, W. J. Mir, A. Nag, *ACS Energy Lett.* **2018,** *3*, 286.

[91] G. E. Eperon, G. M. Paterno, R. J. Sutton, A. Zampetti, A. A. Haghighirad, F. Cacialli, H. J. Snaith, *J. Mater. Chem. A* **2015,** *3,* 19688.

[92] A. Swarnkar, A. R. Marshall, E. M. Sanehira, B. D. Chernomordik, D. T. Moore, J. A. Christians, T. Chakrabarti, J. M.Luther, *Science* **2016,** *354,* 92.

[93] V. M. Goldschmidt, *Naturwissenschaften* **1926**, *14,* 477.

[94] M. A. Green, A. Ho-Baillie, H. J. Snaith, *Nat.Photonics* **2014,** *8,* 506.

[95] C. C. Stoumpos, C. D. Malliakas, M. G. Kanatzidis, *Inorg. Chem.* **2013**, *52*, 9019.

[96] Z. Li, M. Yang, J.-S. Park, S.-H. Wei, J. J. Berry, K. Zhu, *Chem. Mater.* **2016,** *28*, 284.

[97] N. J. Jeon, J. H. Noh, W. S. Yang, Y. C. Kim, S. Ryu, J. Seo, S. Seok, *Nature* **2015**, *517*, 476.

[98] P. Patnaik, *Handbook of Inorganic Chemicals*, McGraw-Hill, NewYork **2003**.

[99] B. Hailegnaw, S. Kirmayer, E. Edri, G. Hodes, D. Cahen, *J.Phys.Chem.Lett*. **2015,** *6*, 1543.

[100] L. Patrick, *Altern Med Rev* **2006**, *11*, 2.

[101] I. R. Benmessaoud, A.-L. Mahul-Mellier, E. Horvath, B. Maco, M. Spina, H. Lashuel, L. Forro, *Toxicol Res* **2015**, *5*, 407.

[102] R. Ludewig, K. Lohs, *Akute Vergiftungen. 6. Auflage*, Gustav-Fischer-Verlag, Stuttgart **1981.**

[103] R. A. Goyer, T. W. Clarkson, *Toxic Effects of Metals*, Vol. 1236, McGraw-Hill, New York **1996**.

[104] A. Demayo, M. C. Taylor, K. W. Taylor, P. V. Hodson, P. B. Hammond, *Crit. Rev. Env. Contr.* **1982**, *12*, 257.

[105] R. A. Goyer, *Environ. Health Perspect.* **1990**, *86*, 177.

[106] K. M. Cecil, C. J. Brubaker, C. M. Adler, K. N. Dietrich, M. Altaye, J. C. Egelhoff, S. Wessel, I. Elangovan, R. Hornung, K. Jarvis, B. P. Lanphear, *PLoS Med* **2008**, *5*, 112.

[107] USA Environmental Protection Agency Lead Laws and Regulations, http://www2.epa.gov/lead/lead-laws-and-regulations (retrieved on 01/08/2018).

[108] Advisory Committee On Childhood Lead Poisoning Prevention (ACCLPP), http://www.cdc.gov/nceh/lead/ACCLPP/acclpp_main.htm (retrieved on 01/09/2018).

[109] G. L. Jr. Kennedy, *Crit. Rev. Toxicol*. **1986,** *17*, 129.

[110] V. Scailteur, E. DeHoffmann, J. P. Buchet, R. Lauwerys, *Toxicol*. **1984,** *29*, 221.

[111] L. E. Fleming, S. L. Shalat, C. A. Redlich, *Scand J. Work Environ. Health* **1990,** *16*, 289.

[112] REACH-clp-biozid-helpdesk. Available online: http://www.reach-clp-biozidhelpdesk.de/de/ REACH/ Kandidatenliste/Listen/N,NDimethylformamid/ N,N-Dimethylformamid_content.html in german (accessed on 8 June 2017).

[113] T. Krishnamoorthy, H. Ding, C. Yan, W. L. Leong, T. Baikie, L. Zhang, M. Sherburne, S. Li, M. Asta, N. Mathews, et al., *J. Mater. Chem. A* **2015,** *3*, 23829.

[114] C. Kagan, D. Mitzi, C. Dimitrakopoulos, *Science* **1999**, *286*, 945.

[115] D. B. Mitzi, C. Feild, Z. Schlesinger, R. Laibowitz, *J. Solid State Chem.* **1995**, *114*, 159.

[116] N. K. Noel, S. D. Stranks, A. Abate, C. Wehrenfennig, S. Guarnera, A.-A. Haghighirad, A. Sadhanala, G. E. Eperon, S. K. Pathak, M. B. Johnston, A. Petrozza, L. M. Herz, H. J. Snaith, *Energy & Environmental Science* **2014**, *7*, 3061.

[117] W. Ke, C. C. Stoumpos, M. Zhu, L. Mao, I. Spanopoulos, J. Liu, O. Y. Kontsevoi, M. Chen, D. Sarma, Y. Zhang, et al., *Sci. Adv.* **2017,** *3*, e1701293.

[118] R. Willett, H. Place, M. Middleton, *J. Am. Chem. Soc.***1988**, *110*, 8639.

[119] L. O. Snively, J. E. Drumheller, K. Emerson, *Phys. Rev. B*: *Condens. Matter Mater. Phys.* **1981,** *23*, 6013.

[120] D. Cortecchia, H. A. Dewi, J. Yin, A. Bruno, S. Chen, T, Baikie, P. P. Boix, M. Grätzel, S. Mhaisalkar, C. Soci, et al., *Inorg. Chem.* **2016,** *55*, 1044.

[121] X.-P. Cui, K.-J. Jiang, J.-H. Huang, Q.-Q. Zhang, M.-J. Su, L.-M. Yang, Y.-L. Song, X.-Q. Zhou, *Synth. Met.* **2015,** *209*, 247.

[122] R. S. Drago, *J. Phys. Chem.* **1958**, *62*, 353.

[123] H. Suzuki, N. Komatsu, T. Ogawa, T. Murafuji, T. Ikegami, Y. Matano, *Organobismuth chemistry*, Elsevier, Netherlands **2001**.

[124] B.-W. Park, B. Philippe, X. Zhang, H. Rensmo, G. Boschloo, E. M. J. Johansson, *Adv. Mater.* **2015**, *27*, 6806.

[125] Z. Zhang, X. Li, X. Xia, Z. Wang, Z. Huang, B. Lei, Y. Gao, *J. Phys. Chem. Lett.* **2017,** *8*, 4300.

[126] I. Turkevych, S. Kazaoui, E. Ito, T. Urano, K. Yamada, H, Tomiyasu, H. Yamagishi, M. Kondo, S.Aramaki, *ChemSusChem* **2017,** *10*, 3754.

[127] Y. Kim, Z. Yang, A. Jain,O. Voznyy, G.-H. Kim, M. Liu, L. N. Quan , F.P.García de Arquer, R. Comin, J. Z. Fan,E. H. Sargent, *Angew.Chem.Int. Ed.* **2016,** *55* ,9586.

[128] H. Zhu, M. Pan, M. B. Johansson, E. Johansson, *ChemSusChem 2017, 10,* 2592.

[129] L. R. Morrs and W. R. Robinson, *Acta Crystallogr., Sect. B: Struct. Crystallogr. Cryst. Chem.*, 1972, **28,** 653.

[130] F. Pelle, B. Jacquier, J. Denis and B. J. Blanzat, *Lumin*., 1978, **17,** 61.

[131] W. Smit, G. Dirksen and D. Stufkens, *J. Phys. Chem. Solids.*, 1990, **51,** 189.

[132] Z. Deng, F. Wei, S. Sun, G. Kieslich, A. K. Cheetham and P. D. Bristowe, *J. Mater. Chem. A 2016, 4,* 12025.

[133] A. Tressaud, S. Khaïroun, J. P. Chaminade and M. Couzi, *Phys. Status Solidi A* 1986, ***98,*** 417–421.

[134] F. Wei, Z. Deng, S. Sun, F. Xie, G. Kieslich, D.M. Evans, M. A. Carpenter, P. D. Bristowe and A. K. Cheetham, *Mater. Horiz*., 2016, **3,** 328.

[135] E. T. McClure, M. R. Ball, W. Windl and P. M. Woodward, *Chem. Mater*., 2016, **28,** 1348.

[136] A. H. Slavney, T. Hu, A. M. Lindenberg and H. I. Karunadasa, *J. Am. Chem. Soc.*, 2016, **138,** 2138.

[137] G. Volonakis, M. R. Filip, A. A. Haghighirad, N. Sakai, B. Wenger, H. J. Snaith, and F. Giustino, *J. Phys. Chem. Lett.*, 2016, **7,** 1254.

[138] F. Wei, Z. Deng, S. Sun, F. Zhang, D. M. Evans, K. Kieslich, S. Tominaka, M. A. Carpenter, J. Zhang, P. D. Bristowe and A. K. Cheetham, *Chem. Mat*., 2017, **29,** 1089.

[139] M. R. Filip, S. Hillman, A. A. Haghighirad, H. J. Snaith and F. Giustino, *J.Phys.Chem.Lett*., 2016, **7,** 2579.

[140] M. R. Filip, C. Verdi and F. Giustino, *J. Phys. Chem. C*, 2015, **119**, 25209–25219.

[141] E. Greul, M. L. Petrus, A. Binek, P. Docampo, T. Bein, *J. Mater. Chem. A* **2017,** *5*, 19972.

[142] C. Wu, Q. Zhang, Y. Liu, W. Luo, X. Guo, Z. Huang, H. Ting, W. Sun, X. Zhong, S. Wei, et al., *Adv. Sci.* **2017,** 1700759.

2 Characterization

2.1 X-Ray Diffraction

X-ray diffraction (XRD) is a widely used technique to determine the atomic structure and the phase composition of crystalline materials. XRD is based on the scattering of electromagnetic waves on structures featuring physical dimensions similar to the wavelength. Since X-rays exhibit wavelengths in the subnanometer range they are suitable for investigations of atomic structures. A schematic representation of the scattering process in an XRD measurement is given in Figure 2-1:

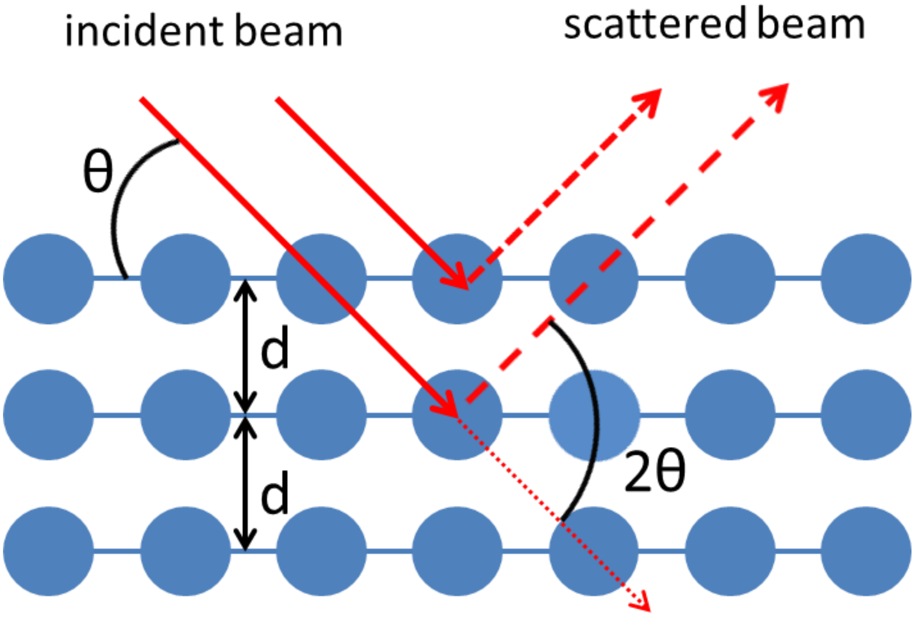

Figure 2-1: Schematic representation of the scattering process in an XRD measurement.

For the generation of X-rays, an evacuated X-ray tube can be used, which mainly consists of a cathode and an anode. The cathode is typically built of a heated filament which emits electrons upon the application of a high electric field. The emitted electrons get accelerated towards the anode by a high voltage until they impinge onto the anode material. This leads to the emission of X-rays featuring a continuous energy spectrum (Bremsstrahlung) with energies not higher than the acceleration voltage. Common anode materials like copper or molybdenum additionally emit characteristic X-rays, which can be used for X-diffraction.[1–3]

In order to obtain an XRD pattern, constructive interference of the X-rays with the atomic structure of the investigated materials has to occur, which is the case for periodic lattices. The relationship between the incoming X-ray with its wavelength λ, the lattice spacing d and the angle of incidence θ is given by the following Bragg`s equation.

$$\mathrm{n}\lambda = 2\ \mathrm{d}\sin(\theta) \tag{2-1}$$

With a given wavelength of λ = 1.540562 Å for Cu Kα radiation and considering a measurement range from 0.5° 2θ to 100° 2θ structures with dimensions from 0.1 nm to 20 nm can be resolved.[4]

In this thesis X-ray diffraction measurements on films and powder samples were performed using a Bruker D8 Discover X-ray diffractometer operating at 40 kV and 30 mA, employing Ni-filtered Cu Kα radiation (λ = 1.5406 Å) and a position-sensitive detector (LynxEye) in reflection mode. Additionally, powder X-ray patterns were also obtained in transmission mode by a STOE Stadi MP diffractometer with a Cu Kα1 radiation source (λ = 1.54060 Å) operating at 40 kV and 40 mA. The diffractometer was equipped with a DECTRIS MYTHEN 1K solid-state strip detector.

2.2 Scanning Electron Microscopy

Due to the resolution limit of optical microscopes, scanning electron microscopy (SEM) is a useful tool to charcterize surfaces and morphologies at the nanometer scale.[5] This is due to the wavelength dependence of the resolution limit given in Equation 2:

$$d = \frac{\lambda}{2\mathrm{NA}} \tag{2-2}$$

Where d is the resolution limit, λ is the wavelength of the incident photons and NA the numerical aperture. Assuming a typical NA between 1 and 1.5 and a wavelength of about 550 nm, which is usually used in fluorescence microscopy, a diffraction limit d of about 200 nm can be achieved.[6,7] In contrast, SEM allows for spatial resolution close to one nanometer.[8] A typical setup of an SEM in depicted in Figure 2-2.

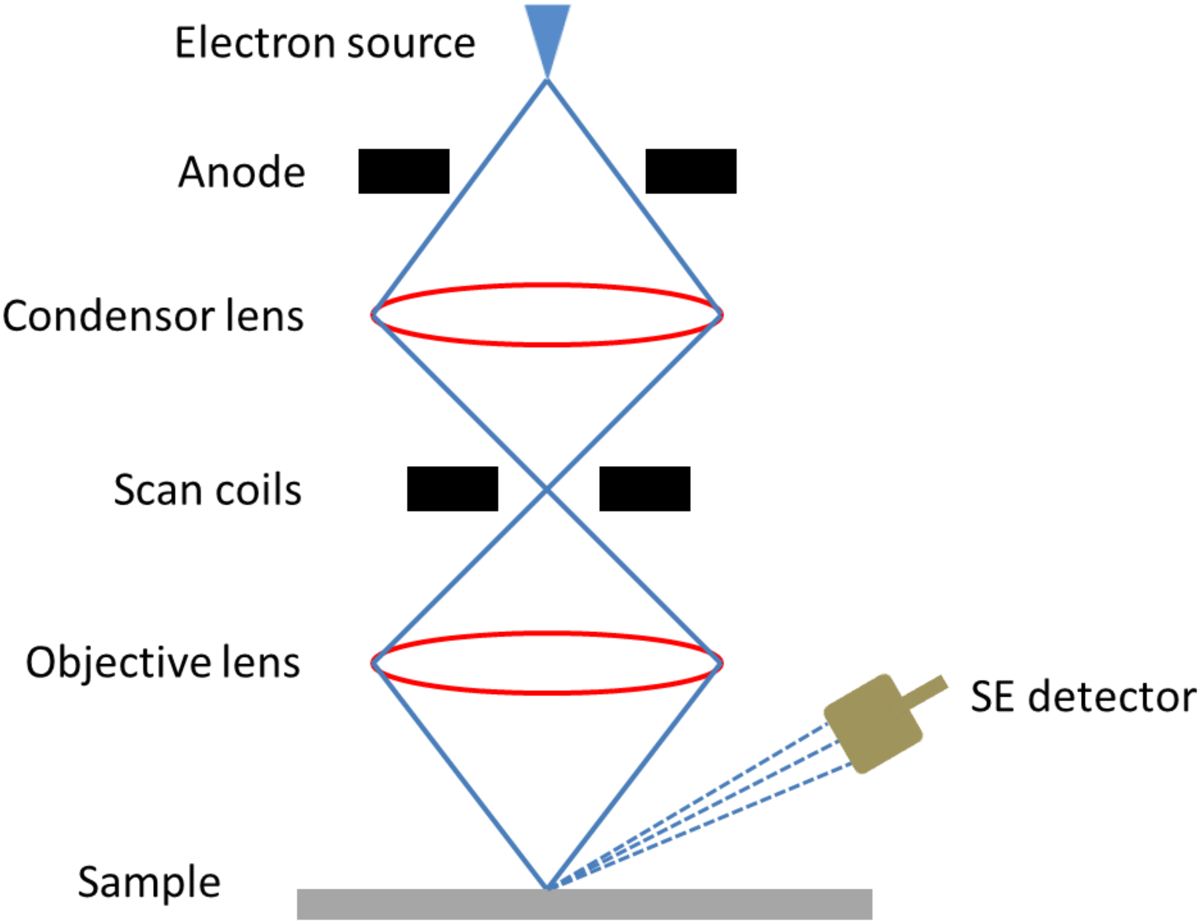

Figure 2-2: Schematic setup of a scanning electron microscope

The two most common ways to generate the electron beam are thermal emission and field emission. For thermal emission a wire of tungsten or a lanthanium hexaboride crystal is heated until it emits electrons. In the case of field emission a potential difference, between an anode and a nearby metal tip, causes electron emission. Regardless of the electron source, the emitted electrons are subsequently accelerated via a voltage of up to 30 kV and focused on the sample by several condenser lenses and an objective lens. The scan coils allow for scanning the focused electron beam across the sample.[8,9]

The electrons hitting the sample can interact in many different ways with the specimen leading to a series of different signals that can be detected. For example, the electrons can be transmitted through the sample, which is used for transmission electron microscopy (TEM) to gain phase and diffraction information from the sample. Also elastic backscattering of the incident electrons from the surface, without a loss of energy, occurs (BS). The most relevant electrons for SEM are so-called secondary electrons, which arise from electrons of the primary beam getting absorbed by the sample (SE). The absorbed electrons interact with atoms within the sample and can be re-emitted as electrons with lower energy. A schematic illustration of the emitted particles and electromagnetic radiation caused by the interaction of the sample with incident high energetic electrons is depicted in Figure 2-3.[8,9]

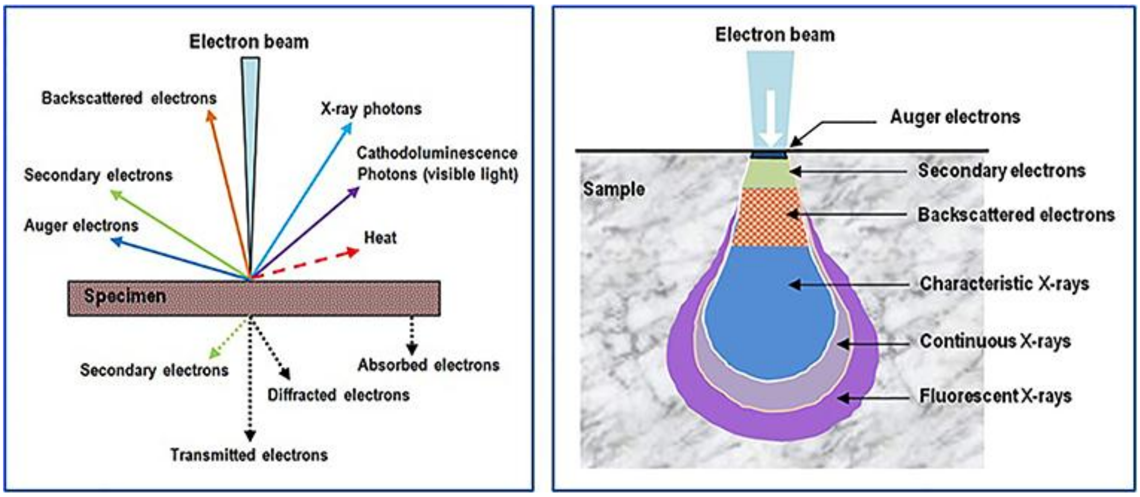

Figure 2-3: left: Schematic illustration of the different particles and electromagnetic radiation emitted from the sample upon interaction with incident high energy electrons. right: Schematic illustration of the volume within the specimen where the emission of the particles and electromagnetic radiation occurs.[10]

The emitted SE can be detected by an SE detector which is placed at a certain angle close to the sample holder. Since SE arise from areas close to the surface of the sample and the amount of SE reaching the detector is strongly influenced by the surface height, orientation and composition of the illuminated spot, SE provide a lot of morphological information. By moving the electron beam across the sample point for point, a microscopic image of the specimen can be generated.[8,9,11]

According to Figure 2-3, the sample also emits characteristic X-rays when it gets hit by high energy electrons. The energy of the emitted characteristic X-rays depends on the atomic structure of the sample. Therefore, characteristic X-rays can be used to estimate the atomic composition of the analyzed sample via energy dispersive X-ray spectroscopy (EDX). The emitted characteristic X-rays are sorted by their energies in an analyzer and detected by a X-ray detector, leading to spectrum which provides information about the composition of the structure.[12]

In this thesis SEM images and EDX data were acquired on an FEI Helios NanoLab G3 UC microscope.

2.3 UV-Vis Absorption Spectroscopy

In order to gain information of the electronic structure of liquid or solid samples, ultraviolet-visible (UV-vis) absorption spectroscopy is a commonly used method. UV-Vis is based on the investigation of optical transitions from the ground state to various excited states which provides quantitative and qualitative information about the absorption properties of the specimen.

The absorbance at a certain wavelength $A(\lambda)$ represents the weakening of the light intensity of the incident beam after running through the sample and is defined by equation 2-3, where I is measured intensity after the incident beam has ran through the specimen and I_0 is the intensity of the incident beam.

$$\boldsymbol{A(\lambda) = -log\frac{I(\lambda)}{I_0(\lambda)}} \qquad \textbf{(2-3)}$$

In the case of a liquid sample where the chromophore is dissolved in a proper solvent $A(\lambda)$ is related to the concentration c of the chromophore. A mathematical relation between $A(\lambda)$ and c is given by the Lambert-Beer law (equation 2-4), where ε is the specific extinction coefficient of the absorbing species and L the optical path length through the sample.

$$\boldsymbol{A(\lambda) = \varepsilon(\lambda)\, c\, L} \qquad \textbf{(2-4)}$$

The determination of the amount of light absorbed by the Lambert-Beer law works only with samples that are perfectly translucent without any light scattering within the sample. Therefore, the Lambert-Beer law is not applicable for investigations of solar cells featuring a typical layer assembly of materials with very different refractive indices leading to many different interfaces between the layers where scattering and refracting events can occur. Even a very simple model of a solar cell, consisting of the absorber material on a glass substrate, exhibits already three different interfaces, namely air-glass, glass-absorber and absorber-air interface. Since this gets even more complicated in a fully assembled device containing several charge selective layers and reflective metal contacts, the following procedure has been found to produce reliable results for many types of thin film samples, including fully assembled solar cells and has been utilized throughout this thesis to estimate the absorption of thin films.[13–15]

Assuming that all light is either absorbed, transmitted or reflected by the sample, the intensity of the incident light can therefore be written as the sum of the percentages of absorbed ($\%A$), transmitted ($\%T$) and reflected ($\%R$) light, see equation 2-5.

$$\boldsymbol{\%T + \%A + \%R = 1} \qquad \textbf{(2-5)}$$

In order to determine $\%A$, the quantities $\%T$ and $\%R$ of the reference and the sample can be measured with an UV-Vis spectrometer equipped with an integrating sphere.

For transmission measurements the sample has to be placed right at the entrance port of the integrating sphere. This allows for the collection of all transmitted light or light which gets scattered towards the edges of the sample. Reflection measurements will be performed by positioning the sample at the opposite end of the integrating sphere, just outside the sphere. This assembly ensures that only light which gets reflected by the sample is taken into account in this measurement. For all measurements the reference has to be measured in the same way as the sample. A suitable reference is the transparent substrate without the absorbing layer. Prior to all measurements, an instrument transmission baseline (100% T), without any optical obstacles in the beam path, and a Spectralon white standard (100% R) have to be measured.

As shown in equation 2-5, the absorption can be calculated by subtracting the portions of the transmitted and reflected light from the total incident light intensity, which represents 100 %. The absorption in turn is related to the absorbance by the expression given in equation 2-6.

$$\boldsymbol{A = -\log(1 - \%A)} \qquad \textbf{(2-6)}$$

According to equation 2-6, the absorbance of the sample can calculated from the absorption of the sample which was determined by transmission and reflection measurements. In order to obtain only the absorbance of the active layer it is necessary to subtract the absorbance of the reference from the absorbance of the complete sample.

In this thesis absorption spectra were acquired with a Lambda 1050 UV-Vis spectrophotometer (Perkin Elmer) using an integration sphere.

2.4 Steady State Photoluminescence (ssPL) Spectroscopy

Generally, photoluminescence (PL) occurs when electrons are excited to an excited state and subsequently relax to their ground state. The energy difference between these two states is often released as a photon, which can be detected by steady state photoluminescence (ssPL) spectroscopy. A schematic illustration of the processes involved in a PL process is given in Figure 2-4.

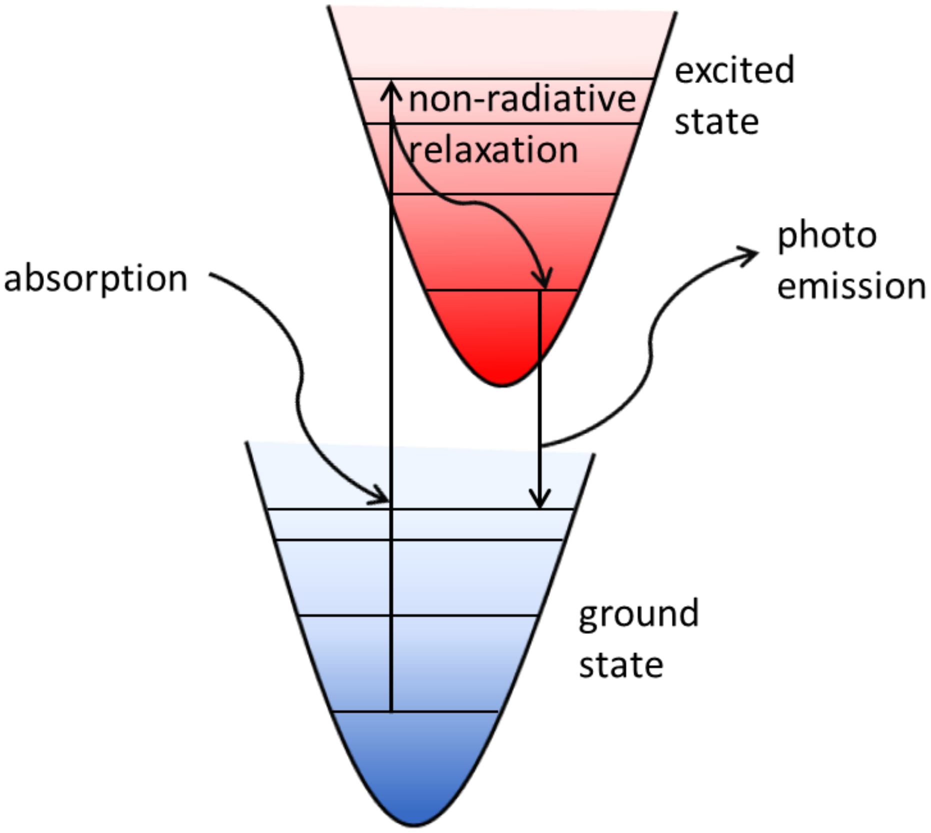

Figure 2-4: Schematic illustration of the processes involved in a PL event

According to Figure 2-4, the electrons mostly get excited to higher vibrational states than the lowest possible excited electronic state. Therefore, the excited electrons rapidly thermalize into the vibrational ground state of the excited electronic state, leading to emission of a photon exhibiting a lower energy than the energy of the exciting photons. Thus, the PL emission spectrum is shifted towards longer wavelength with respect to the spectrum of the excitation source. A schematic illustration of this so-called Stokes shift is depicted in Figure 2-5.[16]

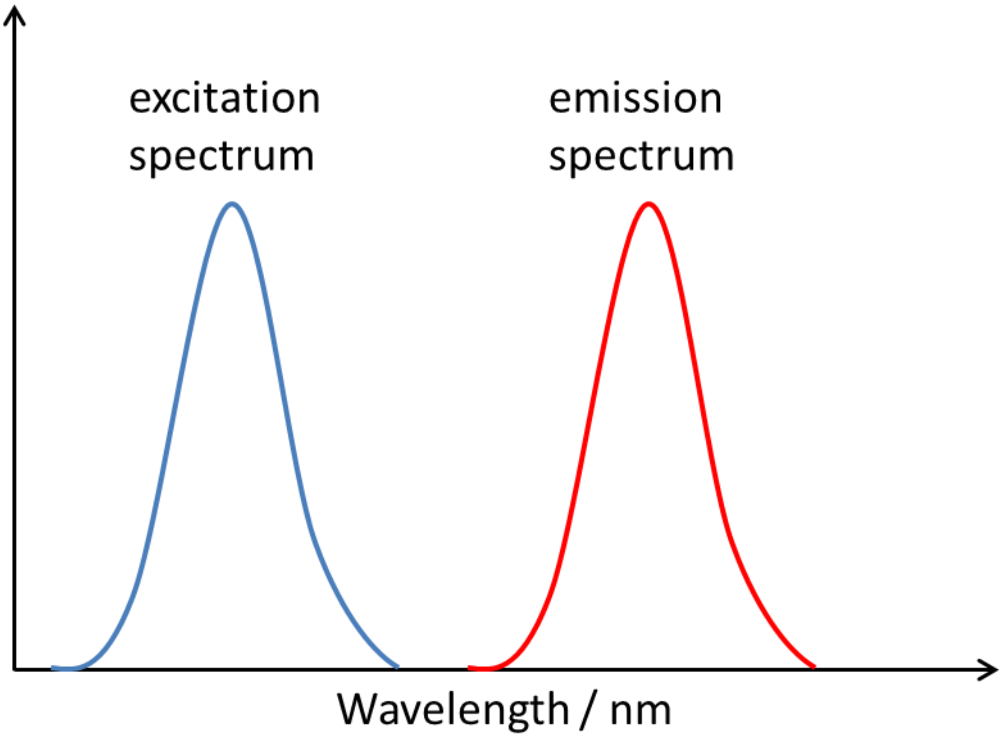

Figure 2-5: Schematic illustration of the Stokes shift

Although shown as such in Figure 2-5, the PL emission spectrum does not necessarily exhibit the same shape as the excitation spectrum.

However, since the emitted photons possess information about the band gap of the sample, ssPL spectroscopy is applicable for the investigation of semiconductors like absorber materials for solar cells.

In this thesis steady state measurements were performed with a Fluotime 300 Spectrofluorometer (Picoquant GmbH).

2.5 Time Correlated Single Photon Counting (TCSPC)

While ssPL is only able to detect the total energy and intensity of the emitted photons, time correlated single photon counting (TCSPC) offers the possibility to investigate the time-resolved kinetics of the photoemission from the band edge of a semiconductor. As already indicated by the name TCSPC, it is based on a precisely timed registration of single photons emitted by the sample.

TCSPC measurements are performed by measuring the time lag between a pulse of a pulsed laser source and the detection of the photon emitted by the sample. Due to quantum mechanical principles, it is not possible to know exactly when a single relaxation process is occurring, hence the time between a laser pulse and the detection of an emitted photon is not constant, see Figure 2-6.

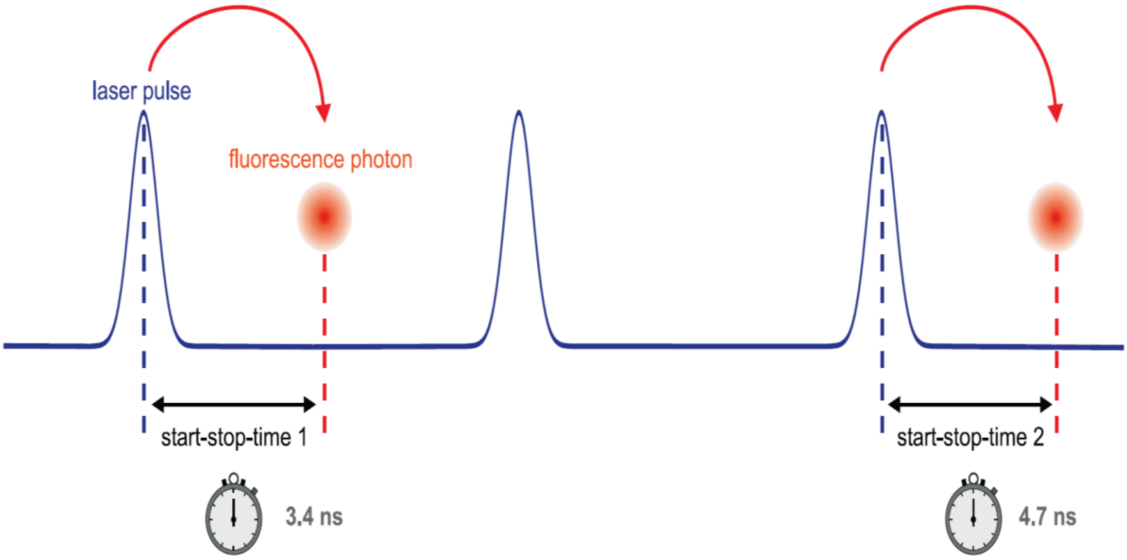

Figure 2-6: Measurement of start-stop times in time-resolved fluorescence measurement with TCSPC.[17]

Therefore, a multitude of subsequent single photon counting measurements has to be performed to obtain the photoluminescence decay dynamics, which is realized by a high repetition frequency of the excitation laser. In a TCSPC set-up the laser is typically pulsed at frequencies between 80 and 100 MHz. In order to collect a maximum of only one photon per excitation event the laser intensity has to be adjusted weak enough. All measured photon counts are sorted in a histogram consisting of a range of time bins (Figure 2-7).

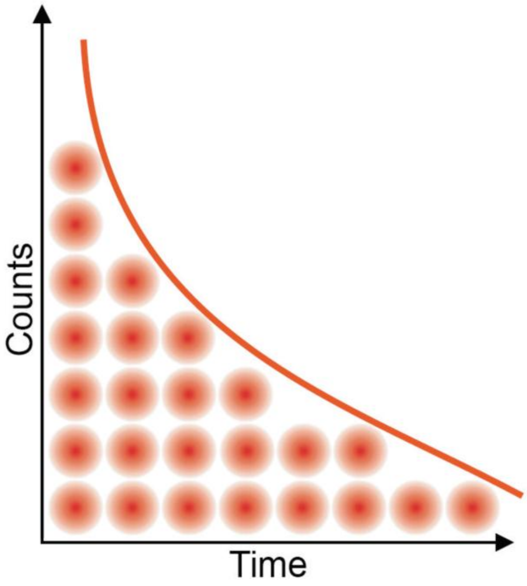

Figure 2-7: Histogram of start-stop times in a time-resolved fluorescence measurement with TCSPC.[17]

The exponential decrease of the histogram given in Figure 2-7 can be explained by a quantum mechanical interpretation, which predicts that only half of the excited species will relax in a given time interval. The resulting exponential decay can be fitted with a matching function to extract the half-life time of the excited species.

In this thesis time-resolved PL measurements were performed with a Fluotime 300 Spectrofluorometer (Picoquant GmbH).

2.6 Current-Voltage Measurements

The most important characteristic of solar cells is their power conversion efficiency (PCE, η), which is used to rate them and to compare them with each other. In order to ensure the comparability of PCEs measured in different laboratories, the testing takes place under standard conditions. The current standard for solar cell measurements is the ASTM G173-03 air mass 1.5 global (AM1.5G) at a total light intensity of 100 mW/cm^2 (1 sun).[18] This spectrum corresponds to the standard spectrum emitted by the sun corrected for absorption and scattering by the atmosphere.

The efficiency of solar cells is determined by current density-voltage (J-V) measurements under 1 sun illumination with a range of bias voltages applied to the test device. The resulting current flow is recorded to determine the characteristics of the solar cell. A typical *J*-*V* curve is shown in Figure 2-8.

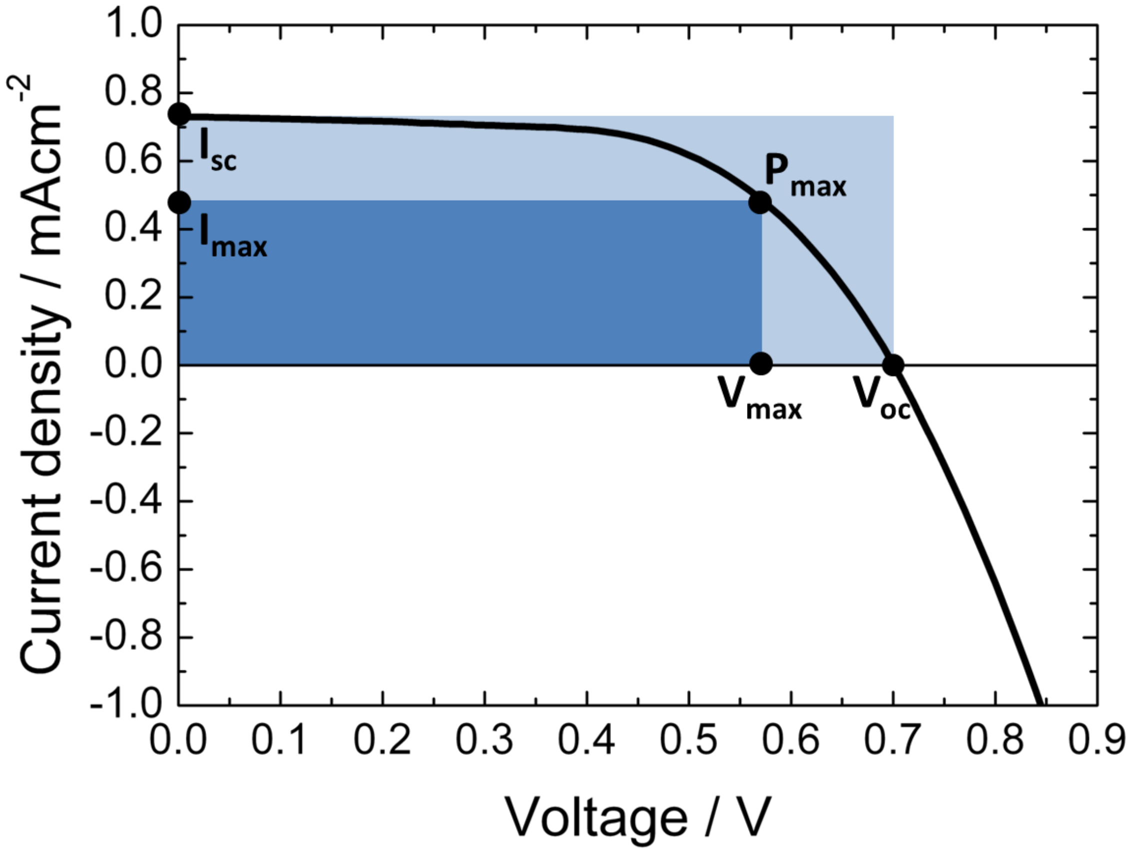

Figure 2-8: Typical *J*-*V* curve of a solar cell including characteristic points.

The intersection of the graph with the y-axis represents the short-circuit current (I_{sc}) (or J_{sc}, the short-circuit current density), which is the current running through the device without any applied bias voltage. The I_{sc} of a solar cell is influenced by its optical absorption properties, the ability to produce charge under illumination and transport of the generated charge carriers to the electrodes. The open-circuit voltage (V_{oc}) is the maximum voltage available from the measured device and is obtained at the point where the net current is zero, meaning that the applied bias neutralizes the current generated by the solar cell under illumination.

Since the electrical power is defined as the product of current and voltage, I_{sc} and V_{oc} correspond to the power generated by the device at any applied voltage. The point where the power produced of the solar cell is at its maximum is called the maximum power point (P_{max}) and is defined by I_{max} and V_{max}.[19] P_{max} indicates the voltage needed for the solar cell to work most efficiently. P_{max} is related to the PCE by the following equation

$$\boldsymbol{PCE = \frac{P_{max}}{P_{in}} = \frac{V_{max} \cdot I_{max}}{P_{in}}} \tag{2-7}$$

where P_{in} is the power of the incident light.

As depicted in Figure 2-8, P_{max} is defined by the rectangle given by I_{max} and V_{max} which are smaller than the I_{sc} and V_{oc} of the tested device. Since I_{sc} and V_{oc} determine the theoretical maximum efficiency of a solar cell, the ratio between the areas of the rectangles given by I_{max} and V_{max} and I_{sc} and V_{oc} provides information about the performance of a photovoltaic device with respect to its theoretical maximum PCE. This ratio is called fill factor (*FF*) and is given by equation 2-8.

$$\boldsymbol{FF = \frac{V_{max} \cdot I_{max}}{V_{oc} \cdot I_{sc}} = \frac{P_{max}}{V_{oc} \cdot I_{sc}}} \tag{2-8}$$

According to equation 2-8, a well-performing solar cell should feature a *FF* close to one. Usually, real solar devices exhibit a *FF* much lower due to losses from serial and shunt resistances. However, a *FF* of more than 0.7 can be realized in high quality solar cells.

In this thesis *J-V* curves were recorded with a Keithley 2400 source meter under simulated AM 1.5 sunlight, calibrated to 100 mW cm^{-2} with a Fraunhofer ISE certified silicon cell. The active area of the solar cells was defined with a square metal aperture mask of 0.0831 cm^2.

2.7 External Quantum Efficiency (EQE)

Besides *J-V* measurements, external quantum efficiency (EQE) measurements can be performed to investigate photovoltaic devices under working conditions. In contrast to *J-V* measurements, which provide information about the overall PCE of a solar cell under sun-like white light illumination, EQE measurements take place under monochromatic illumination to study the response of the tested device towards illumination at a distinct wavelength. The method to determine the EQE is equivalent to incident photon to current conversion efficiency (IPCE) measurements. It depends on the light harvesting efficiency η_{LHE}, the electron injection efficiency η_{inj} and the charge collection efficiency η_{cc}. The mathematical relation between these three parameters and the *IPCE* at a distinct wavelength is given in equation 2-9.

$$\boldsymbol{IPCE\ (\lambda) = \eta_{LHE} \cdot \eta_{inj} \cdot \eta_{cc}} \qquad \textbf{(2-9)}$$

In order to determine the IPCE at a certain wavelength, the device is illuminated with monochromatic light and the resulting J_{sc} (λ) is measured. The IPCE can be calculated with the determined J_{sc} (λ) according to the following equation

$$\boldsymbol{IPCE(\lambda) = 1240 \frac{J_{sc}}{\lambda \cdot P_{in}}} \qquad \textbf{(2-10)}$$

where λ is the wavelength and P_{in} the power of the incident light. Accordingly, the overall short-circuit current of the solar cell under white light illumination can be calculated as the integral of the product of the wavelength dependent IPCE(λ) and the incident photon flux density (F(λ)), multiplied with the elemental charge of an electron *e*, see equation 2-11.

$$\boldsymbol{J_{sc} = \int e \cdot F(\lambda) \cdot IPCE(\lambda) d\lambda} \qquad \textbf{(2-11)}$$

For an ideal solar cell, the J_{sc} calculated from the IPCE measurements should be equal to the J_{sc} obtained from the *J-V* measurements under sun-like white light illumination.

In this thesis EQE) measurements were performed at short circuit with a bias illumination of 0.1 sun provided by an AM 1.5 solar simulator (Solar Light Model 16S). The measurements were conducted with a 150 W xenon lamp equipped with a monochromator and order-sorting filters as the primary light source. The light intensity reaching the electrode was measured using a certified Fraunhofer ISE silicon reference cell equipped with a KG5 filter. For signal detection a Signal Recovery 7265 lock-in amplifier combined with a low-noise current amplifier (Femto DLPCA-200) was employed.

2.8 Literature

[1] E. A. Underwood, *Proc. Roy. Soc. of Medicine-London* **1945,** *38*, 697.

[2] W. W. Strong, *Science* **1914,** *40*, 709.

[3] C. E. Pfluger, *Anal. Chem.* **1972,** *44*, R563.

[4] W. H. Bragg, W. L. Bragg, *The Reflection of X-rays by Crystals*, Vol. 88, **1913**.

[5] V. Westphal, S. W. Hell, *Phys. Rev. Lett.* **2005,** *94*, 143903.

[6] E. G. van Putten, D. Akbulut, J. Bertolotti, W. L. Vos, A. Lagendijk, A. P. Mosk, *Phys. Rev. Lett.* **2011,** *106*, 193905.

[7] J. J. Cargille, *Immersion oil and the microscope*, 2nd ed., **1985.**

[8] P. W. Hawkes, J. C. H. Spence, *Science of Microscopy*, Vol. 1, **2007**.

[9] R. F. Egerton, *Physical Principles of Electron Microscopy*, Springer Science+Business Media, Inc: **2005**.

[10] S. Yilmaz, H. B. Ozmen, *High Performance Concrete Technology and Applications*, **2016**.

[11] M. von Ardenne, *Z. Physik* **1938**, *109*, 553.

[12] C. G. Barkla, C. A. Sadler, *Lond. Edinb. Dubl. Phil. Mag.* **1909**, *17*, 739.

[13] G. F. Burkhard, E. T. Hoke, M. D. McGehee, *Adv. Mater.* **2010**, *22*, 3293.

[14] H. J. Snaith, C. Ducati, *Nano Lett.* **2010**, *10*, 1259.

[15] B. M. Klahr, A. B. F. Martinson, T. W. Hamann, *Langmuir* **2011**, *27*, 461.

[16] A. Polimeni, A. Patanè, M. Grassi Alessi, M. Capizzi, F. Martelli, A. Bosacchi, S. Franchi, *Phys. Rev. B* **1996,** *54*, 16389.

[17] M. Wahl, *Technical Note: Time-Correlated Single Photon Counting (TCSPC)*, PicoQuant GmbH, Berlin, **2014**.

[18] http://rredc.nrel.gov/solar/spectra/am1.5/

[19] M. A. Green, *Sol. Cells* **1982,** *7*, 337.

[20] J. Nelson, *The Physics of Solar Cells*, Imperial College Press, **2003**.

3 Investigation of the optoelectronic and stability properties of the 2D layer perovskites $(C_4H_{12}NH_3)_2SnI_4$ and $(C_8H_{12}NH_3)SnI_4$ for applications in lead-free perovskite based optoelectronics

The results described in this chapter were partially obtained with the help of the research trainee (Forschungspraktikant) B. Sc. Minh Trung Cong.

3.1 Introduction

Considering the constantly rising global energy demand in connection with the decline of fossil fuels, which are currently the main sources for the generation of electrical power, humankind is running into severe problems regarding the sufficient supply with electricity.[1] Furthermore, extensive burning of fossil fuels results in the emission of huge amounts of so-called green-house gases being considered to be responsible for the global warming, which causes an increased number of extreme weather phenomena, such as droughts, floods and storms. Thus, there is a strong demand for the production of sufficiently high amounts of electric power without emitting green-house gasses.[2]

Considering that 3.5 x10^{24} J of solar energy are reaching the earth every year, which is about 10000 times more than the annual human energy consumption, the conversion of this energy into electricity by photovoltaic devices is one of the most promising approaches for environmentally friendly production of electric power.[3] Although state-of-the-art silicon based photovoltaics already generate electricity from solar energy with power conversion efficiencies (PCE) of more than 20 %, the energy-costly production of such solar cells is still an impediment for the rapid deployment of large-scale photovoltaics. In order to increase the impact of photovoltaics on the global energy production, less expensive and more efficiently produced photovoltaics are strongly needed. During the quest for possible alternatives to silicon based photovoltaics, hybrid organic-inorganic lead iodide perovskites have attracted much attention in 2012, due to solar cells based on such a compound, namely methyl ammonium lead iodide ($MAPbI_3$), showing PCEs of more than 10 %.[4] During the last few years, hybrid lead halide perovskite based photovoltaics have experienced a rapid increase of device efficiency featuring PCEs of more than 20 % for state-of-the-art devices, making this technology a promising candidate for next generation photovoltaics.[5] Furthermore, hybrid lead halide based perovskites have been shown to be feasible for applications in lasers and light emitting diodes (LED).[6,7] Despite their outstanding optoelectronic properties, hybrid lead halide perovskites still suffer from several disadvantages.[8–17] In particular, the sensitivity of hybrid lead halide perovskites towards moisture, which leads to the formation of hydrated species or to the complete degradation of the perovskite may impede their wide-spread application.[18] Furthermore, the toxicity of lead, in combination with the relatively high solubility of lead halide salts in water, can be considered a major obstacle for the commercialization of this technology.[19–22] Accordingly, a great deal of effort has been put into the development of less hazardous perovskite related compounds for photovoltaic applications. Previous studies involving several different elements such as Ge^{2+}, Sn^{2+}, Bi^{3+}, Sb^{3+} or Cu^{2+} have revealed that the best performing lead-free solar cells can be achieved with devices comprising Sn^{2+} based hybrid perovskite absorber layers.[23–27] In particular, solar cells based on methylammonium tin iodide ($MASnI_3$) exhibited encouraging PCEs of about 6 %, making it an excellent candidate for highly efficient lead-free hybrid perovskite based photovoltaics.[28,29] However, although tin is also a group 14 element, such as lead, its oxidation state 2+ is much less stable than that of the corresponding lead cation. This instability leads to a strong sensitivity of Sn^{2+} towards oxygen, resulting in the facile oxidation of Sn^{2+} to Sn^{4+}.[28,29] The formation of Sn^{4+} can be considered as p-type doping which leads to high hole mobilities for tin halide based perovskites. Accordingly, tin halide perovskites have been used as solid-state hole transport materials for dye sensitized solar cells.[30-32] On the other hand, the formation of Sn^{4+} leads to the introduction of defect sites into the perovskite structure, which act as recombination centers for photoexcited charge carriers. Thus, the lifetime of photoexcited species within the tin halide perovskite is drastically reduced, resulting in a performance loss of photovoltaics comprising tin halide perovskite based absorber layers due the strong decrease of the mobility of the photoexcited species.[28,29] The instability of Sn^{2+} based perovskites is considered to be the major drawback which has to be solved before such materials are viable for wide-spread applications.

Because moisture promotes the formation of Sn^{4+} within hybrid tin halide based perovskites, the stability of these compounds could possibly be enhanced by protecting the Sn^{2+} cation from a direct contact with water molecules.[33] Recently, several groups showed that the moisture stability of hybrid lead halide perovskites can be strongly improved by the introduction of ammonium cations featuring large hydrophobic organic residues.[34,35] Accordingly, hybrid tin halide based perovskites featuring organic cations with large organic residues are interesting candidates for applications in stable Sn^{2+} based photovoltaics.

Previous studies on n-butylammonium (BuA) and phenylethylammonium (PEA) showed that these organic cations can efficiently block water from reacting with the metal halide octahedra in lead iodide based perovskites, leading to a significant increase of the stability of the perovskite, which results in enhanced device stability.[35,36] However, no stability studies on tin iodide based perovskites featuring large organic cations have been reported so far.

Here, we present a comprehensive study of n-butylammonium tin iodide ($(BuA)_2SnI_4$) and phenylethylammonium tin iodide ($(PEA)_2SnI_4$) with a view on serving as potential absorbers in lead-free perovskite solar cells. The obtained results were compared to those of their lead based counterparts n-butylammonium lead iodide ($(BuA)_2PbI_4$) and phenylethylammonium lead iodide ($(PEA)_2PbI_4$), and their related lead and tin based methylammonium compounds, $MAPbI_3$ and $MASnI_3$, which are the most common materials for metal halide perovskite based optoelectronics. We investigated the structural and optoelectronics properties of these compounds via X-ray diffraction (XRD), ultraviolet/visible (UV/vis) spectroscopy, photoluminescence (PL) spectroscopy and time-correlated single photon counting (TCSPC) measurements, in order to investigate the viability of $(BuA)_2SnI_4$ and $(PEA)_2SnI_4$ for optoelectronic applications, such as photovoltaics and LEDs. Furthermore, we conducted the first moisture stability study of $(BuA)_2SnI_4$ and $(PEA)_2SnI_4$ by exposing the compounds to moderate and high relative humidity levels. The degradation of the samples was monitored by XRD and UV/vis measurements. It turns out that $(BuA)_2SnI_4$ and $(PEA)_2SnI_4$ feature optoelectronic properties making them interesting candidates for many different optoelectronic applications. Furthermore, regarding the moisture stability, we demonstrate that the choice of the organic cation is much more critical for tin based perovskites than for their lead-based counterparts. Our results reveal new possible routes for the development of stable Sn^{2+} based optoelectronics.

3.2 Results and Discussion

Since the application of hybrid metal halide perovskites in optoelectronics is mainly realized by thin films of those materials, we prepared films of our investigated compounds. All films were manufactured via spin-coating a DMF-based precursor solution on top a glass substrate with a subsequent annealing step. For experimental details see section 3.4. The phase purity of the prepared films was checked by powder X-ray diffraction measurements (PXRD) of powders scratched off from the manufactured films, see Figure 3-1a-f.

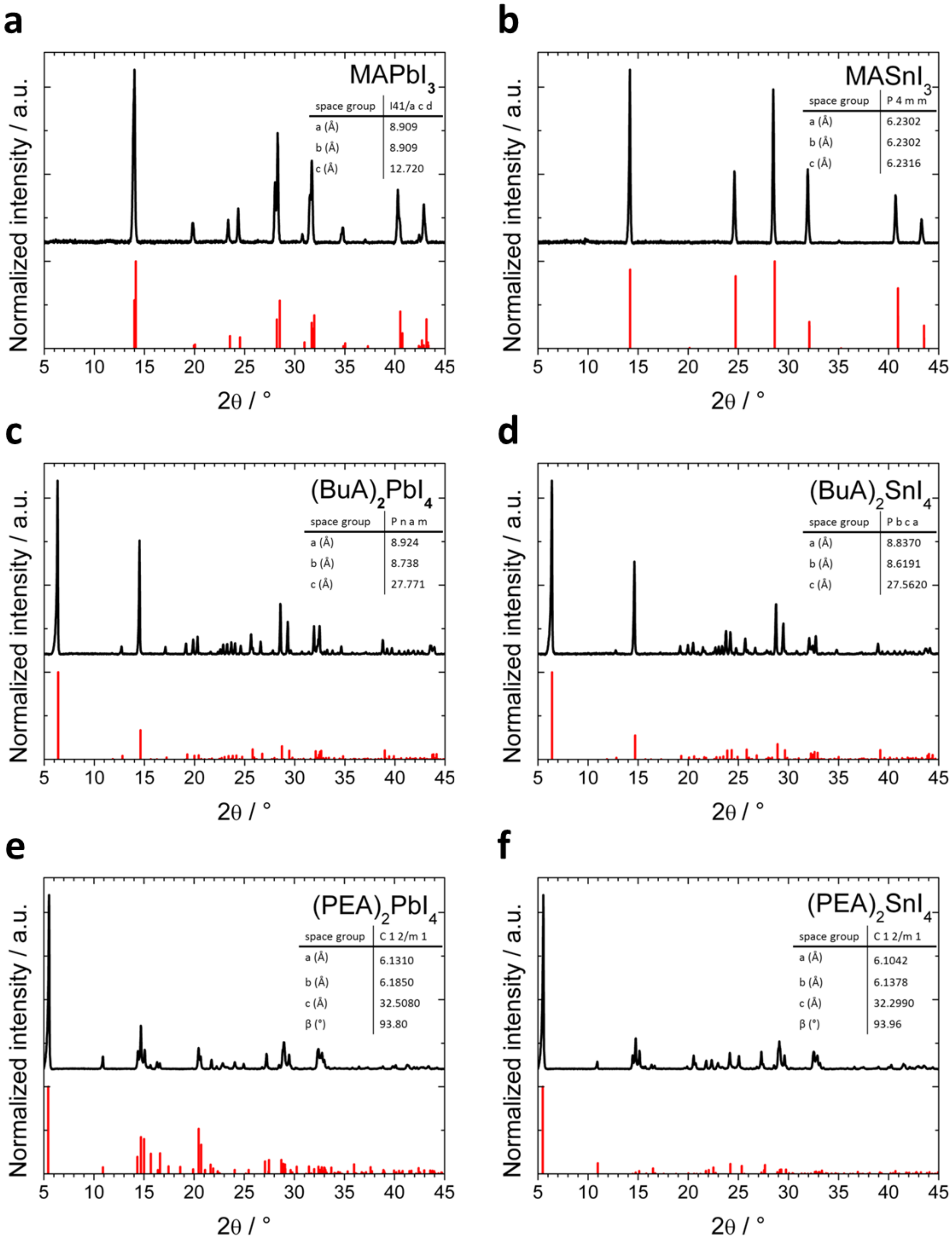

Figure 3-1: PXRD patterns of a) $MAPbI_3$, b) $MASnI_3$, c) $(BuA)_2PbI_4$, d) $(BuA)_2SnI_4$, e) $(PEA)_2PbI_4$ and f) $(PEA)_2SnI_4$.The insets show the space group and the lattice parameters of each compound. The red lines indicate the simulated PXRD pattern of each perovskite.

According to the lattice parameters given in the insets, the substitution of the relatively small methylammonium cation (MA) by the much larger BuA or PEA cation results in a strong increase of one unit cell axis accompanied by a structural change from tetragonal to orthorhombic for BuA and monoclinic for PEA, regardless of which type of metal ions reside inside the structure. This transition is caused by the increased distance of the metal iodide octahedra layers due the larger alkyl chains of BuA and PEA.[34] In the case of MA the organic cation is small enough to fit into the voids created by the interconnected metal halide octahedra without destroying the three-dimensional structure. This holds also for other cations that are not too large, such as formamidinium (FA) or cesium (Cs). Organic cations that exhibit larger aliphatic or aromatic residues can only be incorporated into the metal halide octahedra scaffold by disrupting the 3D assembly. Typically, 2D layered structures consisting of metal halide sheets separated by the organic cations are formed in this case. A schematic, showing the transition from a 3D structure to a 2D structure due the introduction of larger organic cations is given in Figure 3-2.

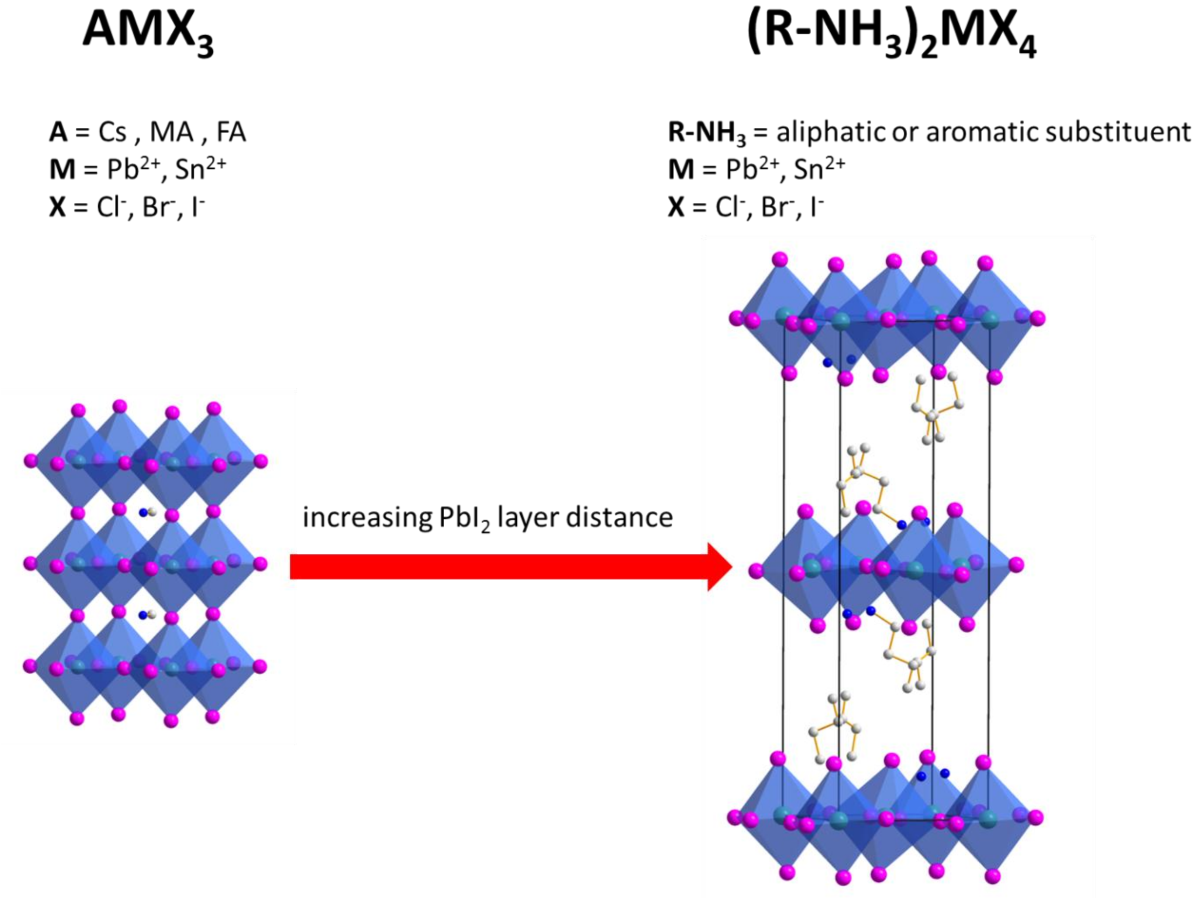

Figure 3-2: Schematic of the transition from a 3D perovskite structure to a 2D layered perovskite structure caused by the incorporation of large organic cations. The general formula of each compound including possible components is given above the structure.

Since the metal halide layers are separated by bilayers of the organic cations, the stoichiometry changes from AMX_3 to $(R\text{-}NH_3)_2MX_4$, see Figure 3-2.[34]

The transition from a 3D to a 2D structure is accompanied by a drastic change of the optoelectronic properties. Thus, we investigated the absorption properties of $(BuA)_2SnI_4$, $(PEA)_2SnI_4$, $MASnI_3$ and their lead based counterparts via UV/vis measurements. According to the absorption spectra of $MAPbI_3$, $(BuA)_2PbI_4$ and $(PEA)_2PbI_4$ given in Figure 3-3a, the transition from a 3 D to a 2D structure is accompanied by a large blue shift of the absorption onset leading to an increase of the band gap energy (E_g) of the perovskite. The E_g´s for $MAPbI_3$ and for $(BuA)_2PbI_4$ and $(PEA)_2PbI_4$ were determined by Tauc plots, see Figure 3-3b. The obtained values of 1.58 eV for $MAPbI_3$ and 2.3 eV for $(BuA)_2PbI_4$ and $(PEA)_2PbI_4$ are in good agreement with values reported in the literature.[4,38]

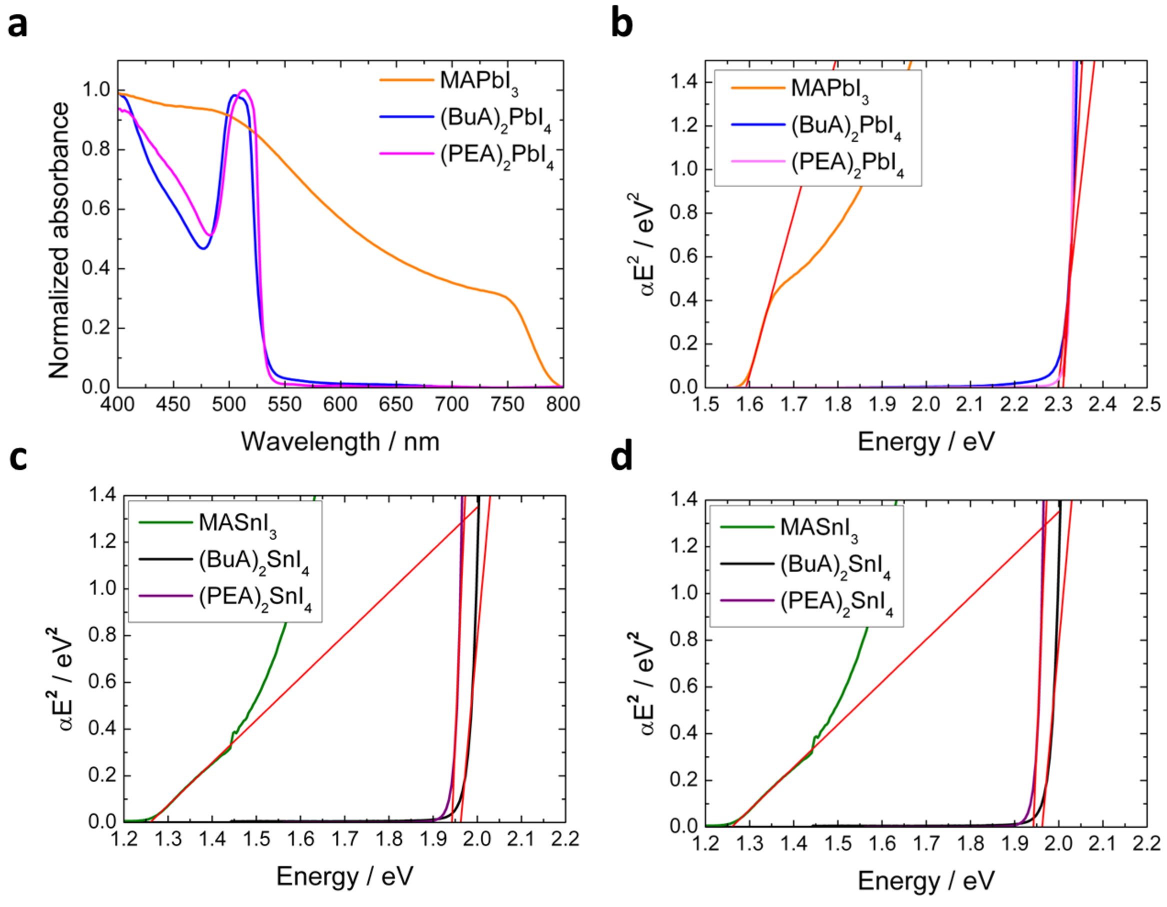

Figure 3-3: a) Absorbance spectra of $MAPbI_3$, $(BuA)_2PbI_4$ and $(PEA)_2PbI_4$, b) Tauc plots of $MAPbI_3$, $(BuA)_2PbI_4$ and $(PEA)_2PbI_4$, c) Absorbance spectra of $MASnI_3$, $(BuA)_2SnI_4$ and $(PEA)_2SnI_4$, d) Tauc plots of $MASnI_3$, $(BuA)_2SnI_4$ and $(PEA)_2SnI_4$ for direct E_g´s. The E_g´s were estimated via fitting the linear part of the graph.

The large increase of the E_g due to the transition from a 3D to 2D structure can be explained by confinement effects caused by the formation of separated PbI_2 layers due to incorporation of large organic cations. Furthermore, a strong excitonic feature appears in the absorbance spectrum of $(BuA)_2PbI_4$ and $(PEA)_2PbI_4$ at around 500 nm. This indicates that the 2D compounds exhibit a much higher exciton binding energy than $MASnI_3$, which is caused by the different dielectric constants of the organic and the inorganic layers leading to the stabilization of the created excitons.[39,40] A similar behavior can also be observed for the tin-based compounds revealing an E_g of about 1.25 eV for $MASnI_3$ and an E_g of 1.95 eV for $(BuA)_2SnI_4$ and $(PEA)_2SnI_4$, which is also in good agreement with literature data, see Figure 3-3c & d.[28,29,41] Interestingly, the E_g´s of the tin based layered perovskites are significantly smaller than those of their lead-based counterparts, being very close to the optimal E_g for a top cell in a tandem solar cell assembly.[42] Accordingly, these materials are interesting candidates for applications in this kind of photovoltaics.

All investigated compounds feature a strong PL signal pointing to low non-radiative recombination rates within the metal halide perovskites, making them interesting candidates for light emitting applications, such as LEDs.[28,43,44] Furthermore, the low frequency of non-radiative recombination events is also a key feature of the photoactive layer in highly efficient perovskite based photovoltaics.[45] According to Figure 3-4a & b, the PL signals of the layered compounds exhibit a strong blue shift with respect to their three-dimensional counterparts due to confinement effects, similar to the UV/vis spectra given in Figure 3-3a & d.[39,40] Besides their number, the lifetime of the photoexcited species is also an important factor for photovoltaic applications. Since the photoexcited charge carriers have to be extracted from the photoactive material of a solar cell before they recombine, the lifetime of the photoexcited species has to be reasonable long. Accordingly, we performed TCSPC measurements with our compounds to evaluate if layered perovskites meet the requirements for highly efficient photovoltaics. The PL decays obtained for the lead and tin based perovskites are given in Figure 3-4c & d, respectively. According to common procedures, the decay curves were fitted either to a biexponential or triexponential decay model to obtain the lifetimes of the photo-excited species.[46,47] Typically, the decay models feature one slow decay component τ_{slow} and a fast decay component τ_{fast}. For the triexponential fitting model an additional intermediate decay component τ_{inter} is present. The values of the different decay components are given in Table 3-1.

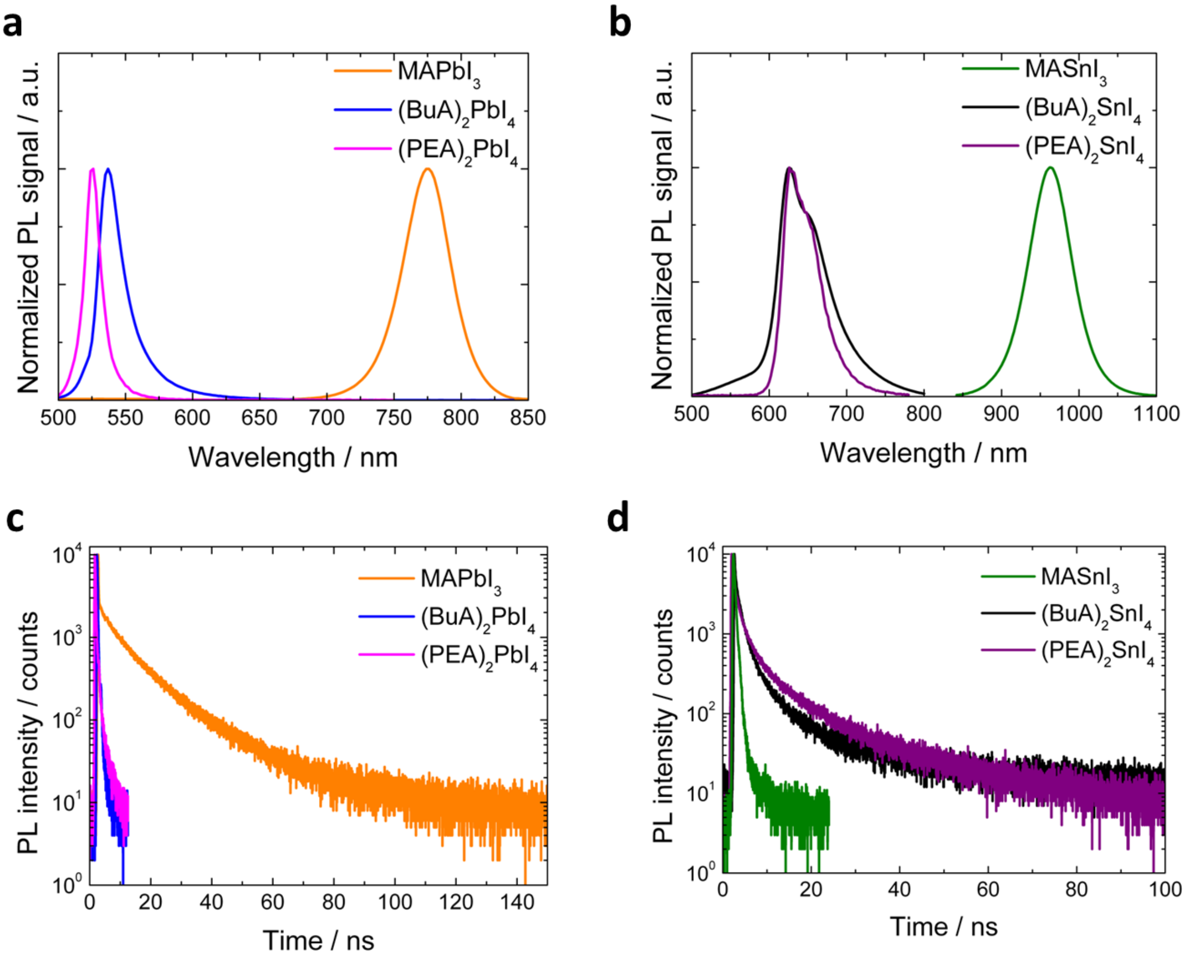

Figure 3-4: a) PL emission spectra of MAPbI$_3$, (BuA)$_2$PbI$_4$ and (PEA)$_2$PbI$_4$, b) PL emission spectra of MASnI$_3$, (BuA)$_2$SnI$_4$ and (PEA)$_2$SnI$_4$, c) TCSPC decays of MAPbI$_3$, (BuA)$_2$PbI$_4$ and (PEA)$_2$PbI$_4$, d) TCSPC decays of MASnI$_3$, (BuA)$_2$SnI$_4$ and (PEA)$_2$SnI$_4$.

Table 3-1: Summary of the decay components for the PL decays shown in Figure 3-4c & d.

	τ_{slow} / ns	τ_{inter} / ns	τ_{fast} / ns
MAPbI$_3$	16.27	-	4.77
(BuA)$_2$PbI$_4$	0.25	-	0.008
(PEA)$_2$PbI$_4$	1.51	-	0.28
MASnI$_3$	1.04	-	0.25
(BuA)$_2$SnI$_4$	10.61	1.88	0.34
(PEA)$_2$SnI$_4$	20.77	4.46	0.95

According to Figure 3-4c and Table 3-1, $MAPbI_3$ shows by far the slowest decay time for the lead based compounds, which is caused by the relatively low exciton binding energy leading to the generation of free charge carries, which can diffuse for a relatively long time inside the perovskite before they recombine.[48–50] On the other hand, the decay times for the layered compounds $(BuA)_2PbI_4$ and $(PEA)_2PbI_4$ are drastically decreased. We note that for the layered compounds the fast component τ_{fast} refers to radiative recombination while the slow component τ_{slow} is most likely caused by trap state formation.[51] The reduced lifetime of the photo-generated charge carriers is attributed to confinement effects present in the layered perovskites leading to a significant increase of the exciton binding energy.[39,40] Accordingly, no efficient charge collection from a several hundred nanometer thick layered perovskite-based absorber layer can be expected. Referring to the decay curves of the tin-based perovskites, depicted in Figure 3-4d, a trend contrary to that of the lead-based perovskites can be observed, wherein the three-dimensional compound $MASnI_3$ shows the shortest decay times. These very short lifetimes of the photoexcited species are attributed to a large number of defects acting as recombination centers for the photo-generated charge carriers. The defect sites are introduced by the self-doping of $MASnI_3$ with Sn^{4+} due the facile oxidation of the highly oxygen sensitive Sn^{2+}.[28,29]

However, previous studies showed that the optimization of the composition and synthesis procedure under highly inert conditions can significantly increase the lifetime of the photoexcited charge carriers, leading to rather efficient Sn^{2+}-perovskite based solar cells.[52,53] Similar to their lead-based counterparts, only the fast decay component τ_{fast} can be referred to radiative recombination in the layered tin iodide perovskites, while the two slower decay components τ_{inter} and τ_{slow} are most likely caused by trap state formation.[51] The much longer decay times for $(BuA)_2SnI_4$ and $(PEA)_2SnI_4$ indicate a much larger number of trap states in these compounds compared to their lead-based counterparts. This could probably be explained by the high sensitivity of the Sn^{2+} ions towards oxidation. Although radiative recombination in $(BuA)_2SnI_4$ and $(PEA)_2SnI_4$ is much faster than in $MAPbI_3$, it is slower than in $(BuA)_2PbI_4$ and $(PEA)_2PbI_4$, in particular for $(PEA)_2SnI_4$. Since $MASnI_3$ based solar cells comprising a mesoporous titania scaffold showed efficiencies of about 6 % with decay times for the photo-generated species of less than 200 ps,[28,29] layered tin-based perovskites are promising candidates for novel absorber materials in solar cells featuring a mesoporous scaffold.

Besides the optoelectronic properties, the stability of the active material is also an important issue that has to be resolved before the commercialization of perovskite-based optoelectronics. Previous studies showed that $MAPbI_3$ gradually degrades under humid conditions of more than 50 % RH.[18] This effect is even more pronounced for its tin-based counterpart $MASnI_3$, which degrades under ambient conditions within several minutes, mainly due to the highly oxygen and moisture sensitive Sn^{2+} ions.[54] In particular, the combination of moisture and oxygen promotes the degradation of $MASnI_3$.[33] A possible way to prevent water molecules from infiltrating the perovskite structure is the utilization of ammonium cations featuring large hydrophobic residues, as demonstrated for lead-based perovskites.[35,36] Since no studies on tin-based layered perovskites are available so far, we performed an extensive moisture stability study with our lead-free compounds by means of XRD and UV/vis measurements. For reference purposes, we also investigated the moisture stability of the corresponding lead-based perovskites with XRD. Since hybrid lead halide perovskites are typically more stable than their tin-based counterparts, the lead halide perovskite films were placed in a desiccator which contained a saturated aqueous NaCl solution to provide a humid atmosphere with a relatively high moisture level of about 75 % RH to accelerate the degradation of the samples, see Figure 3-5a.

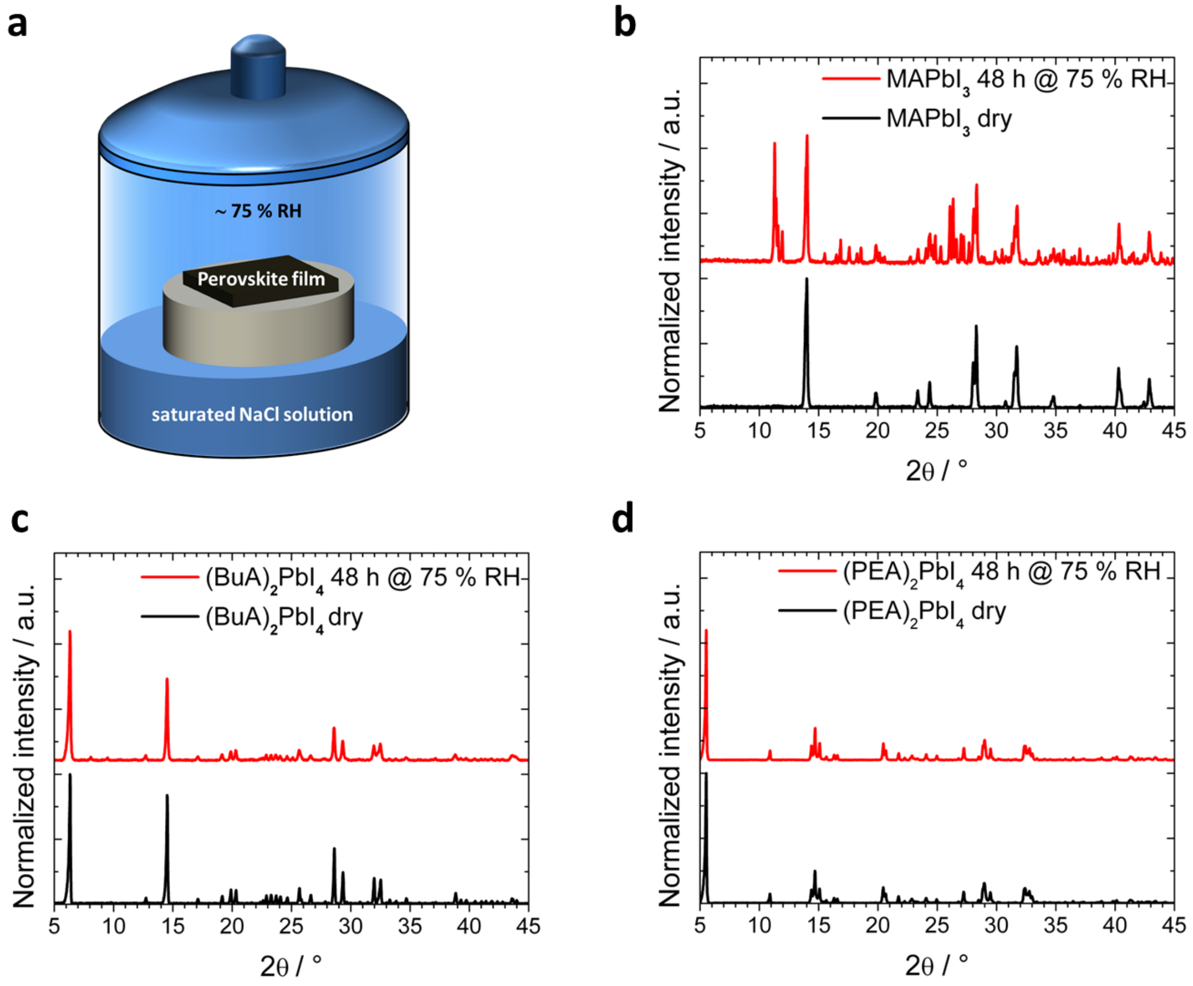

Figure 3-5: a) Schematic of the assembly used for the moisture stability test at high humidity levels, b) PXRD pattern of dry $MAPbI_3$ and $MAPbI_3$ exposed to 75 % RH for 48 h, c) PXRD pattern of dry $(BuA)_2PbI_4$ and $(BuA)_2PbI_4$ exposed to 75 % RH for 48 h, d) PXRD pattern of dry $(PEA)_2PbI_4$ and $(PEA)_2PbI_4$ exposed to 75 % RH for 48 h.

According to Figure 3-5b, the exposure of $MAPbI_3$ to elevated humidity levels results in the formation of many different degradation products, such as various hydrated species and PbI_2,[18,55] which are observable by the additional reflections in the PXRD pattern. In contrast, the compounds comprising the large organic cations exhibit almost no changes in their PXRD pattern, which indicates that ammonium cations featuring large organic residues can efficiently block water from reacting with the perovskite layer, leading to a strongly enhanced stability of the material. We note that even a relatively small cation like BuA is able to increase the moisture stability of the perovskite layer significantly.

For the investigation of the tin-based materials, the samples were also exposed to moderate humidity levels of about 35 % RH in addition to the high humidity level exposure, due to the fact that tin halide perovskites are much less stable than their lead-containing relatives. Furthermore, the evolution of the degradation of the tin-based compounds was monitored more often and in shorter intervals. The resulting PXRD patterns of the investigated compounds for the low and high humidity treatments are given in Figure 3-6a-f.

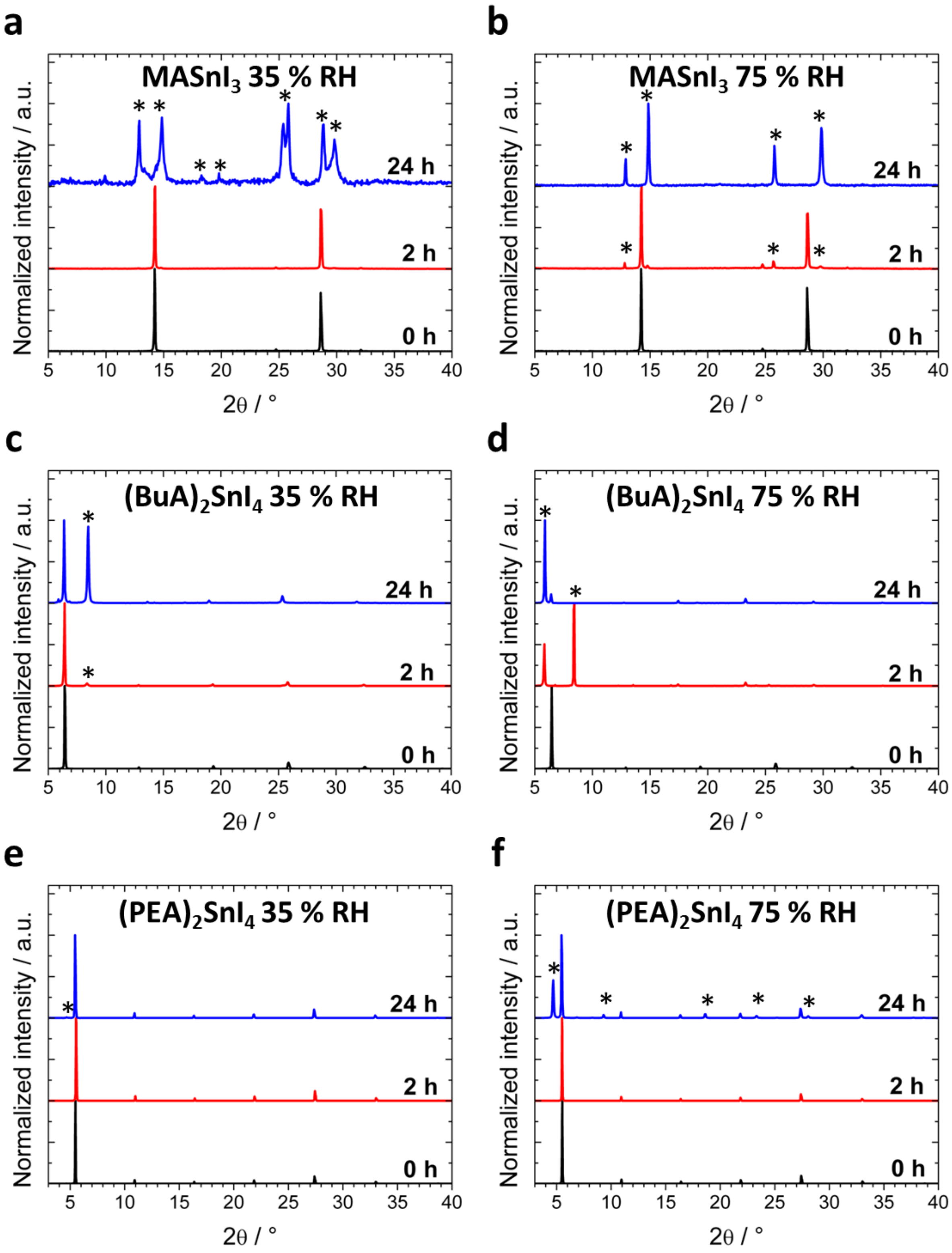

Figure 3-6: PXRD patterns of a) $MASnI_3$ exposed to 35 % RH, b) $MASnI_3$ exposed to 75 % RH, c) $(BuA)_2SnI_4$, exposed to 35 % RH, d) $(BuA)_2SnI_4$, exposed to 75 % RH, e) $(PEA)_2SnI_4$ exposed to 35 % RH, and f) $(PEA)_2SnI_4$, exposed to 75 % RH. The asterisks indicate the reflections of the degradation products.

The XRD patterns depicted in Figure 3-6a & b show that $MASnI_3$ exhibits strong signs of degradation after 24 h exposure to humidity, regardless of whether the humidity level was moderate or high, confirming the expected high sensitivity of $MASnI_3$ to oxygen and moisture. Since Sn^{2+} is much less stable than Pb^{2+}, the final degradation products of $MASnI_3$ do not mainly consist of hydrated species as shown for $MAPbI_3$. Instead, it is supposed that the degradation of $MASnI_3$ finally results in a compound or compounds based on Sn^{4+}, as shown for the oxidation of $CsSnI_3$ to Cs_2SnI_6 upon exposure to ambient conditions.[33,56,57] Surprisingly, no beneficial effect on the stability can be observed for the BuA-containing compound, see Figure 3-6c & d. $(BuA)_2SnI_4$ significantly degrades even at moderate humidity conditions (see Figure 3-6c), behaving contrary to its lead based counterpart, which exhibits a strongly increased moisture stability compared to $MAPbI_3$, see Figure 3-5c. This indicates that, due to the high sensitivity of Sn^{2+} towards oxygen and water, BuA is not able to sufficiently prevent water molecules from reacting with the metal cations. On the other hand, the PEA-based compound $(PEA)_2SnI_4$ features a significantly improved stability against moisture compared to its 3D relative $MASnI_3$, see Figure 3-6e & f. Although additional reflections appear, reflections of the original compound can still be observed even after 24 h at high humidity conditions (see Figure 3-6f). This is not the case for the MA and BuA based materials, indicating the strong ability of PEA to block water molecules from reacting with the Sn^{2+} cations. Similar to $MASnI_3$, Sn^{4+} based compounds can also be expected as final degradation products of $(BuA)_2SnI_4$ and $(PEA)_2SnI_4$, since all materials comprise the highly sensitive Sn^{2+} cations. Since the degradation of the materials is accompanied by a drastic change of the optical absorption properties, UV/vis spectra can also be utilized as a measure for the stability of tin halide perovskite-based samples.[58] Accordingly, we performed UV/vis measurements of our tin-based samples to monitor the changes of the absorption with progressive degradation. The resulting spectra are given in Figure 3-7a-f.

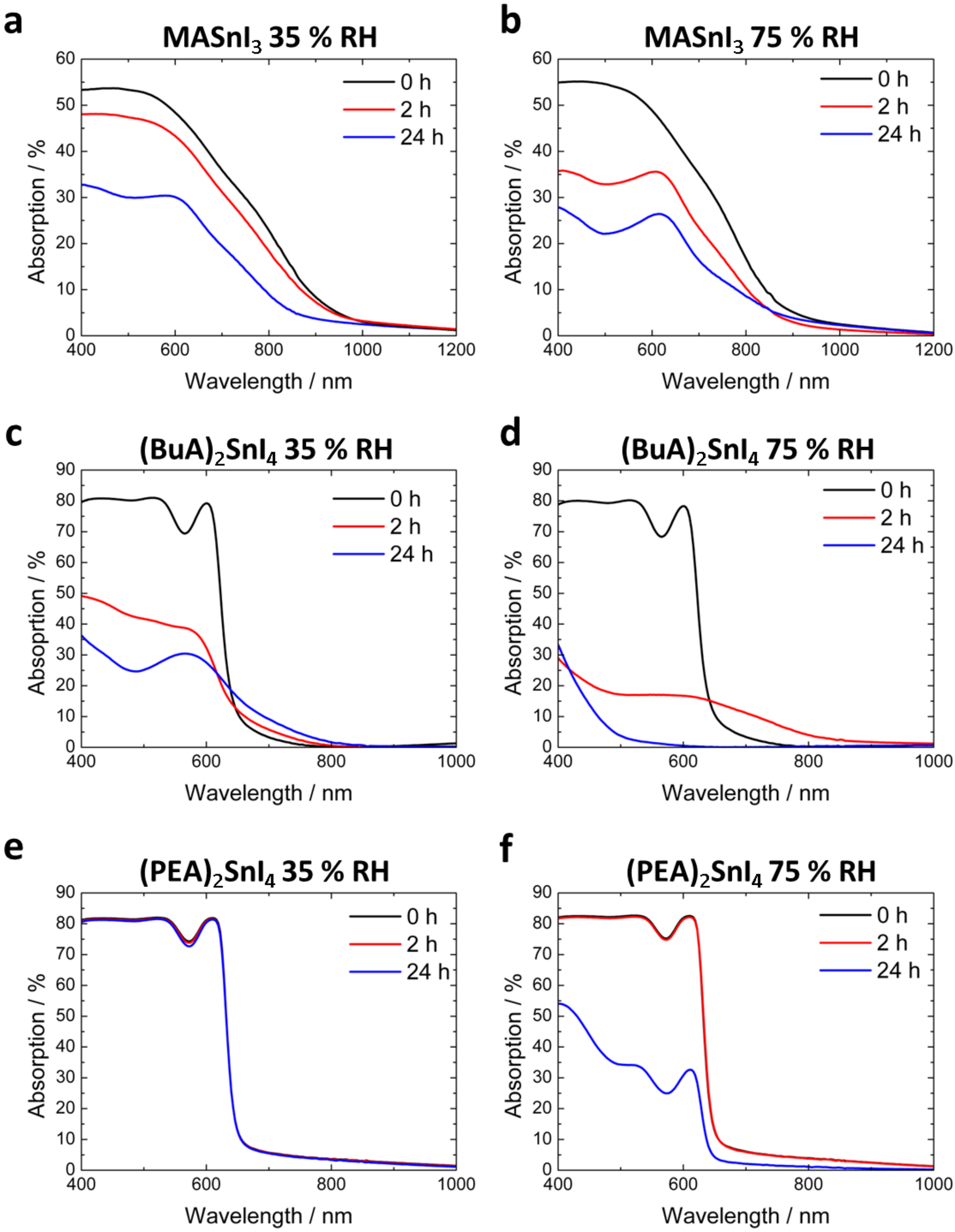

Figure 3-7: UV/vis spectra of a) $MASnI_3$ exposed to 35 % RH, b) $MASnI_3$ exposed to 75 % RH, c) $(BuA)_2SnI_4$, exposed to 35 % RH, d) $(BuA)_2SnI_4$ exposed to 75 % RH, e) $(PEA)_2SnI_4$ exposed to 35 % RH, and f) $(PEA)_2SnI_4$ exposed to 75 % RH. The asterisks indicate the reflections of the degradation products. All spectra were obtained from films on glass substrates in transmission mode.

A comparison of the UV/vis spectra with their corresponding XRD patterns shows that the degradation of the perovskite films is accompanied with a strong absorption loss, which can result in an almost complete disappearance of the light absorption in the visible range, see Figure 3-7d. The relatively strong light absorption across the whole visible range of $MASnI_3$ even after 24 h exposure to high humidity levels (see Figure 3-7b) is most likely caused by the formation of a Sn^{4+} based compound, similar to Cs_2SnI_6 which features a strong light absorption in the visible range.[57] On the other hand, the spectra of $(PEA)_2SnI_4$ show no significant change of the light absorption for the sample exposed to moderate humidity levels (see Figure 3-7e). Furthermore, in contrast to $(BuA)_2SnI_4$, the absorption characteristics of $(PEA)_2SnI_4$ are still observable after exposure to high humidity conditions for 24 h. Due to the high moisture stability of $(PEA)_2SnI_4$ under moderate humidity conditions, we extended the investigation of $(PEA)_2SnI_4$ to five consecutive days to reveal when a significant degradation of the material under moderate humidity conditions occurs, see Figure 3-8a & b.

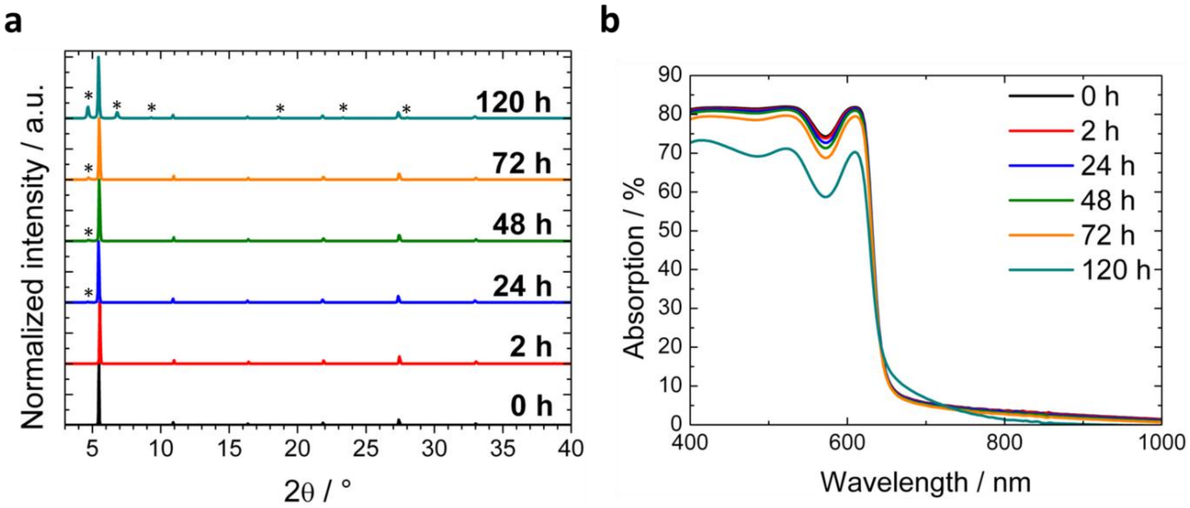

Figure 3-8: a) XRD patterns of $(PEA)_2SnI_4$, exposed to 35 % RH for different time spans. b) UV/vis spectra of $(PEA)_2SnI_4$ exposed to 35 % RH for different time spans. The asterisks indicate the reflections of the degradation products.

The XRD patterns in Figure 3-8a and the UV/vis spectra in Figure 3-8b clearly show that $(PEA)_2SnI_4$ is quite stable for several days of exposure to moderate humidity conditions. Even after five days only small signs of degradation can be observed in the XRD pattern and in the UV/vis spectra, hence supporting the viability of PEA to significantly improve the stability of tin iodide-based perovskites.

3.3 Conclusion

We have studied the structural and optoelectronic properties of $MASnI_3$, $(BuA)_2SnI_4$ and $(PEA)_2SnI_4$. We showed that the introduction of ammonium cations featuring large organic residues leads to the formation of layered compounds accompanied with a strong blue shift of the absorption onset. However, since the E_g of the tin based compounds is significantly smaller than that of their lead-based counter parts, layered hybrid tin iodide based perovskites are interesting candidates for applications as top cell in a tandem solar cell assembly. Furthermore, our investigated layered compounds feature a strong PL signal in the visible range, making them interesting for applications in light-emitting devices. Additionally, moisture stability studies revealed that only large, bulky and highly hydrophobic organic residues like aromatic rings are able to efficiently block water from reacting with the highly sensitive Sn^{2+} cations. Accordingly, the substitution of MA by PEA resulted in an increased stability of the hybrid tin halide perovskite from a few hours to several days under moderate humidity conditions. Regarding the significant stability improvements achieved by the utilization of an ammonium cation featuring a large aromatic residue, we consider our work as a first step towards the development of highly stable lead-free tin halide perovskites based on large hydrophobic cations for different optoelectronics applications.

3.4 Experimental Section

Preparation of the precursors

Methylammonium iodide (MAI) was prepared by first diluting 24 mL of a 33 % ethanolic methylamine solution (18 g, 0.2 mol, Sigma Aldrich) with 100 mL ethanol absolute in a 250 mL roundbottom flask. Subsequently, 10 mL (17 g, 0.07 mol) of hydroiodic acid (57 %wt in water, Sigma Aldrich) were added to the methylamine solution under constant stirring. After one hour reaction time, the solvent was removed by rotary evaporation. The obtained white crystals were washed with dry diethyl ether and finally recrystallized from ethanol.

Butylammonium iodide (BuAI) was prepared by first diluting 25 mL (18.5 g, 0,25 mol) *n*-butylamine (99.5 %, Acros) with 25 mL ethanol absolute in a 250 mL roundbottom flask and cooling it down to 0 °C. Subsequently, 27 mL (46 g, 0.36 mol) of hydroiodic acid (57 %wt in water, Sigma Aldrich) were added to the *n*-butylamine solution under constant stirring. The precipitate was collected by suction filtration and washed several times with diethyl ether. The obtained powder was recrystallized from *iso*-propanol and dried under reduced pressure.

Phenethylammonium iodide (PEAI) was prepared as described for BuAI by using 25 mL (24 g, 0.2 mol) 2-phenylethylamine (≥ 99 %, Sigma Aldrich).

Sample preparation

All samples were prepared on glass substrates, which were plasma cleaned for 5 min before film application, in a nitrogen glove box via spin-coating. The precursor solutions were prepared by dissolving either 461 mg PbI_2 (1.0 mmol, 99 %, Sigma Aldrich) or 372 mg SnI_2 (1,0 mmol, 99.999 %, Alfa Aesar) in 1 mL *N*,*N*-dimethylfomamide (DMF, 99.8%, Sigma-Aldrich). After the metal salt was completely dissolved the solution was added to a vial filled either with 159 mg (1.0 mmol) MAI, 402 mg (2.0 mmol) BuAI or 500 mg (2.0 mmol) PEAI to obtain the final spin-coating solution. 100 µL of the solution were spin-coated on a glass substrate at 3000 rpm for 30 s. Subsequently, the films were annealed at 100 °C for 5 min under nitrogen atmosphere to remove residual solvent. For the optoelectronic investigations, the tin-based samples were sealed with a microscope slide and epoxy resin to avoid the degradation of the specimen.

Charcterization details

Powder X-ray diffraction measurements were performed in transmission mode on a STOE Stadi MP diffractometer with a Cu Kα1 radiation source (λ = 1.54060 Å) operating at 40 kV and 40 mA. The diffractometer was equipped with a DECTRIS MYTHEN 1K solid-state strip detector. X-ray diffraction measurements on thin films were performed using a Bruker D8 Discover X-ray diffractometer operating at 40 kV and 30 mA, employing Ni-filtered Cu Kα radiation (λ = 1.5406 Å) and a position-sensitive detector (LynxEye).

Steady-state optical absorption spectra were acquired with a Lambda 1050 UV-Vis spectrophotometer (Perkin Elmer) using an integrating sphere.

Steady state and time resolved photoluminescence measurements were conducted with a Fluotime 300 Spectrofluorometer (Picoquant GmbH). The excitation wavelength was fixed at

410 nm. The emission during time resolved measurements was monitored at the maximum intensity of the steady state photo-emission of each compound.

3.5 Literature

[1] U.S. Energy Information Administration. Available online: http://www.eia.gov/todayinenergy/detail.cfm?id=12251 (accessed on 8 January 2018)

[2] S. Solomon, D. Qin, M. Manning, Z. Chen, M. Marquis, K. B. Averyt, M. Tignor, H. L. Miller, eds., *Climate Change 2007: The Physical Science Basis*, Contribution of Working Group I to the Fourth Assessment Report of the Intergovernmental Panel on Climate Change, Cambridge University Press, **2007**.

[3] G. Xing, N. Mathews, S. S. Lim, N. Yantara, X. Liu, D. Sabba, M. Grätzel, S. Mhaisalkar, T. C. Sum, *Nat. Mater.* **2014**, *13*, 476.

[4] M. M. Lee, Joël Teuscher, Tsutomu Miyasaka, Takurou N. Murakami, Henry J. Snaith, *Science* **2012,** *338*, 643.

[5] W. S. Yang, J. H. Noh, N. J. Jeon, Y. C. Kim, S. Ryu, J. Seo, S. I. Seok, *Science* **2015**, *348*, 1234.

[6] H. Zhu, Y. Fu, F.Meng, X. Wu, Z. Gong, Q. Ding, M. V. Gustafsson, M. T. Trinh, S. Jin, X.-Y. Zhu, *Nat. Mater.* **2015,** *14*, 636.

[7] Z.-K. Tan, R. S. Moghaddam, M. L. Lai, P. Docampo, R. Higler, F. Deschler, M. Price, A. Sadhanala, L. M. Pazos, D. Credgington, F. Hanusch, T. Bein, H. J. Snaith, R. H. Friend, *Nat. Nanotechnol.* **2014,** *9*, 687.

[8] T. M. Brenner, D. A. Egger, L. Kronik, G. Hodes, D. Cahen, *Nat. Rev. Mater.*, **2016,** *1*, 15007.

[9] S. De Wolf, J. Holovsky, S.-J. Moon, P. SLoiper, B. Niesen, M. Ledinsky, F.-J. Haug, Yum, C. Ballif *J. Phys. Chem. Lett.*, **2014,** *5*, 1035.

[10] S. D. Stranks, G. E. Eperon, G. Grancini, C. Menelaou, M. J. P. Alcocer, T. Leijtens, L. M. Herz, A. Petrozza and H. J. Snaith *Science,* **2013,** *342*, 341.

[11] C. Wehrenfennig, G. E. Eperon, M. B. Johnston, H. J. Snaith, L- M. Herz, *Adv. Mater.*, **2014,** *26*, 1584.

[12] R. E. Brandt, V. Stevanović, D. S. Ginley, T. Buonassisi, *MRS Commun.*, **2015,** *5*, 265.

[13] A. Walsh, D. O. Scanlon, S. Chen, X. G. Gong, S.-H. Wei, *Angew. Chem., Int. Ed.*, **2015,** *54*, 1791.

[14] Y.-Y Zhang, S. Chen, P. Xu, H. Xiang, X.-G. Gong, A. Walsh, S.-H. Wei, *arXiv:1506.01301*, **2015**.

[15] G. P. Nagabhushana, R. Shivaramaiah, A. Navrotsky, *Proc. Natl. Acad. Sci. U. S. A.*, **2016,** *113*, 7717.

[16] N. Aristidou, I. Sanchez-Molina, T. Chotchuangchutchaval, M. Brown, L. Martinez, T. Rath, S. A. Haque, *Angew. Chem., Int. Ed.*, **2015,** *54*, 8208.

[17] Babayigit, A.; Ethirajan, A.; Muller, M.; Conings, B. *Nat. Mater.*, **2016,** *15*, 247.

[18] A. Leguy, Y. Hu, M. Campoy-Quiles, M. I. Alonso, O. J. Weber, P. Azarhoosh, M. van Schilfgaarde, M. T. Weller, T. Bein, J. Nelson, P. Docampo, P. R. F. Barnes, *Chem. Mater.* **2015**, *27*, 3397.

[19] P. Patnaik, *Handbook of Inorganic Chemicals*, McGraw-Hill, NewYork **2003**.

[20] B. Hailegnaw, S. Kirmayer, E. Edri, G. Hodes, D. Cahen, *J.Phys.Chem.Lett*. **2015,** *6*, 1543.

[21] L. Patrick, *Altern Med Rev* **2006**, *11*, 2.

[22] I. R. Benmessaoud, A.-L. Mahul-Mellier, E. Horvath, B. Maco, M. Spina, H. Lashuel, L. Forro, *Toxicol Res* **2015**, *5*, 407.

[23] T. Krishnamoorthy, H. Ding, C. Yan, W. L. Leong, T. Baikie, L. Zhang, M. Sherburne, S. Li, M. Asta, N. Mathews, et al., *J. Mater. Chem. A* **2015,** *3*, 23829.

[24] B. W. Park, B. Philippe, X. Zhang, H. Rensmo, G. Boschloo, E. M. J. Johansson. *Adv. Mater*. 2015, *27*, 6806.

[25] B. Saparov, F. Hong, J. P. Sun, H. S. Duan, W. Meng, S. Cameron, I. G. Hill, Y. Yan, D. B. Mitzi, *Chem. Mater*. 2015, *27*, 5622.

[26] X. P. Cui, K. J. Jiang, J. H. Huang, Q. Q. Zhang, M. J. Su, L. M. Yang, Y. L. Song, X. Q. Zhou, *Synth. Met*. 2015, *209*, 247.

[27] M. Lyu, J. H. Yun, M. Cai, Y. Jiao, P. V. Bernhardt, M. Zhang, Q. Wang, A. Du, H. Wang, G. Liu, L. Wang, *Nano Res.* **2016,** *9*, 692.

[28] F. Hao, C. C. Stoumpos, C. C. Cao, R. P. H. Chang, M. G. Kanatzidis, *Nat. Photonics* 2014, *8*, 489.

[29] N. K. Noel, S. D. Stranks, A. Abate, C. Wehrenfennig, S. Guarnera, A. A. Haghighirad, A. Sadhanala, G. E. Eperon, S. K. Pathak, M. B. Johnston, A. Petrozza, L. M. Herz, H. J. Snaith, *Energy Environ. Sci.* **2014,** *7,* 3061.

[30] Y. Takahashi, R. Obara, Z.-Z. Lin, Y. Takahashi, T. Naito, T. Inabe, S. Ishibashi, K. Terakura, *Dalton Trans.* **2011,** *40*, 5563.

[31] Y. Takahashi, H. Hasegaw, Y. Takahashi, T. Inabe, *J. Solid State Chem.* **2013,** *205,* 39.

[32] I. Chung, B. Lee, J. He, R. P. H. Chang, M. G. Kanatzidis, *Nature* **2012,** *485*, 486.

[33] F. Wang, J. Ma, F. Xie, L. Li, J. Chen, J. Fan, Ni Zhao, *Adv. Funct. Mater.* **2016,** *26*, 3417.

[34] I. C. Smith, E. T. Hoke, D. Solis-Ibarra, M. D. McGehee, H. I. Karunadasa, *Angew. Chem., Int. Ed.* **2014,** *53*, 11232.

[35] Y. Hu, J. Schlipf, M. Wussler, M. L. Petrus, W. Jaegermann, T. Bein, P. Müller-Buschbaum, P. Docampo, *ACS Nano,* **2016,** *10*(6), 5999.

[36] D. H. Cao, C. C. Stoumpos, O. K. Fahra, J. T. Hupp, M. G. Kanatzidis, *J. Am. Chem. Soc.,* **2015,** *137*(24), 7843.

[37] D. B. Mitzi, *Chem. Mater.* **1996,** *8,* 791.

[38] C. C. Stoumpos, D. H. Cao, D. J. Clark, J. Young, J. M. Rondinelli, J. I. Jang, J. T. Hupp, M. G. Kanatzidis, *Chem. Mater.* **2016,** *28*, 2852.

[39] J. Even, L. Pedesseau, C. Katan, *ChemPhysChem* **2014,** *15*, 3733.

[40] X. Hong, T. Ishihara, A. V. Nurmikko, *Phys. Rev. B* **1992,** *45*(12), 6961.

[41] C. C. Stoumpos, L. Mao, C. D. Malliakas,. M. G. Kanatzidis, *Inorg. Chem*. **2017,** *56*, 56.

[42] J. M. Olson, S. R. Kurtz, A. E. Kibbler, P. Faine, *Appl. Phys, Lett.* **1990,** *56*(7), 12.

[43] H.-S. Kim, C.-R. Lee, J.-H. Im, K.-B. Lee, T. Moehl, A. Marchioro, S.-J. Moon, R. Humphry-Baker, J.-H. Yum, J. E. Moser, M. Grätzel, N.-G. Park, *Sci. Rep.* **2012,** *2*, 591.

[44] M. E. Kamminga, H.-H. Fang, M. R. Filip, F. Giustino, J. Baas, G. R. Blake, M. A. Loi, T. T. M. Palstra, *Chem. Mater.* **2016,** *28*(13), 4554.

[45] G.-J. A. H. Wetzelaer, M. Scheepers, A. M. Sempere, C. Momblona, J. Ávila, H. J. Bolink, *Adv.Mater*. **2015,** *27*, 1837.

[46] M. T. Trinh, X. Wu; D. Niesner, X.-Y. Zhu, *J. Mater. Chem. A* **2015,** *3*, 9285.

[47] L. Mao, H. Tsai, W. Nie, L. Ma, J. Im, C. C. Stoumpos, C. D. Malliakas, F. Hao, M. R. Wasielewski, A. D. Mohite, M. G. Kanatzidis, *Chem. Mater.* **2016,** *28*, 7781.

[48] T. Ishihara, *J. Lumin*. **1994,** *60*, 269.

[49] V. D'Innocenzo, G. Grancini, M. J. P. Alcocer, A. R. S. Kandada, S. D. Stranks, M. M. Lee, G. Lanzani, H. J. Snaith, A. Petrozza, *Nat. Commun*. **2014,** *5*, 3586.

[50] F. Deschler, M. Price, S. Pathak, L. E. Klintberg, D.-D. Jarausch, R. Higler, S. Hüttner, T. Leijtens, S. D. Stranks, H. J. Snaith, M. Atatüre, R. T. Phillips, R. H. Friend, *J. Phys. Chem. Lett. 2014,* 1421.

[51] X. Wu, M. T. Trinh, D. Niesner, H. Zhu, Z. Norman, J. S. Owen, O. Yaffe, B. J. Kudisch, X.-Y- Zhu, *J. Am. Chem. Soc.* **2015,** *137*, 2089.

[52] W. Liao, D. Zhao, Y. Yu, C. R. Grice, C. Wang, A. J. Cimaroli, P. Schulz, W. Meng, K. Zhu, R.-G. Xiong, Y. Yan, *Adv.Mater.* **2016,** *28*, 9333.

[53] T.-B. Song, T. Yokoyama, C. C. Stoumpos, J. Logsdon, D. H. Cao, M. R. Wasielewski, S. Aramaki, M. G. Kanatzidis, *J. Am. Chem. Soc.* **2017,** *139*(2), 836.

[54] R. Nishikubo, N. Ishida, Y. Katsuki, A. Wakamiya, A. Saeki, *J. Phys. Chem. C* **2017,** *121*, 19650.

[55] P. Docampo, T. Bein, *Acc. Chem. Res.* **2016**, *49*, 339.

[56] I. Chung, J.-H. Song, J. Im, J. Androulakis, C. D. Malliakas, H. Li, A. J. Freeman, J. T. Kenney, M. G. Kanatzidis, *J. Am. Chem. Soc.* **2012,** *134*, 8579.

[57] B. Lee, C. C. Stoumpos, N. Zhou, F. Hao, C. Malliakas, C.-Y. Yeh, T. J. Marks, M. G. Kanatzidis, R. P. H. Chang, *J. Am. Chem. Soc.* **2014,** *136*, 15379.

[58] Y. Liao, H. Liu, W. Zhou, D. Yang, Y. Shang, Z. Shi, B. Li, X. Jiang, L. Zhang, L. N. Quan, R. Quintero-Bermudez, B. R. Sutherland, Q. Mi, E. H. Sargent, Z. Ning, *J. Am. Chem. Soc.* **2017,** *13*9, 6693.

4 Synthesis of hybrid tin halide perovskite solar cells with less hazardous solvents: methanol and 1,4-dioxane

This chapter is based on the following publication:

Enrico Greul, Pablo Docampo and Thomas Bein, *Zeitschrift für allgemeine und anorganische Chemie* **2017,** *643*, 1704–1711.

Dedicated to Wolfgang Schnick at the occasion of his 60th birthday.

4.1 Introduction

The constant increase of global energy consumption accompanied by the decline of fossil fuels generates a strong demand for new, sustainable energy sources.[1] In the past few years, organic-inorganic lead halide perovskites have emerged as highly efficient and inexpensive absorber materials for solar cells.[2,3] The simple processability and high power conversion efficiencies of over 20 % for state-of-the-art devices, assembled with methylammonium lead iodide ($MAPbI_3$), make these materials interesting candidates for large-scale applications.[4–6]

Due to the solubility of the lead salts in water, the toxicity of high-performing hybrid halide perovskites can be considered as a major barrier for commercializing this technology. Therefore, a great deal of effort has been undertaken to develop lead-free perovskite-related compounds based on Ge^{2+}, Sn^{2+}, Bi^{3+}, Sb^{3+} or Cu^{2+} for photovoltaic applications.[7–11] Sn-based compounds with the general formula $ASnX_3$, where A can be Cs, methylammonium (MA) or formamidinium (FA) and X can be I, Br, Cl or F, are the most promising alternatives to lead-based materials, with reported power conversion efficiencies (PCE) of ~ 6 % for devices based on methylammonium tin iodide ($MASnI_3$) films.[12,13] The lower efficiencies compared to lead-based materials are generally assigned to Sn^{4+} self-doping due to the facile oxidation of Sn^{2+} under ambient conditions.[13–17]

Further toxicity concerns arise from the harmful solvents utilized during the preparation of the perovskite films. The most common solvent, N,N-dimethylformamide (DMF), is known to be strongly hepatotoxic, even at relatively low concentrations, and the European Union has classified it as toxic to reproduction.[18–21] Furthermore, it can easily be taken up by dermal absorption, which is troubling since the dwell time of DMF in the body is much longer for percutaneous uptake than for pulmonary ingestion.[22] The second widespread solvent, dimethylsulfoxide (DMSO), although not acutely toxic, can induce bradycardia, respiratory problems, and alterations in blood pressure.[23,24] Furthermore, it potentially alters the chemical structure of cell membranes and thus their functional properties.[25] However, the most critical property of DMSO is that it can serve as an efficient carrier for other agents by enhancing the penetration through skin tissue, which is particularly critical for toxic substances like soluble lead compounds.[26]

With the prospect of possible commercialization of solution-processable solar cells, the development of less toxic film formation routes is an important issue to minimize the health risks during the film preparation. This must be balanced with the formation of homogenous films which uniformly cover the substrate. Considering Pb-based solar cells, the development of advanced film formation methods has led to homogeneous, smooth and pinhole-free perovskite films and has been the driving factor behind the great leaps in device efficiency.[27] Accordingly, the synthesis of high-quality $MASnI_3$ films can be considered as a key task to enable the system for high-efficiency photovoltaic applications.

$MASnI_3$ forms very rough and inhomogeneous films with micron-sized pinholes when employing common deposition methods based on DMF due to the much faster crystallization process as compared to $MAPbI_3$,. This, in turn, results in severely shunted photovoltaic devices. [12,13,15,28,29] In order to resolve these issues, Hao *et al*. developed a deposition route based on a (DMSO)-SnI_2 intermediate phase which improved the surface coverage by slow crystallization of the perovskite.[30] An alternative route was developed by Yokoyama *et al*. who adapted the well-known vapour-assisted solution process for the preparation of homogeneous but not crack-free $MASnI_3$ films.[31,32] Recently, Long *et al.* have developed a synthetic route for high-quality $FASnI_3$ films based on antisolvent dripping.[33] However, all three methods still rely on the hazardous DMF or DMSO solvents to deposit the metal halide layer. Previous studies on lead based hybrid perovskites showed that the hazardous solvents can be replaced by water to deposit the metal halide layer.[34,35] However, due to the sensitivity of the Sn^{2+} ion to oxygen and moisture this approach cannot be transferred to the lead-free compound.[13]

Here, we demonstrate a new one-step synthesis route for the preparation of high-quality, lead-free $MASnI_3$ films for photovoltaic applications based on less hazardous solvents (methanol (MeOH) and 1,4-dioxane (Dioxane)). Our route provides high quality films which outperform conventional one-step synthesis routes based on DMF and DMSO in photovoltaic devices. Our results represent a further step towards efficient lead-free perovskite based solar cells manufactured under non-dangerous conditions.

4.2 Results and Discussions

Our films were prepared on a 250 nm thick titanium dioxide (TiO_2) scaffold via a one-step spin-coating process from precursors dissolved in a MeOH: Dioxane mixture. As a reference, we also prepared $MASnI_3$ films utilizing the most common conventional one-step routes according to literature.[12,30]

When employing our newly developed MeOH/Dioxane route, the perovskite film forms within a few seconds after application of the solution, as depicted schematically in Figure 4-1. Since MeOH and Dioxane feature rather high vapour pressures of 130 hPa[36] and 37 hPa[37] at 20 °C, rapid solvent evaporation is expected. Accordingly, we propose that the fast supersaturation of the perovskite solution leads to the formation of a large number of small nuclei, resulting in smooth and homogeneous $MASnI_3$ films after complete solvent evaporation. Due to the faster crystallization of $MASnI_3$ compared to $MAPbI_3$, the rapid solvent evaporation is essential to inhibit the growth of large, pointy crystals which protrude from the substrate and lead to substantial pinholes in the hole transporting layer (HTL).

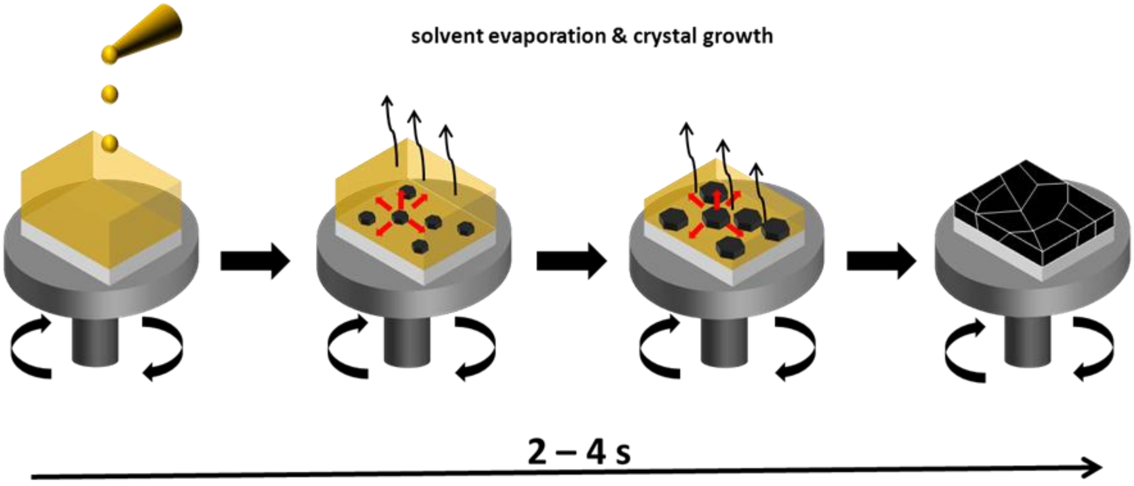

Figure 4-1: Schematic of the MeOH/Dioxane route. For simplification, only a few crystallites are depicted. The arrow underneath indicates the time range within which film formation usually occurs.

The PXRD patterns given in Figure 4-2 show that the films made by our newly developed MeOH/Dioxane route are phase pure, similar to that made by the commonly used one step deposition routes based on DMF and DMSO precursor solutions.

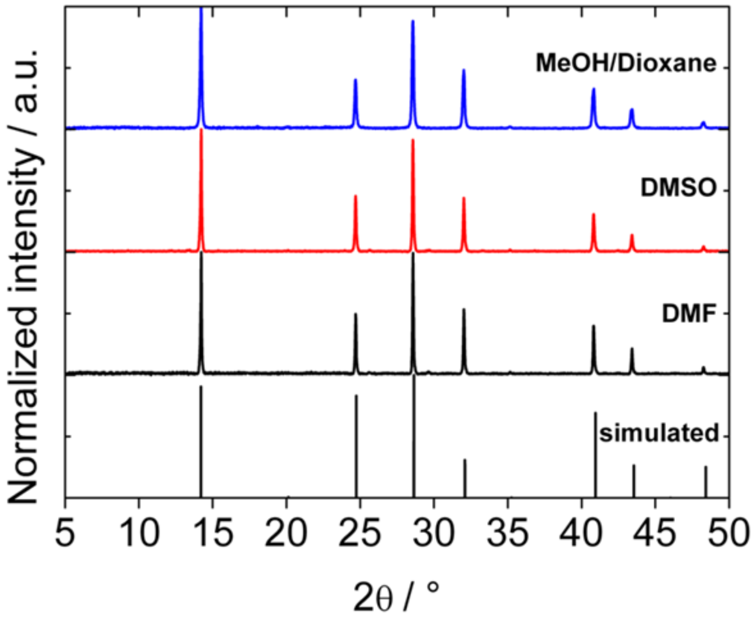

Figure 4-2: PXRD pattern of $MASnI_3$ prepared from DMF, DMSO and MeOH/Dioxane solution. The patterns were taken from powder obtained by scratching off films. To confirm the phase purity, a simulated PXRD pattern of $MASnI_3$ is depicted.

Scanning electron microscopy (SEM) images revealed large differences in the morphology of $MASnI_3$ films made from the different solvents. As shown in Figure 4-3a, films prepared from a DMF solution are inhomogeneous, featuring a pattern of large $MASnI_3$ grains with low surface coverage. Figure 4-3b shows the SEM image of a $MASnI_3$ film made from a DMSO solution featuring enhanced homogeneity with less prominent patterns compared to films prepared from DMF solution. However, films made by our newly developed MeOH/Dioxane method (Figure 4-3c) fully cover the substrate with no visible pinholes or large protruding crystals, similar to those prepared by Long *et al*. via their antisolvent dripping route.[33]

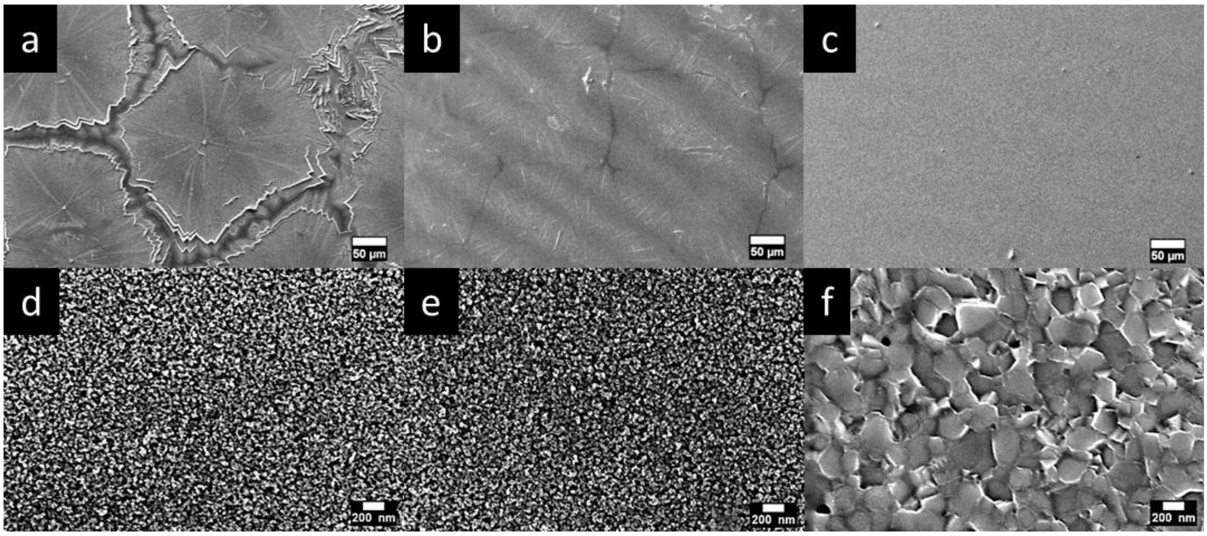

Figure 4-3: SEM images of $MASnI_3$ films on TiO_2 scaffold substrate: (a) DMF solution, (b) DMSO solution, (c) MeOH/Dioxane. Panels d – f represent SEM images of films a – c at higher magnifications, respectively.

Higher magnifications of the depicted films (Figure 4-3d - f) reveal striking morphology differences. In the films manufactured from the conventional solvents DMF and DMSO (Figure 4-3d & e) the porous TiO_2 scaffold is directly visible. In contrast, the film prepared from MeOH/Dioxane features a dense, homogeneous $MASnI_3$ capping layer exhibiting many relatively small crystallites, which supports our proposed film formation mechanism. In contrast with 2-step deposition methods that result in small cuboid crystals, the MeOH/Dioxane route yields a smooth capping layer consisting of irregularly shaped crystals, similar to those from Yokoyama *et al.*[32] This dense capping layer is an important feature of high-efficiency perovskite solar cells,[38] as it prevents the direct contact of the HTL with the electron-transporting TiO_2.

The key enabler of the developed route based on less hazardous solvents is possible due to the higher solubility of SnI_2 in alcohols compared to PbI_2.[29] However, simply employing MeOH, which showed the highest solubility for $MASnI_3$ during our studies, leads to rather low concentrations of ~ 0.1 M. The addition of a miscible co-solvent that can complex with Sn(II) in the form of Dioxane, greatly increases the saturation concentration of the precursor mixture up to ~0.3 M.[39,40]

To gain more knowledge about the influence of Dioxane during the film formation, we prepared perovskite solutions with 25 % (v/v), 50 % (v/v) or 75 % (v/v) of Dioxane at a given $MASnI_3$ concentration of 0.3 M. We observed a decreasing solubility of the perovskite with higher concentrations of Dioxane, eventually leading to the formation of a black $MASnI_3$ precipitate at the highest concentration (see Figure 4-4a), confirmed by PXRD measurements (see Figure 4-4b).

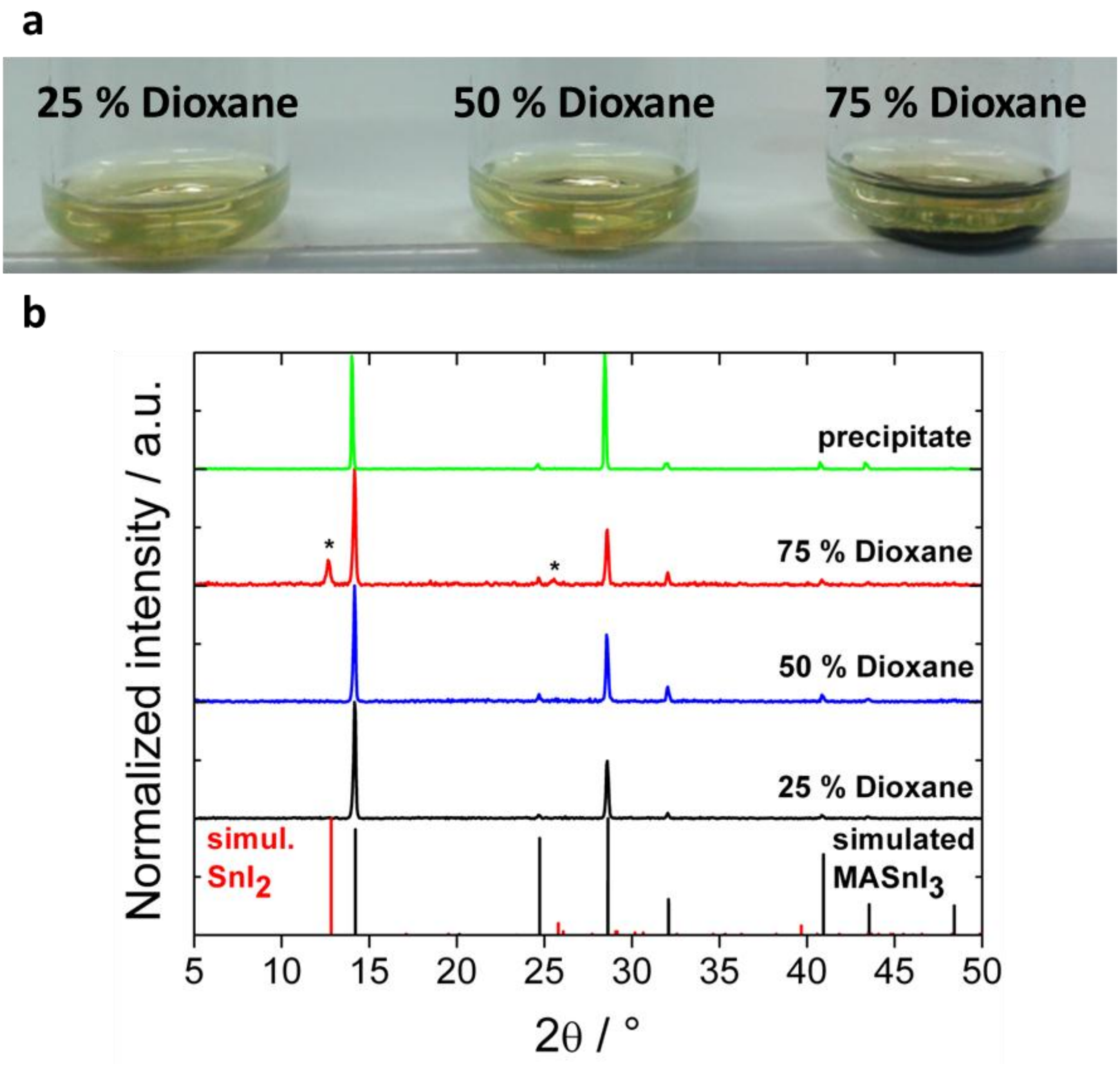

Figure 4-4: a) Images of solutions prepared with 25 % (v/v), 50 % (v/v) or 75 % (v/v) Dioxane. The black precipitate can clearly be seen for the highest Dioxane concentration. b) PXRD pattern of $MASnI_3$ films prepared from precursor solutions containing the three different Dioxane concentrations. The simulated patterns for $MASnI_3$ (black) and SnI_2 (red) are also given. Additionally, the PXRD pattern of the precipitate obtained from the solution with the highest Dioxane concentration is depicted (green).

Since highly polar solvents are commonly used to dissolve $MASnI_3$, it is likely that the reduction of the solubility is due to the small dipole moment of Dioxane.[41] This, in turn, suggests that the enhanced solubility of $MASnI_3$ in the MeOH/Dioxane solvent mixture at low Dioxane concentrations is not caused by the good solubility of the perovskite in Dioxane, but rather by the coordination of the solvent to Sn(II).[38,39] Since stable Sn(II)-( )-(Dioxane) complexes are known for $SnCl_2$[40] and $SnBr_2$[39], we propose an inhibited reaction of MAI with SnI_2 to $MASnI_3$ in solution by the formation of Sn(II)-(Dioxane) adducts, resulting in an increased solubility of $MASnI_3$ in the utilized solvent mixture. The perovskite films form within a few seconds because of the high vapour pressure of the utilized solvents, and therefore a direct proof for the proposed Sn(II)-(Dioxane) adduct by commonly used FTIR measurements is not possible.

In order to address this, we performed XRD measurements to obtain an indirect indication of the adduct, as shown in Figure 4-4b. Here, we observe additional reflections at the highest Dioxane concentration, which can be assigned to SnI_2. This is likely caused by the stabilization of the Sn(II)-(Dioxane) adduct at high Dioxane concentrations, which prevents its complete reaction with MAI to $MASnI_3$. Accordingly, we found an optimum in film quality and no phase segregation for 25 % (v/v) Dioxane. Thus, only the $MASnI_3$ film properties made from solutions containing 25 % (v/v) Dioxane are discussed in the following.

We investigated the influence of the three different film formation methods (Sn-perovskite films prepared either from DMF, DMSO or MeOH/Dioxane solutions) on the photovoltaic properties by incorporating the resulting films in devices with the typical layer assembly of fluorine doped tin oxide (FTO)/compact-TiO_2/mesoporous-TiO_2/perovskite/HTL/Au contact.[31] A schematic of the solar cells and a cross-sectional image of a functional MeOH/Dioxane-derived device utilizing 2,2',7,7'-tetrakis-(N,N-di-pmethoxyphenylamine)9,9'-spirobifluoren (spiro-OMeTAD) as HTL are given in Figure 4-5a & b. The $MASnI_3$ capping layer on top the mesoporous-TiO_2 can clearly be seen, which is a feature of high efficiency devices as it prevents shunting paths in devices. [13,32]

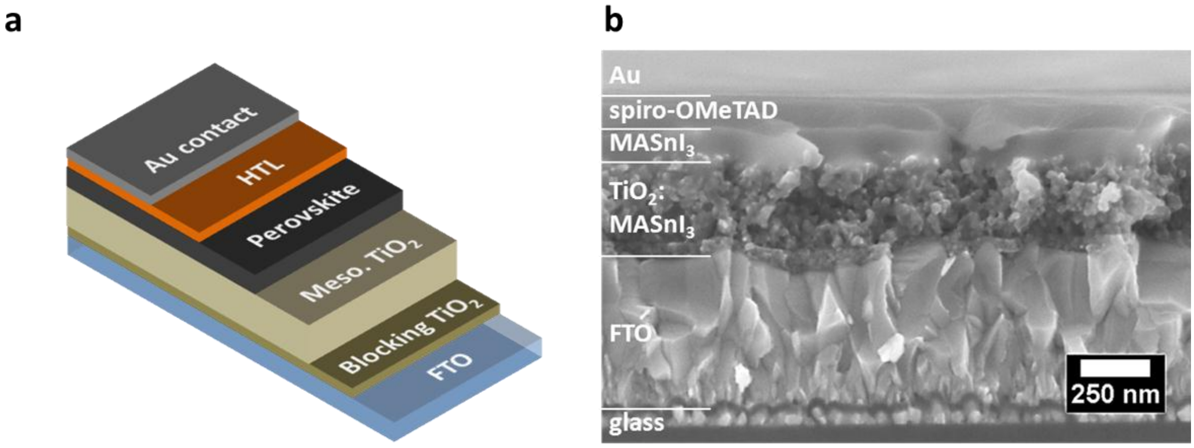

Figure 4-5: a) Schematic of an assembled solar cell. b) Cross-sectional SEM image of a functional device assembled with a MeOH/Dioxane $MASnI_3$ film.

In order to further improve the device performance, we partially substituted iodide by bromide, which leads to a slightly smaller unit cell due to the smaller bromide without changing the tetragonal structure of the perovskite (see Figures 4-6).

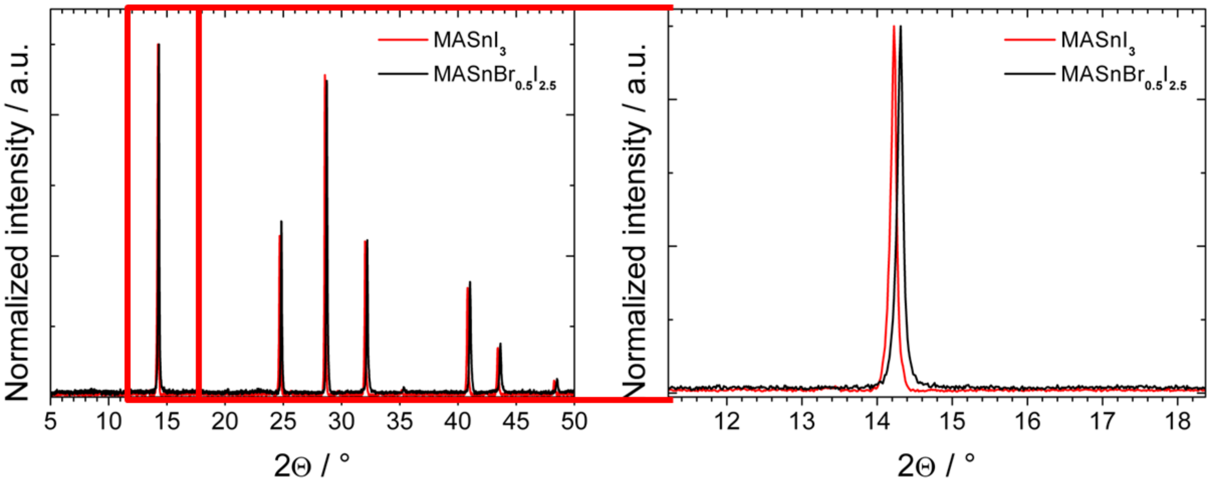

Figure 4-6: PXRD pattern of $MASnI_3$ and $MASnBr_{0.5}I_{2.5}$ powders obtained by scratching off films made via the MeOH/Dioxane route. No additional reflections can be observed for the bromide containing compound. The positions of the reflections of the bromide containing compound are slightly shifted to larger 2Θ values caused by slightly decreased unit cell size due to the insertion of bromide.

Hao *et al*. showed that bromide has a beneficial effect on the device performance, mainly due to the reduction of the series resistance R_S and the increase of the V_{OC}.[12] Additionally, they showed that bromide enhances the lifetime of the photoexcited species by destabilizing Sn^{2+}/Sn^{4+} defects, leading to an enhanced charge collection efficiency resulting in a higher

J_{SC}.[42] Here, we obtained the best performing devices with a perovskite composition of $MASnBr_{0.5}I_{2.5}$. This composition slightly increases the band gap energy (E_g) of the perovskite from about 1.3 eV to 1.4 eV (see Figure 4-7), which is very close to the optimal E_g for a single-junction solar cell. Furthermore, the partial substitution of the iodide by bromide has no observable influence on the morphology of the prepared films, see Figure 4-8a – f.

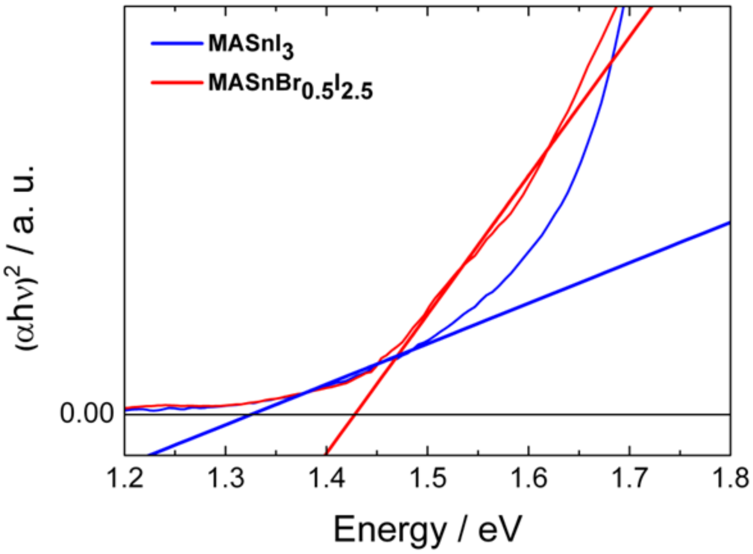

Figure 4-7: Tauc plots of $MASnI_3$ and $MASnBr_{0.5}I_{2.5}$ made from MeOH/Dioxane. The bromide containing compound shows an increased band E_g of about 1.4 eV, which is characteristic for the substitution of iodide by bromide.

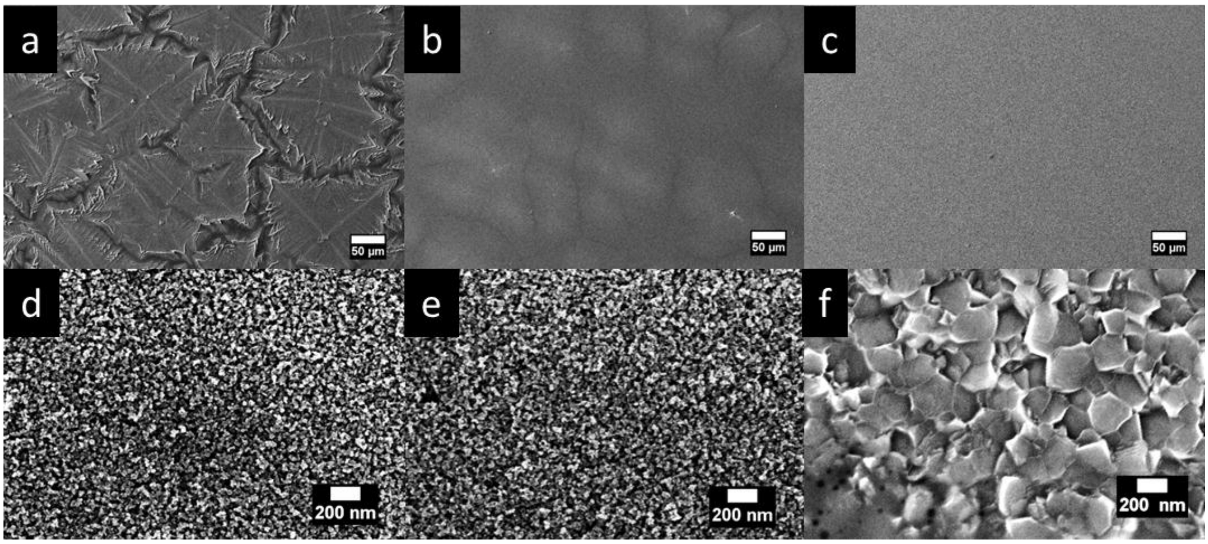

Figure 4-8: SEM images of $MASnBr_{0.5}I_{2.5}$ films on FTO/TiO_2 substrate: (a) DMF solution, (b) DMSO solution, (c) MeOH/Dioxane. Panels d – f represent SEM images of films a – c at higher magnifications, respectively. All films show a similar morphology to its $MASnI_3$ counterpart

The current-voltage (*J*-*V*) curves of the best performing devices out of 36 individual solar cells per synthesis route are displayed in Figure 4-9a. We obtained consistently poor performance for devices assembled with $MASnBr_{0.5}I_{2.5}$ films prepared from DMF or DMSO solutions. In this case, the *J*-*V* curves show severely shunted behavior and PCEs of 0.04 % and 0.01 %, with short-circuit currents (J_{SC}) of 8.84 mA/cm² and 4.67 mA/cm² and open-circuit voltages (V_{OC}) of 0.02 V and 0.01 V for the best devices, which is in good agreement with reported values by Hao *et al*. and Takamichi *et al*..[30, 32] In contrast, the solar cells obtained via the MeOH/Dioxane route exhibit an enhanced performance with the highest PCE of 1.05 % with a J_{SC} of 15.44 mA/cm², V_{OC} of 0.18 V and a FF of 38 %. We note that devices based on films prepared with the MeOH/Dioxane route show prominent hysteresis, similar to that observed for photovoltaic cells based on lead halide perovskite, see Figure 4-9b.[43–46]

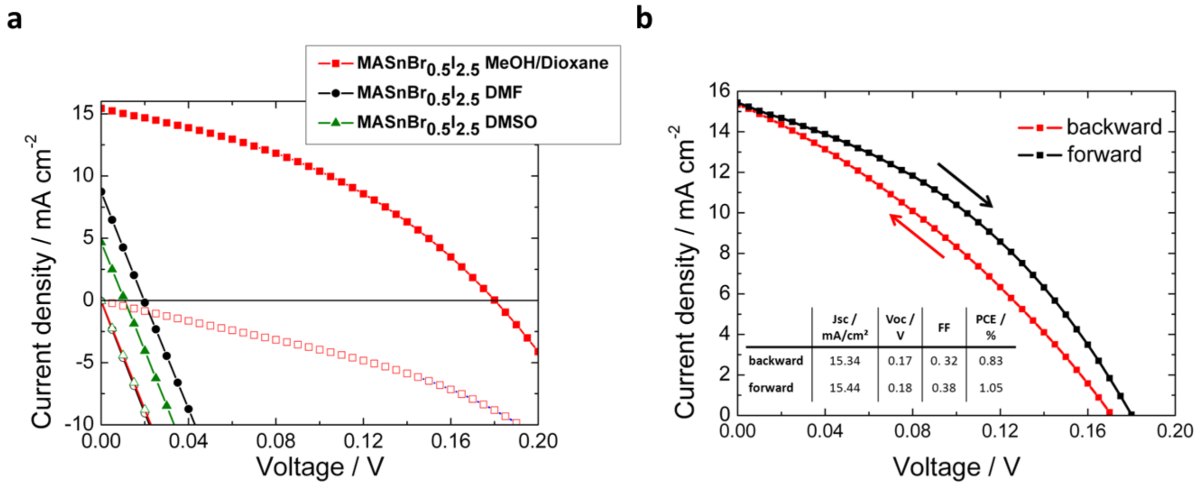

	Jsc / mA/cm²	Voc / V	FF	PCE / %
backward	15.34	0.17	0. 32	0.83
forward	15.44	0.18	0.38	1.05

Figure 4-9: a) Current-voltage characteristic showing the dependence of device performance on the deposition route. Hollow symbols refer to dark current traces. b) Forward and backward scan of the current-voltage curve of the best performing $MASnBr_{0.5}I_{2.5}$ based solar cell prepared via the MeOH/Dioxane route. The hysteresis is clearly visible.

While low, the performance of the MeOH/Dioxane based devices is still in the range of reported results on tin halide perovskite-based solar cells by Yokoyama *et al.* and Long *et al.* showing a best PCE of 1.86 % and 0.11 %, respectively.[32,33] This is likely a result of the encapsulation protocol, which requires a long 12 h curing period in a nitrogen atmosphere lowering the device performance.[12] We note that our champion device exhibits an almost ten times higher PCE compared to that reported by Long *et al.* while both devices feature very similar morphologies, pointing to the high sensitivity of tin halide based perovskite phases to the synthesis conditions.[33]

The V_{OC} value for devices featuring tin-based perovskites is heavily impacted by first order recombination due to intrinsic defects, such as Sn vacancies, which depend on the Sn^{4+} doping level.[13,28] Hence, it is essential to keep the Sn^{4+} doping level as low as possible. Previous studies revealed that commercially available SnI_2 already contains a significant amount of Sn^{4+} similar to the precursor purchased for our studies.[12] Additionally, it has been shown that a voltage loss is also incurred due to the misalignment of the conduction band (CB) of the Sn-perovskite and the CB of TiO_2.[30,32]

In an effort to reduce the defect density, we purified the starting material according to the protocol established by Hao *et al*.[30,32] However, in our lab, we found no enhancement in the performance, see Figure 4-10 and Table 4-1.

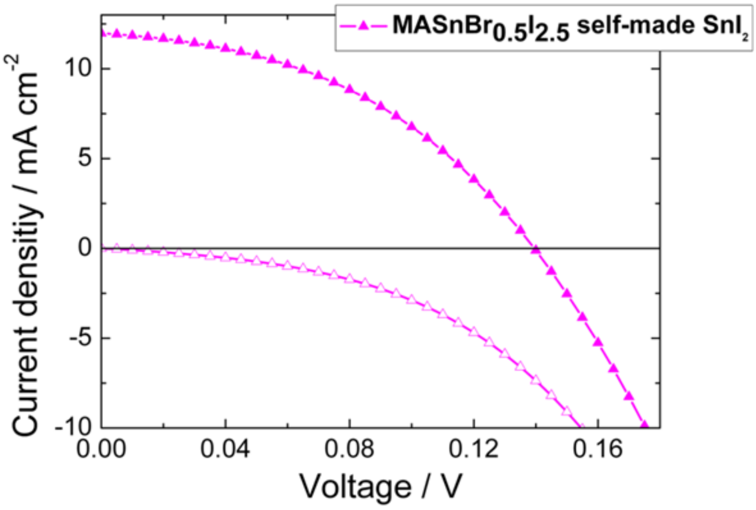

Figure 4-10: Current-voltage curve of a $MASnBr_{0.5}I_{2.5}$ based solar cell prepared from MeOH/Dioxane solution utilizing self-made SnI_2. The characteristic values for the current-voltage curves are given in Table 4-1.

Table 4-1: Short-circuit current J_{SC}, open-circuit voltage V_{OC}, fill factor FF, and power conversion efficiency η for the current-voltage curve depicted in Figure S6. For comparison the values for the best performing device $MASnBr_{0.5}I_{2.5}$ MeOH/Dioxane based on commercially available SnI_2.

Sample	J_{SC} / mA/cm²	V_{OC} / V	FF	η / %
$MASnBr_{0.5}I_{2.5}$ selfmade SnI_2	11.98	0.14	0.43	0.71
$MASnBr_{0.5}I_{2.5}$ MeOH/Dioxane	15.44	0.18	0.38	1.05

Another approach to reducing the defect density is the use of an excess of SnF_2 as reducing agent. Due to the very low solubility of SnF_2 in our solvent mixture, we could not observe an effect on device performance. However, since the highest reported PCE values for $MASnI_3$ based devices were obtained without the addition of SnF_2, we strongly believe that the new MeOH/Dioxane route holds promise for better-performing devices.

Further information about defects in the perovskite materials can be gained through time-resolved photoluminescence (PL) measurements.[13] Previous studies on Pb-based devices revealed that a long lifetime is associated with the presence of long-lived charge carriers, resulting in an increased charge extraction efficiency.[47,48]. Similar studies on $MASnI_3$ yielded lifetimes of the photoexcited species of about 200 ps, being much shorter than for the lead-based counterpart[13,47,48] Here, we performed time-correlated single-photon counting (TCSPC) measurements on Sn-perovskite films prepared either from DMF, DMSO or MeOH/Dioxane solutions. All films show strong PL at around 840 nm (Figure 4-11a), as expected. The corresponding PL decays are depicted in Figure 4-11b. All samples exhibit fast decays with the shortest lifetime values for perovskite films prepared from DMF solution (~310 ps) and DMSO solution (~260 ps), similar to previously reported values for $MASnI_{3.}$[13]. The short lifetimes in these systems are typically assigned to the fast electron-hole pair recombination at Sn^{2+}/Sn^{4+} defect sites, most likely due to self-doping of the Sn-perovskite[13,16,41,49]. Surprisingly, the $MASnBr_{0.5}I_{2.5}$ film deposited from the MeOH/Dioxane route exhibits a significantly longer lifetime of the excited species of ~580 ps, indicating a lower defect density in the material. These TCSPC measurements provide a first indication that our newly developed MeOH/Dioxane route is suitable for preparing Sn-perovskite films with competitive photophysical properties.

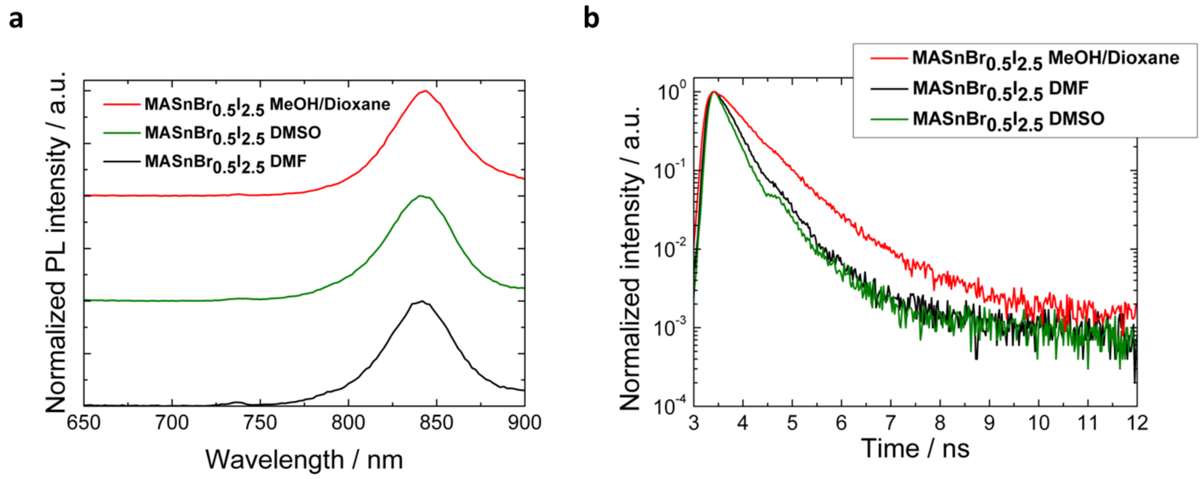

Figure 4-11: a) Photoluminescence (PL) emission spectra of $MASnBr_{0.5}I_{2.5}$ films prepared from DMF, DMSO and MeOH/Dioxane solution. All films show a similar emission maximum at 840 nm. A small signal can be observed at 735 nm. Although, not detectable in the PXRD pattern, we hypothesize that the additional PL signal arises from trace amounts of methylammonium tin halide perovskites which feature a bromide concentration higher than 0.5, leading to a blue shift of the PL signal. b) Time-resolved photoluminescence measurements of $MASnBr_{0.5}I_{2.5}$ films made from DMF, DMSO and MeOH/Dioxane solution.

Regarding toxicity concerns of the new MeOH/Dioxane route, both applied solvents represent less harmful alternatives to the commonly utilized solvents for perovskite film synthesis. Dioxane is a common solvent used in paints, varnishes, inks and dyes. Furthermore, it is a natural component in some food products, like tomatoes, shrimp and coffee. [50] Dioxane is, similar to DMSO, not classified as acutely toxic but animal experiments suggest a potentially carcinogenic effect, which could not be supported by studies on human workers exposed to occupational doses of Dioxane over decades.[50,51] Based on this, the International Agency for Research on Cancer (IARC) classified Dioxane as a 2B carcinogen just as carbon black and TiO_2, leading to the conclusion that Dioxane is not associated with cancer formation under common occupational conditions.[52,53]

MeOH is a widespread chemical for industrial applications, occurring naturally in humans, animals and plants. Excessive uptake of MeOH can cause blindness and death but the lethal dose is about twice as high as for DMF.[54,55] For occupational exposure, not only the toxicity is important but also the ability of the solvents to enter the body by different pathways. The effects of the different uptake pathways such as oral ingestion, percutaneous absorption or inhalation on the body are important factors to assess the overall hazardousness. In particular, dermal absorption and inhalation of the solvents are of special interest, since these are considered to be the most likely uptake routes under occupational conditions.[56]

A comparison of the two solvents MeOH and Dioxane, utilized in our new synthesis route, with the commonly used solvents DMF and DMSO reveals that all solvents except Dioxane feature a high ability to penetrate through the skin, where DMSO exhibits by far the highest permeation rate among the solvents mentioned.[57–60] This high ability to penetrate through the skin tissue combined with the ability to act as an excellent carrier for a wide range of agents makes DMSO a much more critical solvent than Dioxane, although both are not acutely toxic.[26] Furthermore, DMF and MeOH show very similar permeation rates, which means that both solvents have a similar ability to penetrate through the skin tissue.[57,58] Previous studies showed that dermal exposure to MeOH or DMF leads to increased concentrations of the particular chemical in the blood and urine of the experimental subjects.[57,58]

Despite the very similar behaviour regarding dermal uptake, the degradation of the solvents in the body is very different. Chang *et al.* showed that dermal exposure to DMF of workers of a synthetic leather factory for several consecutive working days leads to a significant accumulation of the DMF body burden.[60] Although there are no comparable data available for MeOH, Battermann *et al.* revealed a clearance time of MeOH in the body after dermal exposure of a few hours indicating the absence of MeOH accumulation in the body.[57] However, due to the high volatility of MeOH, the most probable uptake route is considered to be inhalation. Long-term studies on experimental subjects exposed to MeOH vapors for four consecutive days (8h/d) revealed no MeOH accumulation in the blood and urine of the experimental subjects at MeOH concentrations in the air slightly above the permissible exposure limit (PEL) of 260 mg/m^3 stated by the National Institute for Occupational Safety and Health (NIOSH).[54,61] Accordingly, the World Health Organization (WHO) considers MeOH as non-hazardous under occupational conditions, when maintaining the PEL.[62]

In contrast, similar studies with DMF over a period of five consecutive days showed an accumulation of the toxic DMF metabolite N-acetyl-S-(N-methylcarbamoyl)cysteine in the blood and urine of the experimental subjects even at the PEL of 30 mg/m^3.[55,63] Furthermore, long-term exposure to DMF induces negative effects such as stomach pain, loss of appetite, nausea, headache and alcohol intolerance even at air concentrations below the PEL.[64,65] Accordingly, our new route based on MeOH and Dioxane can be regarded as a far less harmful synthesis route for the preparation of lead-free perovskite films.

4.3 Conclusions

In conclusion, we have demonstrated a new synthesis route for high-quality $MASnI_3$ films employing less hazardous solvents in an effort to address toxicity concerns. This new approach is based on the higher solubility of Sn(II) salts in alcoholic solvents compared to the usual lead compounds, which allowed us to deposit films from a MeOH/Dioxane mixture. Here, we found that the addition of Dioxane greatly enhances the solubility of SnI_2, essential to achieve films of several hundred nanometers in thickness, through the formation of Sn(II)-(Dioxane) adducts. Both MeOH and Dioxane feature high vapour pressures which, upon deposition and evaporation on the substrate, quickly lead to supersaturation of the precursor mixture and the formation of a large number of nuclei, leading to far smoother and homogeneous films than those prepared from conventional DMF or DMSO mixtures. Solar cells prepared with our new deposition route perform better than films prepared by conventional one-step routes, mainly due to the better film formation and fewer defects as indicated by time-resolved PL measurements. This opens a new avenue for more environmentally friendly and non-hazardous synthesis routes for perovskite-based solar cells.

4.4 Experimental section

All chemicals were used as received without any further purification. All synthesis steps were conducted in a nitrogen-filled glove box to avoid oxidation of the Sn(II) compounds.

Substrate preparation

Fluorine-doped tin oxide (FTO)-coated glass sheets (7 Ωsq^{-1}, Pilkington, USA) were patterned by etching with zinc powder and 3 M HCl. They were subsequently cleaned with a 2% Hellmanex solution and rinsed with deionized water, ethanol, and acetone. Directly before applying the blocking layer, remaining organic residues were removed by an oxygen plasma treatment for 5 min. A compact titanium dioxide (TiO_2) layer was deposited by spin-coating a sol-gel precursor solution at 2000 rpm for 45 s followed by subsequent annealing at 500 °C for 45 min. For the sol-gel solution a 27.2 mM (70 µL) solution of HCl in 2-propanol (5 mL) was added dropwise to a vigorously stirred 0.43 mM (735 µL) solution of titanium isopropoxide (99.999%, Sigma–Aldrich) in 2-propanol (5 mL). Afterwards, a 250 nm thick, mesoporous TiO_2 layer was applied by spin-coating 100 µL of a TiO_2 nanoparticle paste (Dyesol DSL 18NR-T) diluted in absolute ethanol (1:3.5 weight ratio) onto the compact TiO_2 layer at 2500 rpm for 30 s followed by subsequent annealing at 500 °C for 15 min.

Perovskite film preparation

Method 1: MeOH/Dioxane

The precursor solution was prepared by dissolving 111.6 mg SnI_2 (0.3 mmol, 99.999%, ultra dry, Alfa Aesar) in 1,4-dioxane (0.25 mL, Dioxane, anhydrous, 99.8 %, Sigma-Aldrich). In a second vial, either 48 mg of methylammonium iodide (0.3 mmol, MAI, Dyesol), for the pure iodide perovskite, or a mixture of 24 mg (0.15 mmol) MAI and 17 mg methylammonium bromide (0.15 mmol, MABr, Dyesol), for the mixed halide perovskite, were dissolved in methanol (0.75 mL, MeOH, anhydrous, 99.8 %, Sigma-Aldrich). After complete dissolution of the organic precursor, the MeOH solution was added to the SnI_2 solution to dissolve the remaining SnI_2 completely. Subsequently, 100 µL of the precursor solution was spun onto the TiO_2-covered substrates at 3000 rpm for 15 s. The substrates were annealed at 70 °C for 10 min to remove possible solvent residues directly after spin-coating.

Method 2: DMF

The perovskite solution was prepared by dissolving 372 mg (1.0 mmol) SnI_2 and 159 mg (1.0 mmol) MAI for the pure iodide compound or a mixture of 80 mg (0.5 mmol) MAI and 56 mg (0.5 mmol) MABr, for the mixed halide perovskite, in N,N-dimethylformamide (1 mL, DMF, anhydrous, 99.8 %, Sigma-Aldrich). After mixing, the solution was placed on a hotplate at 100 °C in order to fully dissolve the tin precursor. 100 µL of the precursor solution were spun at 2000 rpm for 30 s onto a TiO_2-covered substrate with subsequent annealing at 100 °C for 10 min.

Method 3: DMSO

The procedure followed is the same as the previous procedure but using dimethylsulfoxide (DMSO, anhydrous, $\geq$99.9 %, Sigma-Aldrich) instead of DMF as the solvent. 100 µL of the precursor solution were spun at 4000 rpm for 30 s onto a TiO_2-covered substrate with subsequent annealing at 100 °C for 10 min.

Solar cell fabrication

After film formation, the films were covered with a hole transporting layer (HTL) of 2,2’,7,7’-tetrakis-(N,N-di-pmethoxyphenylamine)9,9’-spirobifluorene (spiro-OMeTAD Borun Chemicals, 99.5% purity). The HTL solution was prepared by dissolving 73 mg of spiro-OMeTAD in chlorobenzene (1 mL, 99.8%, Sigma–Aldrich). The solution was filtered and mixed with 2,5-lutidine (30 µL, 98+%, Alfa Aesar), and a 520 mg mL^{-1} bis(trifluoromethane)sulfonamide lithium salt (LiTFSI, 99.95%, Sigma–Aldrich) solution in acetonitrile (17.5 µL). This solution was spin-coated dynamically at 1500 rpm for 45 s. In a second step the sample rotation was accelerated to 2000 rpm for 5 s to allow the solvent to dry completely. Finally, the 40 nm thick gold electrodes were evaporated thermally on top of the device. In order to prevent the perovskite film from oxidation, the devices were sealed by a 25 µm thick hot-melting polymer (Surlyn®) and a microscope coverslip. To provide a complete sealing, the edges of the microscope coverslip were treated with epoxy resin. The devices were stored for about 12 h under inert conditions before measurements to allow for complete hardening of the epoxy resin.

Characterization methods:

X-ray diffraction measurements on films and the powder sample of the precipitate were performed using a Bruker D8 Discover X-ray diffractometer operating at 40 kV and 30 mA, employing Ni-filtered Cu Kα radiation (λ = 1.5406 Å) and a position-sensitive detector (LynxEye) in reflection mode. All other powder X-ray patterns were obtained in transmission mode using a STOE Stadi MP diffractometer with a Cu Kα_1 radiation source (λ = 1.54060 Å) operating at 40 kV and 40 mA. The diffractometer was equipped with a DECTRIS MYTHEN 1K solid-state strip detector. All samples were exposed to ambient conditions during the measurement. Scanning electron microscopy (SEM) cross-section images were acquired on a JEOL JSM-6500F microscope. The sample was fixed in a self-made sample holder. SEM top-view images were taken with a Carl Zeiss Ultra Plus scanning electron microscope. The sample was fixed by a sticky carbon pad. All SEM samples were exposed to ambient conditions not longer than one minute during the transfer procedure into the SEM. For the optical characterization, precursor solutions were prepared similarly as used for the devices. 100 µL of the solution was spun using the same conditions as utilized for solar cells onto a glass slide. Subsequently, the film was sealed by a glass coverslip and epoxy resin to avoid oxidation. Steady-state absorption spectra were acquired with a Lambda 1050 UV-Vis spectrophotometer (Perkin Elmer) using an integration sphere. Steady state and time-resolved PL measurements were performed with a Fluotime 300 Spectrofluorometer (Picoquant

GmbH). The excitation wavelength was fixed at 510 nm. The emission for time-resolved measurements was monitored at the maximum intensity of the steady state photo-emission. *J*-*V* curves were recorded with a Keithley 2400 source meter under simulated AM 1.5 sunlight, calibrated to 100 mW cm^{-2} with a Fraunhofer ISE certified silicon cell. The active area of the solar cells was defined with a square metal aperture mask of 0.0831 cm^2.

4.5 Literature

[1] U.S. Energy Information Administration. Available online: http://www.eia.gov/todayinenergy/detail.cfm?id=12251 (accessed on 8 June 2017).

[2] A. Kojima, K. Teshima, Y. Shirai, T. Miyasaka, *J. Am. Chem. Soc.* **2009,** *131*, 6050.

[3] J. M. Ball, M. M. Lee, A. Hey, H. J. Snaith, *Energy Environ. Sci.* **2013,** *6,* 1739.

[4] M. M. Lee, J. Teuscher, T. Miyasaka, T. N. Murakami, H. J. Snaith, *Science* **2012,** *338,* 643.

[5] J. Burschka, N. Pellet, S. J. Moon, R. Humphry-Baker, P. Gao, M. K. Nazeeruddin, M. Grätzel, M. *Nature* **2012,** *499,* 316.

[6] H. Zhou, Q. Chen, G. Li, S. Luo, T. B. Song, H. S. Duan, Z. Hong, Y. Jingbi Y. Yang, *Science* **2014,** *345*, 542.

[7] T. Krishnamoorthy, H. Ding, C. Yan, W. L. Leong, T. Baikie, L. Zhang, M. Sherburne, S. Li, M. Asta, N. Mathews, et al., *J. Mater. Chem. A* **2015,** *3*, 23829.

[8] B. W. Park, B. Philippe, X. Zhang, H. Rensmo, G. Boschloo, E. M. J. Johansson. *Adv. Mater.* **2015,** *27*, 6806.

[9] B. Saparov, F. Hong, J. P. Sun, H. S. Duan, W. Meng, S. Cameron, I. G. Hill, Y. Yan, D. B. Mitzi, *Chem. Mater.* **2015,** *27*, 5622.

[10] X. P. Cui, K. J. Jiang, J. H. Huang, Q. Q. Zhang, M. J. Su, L. M. Yang, Y. L. Song, X. Q. Zhou, *Synth. Met.* **2015,** *209*, 247.

[11] M. Lyu, J. H. Yun, M. Cai, Y. Jiao, P. V. Bernhardt, M. Zhang, Q. Wang, A. Du, H. Wang, G. Liu, L. Wang, *Nano Res.* **2016,** *9*, 692.

[12] F. Hao, C. C. Stoumpos, C. C. Cao, R. P. H. Chang, M. G. Kanatzidis, *Nat. Photonics* **2014,** *8*, 489.

[13] N. K. Noel, S. D. Stranks, A. Abate, C. Wehrenfennig, S. Guarnera, A. A. Haghighirad, A. Sadhanala, G. E. Eperon, S. K. Pathak, M. B. Johnston, A. Petrozza, L. M. Herz, H. J. Snaith, H.J. *Energy Environ. Sci.* **2014,** *7*, 3061.

[14] Y. Ogomi, A. Morita, S. Tsukamoto, T. Saitho, N. Fujikawa, Q. Shen, T. Toyoda, K. Yoshino, S. S. Pandey, T. Ma, et al., *J. Phys. Chem. Lett.* **2014,** *5*, 1004.

[15] M. H. Kumar, S. Dharani, W. L. Leong, P. P. Boix, R. R. Prabhakar, T. Baikie, C. Shi, H. Ding, R. Ramesh, M. Asta, et al., *Adv. Mater.* **2014,** *26*, 7122.

[16] Y. Takahashi, R. Obara, Z.Z. Lin, Y. Takahashi, T. Naito, T. Inabe, S. Ishibashi, K. Terakura, *Dalton Trans*. **2011,** *40*, 5563.

[17] F. Zuo, S. T. Williams, P. W. Liang, C. C. Chueh, C. Y. Liao, A. K. Y. Jen, *Adv. Mater*. **2014,** *26*, 6454.

[18] G. L. Jr. Kennedy, *Crit. Rev. Toxicol*. **1986,** *17*, 129.

[19] V. Scailteur, E. DeHoffmann, J. P. Buchet, R. Lauwerys, *Toxicol*. **1984,** *29*, 221.

[20] L. E. Fleming, S. L. Shalat, C. A. Redlich, *Scand J. Work Environ. Health* **1990,** *16*, 289.

[21] REACH-clp-biozid-helpdesk. Available online: http://www.reach-clp-biozidhelpdesk.de/de/ REACH/ Kandidatenliste/Listen/N,NDimethylformamid/ N,N-Dimethylformamid_content.html in german (accessed on 8 June 2017).

[22] J. Mráz, H. Nahová, *Int Arch Occup Environ. Health* **1992,** *64*, 79.

[23] D. Martin, H. Hauthal, *Dimethyl Sulphoxide*, New York: Worth, **1989**.

[24] M. B. Sulzberger, T. A. Cortese, L. Fishman, H. S. Wiley, P. S. Peyakovich, *Ann. New York Acad. Sci.* **1967,** *141*, 437.

[25] S. V. Rudenko, S. D. Gapochenko, U. A. Bondarenko, *Biophysics* **1984,** *29*, 245.

[26] G. Embery, P. H. Dugard, *J. Invest. Dermatol.* **1971,** *57*, 308.

[27] T. B. Song, Q. Chen, Zhou, C. Jiang, H. H. Wang, Y. M. Yang, Y. Liu, J. You, Y. Yang, *J. Mater. Chem. A* **2015,** *3*, 9032.

[28] M. H. Kumar, S. Dharani, W. L. Leong, P. P Boix, R. R. Prabhakar, T. Baikie, C. Shi, H. Ding, R. Ramesh, M. Asta, M. Graetzel, S. G. Mhaisalkar, N. Mathews, *Adv. Mater.* **2014,** *26*, 7122.

[29] K. Liang, D. B. Mitzi, M. T. Prikas, *Chem. Mater.* **1998,** *10*, 403.

[30] F. Hao, C. C. Stoumpos, P. J. Guo, N. J. Zhou, T. J. Marks, R. P. H. Chang, M. G. Kanatzidis, *J. Am. Chem. Soc.* **2015,** *137*, 11445.

[31] Q. Chen, H. P. Zhou, Z. R. Hong, S. Luo, H. S. Duan, H. H. Wang, Y.S. Liu, G. Li, Y. Yang, *J. Am. Chem. Soc.* **2013,** *136*, 622.

[32] T. Yokoyama, D. H. Cao, C. C. Stoumpos, T. B. Song, Y. Sato, S. Aramaki, M. G. Kanatzidis, *J. Phys. Chem. Lett.* **2016,** *7*, 776.

[33] L. Ji, T. Zhang, Y. Wang, P. Zhang, D. Liu, Z. Chen, S. Li, *Nanoscale Res. Let.* **2017,** *12*(1), 367.

[34] T.-Y. Hsieh, T.-C. Wei, K.-L. Wu, M. Ikegami, T. Miyasaka, *Chem. Commun.* **2015,** *15*, 13294.

[35] Y. Feng, K.-J. Jiang, J.-H. Huang, H.-J. Wang, M.-G. Chen, Y. Zhang, L. Zheng, Y.-L. Song, *Thin Solid Films* **2017,** *636*, 639.

[36] H. F. Gibbard, L. C. Jefferson, *J. Chem. Eng. Data* **1974,** *19*, 308.

[37] E. W. Reid, E. E. Hofmann, *J. Ind. Eng. Chem.* **1929,** *21*, 695.

[38] D. Bi, D. M. El-Zohry, A. Hagfeldt, G. Boschloo, *ACS Appl. Mater. Interfaces* **2014,** *6*, 18751.

[39] R. H. Andrews, J. D. Donaldson, E. Hough, D. G. Nicholson, *Acta. Cryst.* **1977,** *B33*, 307.

[40] E. Hough, D. G. Nicholson, *J. Chem. Soc. Dalton Trans.* **1976,** 1782.

[41] R. D. Jr. Nelson, D. R. Jr. Lide, A. A. Maryott, *Selected Values of Electric Dipole Moments for Molecules in the Gas Phase*, NSRDS-NBS 10, National Bureau of Standards, Washington, D. C. **1967**.

[42] M. G. Kanatzidis, F. Hao, *U.S. Patent Application* Nr. 14/686,539, **2015**.

[43] H. J. Snaith, A. Abate, J. M. Ball, G. E. Eperon, T. Leijtens, N. K. Noel, S. D. Stranks, J. T. W. Wang, K. Wojciechowski, W. Zhang, *J. Phys. Chem. Lett.* **2014,** *5*, 1511.

[44] E. L. Unger, E. T. Hoke, C. D. Bailie, W. H. Nguyen, A. R. Bowring, T. Heumüller, M. G. Christoforo, M. D. McGehee, *Energy Environ. Sci.*, **2014,** *7*, 3690.

[45] H. S. Kim, N. G. Park, *J. Phys. Chem. Lett*. **2014,** *5*, 2927.

[46] R. S. Sanchez, V. Gonzalez-Pedro, J. W. Lee, N. G. Park, Y. S. Kang, I. Mora-Sero, J. Bisquert, *J. Phys. Chem. Lett.* **2014,** *5*, 2357.

[47] C. R. Kagan, D. B. Mitzi, C. D. Dimitrakopoulos, Science **1999,** *286*, 945.

[48] G. Xing, N. Mathews, S. Sun, S. S. Lim, Y. M. Lam, M. Grätzel, S. Mhaisalkar, T. C. Sum, *Science* **2013,** *342*, 344.

[49] Y. Takahashi, H. Hasegawa, Y. Takahashi, T. Inabe, *J. Solid State Chem.* **2013,** *205*, 39.

[50] A. Stickney, S. L. Sager, J. R. Clarkson, L. A. Smith, B. J. Locey, M. J. Bock, R. Hartung, S. F. Olp, *Regul. Toxicol. Pharm.* **2003,** *38*, 183.

[51] R. J. Kociba, S. B. McCollister, C. Park, T. R. Torkelson, P .J. Gehring, *Toxicology App. Pharmacol.* **1974,** *30*, 275.

[52] Netherlands Organization for Applied Scientific Research (TNO) and the National Institute of Public Health and the Environment (RIVM). Chemical Substances Bureau, Ministry of Housing, Spatial Planning and the Environment (VROM) *Risk Assessment: 1, 4-Dioxane*. Final Version, 5 November, EINECS-No.: 204-661-8, Netherlands, **1999**.

[53] International Agency for Research on Cancer (IARC). Available online: http://monographs.iarc.fr/ENG/Classification/latest_classif.php (accessed on 9 June 2017).

[54] Centers for Desease Control and Prevention (CDC). Available online: http://www.cdc.gov/niosh/idlh/67561.html (accessed on 8 June 2017).

[55] Centers for Desease Control and Prevention (CDC). Available online http://www.cdc.gov/niosh/idlh/68122.html (accessed on 8 June 2017).

[56] C. E. Becker, *J. Emerg. Med*. **1983,** *1*, 51.

[57] S. A. Battermann, A. Franzblau, Int. Arch. *Occup. Environ. Health* **1997,** *70*, 341.

[58] H.-Y. Chang, C.-Y. Tsai, Y.-Q. Lin, T.-S. Shi, W.-C. Lin, *Occup. Environ. Med.* **2005,** *62*, 151.

[59] K. Dennerlein, D. Schneider, T. Göen, K. H. Schaller, H. Drexler, G. Korinth, *Toxicol. In Vitro* **2013,** *27*, 708.

[60] C. Ursin, C. M. Hansen, J. W. Van Dyk, P. O. Jensen, I. J. Christensen, J. Ebbehoej, *Am. Ind. Hyg. Assoc. J.* **1995,** *56*, 651.

[61] V. Šedivec, M. Mráz, J. Flek, *Int. Arch. Occup. Environ. Health* **1981,** *48*, 257.

[62] World Health Organization (WHO), International Programme On Chemical Safety (IPCS), *Methanol Health And Safety Guide*, No. 105, **1997**.

[63] J. Mraz, H. Nohova, *Int. Arch. Occup. Environ. Health* **1992,** *64*, 85.

[64] R. R. Lauwerys, A. Kivits, M. Lhoir, P. Rigolet, D. Houbeau, J. P. Buchet, H. A. Roels, *Int .Arch. Occup. Environ. Health* **1980,** *45*, 189.

[65] V. Scailteur, R. R. Lauwerys, *Toxicol.* **1987,** *43*, 231.

5 Highly stable, phase pure $Cs_2AgBiBr_6$ double perovskite thin films for optoelectronic applications

This chapter is based on the following publication:

Enrico Greul, Michiel L. Petrus, Andreas Binek, Pablo Docampo and Thomas Bein, *Journal of Materials Chemistry A* **2017,** *5*, 19972–19981.

5.1 Introduction

Since the first reports of solid-state solar cells in 2012, hybrid organic-inorganic lead halide perovskites emerged as some of the most promising absorber materials for low-cost photovoltaic devices.[1] Published PCEs of over 22% make these materials potential candidates for replacing commonly employed Si-based solar cells.[2] Despite their excellent photophysical properties,[3–8] lead halide perovskites still suffer two serious disadvantages, namely stability issues and the toxicity of lead.[9–12] Many research groups have therefore focused on the development of more stable and/or lead-free perovskite materials. Substitution of the Pb^{2+} by the homovalent group-14 element Sn^{2+} initially led to promising PCEs of ~ 6%. However, the devices showed extremely low stability, even under commonly used inert conditions, due to the facile oxidation of Sn^{2+}. So far, this makes Sn^{2+}-based materials unfeasible for typical photovoltaic applications.[13,14] A recent approach towards lead-free perovskite materials is the substitution of Pb^{2+} by heterovalent M^{3+} cations. A promising candidate for this type of substitution is non-toxic Bi^{3+}, which is isoelectronic with Pb^{2+}. Due to the higher charge of Bi^{3+}, bismuth ions cannot simply be incorporated into the hybrid three-dimensional $A^{1+}M^{2+}X_3$ structure of the lead-based compounds. Generally, related hybrid Bi^{3+} compounds feature low-dimensional structures resulting in less favorable optoelectronic properties than their lead-based counterparts.[15–18]

In order to incorporate Bi^{3+} ions into a three-dimensional structure, a class of materials called elpasolites, also known as double perovskites, could provide an attractive extension of the conventional perovskite system. Elpasolites, with the general formula $A_2M^{1+}M^{3+}X_6$, feature a highly symmetric cubic double perovskite structure, with one monovalent and one trivalent cation.[19] Bismuth-containing elpasolites with A = Rb, Cs, CH_3NH_3; M^{1+} = Na, K, Tl and X =

F, Cl, Br have been investigated for several decades.[20–24] Unfortunately, compounds containing alkali metals do not absorb light in the visible range due to their large band gap energies (E_g) exceeding 3 eV.[20,25] Although the thallium-containing compound features a reasonable small E_g of 2.16 eV, the severe toxicity of thallium excludes this element as a non-toxic alternative for lead.[23]

Recently, several groups have reported Bi^{3+}-based double perovskites with Ag^+ as the monovalent cation featuring E_g´s of ~ 2 eV for the bromide-based material, photoluminescence (PL) lifetimes of several hundred nanoseconds and calculated charge carrier effective masses close to those calculated for methylammonium lead iodide, making it a very interesting candidate for photovoltaic applications.[19, 26–30]

However, the preparation of high quality films of these perovskites for optoelectronic applications is challenging, especially for the bromide and iodide based systems.[26] As a result of the difficulties to process this material, neither films nor photovoltaic devices based on Ag-Bi double perovskites have been reported so far.

Since thin films are critical for making double perovskites accessible for optoelectronic applications, we have developed a synthetic route that allows for the preparation of phase pure, thin films of the double perovskite $Cs_2AgBiBr_6$. Extensive powder X-ray diffraction (PXRD) investigations revealed that high annealing temperatures of at least 250 °C are needed to remove side phases which form during the film synthesis. Light absorption measurements as well as steady-state and time-resolved PL measurements show that our films feature absorption properties and lifetimes of the photoexcited species similar to the lead-based counterparts. First steps to optimize the film synthesis conditions were undertaken to improve the optoelectronic properties of our $Cs_2AgBiBr_6$ films, leading to photovoltaic devices with PCEs of up to 2.43% and a high V_{oc} exceeding one volt. Additionally, the $Cs_2AgBiBr_6$-based devices revealed a high stability under operating conditions. Hence, we demonstrate the potential of highly tunable double perovskites as a novel class of semiconducting materials for optoelectronic applications.

5.2 Results and Discussions

So far, bismuth halide-based double perovskite crystals have only been synthesized by solid state reactions or solution growth from the corresponding halide acids.[19,26–29] The solubility of the double perovskites in these acids is relatively low leading to double perovskite concentrations (< 0.1 M) much lower than that generally used for the preparation of lead or tin perovskite based films by solution based methods,[4–6,13,14] so it is essential to find alternative solvents that can reach a higher precursor concentration in order to prepare $Cs_2AgBiBr_6$ films from solution. Since $Cs_2AgBiBr_6$ is hardly soluble in the most commonly used solvents, we screened several alternatives where dimethylsulfoxide (DMSO) showed the highest ability to dissolve the precursors, AgBr, CsBr and $BiBr_3$, and the double perovskite (Table 4-1)

Table 5-1: Solubility of $Cs_2AgBiBr_6$ in different solvents.

Solvent	Max. concentration / Mol L^{-1}
Hydrobromic acid (HBr)	~ 0.05
***N*,*N*-Dimethylformamide (DMF)**	~ 0.1
Dimethylsulfoxide (DMSO)	~ 0.6
***N*-Methyl-2-pyrrolidone (NMP)**	~ 0.1

As a result, the $Cs_2AgBiBr_6$ films prepared in this study were deposited by spin-coating a DMSO-based precursor solution on top of a substrate. Our utilized synthesis route employs two different heating steps. The first step is named “preheating step” where the substrate and precursor solution are heated to 75 °C prior the spin-coating. Then, the hot precursor solution was spun on top of the hot substrate. This preheating step improves the surface coverage and film quality (Fig. 4-1).

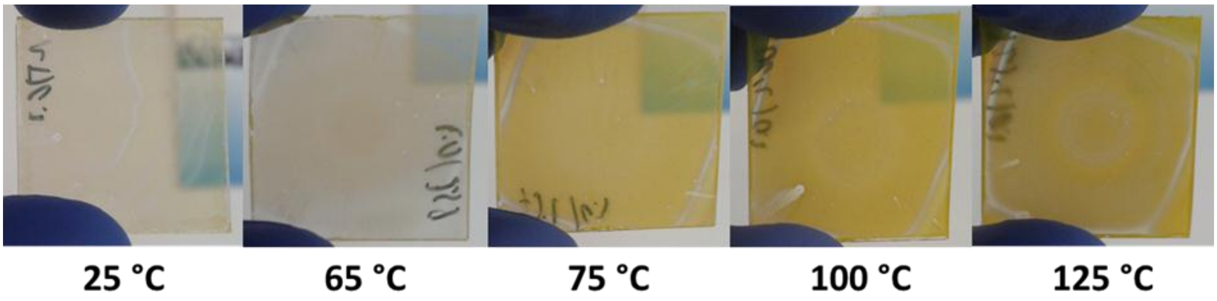

Figure 5-1: Images of $Cs_2AgBiBr_6$ films made on glass prepared with different preheating temperatures. The 25 °C sample was made at room temperature without a preheating step. The increase of the film quality in terms of surface coverage with increasing preheating temperature is clearly visible, in particular for preheating temperatures of 75 °C and higher.

The second heating step named "annealing step", is performed after the spin-coating procedure at a temperature of at least 250 °C and is needed to obtain phase pure films. A scheme of the complete synthesis procedure is given in Fig. 4-2.

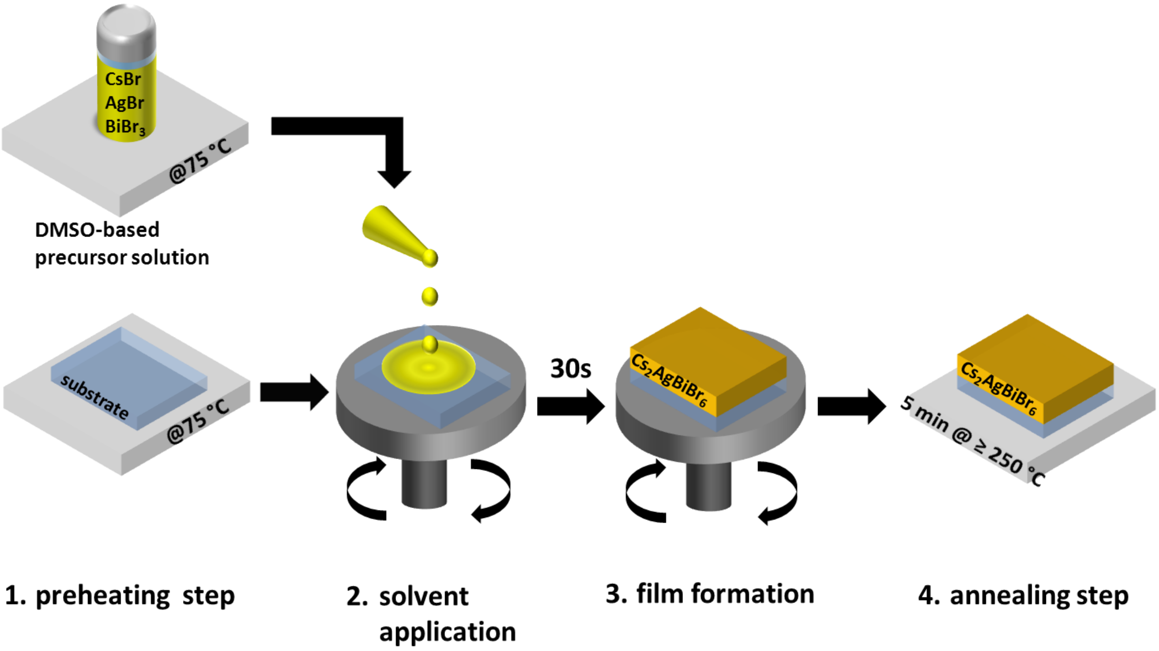

Figure 5-2: Schematic of the synthesis route for $Cs_2AgBiBr_6$ thin films. The film formation (3.) occurs already while the substrate is spinning.

Previous studies by Xiao *et al.* propose the facile formation of side phases due to the narrow chemical potential region for the formation of phase-pure $Cs_2AgBiBr_6$, which could have negative effects on the optoelectronic properties of the double perovskite.[31] Therefore, we performed temperature-dependent PXRD investigations to assure the formation of phase-pure films. We found that two of the predicted side phases, namely $Cs_3Bi_2Br_9$ and AgBr,[31] actually formed during the film synthesis. In order to remove these side phases we performed an extensive annealing temperature study, revealing that an annealing temperature of at least 250 °C is needed to assure complete conversion of the precursors to the desired double perovskite phase. Fig. 4-3 depict PXRD patterns of $Cs_2AgBiBr_6$ powders obtained from $Cs_2AgBiBr_6$ films at different annealing temperatures showing the typical reflections of the cubic elpasolite structure.[26]

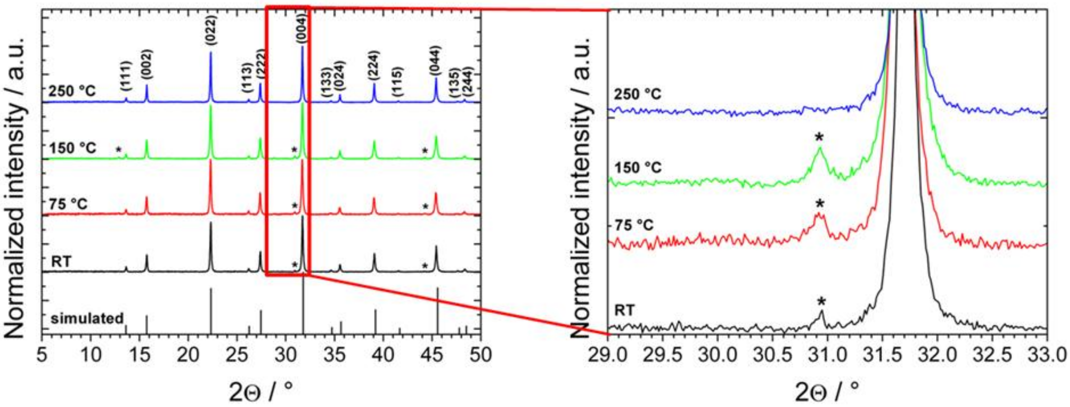

Figure 5-3: XRD patterns of $Cs_2AgBiBr_6$ powders obtained from our prepared films annealed at different temperatures, the asterisk (*) indicates the position of reflections from the side phases AgBr (ICDD No. 00-006-0438) and $Cs_3Bi_2Br_9$ (ICDD No. 01-070-0493), respectively. The sample labelled with RT was kept at room temperature (ca. 25 °C) after film formation without any annealing step.

The patterns from samples annealed at temperatures below 250 °C feature additional reflections at 12.8°, 30.9° and 44.2°, which can be assigned to $Cs_3Bi_2Br_9$ and AgBr, while films annealed at 250 °C appear to be phase-pure. This trend can also be confirmed with the corresponding PL spectra were only the 250 °C sample exhibits the typical PL signal of $Cs_2AgBiBr_6$ (Fig. 4-4). The PXRD patterns in Fig. 4-3, clearly show that the vanishing of the side-phases is not caused by the removal of metal-solvent intermediates, as it was shown for lead and tin based hybrid perovskites.[32,33] This is also supported by the evolution of the intensity of the reflections of the side-phases with temperature. Even at 150 °C annealing temperature, which is usually sufficient to remove the metal-solvent intermediates, no decrease of the reflection intensities could be observed pointing to highly stable side phases. However, McClure *et al.* demonstrated the synthesis of $Cs_2AgBiBr_6$ via solid state reaction at 210 °C for 10 h,[19] which is close to the temperature we use to obtain phase pure double perovskite films. Therefore, we hypothesize that micro scale solid state reactions in our prepared films are responsible for the complete conversion of the precursors and side-phases into the desired $Cs_2AgBiBr_6$ phase.

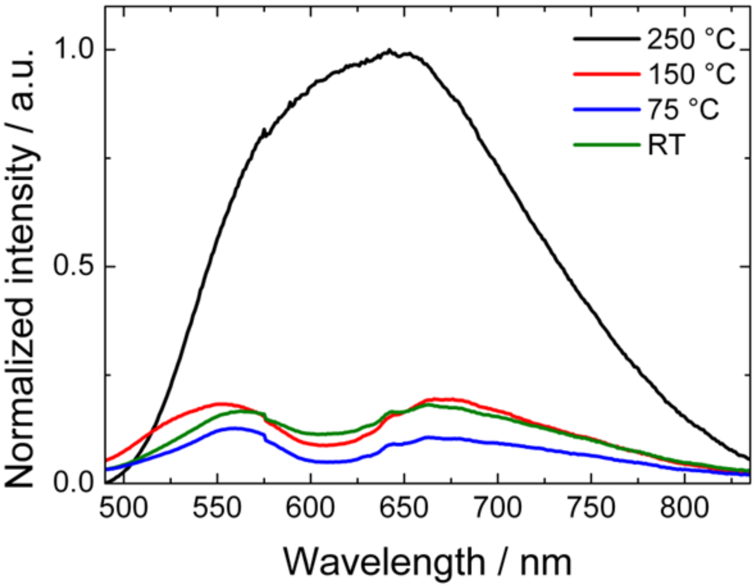

Figure 5-4: The influence of the annealing temperature on the PL signal. The typical PL signal of $Cs_2AgBiBr_6$ is only visible for the 250 °C sample.

As the $Cs_2AgBiBr_6$ films were prepared for photovoltaic applications, sufficient light absorption is mandatory for efficiently working devices. In order to optimize the optical absorption properties of the double perovskite films, we added an additional preheating step to our synthesis protocol where the spin-coating solution and the substrate were put on a hotplate and heated to 75 °C before spin-coating. Fig. 4-5a shows absorption spectra of $Cs_2AgBiBr_6$ films on glass prepared with and without a preheating step at different temperatures. Without the preheating step, insufficient light absorption would limit the photocurrent of the resulting devices to approximately 2 mA cm^{-2}, which is inadequate to prepare efficient solar cells. We found that preheating the substrate and the solution increases the quality of the double perovskite films, by improving the surface coverage, as can be seen with the naked eye, enhancing the optical absorption of the films (Fig. 4-2). In particular, the absorption close to the onset is significantly increased, which is also observable for films made on an mp-TiO_2 scaffold as used for solar cell fabrication (Fig. 4-5b).

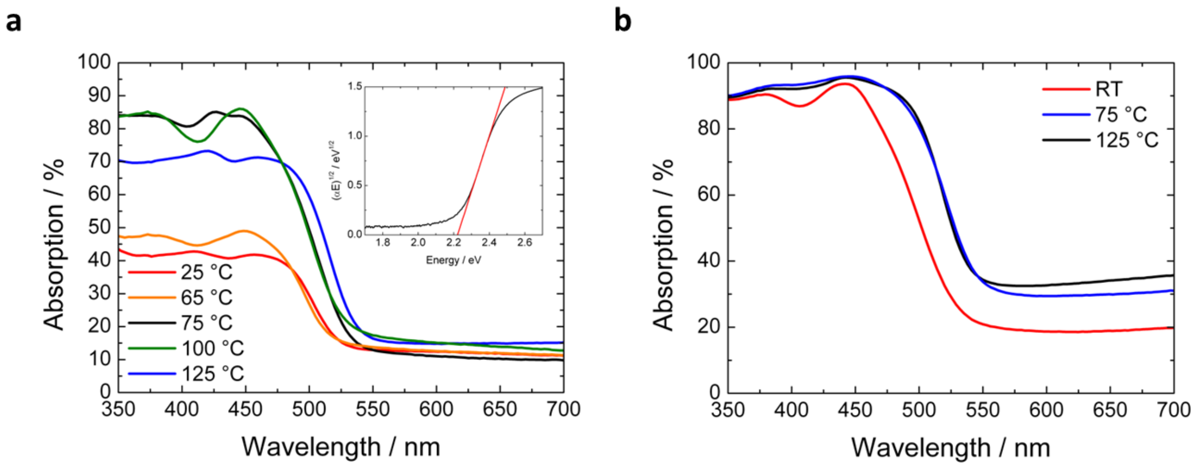

Figure 5-5: a) Optical absorption spectra of $Cs_2AgBiBr_6$ films prepared from DMSO on flat glass substrates. The films were manufactured without a preheating step at room temperature (ca. 25 °C) or with a preheating step at 65 °C, 75 °C, 100 °C or 125 °C before spin-coating. b) UV/vis spectra of $Cs_2AgBiBr_6$ films on mp-TiO_2 scaffolds as used for solar cell assembly prepared without (RT, ca. 25 °C) or with a preheating step (75°C, 125 °C). The improved light absorption close to the onset for the preheated samples is clearly visible. We assign the enhanced light absorption at energies below the onset to light scattering because of the roughness of the preheated samples.

We attribute the increase of the optical absorption to an increased surface coverage on the substrate due to a larger amount of deposited double perovskite caused by the faster solvent evaporation at elevated temperatures. Increasing the amount of deposited $Cs_2AgBiBr_6$ by simply increasing the concentration of the precursors in the spin-coating solution is not possible since the precursor concentration of the utilized solution is already close to the maximum of about 0.6 M.

The band gap of the $Cs_2AgBiBr_6$ films was determined from the absorption spectra given in Fig. 5-5a. The spectra show a steep onset at about 550 nm corresponding to an E_g of 2.21 eV for a direct band gap obtained with a Tauc plot (see inset), which is comparable to the value reported by McClure *et al.*[19] and consistent with other reports ranging from 1.83 eV[26] to 2.19 eV[19]. The relatively large spread of the reported E_g values most likely originates from different synthesis conditions and measurement methods used in the different studies.[29] According to the Shockley-Queisser limit, a theoretical maximum PCE of 16.4% can be obtained with an E_g of 2.2 eV, thus holding promise for working double perovskite based photvoltaics.[34] Although, the theoretical maximum PCE of this material does not reach the highest reported PCEs of single junction methylammonium lead iodide ($MAPbI_3$) based photovoltaics, $Cs_2AgBiBr_6$ is a promising candidate for applications in tandem solar cells as it was already shown for methylammonium lead bromide, which features a slightly larger E_g of 2.3 eV.[35]

The energy level diagram in Fig. 5-6[26] shows that the conduction band (CB) of the $Cs_2AgBiBr_6$ is well aligned with the CB of the electron transporting material (ETM) titania, which was also recently shown in a computational study of Feng *et al.*[36] In contrast, the highest occupied molecular orbital (HOMO) of the hole transporting material (HTM) 2,2',7,7'-tetrakis-(N,N-di-4-methoxyphenylamino)-9,9'-spirobifluorene (spiro-OMeTAD) shows a strong offset compared to the valence band (VB) of the double perovskite, which is likely to limit the potential V_{oc} of a photovoltaic device. In this work, as a first demonstration of the potential of $Cs_2AgBiBr_6$, we focused on the preparation of devices comprising this state-of-the-art material which has been shown to be able to reach V_{oc}'s exceeding 1.5V.[37] Nevertheless, the energy level alignment allows for charge extraction, and functioning devices are expected.

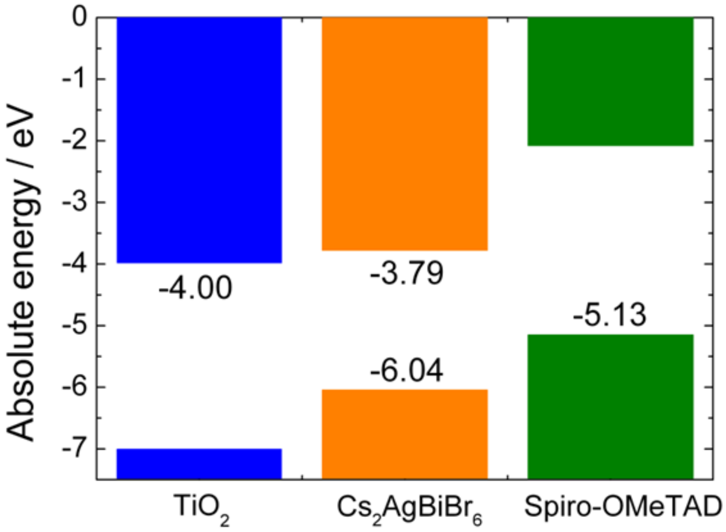

Figure 5-6: Energy level diagram of the double perovskite and the charge extraction materials.[26]

Not only the band gap and energy alignment with the charge extraction layers, but also charge collection efficiency is important to fabricate high-efficiency solar cells. PL lifetime measurements can provide an indication as to whether a material can perform in this area. Here, we investigated the PL decay times of the double perovskite films by time-correlated single photon counting (TCSPC). For comparison, additional TCSPC measurements were performed on polycrystalline powder samples that were obtained by the conventional approach from HBr solution.[26] The PL decays are displayed in Fig. 5-7a. Although the PL of

$Cs_2AgBiBr_6$ features three differently fast decay processes, only the value for the long-lived process is given in Fig. 5-7a. We attribute the two short lifetime processes to trap and/or surface state emission, while the long lifetime process is suggested to be the fundamental PL decay time of the material.[26] Both the powder and the film show long PL decay times in the range of hundreds of nanoseconds, similar to the values observed for lead-based hybrid perovskites,[38] hinting at the potential for well-performing devices. We note that the decay times do not differ significantly between single crystals and polycrystalline powders, which suggest a high defect tolerance of this material.[26] The slightly faster decay for films is likely the result of a larger concentration of trap states in the perovskite film, as has been previously shown for lead halide-based films.[39] Here, the fast formation of the perovskite during the spin-coating process causes a broad grain size distribution within the film and, consequently, a large number of grain boundaries.

PL quenching experiments are widely used to study the charge transfer from a photoabsorber to the charge-selective contacts'[40,41] From the energy diagram (Fig. 5-7b) we expect favorable charge transfer behavior from $Cs_2AgBiBr_6$ to the electrodes, which was experimentally tested with PL quenching experiments. For the measurements, mp-TiO_2 and spiro-OMeTAD were chosen as ETM and HTM, respectively, while mp-Al_2O_3 was used as reference as no charge transfer is expected (for experimental details see the characterization section). Fig. 5-7d shows the quenching of the PL emission of $Cs_2AgBiBr_6$ on TiO_2 by approximately 60%, while the PL was reduced by more than 80% in contact with spiro-OMeTAD. These results indicate that charge transfer from the double perovskite to the charge-selective materials is taking place, as required for working photovoltaic devices. However, the low PL quantum yield of $Cs_2AgBiBr_6$ indicates that the main recombination pathways in $Cs_2AgBiBr_6$ are nonradiative[26] and therefore not detectable in PL quenching experiments. It has to be mentioned that, the PL signal of our films is relatively broad but similar to that reported for single crystals.[26] The broad PL signal is most likely caused by defects and excitonic effects.[29] Furthermore, previous studies by Slavney *et al.* revealed that in addition to the direct band gap at about 2.2 eV, $Cs_2AgBiBr_6$ features an indirect band gap at about 1.9 eV, which was not detectable in the light absorption spectra of our prepared films.[26] Considering that the value of the indirect band gap matches quite closely the position of the observed PL maximum, we believe that the relatively large red shift of the maximum of the PL signal with respect to the absorption onset can be assigned to contributions of this indirect band gap at about 1.9 eV.

Nevertheless, the PL results indicate that $Cs_2AgBiBr_6$ films can be incorporated in working photovoltaic devices.

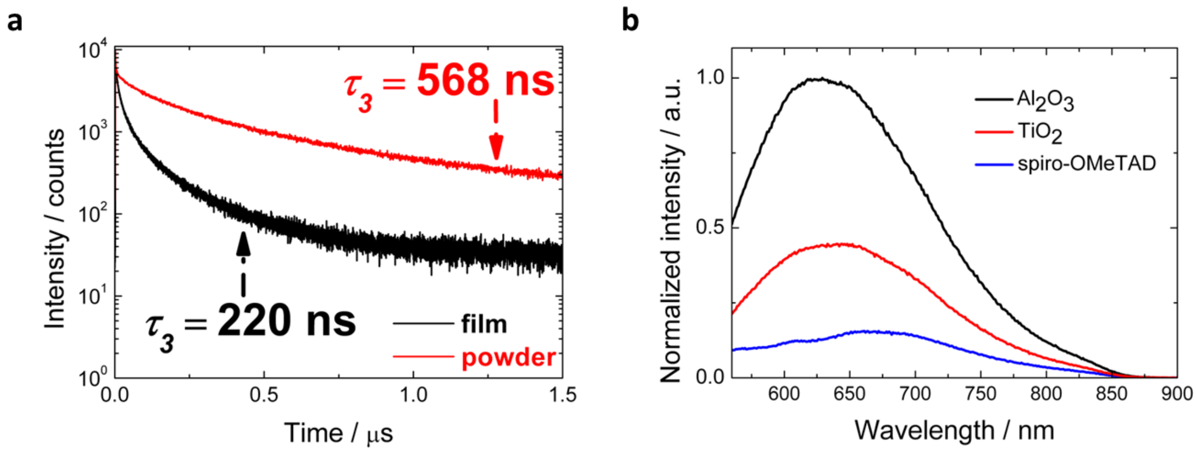

Figure 5-7: a) TCSPC decays of a $Cs_2AgBiBr_6$ film on glass and polycrystalline powder. b) PL emission spectra of $Cs_2AgBiBr_6$ films on mp-Al_2O_3, mp-TiO_2 and mp-Al_2O_3 covered with spiro-OMeTAD. The films presented in 3d were prepared on an 800 nm thick mp scaffold. All films were prepared according the procedure depicted in Fig. 1 with a 285 °C annealing step.

The morphology of the double perovskite films prepared according the procedure shown in Fig. 5-3 was investigated with scanning electron microscopy (SEM). Fig. 5-8a shows a SEM top-view image of a $Cs_2AgBiBr_6$ film, on an 800 nm thick mp-TiO_2 scaffold as used for the preparation of photovoltaic devices. Here, no dense and homogeneous capping layer on top of the mp-TiO_2 is observable, instead many agglomerates at the scale of about one micron have formed. This is most likely caused by the fast crystallization process during the spin-coating procedure induced by fast solvent evaporation due to the performed preheating step, as shown in Fig. 5-3. We believe that this fast crystallization process impedes homogeneous crystal growth, leading to the observed agglomerates. Energy dispersive X-ray spectroscopy (EDX) measurements were performed to evaluate the penetration depth of the double perovskite into the mp-TiO_2 scaffold. Fig. 5-8b-g show a SEM cross-section of the film presented in Fig. 4a and the elemental maps of Ti, Cs, Ag, Bi and Br, respectively. The cross-section image and EDX maps clearly establish complete infiltration of $Cs_2AgBiBr_6$ into the mp-TiO_2 scaffold, which is important to obtain efficient devices, while some additional $Cs_2AgBiBr_6$ agglomerates are formed on top of the scaffold.

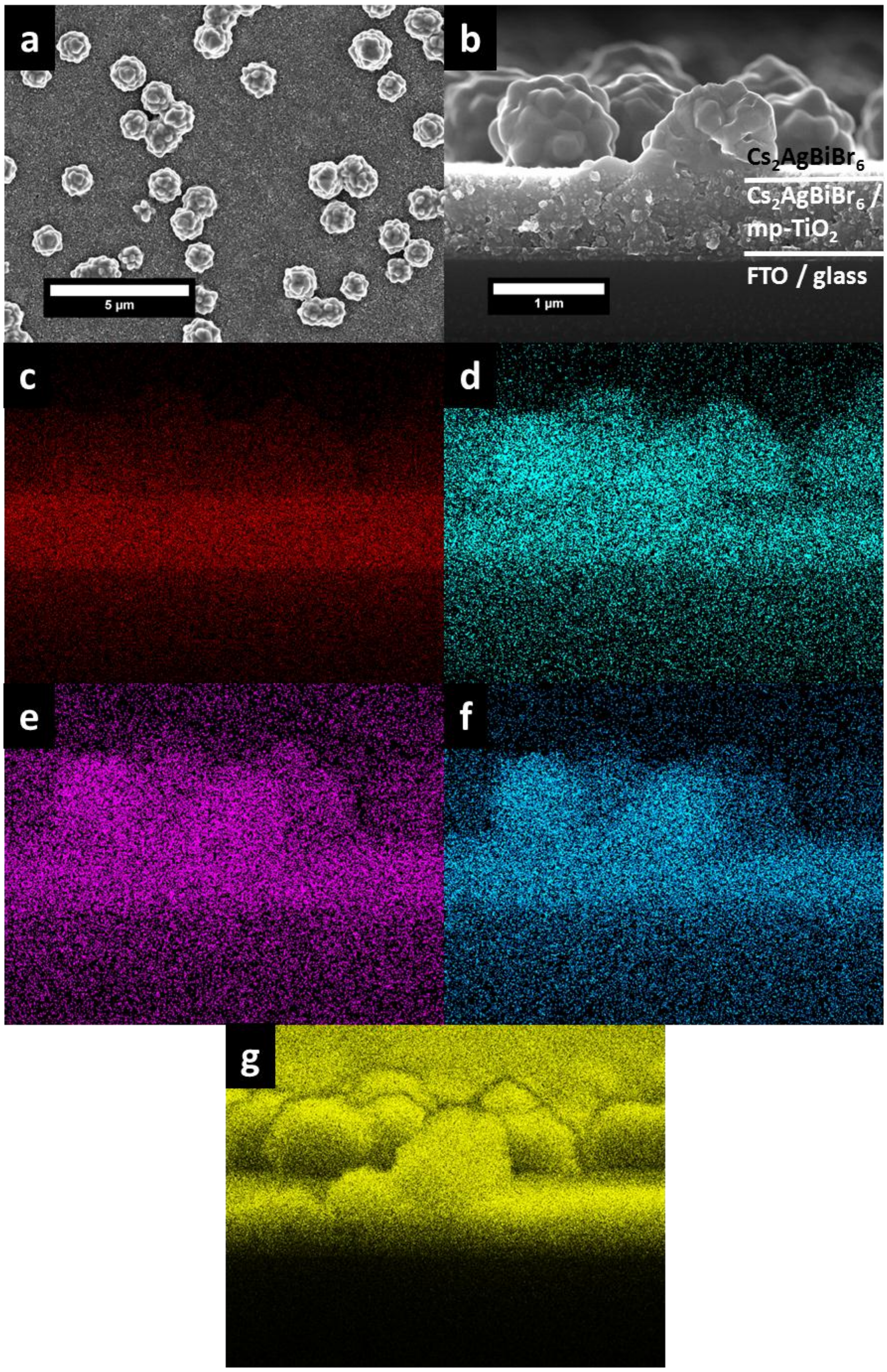

Figure 5-8: a) SEM top-view image of a $Cs_2AgBiBr_6$ film prepared with a 75 °C preheating step on mp-TiO_2. (b) SEM cross-section image of the film presented in (a). c-g) EDX elemental maps of Ti (red), Cs (turquoise), Ag (purple), Bi (blue) and Br (yellow).

Based on the promising results of the above investigations, we incorporated the newly developed $Cs_2AgBiBr_6$ films into photovoltaic devices featuring a layer assembly of fluorine doped tin oxide (FTO)/dense TiO_2/mp-TiO_2/$Cs_2AgBiBr_6$/spiro-OMeTAD/Au to investigate their photovoltaic characteristics. As mentioned before, the thickness of the utilized mp-TiO_2 layer was approx. 800 nm as depicted in Fig. 5-8b.

Fig. 5-9a displays the statistical parameter distribution of 48 solar cells (per treatment temperature) that were assembled with $Cs_2AgBiBr_6$ films prepared without a preheating step and with a preheating step at different temperatures. The studies revealed a PCE maximum at 75 °C, we attribute to the improved optical properties of those films shown in Fig. 3a and S3. Furthermore, the J-V curves given in Fig. 5-9b show that the increased device performance at 75 °C preheating is not only caused by an increased short-circuit current (J_{sc}) due to the enhanced optical absorption properties because of the preheating, but also by the enhanced fill factor (FF) and by the V_{oc} increase observed with increasing preheating temperature. We hypothesize that the preheating also improves the mp-TiO_2/double perovskite interface, for e.g. by reducing trap states, resulting in an enhanced performance.[42] The large spread of the device performance observable for films preheated at 25 °C and 65 °C indicates that the improvement of the TiO_2/double perovskite interface is not as reliable as for preheating at 75 °C, which results in the smallest performance spread of all investigated preheating temperatures. The PCE decrease and the broadening of the PCE distribution at higher preheating temperatures (>100 °C) is tentatively attributed to the formation of a top layer consisting of large crystallites on the mp-TiO_2 scaffold, caused by a strongly accelerated precipitation of the double perovskite due to the relatively high deposition temperature, as shown in Fig. 5-9c & d, which is apparently too thick for efficient charge transport. We note that $Cs_2AgBiBr_6$ films prepared without a preheating step feature the most homogeneous morphology, with the lowest number of agglomerates on top the mp-TiO_2 scaffold (see Fig 5-9e & f), without resulting in the best performing devices. Accordingly, it is likely that preheating to 75 °C results in double perovskite films featuring strongly improved optoelectronic properties, which overcome the possible detrimental effects of a less homogeneous morphology due to the agglomerate formation on top of the mp-TiO_2 induced by the preheating.

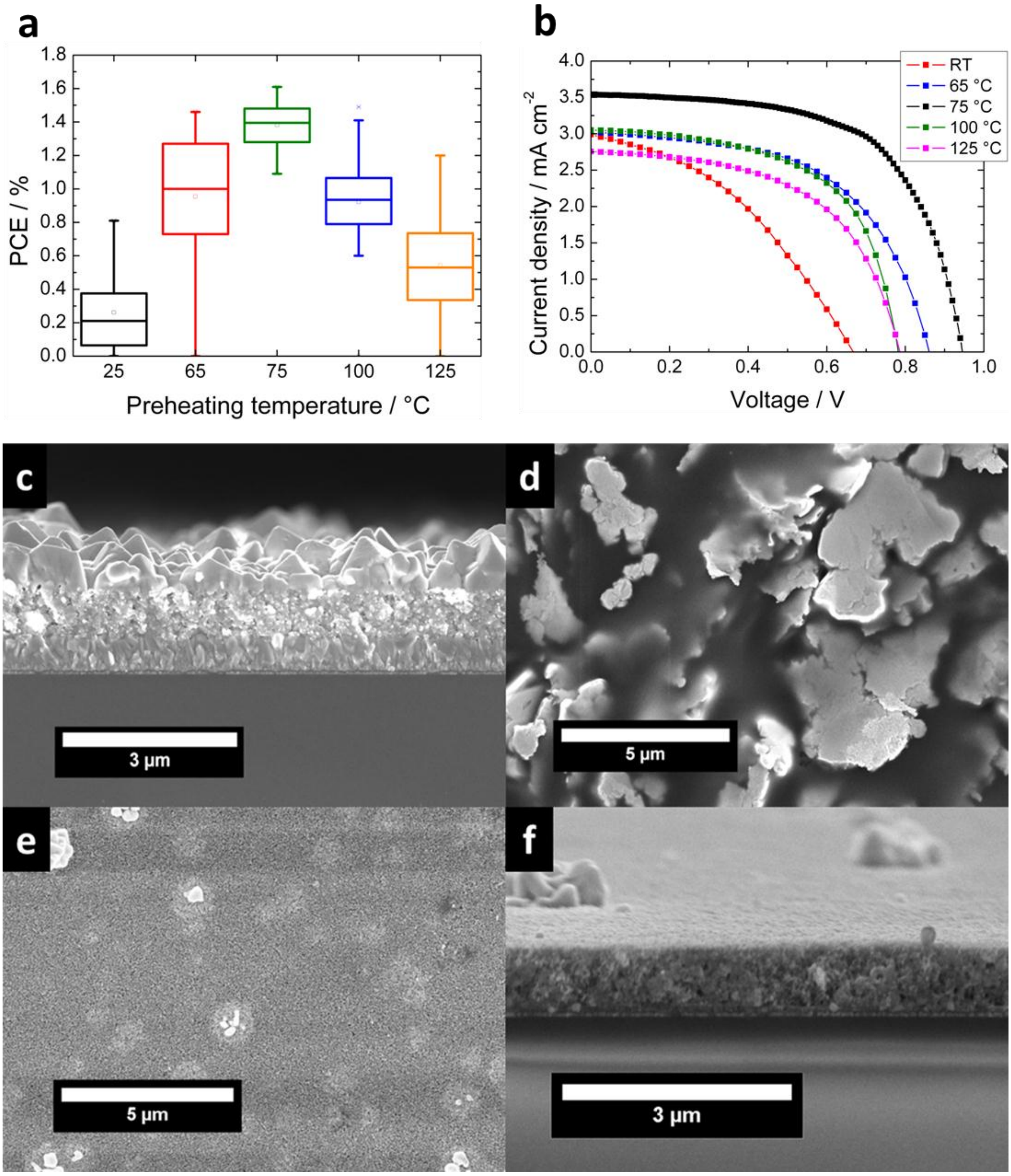

Figure 5-9: a) Device performance as a function of preheating temperature, values obtained from 48 individual devices per temperature. All films were annealed at 250 °C after spin-coating to achieve phase pure $Cs_2AgBiBr_6$ films. b) J-V characteristics of $Cs_2AgBiBr_6$ based devices prepared with a preheating step at different temperatures. The depicted J-V curves show only the backwards scan. The characteristic values of the J-V curves are given in Table 5-2. c) SEM cross-section and (d) top-view image of a $Cs_2AgBiBr_6$ film deposited with a preheating step at 125 °C. The presence of a top layer consisting of large crystallites is clearly observable. e) SEM cross-section and (f) top-view image of a $Cs_2AgBiBr_6$ film deposited without a preheating step at There are only a few agglomerates visible on top the mp-TiO_2 scaffold.

Table 5-2: J_{sc}, V_{oc}, FF and PCE of the J-V curves shown in Figure 5-9b.

Preheating temperature	J_{sc} / mA/cm²	V_{oc} / V	FF	PCE / %
RT	2.99	0.67	0.39	0.81
65 °C	3.02	0.86	0.55	1.45
75 °C	3.54	0.95	0.62	2.15
100 °C	3.05	0.78	0.58	1.41
125 °C	2.75	0.78	0.54	1.20

Although a full conversion of the precursors into the double perovskite phase is achieved by 250 °C annealing after film formation, the obtained PCEs showed a large spread. Therefore, an extensive study of the influence of the annealing temperature on device performance was conducted. Fig. 5-10a shows the relation between annealing temperature and the statistical distribution of PCEs of 48 individual devices. The highest and most reproducible PCEs were obtained for an annealing temperature of 285 °C. The increase in PCE with increasing annealing temperature is dominated by an increase of J_{sc} and FF at annealing temperatures below 250 °C, whereas only the J_{sc} rises significantly at higher annealing temperatures (Fig. 5-10b). Up to 250 °C, this trend is most likely caused by a decrease of the side phases observed in the PXRD pattern (Fig. 5-3), until the phase-pure $Cs_2AgBiBr_6$ has formed at 250 °C. This temperature is the lower end of the range of the annealing temperature required to fully convert the precursors into the double perovskite phase. Annealing at slightly higher temperatures (285 °C) make this process more robust, leading to slightly higher PCEs and more importantly, better reproducibility. The decrease in PCE at even higher temperature (300 °C) is associated with a reduction in J_{sc}, which we attribute to the degradation of the $Cs_2AgBiBr_6$ films as the double perovskite slowly starts to come off the substrate at annealing temperatures at about 300 °C (Fig. 5-10b).

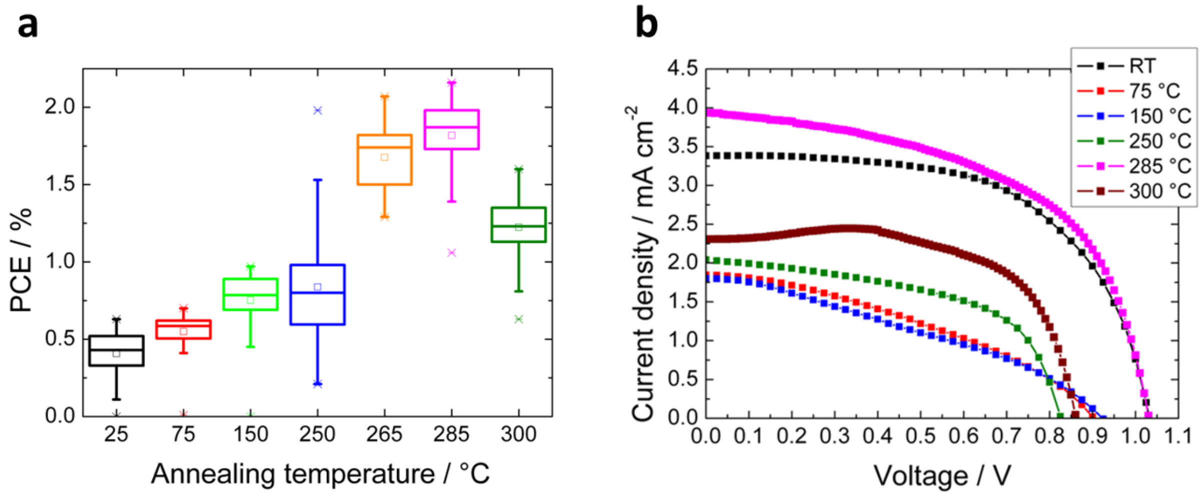

Figure 5-10: a) Device performance of solar cells assembled with $Cs_2AgBiBr_6$ films preheated at 75 °C as a function of annealing temperature, values obtained from 48 individual devices per temperature. b) *J*-*V* charcteristics of $Cs_2AgBiBr_6$ based solar cells prepared with a 75 °C preheating step and annealed at different temperatures. The depicted *J*-*V* curves show only the backwards scan. The characteristic values of the *J*-*V* curves are given in Table 5-3. The *J*-*V* curves show a clear decrease of device performance upon 300 °C annealing. Furthermore, for annealing steps at 250 °C and 285 °C, V_{oc}´s of more than one volt could be obtained.

Table 5-3: J_{sc}, V_{oc}, FF and PCE of the J-V curves shown in Figure 5-10b.

Annealing temperature	J_{sc} / mA/cm²	V_{oc} / V	FF	PCE / %
RT	1.80	0.92	0.34	0.58
75 °C	1.85	0.90	0.37	0.63
150 °C	2.02	0.82	0.55	0.93
250°C	3.38	1.03	0.59	2.15
285 °C	3.94	1.03	0.54	2.20
300 °C	2.30	0.86	0.66	1.25

The application of our optimized synthesis conditions resulted in devices showing PCEs of more than two percent. Remarkable is the relatively narrow distribution in the performance, taking into consideration the surface of the film that contains the perovskite agglomerates. Fig. 5-11 displays the *J*-*V* curve of the best performing device exhibiting a PCE of 2.43%. In particular, the V_{oc} of 0.98 V is significantly higher than that of other bismuth-based compounds featuring comparable E_g´s.[43-45] Moreover, V_{oc}´s exceeding 1 V were measured, which are, with the best of our knowledge, the highest V_{oc} values reported for bismuth halide based materials (see Fig. 5-10b), confirming the good alignment of the conduction band of the perovskite with TiO_2 as predicted from the energy level diagram in Fig. 5-6 and in computational studies.[36]

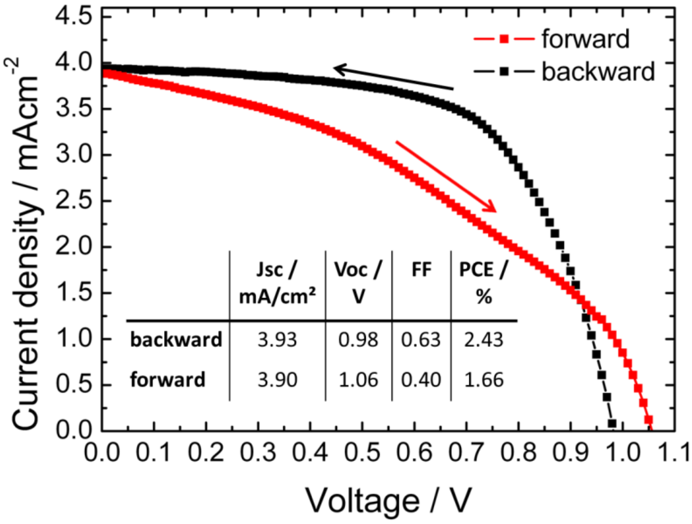

	Jsc / mA/cm²	Voc / V	FF	PCE / %
backward	3.93	0.98	0.63	2.43
forward	3.90	1.06	0.40	1.66

Figure 5-11: *J-V* curve of the best performing device showing a PCE of 2.43 %. Regarding the forward and backward scan, the device features strong hysteresis.

These PCEs are viewed as an excellent starting point for double perovskite absorbers in solar cells if one considers that the spectroscopically predicted maximum efficiency of $Cs_2AgBiBr_6$ is reaching 7.92% determined from density functional theory calculations by Savory *et al.*.[46] As the band gap of $Cs_2AgBiBr_6$ is 2.2 eV, the current of solar cells comprising this absorber is limited to ~6.8 mA cm^{-2} under 1 sun illumination. External quantum efficiency (EQE) measurements show an integrated current of 3.6 mA cm^{-2} (Fig. 5-12a), which is in good agreement with the J_{sc} of 3.7 mA cm^{-2} obtained from the *J-V* curve (Fig. 5-12b). The EQE spectrum (Fig. 5-12a) shows an onset around 550 nm, which is in agreement with the absorbance data, and is above 50% from 375 to 470 nm with a maximum of 60% at 415 nm. According to Fig. 5-11 the *J-V* curves show hysteresis, comparable to behavior observed in devices employing lead-based perovskites.[47–50] Computational studies by Eames *et al.* reveal that the migration of the halide anions contributes to the hysteresis in hybrid lead halide perovskite based photovoltaics due to their very low activation barrier.[51] Therefore, we believe that similar effects, including trapping/de-trapping of charge carriers,[47,52] are likely to be responsible for the hysteresis in our $Cs_2AgBiBr_6$ based devices since the crystal structure of the double perovskite is very similar.

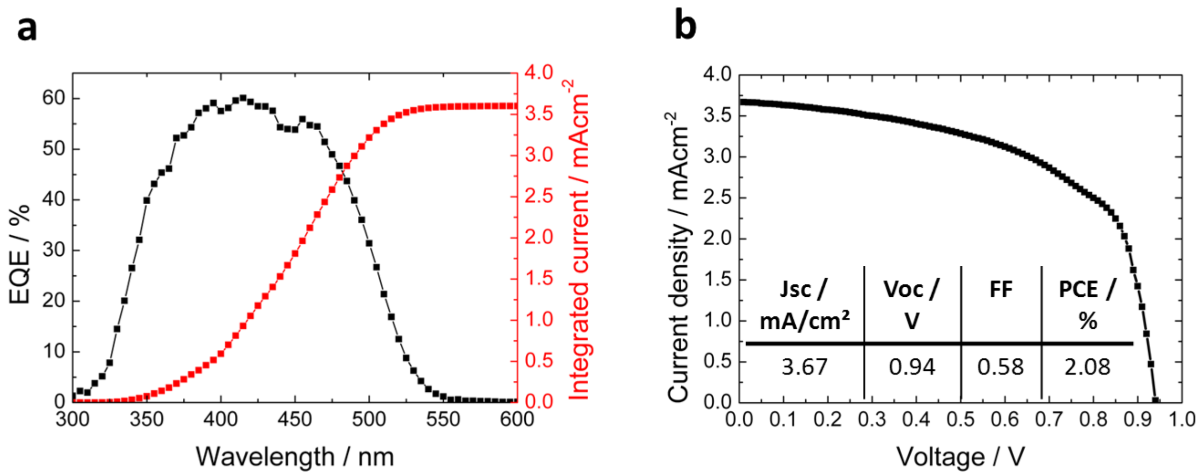

Jsc / mA/cm²	Voc / V	FF	PCE / %
3.67	0.94	0.58	2.08

Figure 5-12: a) EQE spectrum (black) and integrated predicted current (red) of a device showing a J_{sc} of 3.7 mA cm^{-2}. b) J-V curve of the solar cell used for the EQE measurements.

Besides performance, stability is also an important issue for widespread applications as devices need to work for many years at high intensity illumination. Accordingly, we conducted the first stability studies on $Cs_2AgBiBr_6$-based solar cells. Fig. 5-13 displays the stabilized power output under ambient conditions. The device shows a rapid response after illumination, resulting in a PCE of around 2.0%. During the next 30 s, only a very small decay of around 5% in the PCE was observed, after which the PCE stabilizes just above 1.9% and no further decay was observed over a period of five minutes, indicating a similar performance stability like lead halide based solar cells.

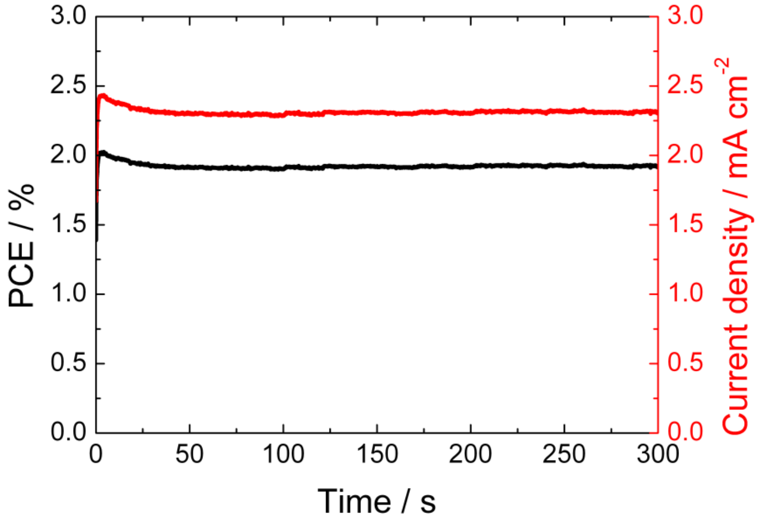

Figure 5-13: Stabilized power output and current density measured under ambient conditions without encapsulation. The device was manufactured according the procedure described in Fig. 5-3 with a 285 °C annealing step.

Another device was illuminated using an AM1.5 solar simulator under ambient conditions for a period of 100 min while at regular intervals *J*-*V* scans were taken (Fig 5-14a & b).

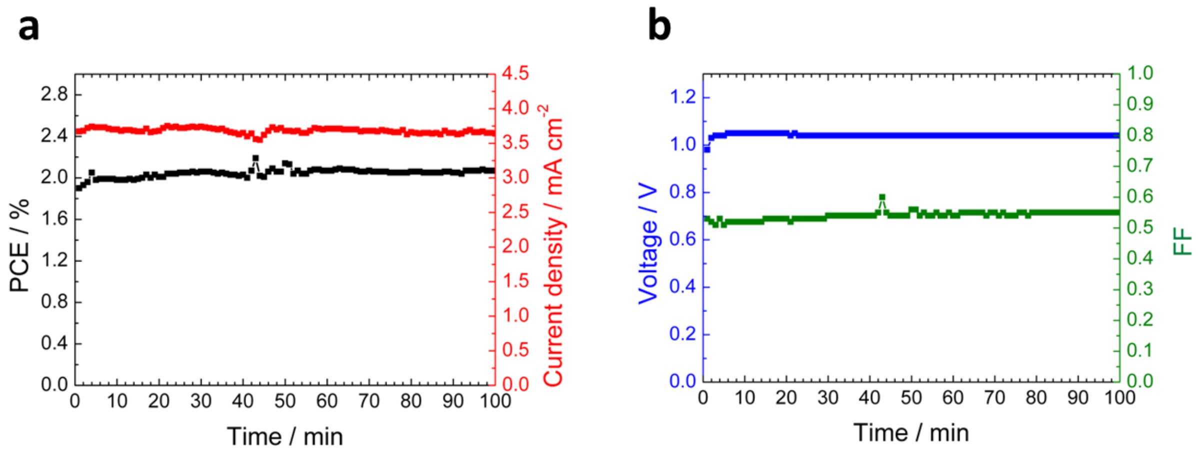

Figure 5-14: a) Photovoltaic performance as a function of time under continuous illumination under ambient conditions. b) V_{oc} and FF of the device given in Figure 5-14a. The device was manufactured according the procedure described in Fig. 5-3 with a 285 °C annealing step.

During the first couple of minutes an increase in the PCE was observed as a result of an increase in the V_{oc}, which we assign to light soaking effects.[53] This indicates the presence of (interfacial) defects that can be neutralized with photogenerated charge carriers.[53–59] After this period the V_{oc} and J_{sc} turn out to be very stable. Some fluctuation in the FF (Fig. 5-14b) are observed, which are also reflected in the PCE, nevertheless after 100 min the PCE did not significantly decay and at 2.06%, it was even higher than the initial value measured before the light soaking. The results presented in Figure 5-14a & b indicate a high device stability under permanent illumination, higher than that of reported $MAPbI_3$ based devices showing a significant drop of J_{sc} within the first two hours.[60] Furthermore, initial longer-term stability studies on the new $Cs_2AgBiBr_6$-based devices revealed an excellent stability under ambient conditions for at least 25 days (Fig. 5-15). The devices were stored in the dark to avoid any possible light driven degradation processes of the double perovskite as indicated by Slavney *et al.*.[26]

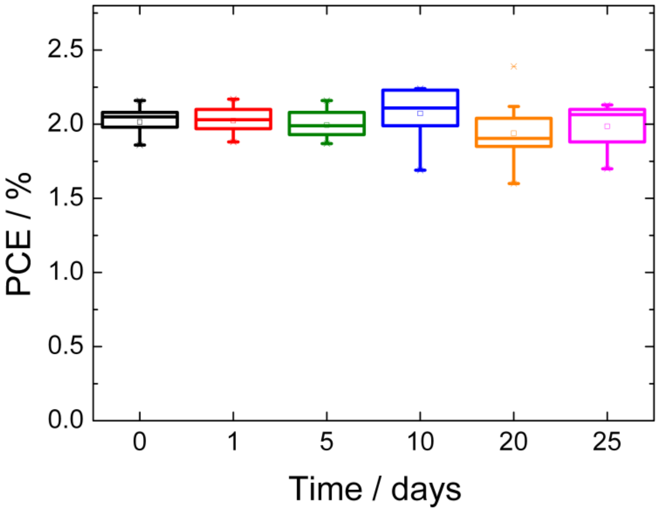

Figure 5-15: Development of the PCEs of 12 devices, prepared according the procedure described in Figure 5-3, stored under ambient conditions in the dark for 25 days, revealing excellent device stability. No significant performance loss is observable.

Another important stability aspect is the sensitivity of the absorber material against moisture. The state-of-the-art materials methylammonium lead iodide perovskites are known to be very sensitive to humidity,[61] which leads to the fast degradation of the material. In contrast, $Cs_2AgBiBr_6$ solar cells have shown to possess a high stability.[26] In order to study the sensitivity of the prepared $Cs_2AgBiBr_6$ films we performed in-situ hydration measurements at elevated humidities (Figure 5-15a & b).

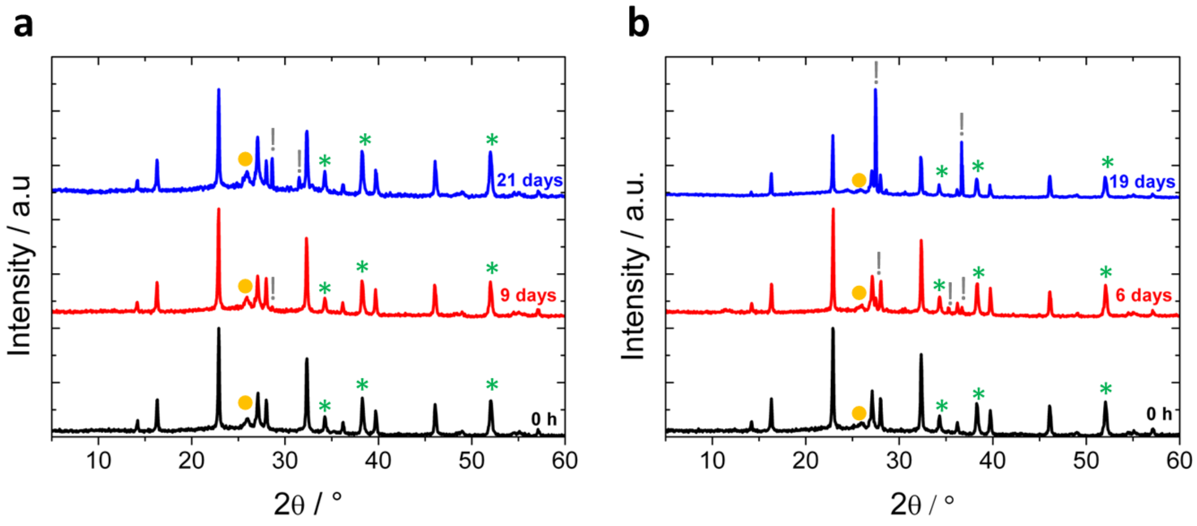

Figure 5-16: XRD measurements of the hydration a $Cs_2AgBiBr_6$ film exposed to (a) 75% RH and (b) 90 % RH in air for 21 days and 19 days, respectively. The XRD reflection for the degradation products (grey exclamation mark), and the FTO substrate (green asterisk) and TiO_2 extraction layer (yellow dot) are marked in the graph

Figure 5-16a shows the XRD patterns of a $Cs_2AgBiBr_6$ film on mp-TiO_2/FTO which was continuously exposed to 75% RH in air. No reorganization of the crystal was observed up on exposure of the film to humidity, while degradation of the $Cs_2AgBiBr_6$ film was only observed after nine days of continues exposure. Up on exposure of the films to higher humidity (90% RH) we observed the formation of another degradation product, which appeared after 6 days (Figure 5-16b). In comparison, commonly used lead iodide based perovskites such as $CH3NH_3PbI_3$, $HC(NH_2)_2PbI_3$, ($FAPbI_3$) and FA $_{0.9}Cs_{0.1}PbI_3$ films have shown to degrade within a couple of hours.[61–66] The XRD study confirms the anticipated high stability against humidity for $Cs_2AgBiBr_6$ films. We found that the degradation of the $Cs_2AgBiBr_6$ perovskite is irreversible, which indicates that the degradation product is not a hydrated species, while a crystallographic database survey indicates that oxides, hydroxides or oxyhalides can be excluded. Additional studies have to be conducted to identify the degradation products of $Cs_2AgBiBr_6$

Additionally, the performance of solar cells based on $Cs_2AgBiBr_6$ was recorded after exposure to elevated humidities (75 and 90% RH), see Figure 5-17. Here, we observe impressive stability of the $Cs_2AgBiBr_6$ perovskite solar cells. Devices based on $Cs_2AgBiBr_6$ stored at 75% RH show some fluctuation in their performance, but do not lose more than 15 % of their efficiency over a period of 9 days. Afterwards a strong decrease in device efficiency can be observed which corresponds with the film degradation as was observed by PXRD and shown in Figure 5-16a. By exposing the devices to 90% RH, we observed a drop in PCE already after 24 hours. The XRD study showed that the perovskite degrades fast at high humidities, which our data suggests is the main culprit behind the degradation of the solar cell performance, although degradation of the HTM and its interfaces might also play a role.[67] Nevertheless our devices show an impressive enhancement in the stability compared to state-of-the-art lead-based perovskites.

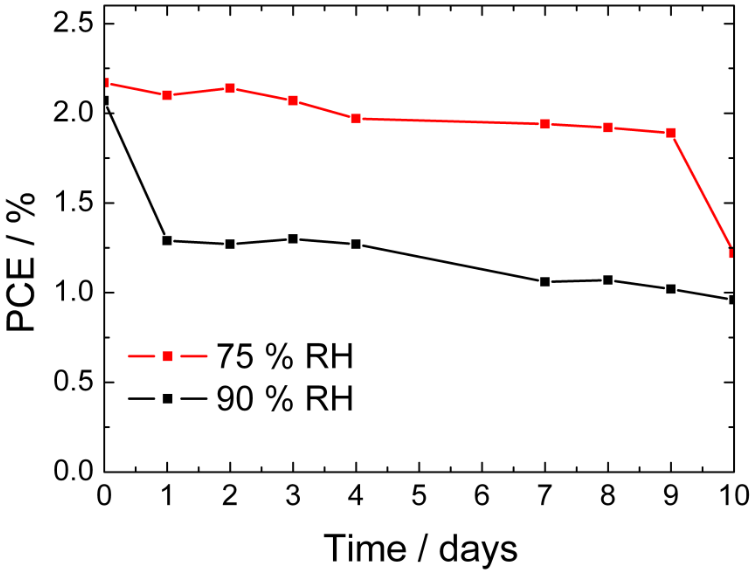

Figure 5-17: Development of the PCEs of devices exposed to humidity levels of 75 % RH and 90 % RH for 10 days.

5.3 Conclusions

In conclusion, we have demonstrated the solution-based formation of double perovskite films via a fast and efficient spin-coating method. Extensive studies of the synthesis conditions revealed the necessity of a high-temperature annealing step to fully convert the precursors into the desired double perovskite phase, and the requirement of an additional preheating step to improve the optical properties of the $Cs_2AgBiBr_6$ films. The resulting $Cs_2AgBiBr_6$ films feature an E_g comparable to that of single crystals and polycrystalline powders, and solar cells comprising these new films exhibit very promising PCEs close to 2.5% with V_{oc}´s exceeding one volt, demonstrating the suitability of double perovskites for optoelectronic devices. Furthermore, our $Cs_2AgBiBr_6$-based devices feature a high stability under constant illumination at ambient conditions, higher than that of reported $MAPbI_3$ based solar cells.

Since the elpasolite structure allows for numerous different combinations of elements, this work shows the potential for developing a wide range of double perovskites for diverse environmentally friendly optoelectronic applications.

5.4 Experimental section

All chemicals were used as received without any further purification. All synthesis steps were conducted under ambient conditions except the application of the hole transporting layer (HTL) which was performed in a nitrogen-filled glove box.

Substrate preparation

Fluorine-doped tin oxide (FTO)-coated glass sheets (7 Ωsq^{-1}, Pilkington, USA) were patterned by etching with zinc powder and 3 M HCl. They were subsequently cleaned with a 2% Hellmanex solution and rinsed with deionized water and ethanol. Directly before applying the blocking layer, remaining organic residues were removed by an oxygen plasma treatment for 5 min. A compact titanium dioxide (TiO_2) layer was deposited by spin-coating a sol-gel precursor solution at 2000 rpm for 45 s followed by subsequent annealing at 500 °C for 45 min. For preparing the sol-gel solution, a 27.2 mM (70 µL) solution of HCl in 2-propanol (5 mL) was added dropwise to a vigorously stirred 0.43 mM (735 µL) solution of titanium isopropoxide (99.999%, Sigma–Aldrich) in 2-propanol (5 mL). Afterwards, an approx. 800 nm thick, mesoporous (mp)-TiO_2 layer was applied by spin-coating 100 µL of a TiO_2 nanoparticle paste (Dyesol DSL 18NR-T) diluted in absolute ethanol (1:2 weight ratio) onto the compact TiO_2 layer at 2500 rpm for 30 s, followed by subsequent annealing at 500 °C for 15 min under ambient conditions.

Perovskite film preparation

The precursor solution was prepared by dissolving 268 mg $BiBr_3$ (0.6 mmol, $\geq$ 98%, Sigma Aldrich), 112.8 mg of AgBr (0.6 mmol, 99.5%, Alfa Aesar) and 254 mg CsBr (1.2 mmol, 99 %, Alfa Aesar) in dimethylsulfoxide (1 mL, DMSO, anhydrous, 99.9%, Sigma-Aldrich). After complete dissolution of the precursors, both the solution and the substrate were *preheated* to 75 °C before spin-coating. 100 µL of the hot precursor solution was spin-coated onto the TiO_2-covered substrate at 2000 rpm for 30 s. The substrates were subsequently *annealed* at 285 °C for 5 min under ambient conditions to allow for a complete formation of the desired double perovskite phase. The temperatures for both the *preheating* and the *annealing* steps were also varied to identify the optimal conditions for phase pure films.

Solar cell fabrication

After film formation, the films were covered with a HTL of 2,2',7,7'-tetrakis-(*N*,*N*-di-4-methoxyphenylamino)-9,9'-spirobifluorene (spiro-OMeTAD, Borun Chemicals, 99.5% purity). The HTL solution was prepared by dissolving 73 mg of spiro-OMeTAD in chlorobenzene (1 mL, 99.8%, Sigma–Aldrich). The solution was filtered and mixed with 4-*tert*-butylpyridine (10 µL, TBP, 96% Sigma Aldrich) and a 173 mg mL^{-1} bis(trifluoromethane)sulfonamide lithium salt (LiTFSI, 99.95%, Sigma–Aldrich) solution in acetonitrile (30 µL). This solution was spin-coated dynamically at 1500 rpm for 45 s. In a second step the sample rotation was accelerated to 2000 rpm for 5 s to allow the solvent to dry completely. Finally, 40 nm thick gold electrodes were thermally deposited under a high vacuum on top of the device.

Characterization

PXRD measurements were performed in transmission mode on a STOE Stadi MP diffractometer with a Cu Kα1 radiation source (λ = 1.54060 Å) operating at 40 kV and 40 mA. The diffractometer was equipped with a DECTRIS MYTHEN 1K solid-state strip detector. PXRD measurements on thin films were performed using a Bruker D8 Discover X-ray diffractometer operating at 40 kV and 30 mA, employing Ni-filtered Cu Kα radiation (λ = 1.5406 Å) and a position-sensitive detector (LynxEye). Scanning electron microscopy (SEM) images and EDX data were acquired on a FEI Helios NanoLab G3 UC microscope. The sample was fixed by silver paste. For the optical characterization, precursor solutions were prepared similar to those used for the devices. Similar deposition conditions were also chosen. For UV-Vis measurements the films were prepared on glass substrates or on the mp-TiO_2 substrates also used for solar cells. For PL measurements the double perovskite films were either prepared on approximately 800 nm thick mp-TiO_2 or mp-Al_2O_3 films deposited on a glass slide. For the mp-TiO_2 on glass, similar solutions and conditions were chosen as for the solar cell preparation. For the formation of the mp-Al_2O_3 film, Al_2O_3 nanoparticles dispersed in isopropanol (Sigma Aldrich, <50 nm, 20%wt) were diluted with isopropanol (Sigma Aldrich, 99.8%) in 1 : 1 ratio. 100 µL of the Al_2O_3 dispersion was spun on a glass substrate at 2500 rpm for 30 s with subsequent annealing at 120 °C for 10 min. Steady-state absorption spectra were acquired with a Lambda 1050 UV-Vis spectrophotometer (Perkin Elmer) using an integrating sphere. Steady state and time resolved PL measurements were conducted with a Fluotime 300 Spectrofluorometer (Picoquant GmbH). The excitation wavelength was fixed at 405 nm. The emission for time resolved measurements was monitored at 630 nm being the wavelength of the maximum intensity of the steady state photo-emission. *J-V* curves were recorded with a Keithley 2400 sourcemeter under simulated AM 1.5 sunlight, calibrated to 100 mW cm^{-2} with a Fraunhofer ISE certified silicon cell. The active area of the solar cells was defined with a square metal aperture mask of 0.0831 cm^2. External quantum efficiency (EQE) measurements were performed at short circuit with a bias illumination of 0.1 sun provided by an AM 1.5 solar simulator (Solar Light Model 16S). The measurements were conducted under low-frequency chopped monochromatic light (12 Hz). A 150 W xenon lamp equipped with a monochromator and order-sorting filters was used as a light source. The light intensity reaching the electrode was measured using a certified Fraunhofer ISE silicon reference cell equipped with a KG5 filter at a frequency of 40 Hz. For signal detection a Signal Recovery 7265 lock-in amplifier combined with a low-noise current amplifier (Femto DLPCA-200) was employed.

5.5 Literature

[1] M. M. Lee, J. Teuscher, T. Miyasaka, T. N. Murakami, H. J. Snaith, *Science* **2012,** *338*, 643.

[2] NREL chart, http://www.nrel.gov/ncpv/images/efficiency_chart.jpg, (accessed July 2017).

[3] T. M. Brenner, D. A. Egger, L. Kronik, G. Hodes, D. Cahen, *Nat. Rev. Mater*. **2016,** *1*, 15007.

[4] S. De Wolf, J. Holovsky, S.-J. Moon, P. SLoiper, B. Niesen, M. Ledinsky, F.-J. Haug, Yum, C. Ballif *J. Phys. Chem. Lett*. **2014,** *5*, 1035.

[5] S. D. Stranks, G. E. Eperon, G. Grancini, C. Menelaou, M. J. P. Alcocer, T. Leijtens, L. M. Herz, A. Petrozza, H. J. Snaith *Science* **2013,** *342*, 341.

[6] C. Wehrenfennig, G. E. Eperon, M. B. Johnston, H. J. Snaith, L- M. Herz, *Adv. Mater*. **2014,** *26*, 1584.

[7] R. E. Brandt, V. Stevanović, D. S. Ginley, T. Buonassisi, *MRS Commun*. **2015,** *5*, 265.

[8] A. Walsh, D. O. Scanlon, S. Chen, X. G. Gong, S.-H. Wei, *Angew. Chem., Int. Ed*. **2015,** *54*, 1791.

[9] Y.-Y Zhang, S. Chen, P. Xu, H. Xiang, X.-G. Gong, A. Walsh, S.-H. Wei, *arXiv:1506.01301*, **2015**.

[10] G. P. Nagabhushana, R. Shivaramaiah, A. Navrotsky, *Proc. Natl. Acad. Sci. U. S. A*. **2016,** *113*, 7717.

[11] N. Aristidou, I. Sanchez-Molina, T. Chotchuangchutchaval, M. Brown, L. Martinez, T. Rath, S. A. Haque, *Angew. Chem., Int. Ed.* **2015,** *54*, 8208.

[12] Babayigit, A.; Ethirajan, A.; Muller, M.; Conings, B. *Nat. Mater*. **2016,** *15*, 247.

[13] F. Hao, C. C. Stoumpos, D. H. Cao, R. P. H. Chang, M. G. Kanatzidis, *Nat. Photonics*, **2014,** *8*, 489.

[14] N. K. Noel, S. D. Stranks, A. Abate, C. Wehrenfennig, S. Guarnera, A. A. Haghighirad, A. Sadhanala, G. E. Eperon, S. K. Pathak, M. B. Johnston, A. Petrozza, L. M. Herz, H. J. Snaith, *Energy Environ. Sci.* **2014,** *7*, 3061.

[15] R. Jakubas, J. Zaleski, L. Sobczyk, *Ferroelectrics* **1990,** *108*, 109.

[16] S. Sun, S. Tominaka, J-H. Lee, F. Xie, P. D. Bristowe, A. K. Cheetham, *APL Mater*. **2016,** *4*, 031101.

[17] B. Chabot, E. Parthé, *Acta Cryst.* **1978,** *B34*, 645.

[18] A. J. Lehner, D. H. Fabini, H. A. Evans, C. A. Hébert, S. R. Smock, J. Hu, H. Wang, J. W. Zwanziger, M. I. Chabinyc, R. Seshadri, R. *Chem. Mater*. **2015,** *27*, 7137.

[19] E. T. McClure, M. R. Ball, W. Windl, P. M. Woodward, *Chem. Mater*. **2016,** *28*, 1348.

[20] L. R. Morrs, W. R. Robinson, *Acta Crystallogr., Sect. B: Struct. Crystallogr. Cryst. Chem.* **1972,** *28*, 653.

[21] F. Pelle, B. Jacquier, J. Denis, B. J. Blanzat, *Lumin*. **1978,** *17*, 61.

[22] W. Smit, G. Dirksen, D. Stufkens, *J. Phys. Chem. Solids.* **1990,** *51*, 189.

[23] Z. Deng, F. Wei, S. Sun, G. Kieslich, A. K. Cheetham, P. D. Bristowe, *J. Mater. Chem., A* **2016,** *4*, 12025.

[24] A. Tressaud, S. Khaïroun, J. P. Chaminade, M. Couzi, *Phys. Status Solidi A* **1986,** *98*, 417.

[25] F. Wei, Z. Deng, S. Sun, F. Xie, G. Kieslich, D.M. Evans, M. A. Carpenter, P. D. Bristowe, A. K. Cheetham, *Mater. Horiz*. **2016,** *3*, 328.

[26] A. H. Slavney, T. Hu, A. M. Lindenberg, H. I. Karunadasa, *J. Am. Chem. Soc.* **2016,** *138*, 2138.

[27] G. Volonakis, M. R. Filip, A. A. Haghighirad, N. Sakai, B. Wenger, H. J. Snaith, F. Giustino, *J. Phys. Chem. Lett.* **2016,** *7*, 1254.

[28] F. Wei, Z. Deng, S. Sun, F. Zhang, D. M. Evans, K. Kieslich, S. Tominaka, M. A. Carpenter, J. Zhang, P. D. Bristowe, A. K. Cheetham, *Chem. Mat*. **2017,** *29*, 1089.

[29] M. R. Filip, S. Hillman, A. A. Haghighirad, H. J. Snaith, F. Giustino, *J. Phys. Chem. Lett*. **2016,** *7,* 2579.

[30] M. R. Filip, C. Verdi, F. Giustino, *J. Phys. Chem. C* **2015,** *119*, 25209.

[31] Z. Xiao, W. Meng, J. Wang, Y. Yan, *ChemSusChem* **2016,** *9*, 2628.

[32] N. J. Jeon, J. H. Noh, Y. C. Kim, W. S. Yang, S. Ryuand, S. I. Seok, *Nat. Mater*. **2014,** *13*, 897.

[33] F. Hao, C. C. Stoumpos, P. Guo, N. Zhou, T. J. Marks, R. P. H. Chang, M. G. Kanatzidis, *J. Am. Chem. Soc.* **2015,** *137*, 11445.

[34] S. Rühle, *Phys. Status Solidi A* **2017,** 1600955.

[35] R. Sheng, A. W. Y. Ho-Baillie, S. Huang, M. Keevers, X. Hao, L. Jiang, Y.-B Cheng, M. A. Green, *J. Phys. Chem. Lett.*, **2015**, *6*, 3931.

[36] H.-J. Feng, W. Deng, K. Yang, J. Huang, X. C. Zeng, *J. Phys. Chem. C* **2017,** *121*, 4471.

[37] S. Gholipour, A. M. Ali, J.-P. Correa-Baena, S.-H. Turren-Cruz, F. Tajabadi, W. Tress, N. Taghavinia, M. Grätzel, A. Abate, F. De Angelis, C. A. Gaggioli, E. Mosconi, A. Hagfeldt, M. Saliba, *Adv. Mater.* **2017,** 1702005.

[38] D. Shi, V. Adinolfi, R. Comin, M. Yuan, E. Alarousu, A. Buin, Y. Chen, S. Hoogland, A. Rothenberger, K. Katsiev, Y. Losovyj, X. Zhang, P. A. Dowben O. F. Mohammed, E. H. Sargent, O. M. Bakr, *Science* **2015,** *347*, 519.

[39] D. W. deQuilettes, S. M. Vorpahl, S. D. Stranks, H. Nagaoka, G. E. Eperon, M. E. Ziffer, H. J. Snaith, D. S. Ginger, *Science* **2015,** aaa5333.

[40] D. S. Ginger, N. C. Greenham, *Phys. Rev. B* **1999,** *59*, 10622.

[41] P. Docampo, J. M. Ball, M. Darwich, G. E. Eperon, H. J. Snaith, *Nat. commun* **2013,** *4*, 2761.

[42] M. Abdi-Jalebi, M. I. Dar, A. Sadhanala, S. P. Senanayak, F. Giordano, S. M. Zakeeruddin, M. Grätzel, R. H. Friend, *J. Phys. Chem. Lett.* **2016,** *7*, 3264.

[43] Y. Kim, Z. Yang, A. Jain, O. Voznyy, G.-H. Kim, M. Liu, L. N. Quan, F. p. García de Arquer, R. Comin, J. Z. Fan, E. H. Sargent, *Angew. Chem., Int. Ed.* **2016,** *55,* 9586.

[44] B.-W. Park, B. Philippe, X. Zhang, H. Rensmo, G. Boschloo, E. M. Johansson, *J. Adv. Mater.* **2015,** *27*, 6806.

[45] I. Turkevych, S. Kazaoui, E. Ito, T. Urano, K. Yamada, H. Tomiyasu, H. Yamagishi, M. Kondo, S. Aramaki, *ChemSusChem* **2017,** *10,* 1.

[46] C. N. Savory, A. Walsh, D. O. Scanlon, *ACS Energy Lett.* **2016,** *1*, 949.

[47] H .J. Snaith, A. Abate, J. M. Ball, G. E. Eperon, T. Leijtens, N. K. Noel, S. D. Stranks, J. T. W. Wang, K. Wojciechowski, W. Zhang, *J. Phys. Chem. Lett.* **2014,** *5*, 1511.

[48] E. L. Unger, E. T. Hoke, C. D. Bailie, W. H. Nguyen, A. R. Bowring, T. Heumüller, M. G. Christoforo, M. D. McGehee, *Energy Environ. Sci*. **2014,** *7*, 3690.

[49] H. S. Kim, N. G. Park, *J. Phys. Chem. Lett*. **2014,** *5*, 2927.

[50] R. S. Sanchez, V. Gonzalez-Pedro, J. W. Lee, N. G. Park, Y. S. Kang, I. Mora-Sero, J. Bisquert, *J. Phys. Chem. Lett.* **2014,** *5*, 2357.

[51] C. Eames, J. M. Frost, P. R. F. Barnes, B. C. O´Regan, A. Walsh, M. S. Islam, *Nat. Commun.* **2015**, 7497.

[52] A. Dualeh, T. Moehl, N. Tétreault, J. Teuscher, P. Gao, M. K. Nazeeruddin, M. Grӓtzel, *ACS Nano* **2013,** *8*, 362.

[53] C. Zhao, B. Chen, X. Qiao, L. Luan, K. Lu, B. Hu, *Adv. Energy Mater.* **2015**, *5*, 1500279.

[54] P. Tiwana, P. Docampo, M. B. Johnston, L. M. Herz, H. J. Snaith, *Energy Environ. Sci*. **2012,** *5*, 9566.

[55] L. Cabau, L. Pellejà, J. N. Clifford, C. V. Kumar, E. Palomares, *J. Mater. Chem. A*, **2013,** *1*(31), 8994.

[56] T. Kobayashi, H. Yamaguchi, T. Nakada, *Prog. Photovolt: Res. Appl.* **2014,** *22*, 115.

[57] L. Yang, B. Xu, D. Bi, H. Tian, G. Boschloo, L. Sun, E. M. Johansson, *J. Am. Chem. Soc.* **2013,** *135*, 7378.

[58] J. Kim, G. Kim, Y. Choi, J. Lee, S. Heum Park, K. Lee, *Appl. Phys.* **2012,** *111*, 114511.

[59] S. Trost, K. Zilberberg, A. Behrendt, A. Polywka, P. Görrn, P. Reckers, J. Maibach, T. Mayer, T. Riedl, *Adv. Energy Mater.* **2013,** *3*, 1437.

[60] T. Leijtens, G. E. Eperon, S. Pathak, A. Abate, M. M. Lee, H. J. Snaith *Nat. Commun.* **2013,** *4*, 2885.

[61] J. S. Manser, M. I Saidaminov, J. A. Christians, O. M. Bakr, P. V. Kamat, *Acc. Chem. Res.* **2016,** *49*, 330.

[62] J. H. Noh, S. H. Im, J. H. Heo, T. N. Mandal, S. I. Seok, *Nano Lett.* **2013,** *13*, 1764.

[63] L. M. Petrus, Y. Hu, D. Moia, P. Calado, A. Leguy, P. R. Barnes, P. Docampo, *ChemSusChem*, **2016,** *9*(18), 2699.

[64] F. Liu, Q. Dong, M. K. Wong, A. B. Djurišić, A. Ng, Z. Ren, A. M. C. Ng, *Adv. Energy Mater* **2016,** *6*, 1502206.

[65] Y. Hu, J. Schlipf, M. Wussler, M. L. Petrus, W. Jaegermann, T. Bein, P. Docampo, *ACS nano* **2016,** *10*(6), 5999.

[66] D. P McMeekin, G. Sadoughi, W. Rehman, G. E. Eperon, M. Saliba, M. T. Hörantner, A. Haghighirad, N. Sakai, L. Korte, B. Rech, M. B. Johnston, L. M. Herz, H. J. Snaith, *Science*, **2016,** *351*(6269), 151.

[67] J. Liu, Y. Wu, C. Qin, X. Yang, T. Yasuda, A. Islam, K. Zhang, W. Peng, W. Chen, L.Han, *Energy Environ. Sci.* **2014,** *7*, 2963.

6 Fully solution processed $Cs_2AgBiBr_6$ high quality films for planar heterojunction solar cells

This chapter is based on the following manuscript

Enrico Greul, Maximilian Sirtl, Pablo Docampo and Thomas Bein, *manuscript in preparation*

6.1 Introduction

During the last six years, hybrid organic-inorganic lead halide perovskites have been shown to be outstanding materials for applications in many different optoelectronic devices, such as lasers, light emitting diodes and solar cells.[1–4] In particular, hybrid lead halide based photovoltaics have achieved strikingly high power conversion efficiencies (PCE) of more than 22 %, being competitive with efficiencies achieved by conventional silicon based solar cells.[5] This high performance in combination with the high abundance of the raw materials and their facile, low temperature processability make hybrid lead halide based solar cells interesting candidates for replacing conventional photovoltaics. However, hybrid lead halide perovskites suffer from two major drawbacks, namely stability issues and the toxicity of lead, so far impeding large scale applications.[6–9] Accordingly, since the appearance of hybrid lead halide based solar cells, many research groups put much effort into the development of less toxic and/or more stable alternatives. As a result, state-of-the-art solar cells based on lead-free hybrid perovskites comprising the most obvious substitute tin, which is also a group-14 element such as lead, feature PCEs of more than 9 %.[10] However, the Sn^{2+} cation used as substitute for Pb^{2+} in hybrid metal halide perovskites drastically reduces the device stability due to the facile oxidation of Sn^{2+} to Sn^{4+}, even under common inert conditions.[11] This process leads to the formation of defect sites within the photoactive material, resulting in a rapid decrease of the performance of photovoltaics based on hybrid perovskites comprising Sn^{2+} cations.[11,12] Accordingly, several other cations including Ge^{2+}, Bi^{3+}, Sb^{3+} or Cu^{2+} have been investigated for their viability to perform in perovskite-related photovoltaic systems.[13–16] Among the alternatives to Pb^{2+}, Bi^{3+} is one of the most promising substitutes since it is highly stable and non-toxic. While Bi^{3+} features a higher charge than Pb^{2+}, often resulting in low-dimensional structures that make the optoelectronic properties of such compounds less favorable, Bi^{3+} can also be incorporated into a desirable three-dimensional structure by utilizing a monovalent co-cation.[17–20] A common class of 3D bismuth-based compounds are the elpasolites, which feature a highly symmetric cubic, so-called double perovskite structure with the general formula $A_2M^{1+}M^{3+}X_6$.[21] Although bismuth-containing elpasolites with A^+ = Rb, Cs, CH_3NH_3; M^{1+} = Na, K, Tl and X^- = F, Cl, Br have been investigated for several decades,[22–26] they have not been considered for photovoltaic applications due to their large band gap energy (E_g) of more than 3 eV.[22,27] The only compound exhibiting a E_g suitable for photovoltaics comprises thallium which is even more toxic than lead.[25] A great leap towards the practical application of bismuth-based elpasolites has been made in 2016, when several groups reported on a silver-bismuth based double perovskite with the formula $Cs_2AgBiBr_6$ featuring an E_g of about 2 eV, photoluminescence (PL) lifetimes of several hundred nanoseconds and calculated charge carrier effective masses close to those calculated for methylammonium lead iodide, making it a very interesting candidate for photovoltaic applications.[21,28–32] Corresponding studies indeed revealed that $Cs_2AgBiBr_6$ can be incorporated into solar cells featuring a mesoporous TiO_2 scaffold, resulting in encouraging PCEs close to 2.5 % with open-circuit voltages (V_{oc}) of more than one Volt, which are the highest V_{oc} values of all lead-free perovskite based photovoltaics with a comparable E_g.[33–36] However, the morphology of the double perovskite films utilized in those solar cells was poorly defined and therefore not suitable for applications in planar heterojunction devices without a mesoporous scaffold.[36] Considering that the film morphology has a strong impact on the device performance and that the E_g of $Cs_2AgBiBr_6$ is suitable for tandem solar cell applications, which require excellent film morphologies without the use of a supporting mesoporous metal oxide network, the formation of high quality double perovskite thin films is highly desirable.[37,38]

Recently, Wu *et al.* reported on planar heterojunction solar cells based on high quality $Cs_2AgBiBr_6$ films showing PCEs of up to 1.44 %.[39] However, the synthesis presented by Wu *et al.* is based on a low-pressure step, which creates the demand for additional equipment, such as a pump and a vacuum chamber, making the film synthesis more costly.

In order to simplify the preparation of such planar films, here we present a fully solution-based synthesis route for high quality $Cs_2AgBiBr_6$ films, which can be performed under ambient conditions. Our newly developed route is based on a two-step spin-coating process where *iso*-propyl ether is added as an antisolvent in the second step. This leads to the formation of $Cs_2AgBiBr_6$ films featuring an excellent morphology similar to that of already published films. Extensive optoelectronic studies revealed that high temperature annealing at 300 °C drastically improves the optoelectronic properties of the prepared films, leading to planar heterojunction solar cells exhibiting PCEs of about 1 %. Hence, we demonstrate for the first time the simple and fast synthesis of high quality $Cs_2AgBiBr_6$ films under ambient conditions, opening an avenue for further developing optoelectronic applications of double perovskite materials.

6.2 Results and Discussion

Our high quality $Cs_2AgBiBr_6$ films were prepared via spin-coating a DMSO-based precursor solution on the substrate with subsequent antisolvent addition. The films, which form almost immediately after the addition of the antisolvent, were annealed at 300 °C for 10 minutes after the spin-coating procedure. A schematic of the employed synthesis route is given in Figure 6-1.

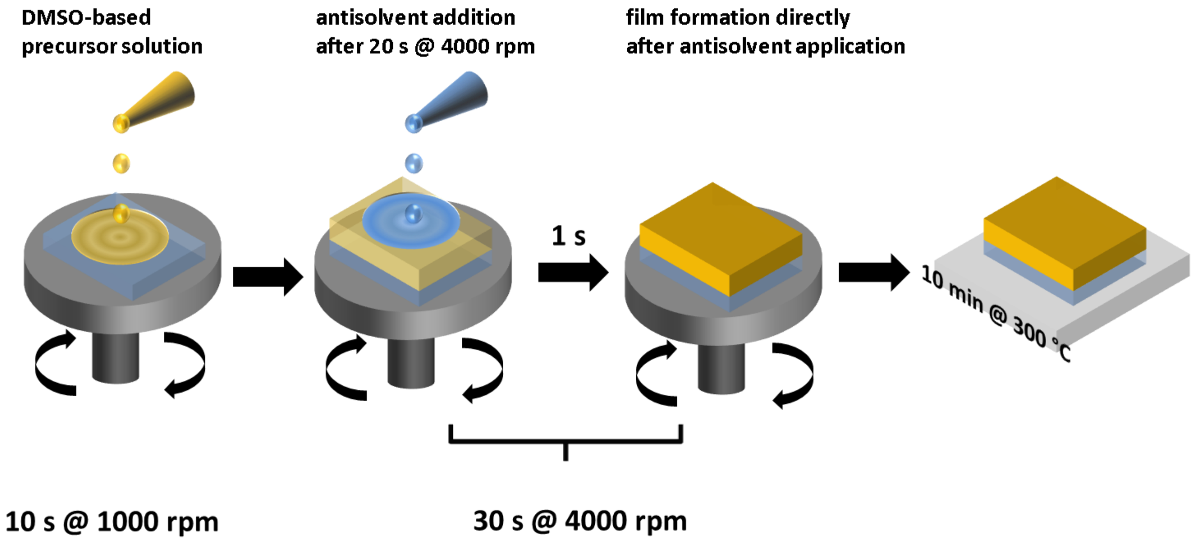

Figure 6-1: Schematic of the synthesis route utilized for the preparation of high quality $Cs_2AgBiBr_6$ films.

The synthesis protocol illustrated in Figure 6-1 is based on a common synthesis route for the preparation of highly efficient hybrid lead halide based photovoltaics featuring a slow and a fast spinning step.[40] The slow spinning step allows for a slow spread of the precursor solution all over the substrate, while the fast spinning step provides a rapid and homogeneous distribution of the antisolvent across the wet film, ensuring a uniform crystallization of the double perovskite. The duration of the spinning steps and the moments of precursor solution and antisolvent addition are depicted in the scheme given in Figure 6-2.

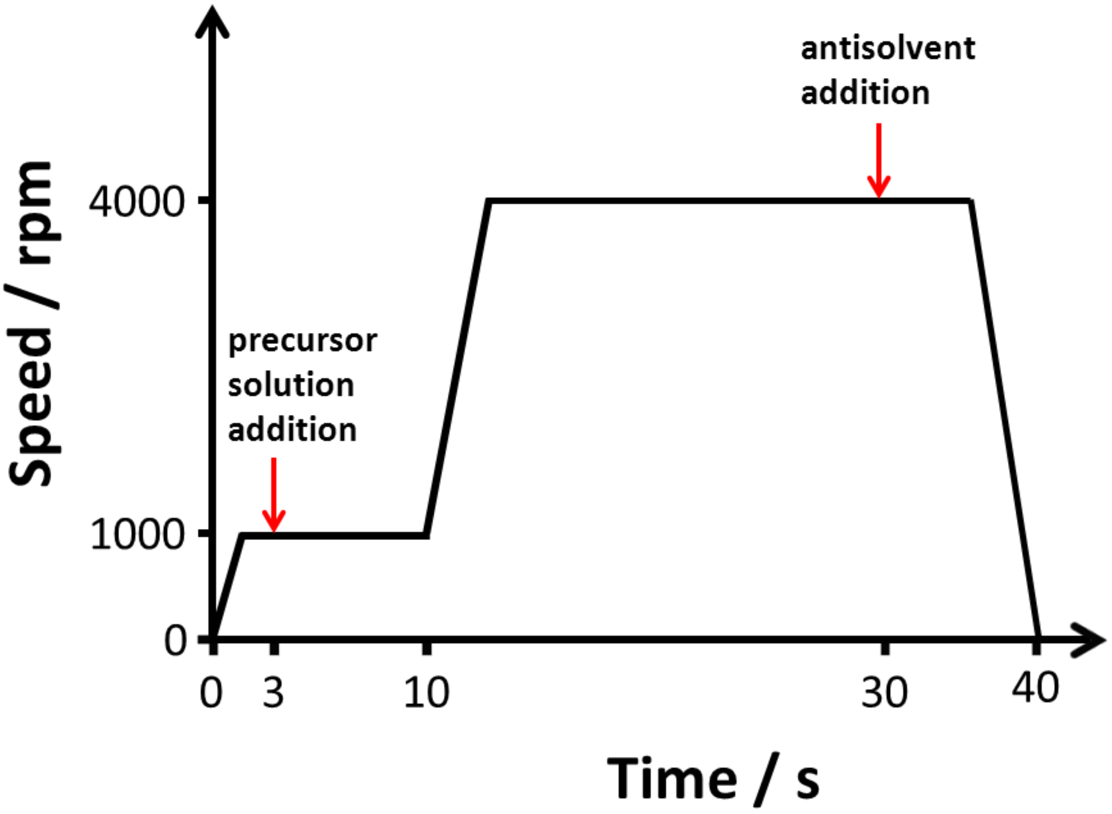

Figure 6-2: Graph of the utilized spinning protocol and the moments of precursor solution and antisolvent addition.

Previous studies have revealed that several different organic solvents, such as chlorobenzene, anisole or diethyl ether, are suitable antisolvents for the preparation of high quality hybrid lead halide films. Accordingly, a few of such solvents have been tested for their viability for the synthesis of homogeneous and pin-hole free $Cs_2AgBiBr_6$ thin films.[41–43] Here we compare the impact of different potential antisolvents on the resulting double perovskite film morphologies. Top-view scanning electron microscopy (SEM) images of the resulting films are shown in Figure 6-3. An SEM image of a double perovskite film made without any antisolvent addition is given for comparison (Figure 6-3a).

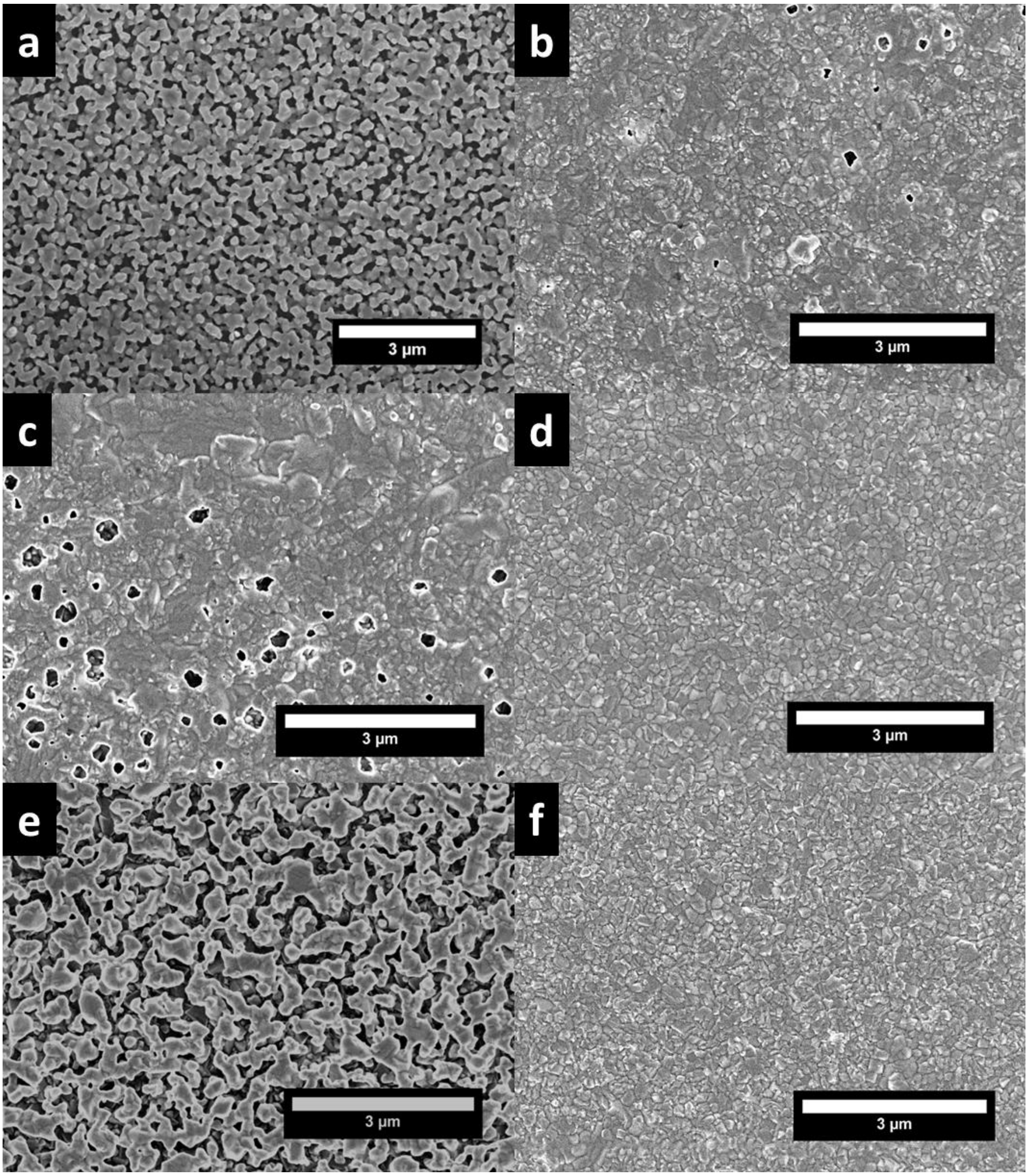

Figure 6-3: SEM top-view images of $Cs_2AgBiBr_6$ films prepared without antisolvent addition (a), and with addition of chlorobenzene (b), anisole (c), diethyl ether (d), n-propyl ether (e), or *iso*-propyl ether (f) serving as antisolvent. The deposition conditions are the same for each sample (see Figures 6-1 and 6-2).

The SEM images given in Figure 6-3a-d clearly show that the addition of an antisolvent significantly improves the film morphology. Among these samples, only the film where diethyl ether was used as antisolvent shows a perfectly pin-hole free $Cs_2AgBiBr_6$ layer, which is mandatory for well-performing devices. Despite the good results obtained by dripping diethyl ether on top of the wet double perovskite film, the relatively high vapor pressure of diethyl ether remains a critical issue. Due to the high vapor pressure of diethyl ether of about 560 hPa at 20 °C, the handling of the solvent with a pipet is rather difficult, leading to the premature release of the diethyl ether from the pipet which makes the preparation of homogeneously covered substrates more difficult, see Figure 6-4a.[44] Accordingly, alkyl ethers with lower vapor pressures were also tested. Thus, the two C3 analogs of diethyl ether, *n*-propyl and *iso*-propyl ether were utilized as antisolvents.[45,46] It turned out that the addition of *n*-propyl ether does not result in densely covered and pin-hole free double perovkite films, while dripping of *iso*-propyl ether leads to perfectly homogeneous and pin-hole free $Cs_2AgBiBr_6$ films, see Figure 6-3e & f. Our results, obtained with the different ethers, indicate that a high vapor pressure is beneficial for the resulting film morphology. On the other hand, the vapor pressure of the ether utilized as antisolvent should not be too high to ensure proper handling with the pipet. Accordingly, *iso*-propyl ether turned out to be an excellent antisolvent featuring a vapor pressure suitable for the reproducible preparation of high quality $Cs_2AgBiBr_6$ films, see Figure 6-4b.

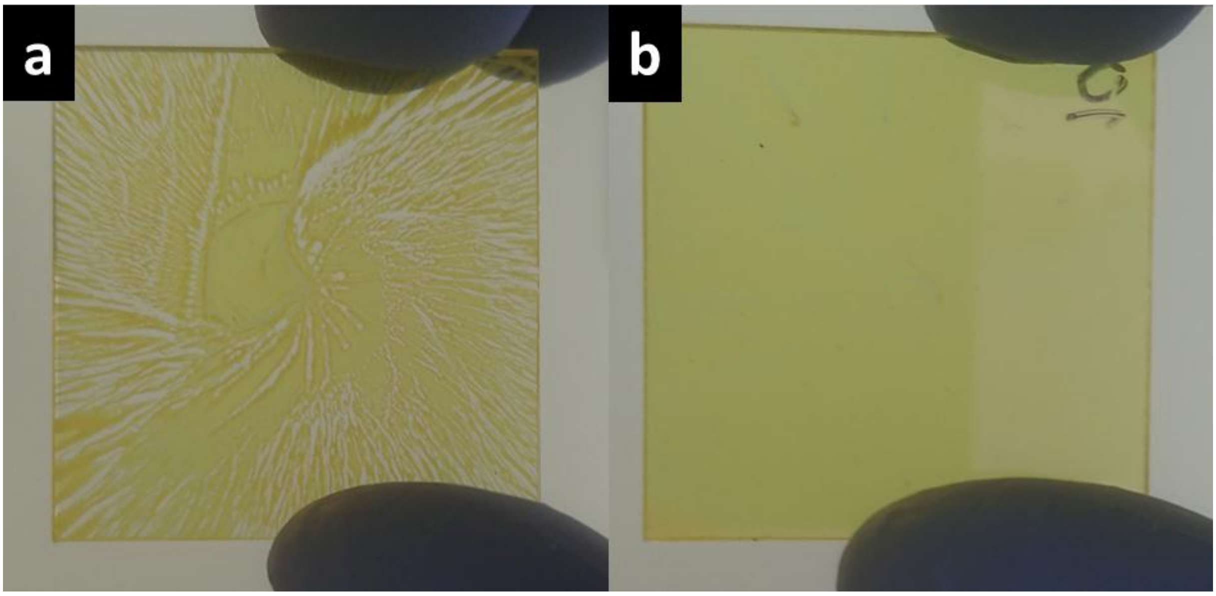

Figure 6-4: a) Image of a $Cs_2AgBiBr_6$ film made with diethyl ether antisolvent drip. b) Image of a $Cs_2AgBiBr_6$ film made with *iso*-propyl ether antisolvent drip.

Based on the above morphological investigations, the most promising antisolvent for the preparation of $Cs_2AgBiBr_6$ thin films suitable for the application in planar heterojunction photovoltaics appears to be *iso*-propyl ether. Thus, all following discussions refer to high quality $Cs_2AgBiBr_6$ films made by the addition of *iso*-propyl ether as an antisolvent.

Since our high quality $Cs_2AgBiBr_6$ films were developed for applications in planar heterojunction photovoltaics, the optoelectronic properties of the films also play an important role. The ultraviolet-visible (UV-vis) optical absorption spectrum is shown in Figure 6-5a.

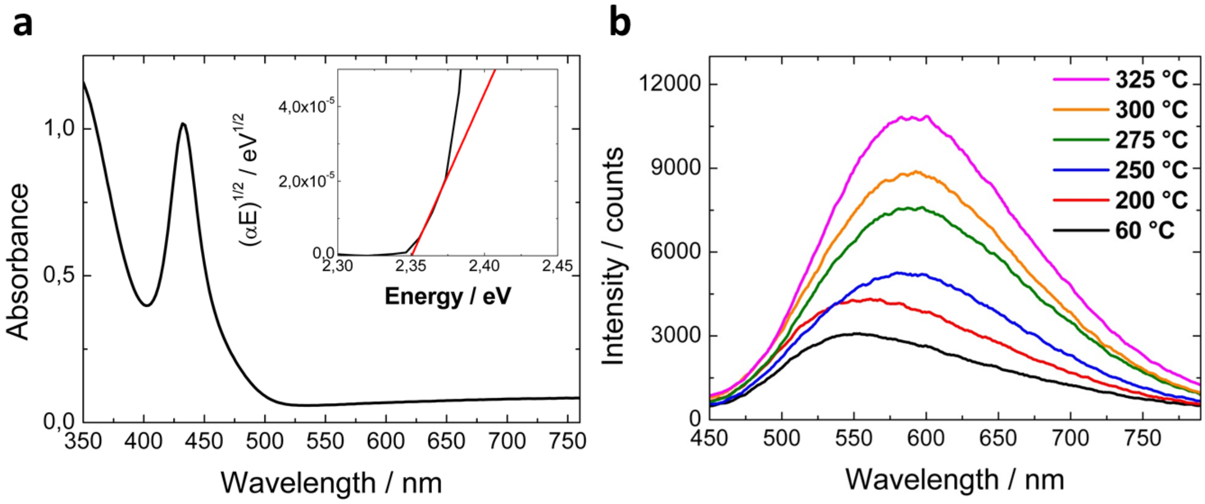

Figure 6-5: a) UV-vis spectrum of a $Cs_2AgBiBr_6$ film made by *iso*-propyl ether antisolvent drip. b) PL emission spectra of $Cs_2AgBiBr_6$ films annealed at different temperatures for 10 minutes each.

The spectrum given in Figure 6-5a shows an absorption onset at about 525 nm and a strong absorption feature with its maximum at about 440 nm, which is attributed to the formation of excitons.[39] The inset of Figure 6-5a shows a Tauc plot of the absorption spectrum given in Figure 6-5a. The E_g of 2.35 eV corresponds very well with the absorption onset at 525 nm visible in the absorption spectrum. The shape of the spectrum is very similar to that given by Wu *et al.*, who reported on planar heterojunction double perovskite solar cells featuring a maximum PCE of 1.44 %.[39] However, the overall absorbance is slightly lower than that presented by Wu *et al.*, which is most likely caused by the thickness of our prepared double perovskite films, which is about 30 % less than that presented by Wu *et al.*.[39] The estimated E_g of our double perovskite films is slightly larger than the values reported in the literature.[28,36] We attribute the larger E_g to the low film thickness which reduces the absorbance of the films, in particular in the long wavelength region (500 nm and more), making it more difficult to determine the exact E_g.[36]

Furthermore, the photoluminescence (PL) of the double perovskite films was examined. We find that the PL emission intensity strongly depends on the temperature at which the manufactured films were annealed after the spin-coating procedure, see Figure 6-5b. The spectra in Figure 6-5b clearly show that the PL emission intensity increases with increasing annealing temperature (in addition to a slight red shift of the emission maximum). A possible explanation could be the reduction of defect states within the double perovskite that act as quenching/recombination sites. This hypothesis is also supported by time-resolved single photon counting (TCSPC) measurements performed on $Cs_2AgBiBr_6$ films annealed at different temperatures. The obtained emission decays are given in Figure 6-6a.

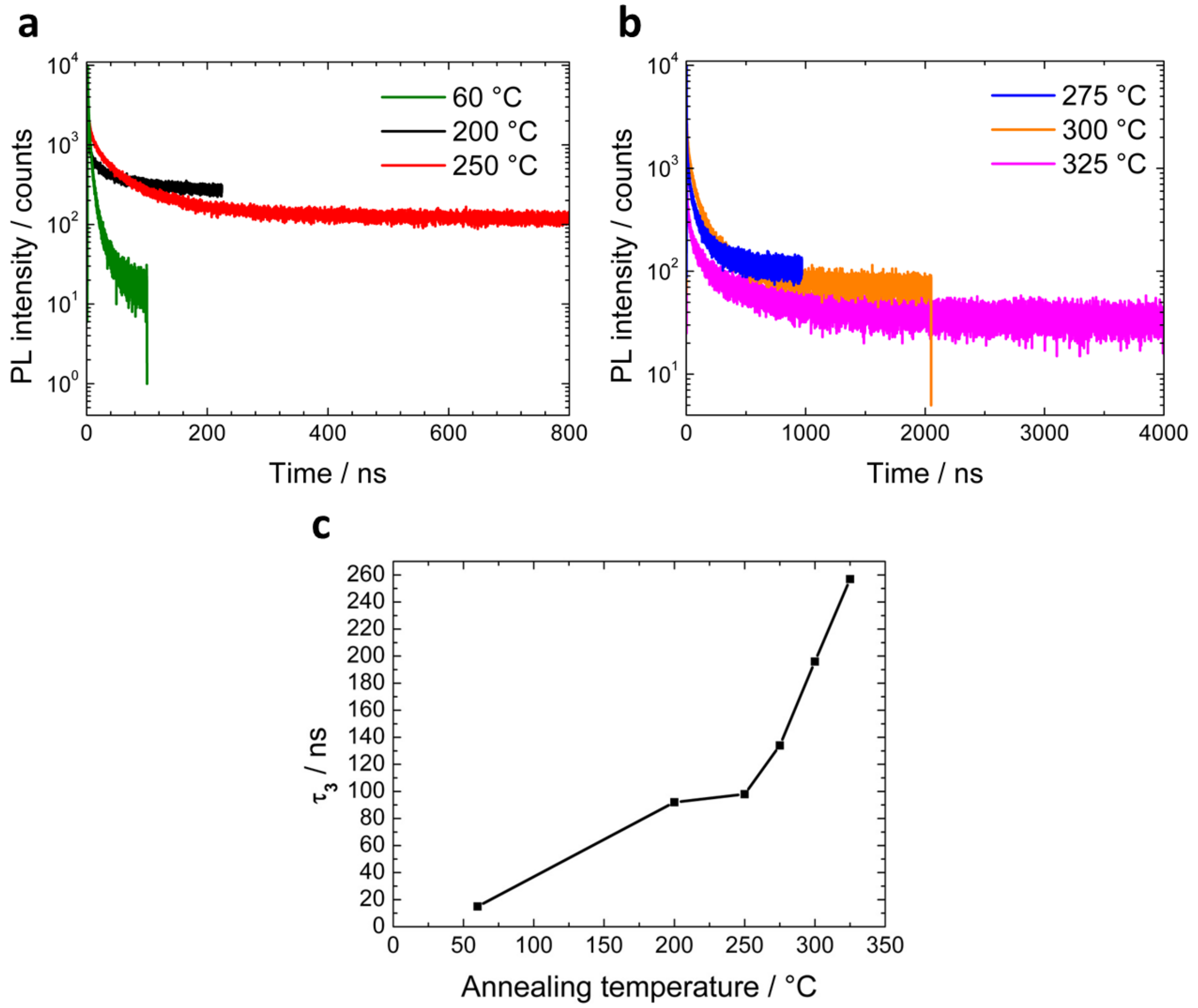

Figure 6-6: a) TCSPC decay curves of $Cs_2AgBiBr_6$ films annealed at 60 °C, 200 °C, 250 °C for ten minutes. b) TCSPC decay curves of $Cs_2AgBiBr_6$ films annealed at 275 °C, 300 °C or 325 °C for 10 minutes. b) Evolution of the lifetime (long-life component τ_3) of the photoexcited species with the annealing temperature.

The decay traces shown were fitted, as common in the literature, to a triexponential model curve to extract the specific lifetimes of the photoexcited species.[28,36] Since only the longest decay time τ_3 is assumed to represent the specific lifetime of the photoexcited species in $Cs_2AgBiBr_6$, τ_3 was used to show the evolution of the lifetimes with annealing temperature as depicted in Figure 6-6b.[28] We attribute the two short lifetime processes τ_1 and τ_2 to trap and/or surface state emission, while the long lifetime process is suggested to be the fundamental PL decay time of the material.[28] The lifetime of the photoexcited species features a dramatic increase with increasing annealing temperature, matching well with the development of the PL intensities given in Figure 6-5b. Considering that polycrystalline powders of $Cs_2AgBiBr_6$ grown from solution exhibit decay times τ_3 of more than 600 ns, the very low value for the 60 °C sample is most likely caused by the formation of a large number of defect states induced by the rapid crystallization of the $Cs_2AgBiBr_6$ film after antisolvent addition.[47] Accordingly, heating the films could lead to a decrease of defect states due to a rearrangement of the ions in the crystal lattice. In particular, heating to temperatures above 250 °C, which is in the temperature range used for the synthesis of $Cs_2AgBiBr_6$ via solid state reactions, should be suitable to remove defect states efficiently, as indicated by the corresponding strong increase of the lifetimes of the photoexcited species depicted in Figure 6-6b.[21] Complementary studies of the impact of annealing times on the lifetimes revealed a much less striking effect compared to that of the annealing temperatures, see Figure 6-7a & b.

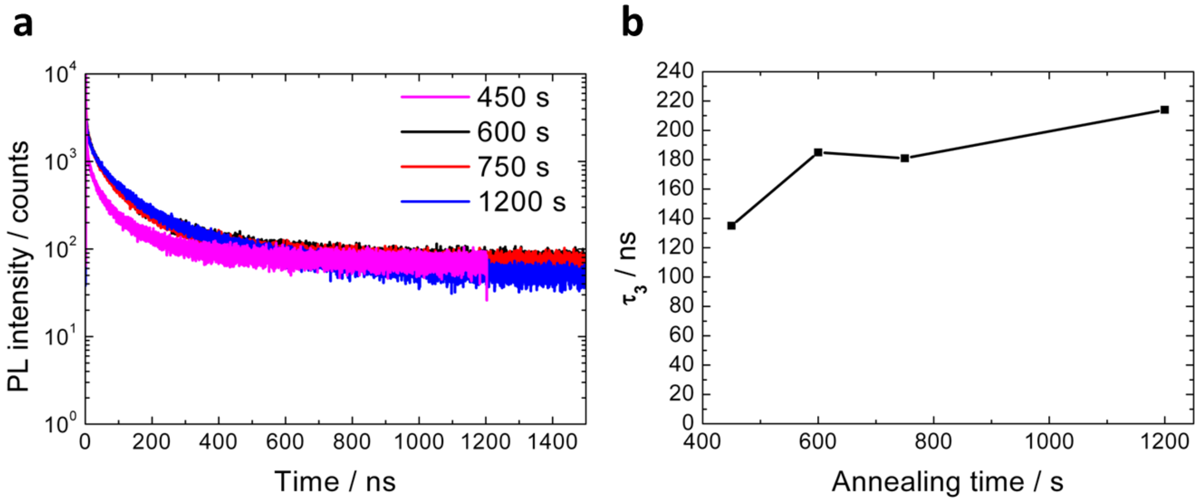

Figure 6-7: a) TCSPC decay curves of $Cs_2AgBiBr_6$ films annealed at 300 °C for 450 s, 600 s, 750 s, and 1200 s. b) Evolution of the lifetimes of the photoexcited species (long-life component τ_3) with the annealing time at 300 °C.

Nevertheless, the graph given in Figure 6-7b indicates that the double perovskite thin films should be annealed for at least 600 s to obtain long lifetimes of the photoexcited species of about 200 ns and higher, which hold promise for the design of efficient photovoltaic devices.

Since annealing temperatures above 250 °C are in the range or even higher than that used for the solid state synthesis of $Cs_2AgBiBr_6$, powder X-ray diffraction (PXRD) measurements were performed to investigate if the formation of side phases occurs. The powders for the PXRD measurements were obtained by scraping off Cs_2AgBiB_{r6} films that had been annealed at different temperatures, see Figure 6-8a.

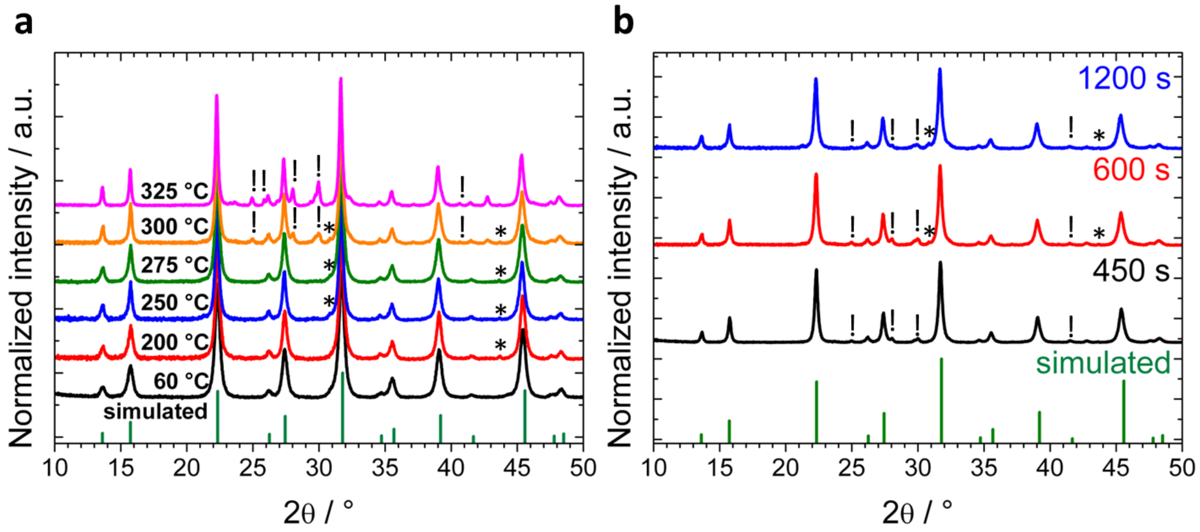

Figure 6-8: a) PXRD pattern of powders obtained from $C_{s2}AgBiBr_6$ films which were annealed at different temperatures for 600 s. b) PXRD pattern of powders obtained from $C_{s2}AgBiBr_6$ films which were annealed at 300 °C for 450 s, 600 s or 1200 s. The asterisks and exclamation marks indicate reflections attributed to side phases, where the asterisks represent AgBr and the exclamation marks represent Cs_2AgBr_3.

According to Figure 6-8a, side phase formation upon heating can be observed, where, depending on the annealing temperature, one or two different side phases, namely AgBr and Cs_2AgBr_3, are formed in small amounts. While AgBr vanishes with increasing temperature, which is consistent with previous studies,[36] the intensities of Cs_2AgBr_3 reflections increase with increasing annealing temperature. A possible explanation for the formation of Cs_2AgBr_3, which was predicted to form under non-optimized conditions,[48] could be the separation of $Cs_2AgBiBr_6$ into Cs_2AgBr_3 and $BiBr_3$ at elevated temperatures. Since the annealing temperatures are close or even above the melting point of $BiBr_3$, sublimation/evaporation of $BiBr_3$ could also occur, which would explain the absence of $BiBr_3$ reflections in the PXRD patterns.[49] However, these results appear to be inconsistent with previous reports on single crystals (sizes at the order of millimeters) which revealed that the double perovskite is thermally stable up to temperatures of more than 350 °C.[28] Our results suggest that $Cs_2AgBiBr_6$ crystals featuring small grain sizes of a few hundred nanometers (and associated large surface area) may be less thermally stable than crystals with sizes at the order of millimeters. Moreover, as the heating step was performed under ambient conditions also a degradation of the double perovskite due to reactions with water and/or oxygen, which are always present in ambient atmosphere, could be conceivable. We note that a degradation of the double perovskite films was not observed by Wu *et al.* although they perfomed the annealing step also under ambient conditions for the same time span we utilized, and although their films feature very similar crystallite sizes. This could be due to the different ways of measuring the PXRD pattern. While the present work shows PXRD pattern obtained from powders measured in transmission mode, Wu *et al.* shows XRD pattern of films measured in reflection mode. Since crystal orientation effects also play a role in the method used by Wu *et al.*, reflections of the measured compound are typically not represented with their correct intensity distribution. Furthermore, reflections that are clearly visible in a pattern obtained by PXRD measurements in transmission mode, can completely vanish when measured in reflection mode. Thus, the absence of side phases in the XRD pattern presented by Wu *et al.* does not necessarily mean that no such phases were present within the film. Additional PXRD measurements of $Cs_2AgBiBr_6$ powders obtained from films annealed for different time spans (see Figure 6-8b) revealed no significant variation in the pattern, which indicates that the annealing temperature is more critical for the film properties than the annealing time – this is consistent with the observations regarding the lifetimes of the photoexcited species given in Figures 6-6a & b and 6-7a & b.

To investigate the influence of the annealing temperature and the annealing time on the photovoltaic performance, our newly developed films were incorporated into planar heterojunction solar cells where the double perovskite layer is sandwiched between an electron transporting TiO_2 layer and a spiro-OMeTAD layer that acts as a hole transporter with a gold electrode on top. All layers were deposited on an FTO substrate. A schematic of the device and an SEM cross-section image of a fully assembled device are given in Figure 6-9a & b.

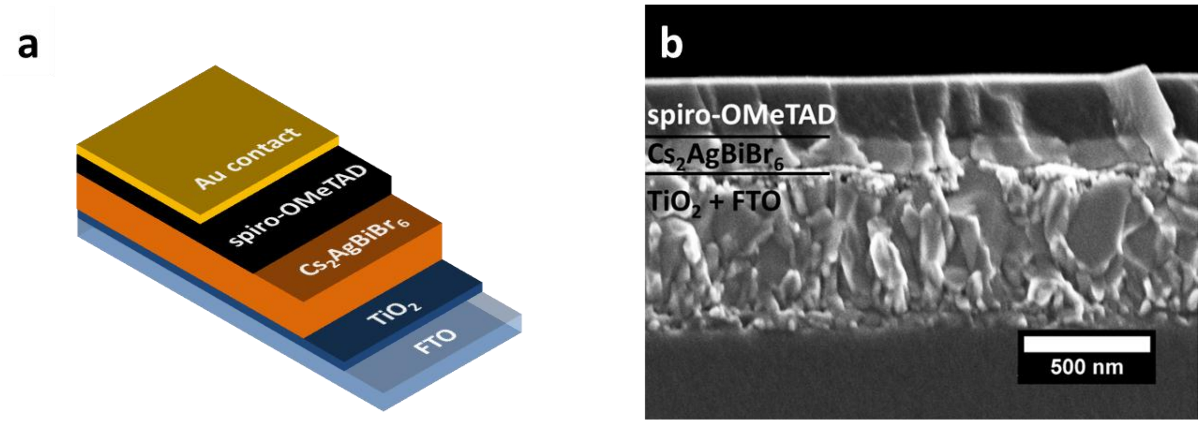

Figure 6-9: a) Schematic of an assembled planar heterojunction solar cell containing an active layer of $Cs_2AgBiBr_6$. b) SEM cross-section image of completely assembled solar cell.

The SEM cross-section image depicted in Figue 6-9b reveals that the photoactive $Cs_2AgBiBr_6$ layer is only about 100 nm thick, which is thinner than a typical lead halide perovskite based absorber layer.[50,51] As mentioned before, the absorbance of our double perovskite films is slightly lower than that presented by Wu *et al*. (see Figure 6-5a). Accordingly, a lower performance of the devices assembled with our double perovskite films is expectable due to the lower amount of absorbed photons. However, as the absorption properties of our double perovskite films are just slightly lower than that of the double perovskite films presented by Wu *et al*., working solar cells could b expected. In case of $Cs_2AgBiBr_6$, the thickness of the films is limited by the relatively low solubility of the double perovskite in the utilized solvent. Nevertheless, the absorber layer shows a very homogeneous thickness without any visible defects which is mandatory for efficient photovoltaic devices. Accordingly, we were able to obtain working solar cells comprising our newly developed films. At first, the influence of the annealing temperature on the device performance was investigated. Hence, statistics of 120 individual devices comprising $Cs_2AgBiBr_6$ films annealed at different temperatures are shown in Figure 6-10a-d.

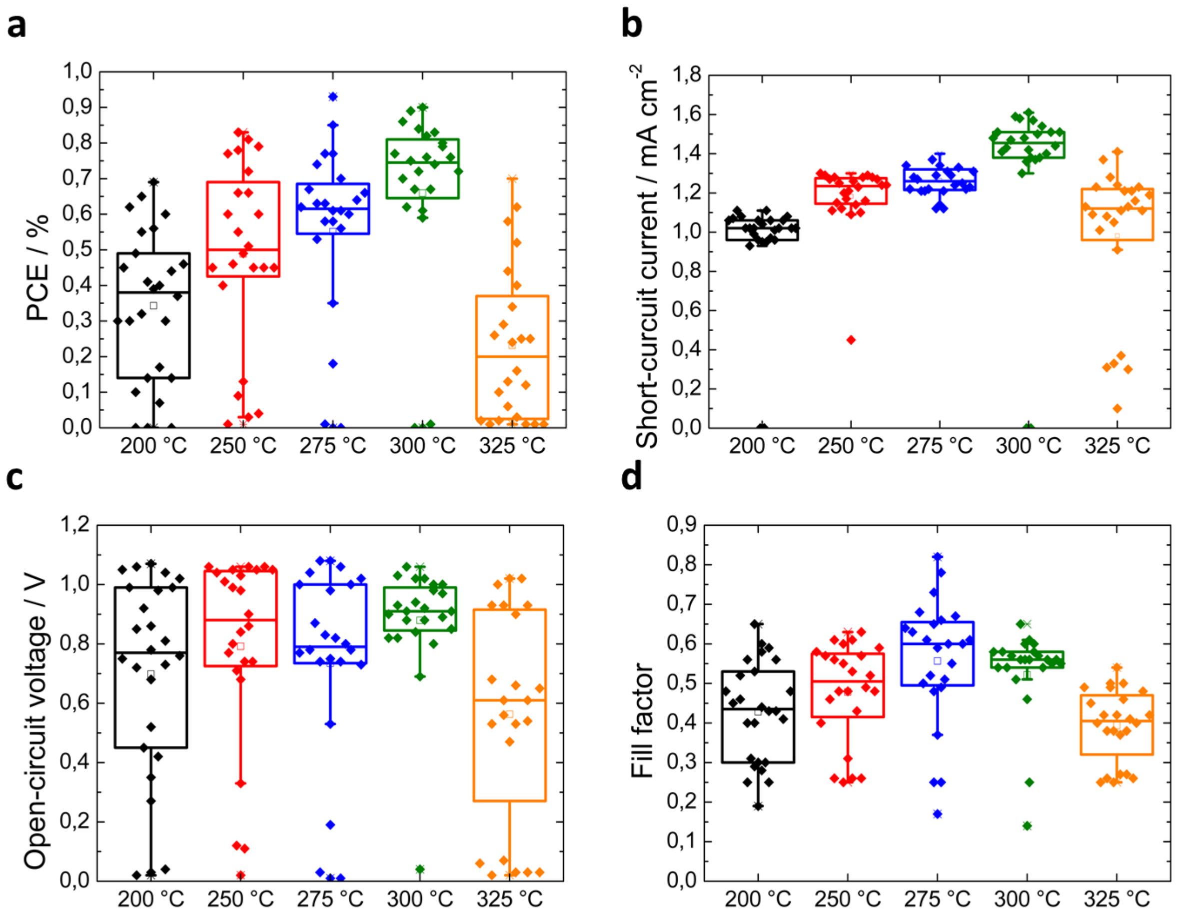

Figure 6-10: a) Device performance of solar cells assembled with $Cs_2AgBiBr_6$ films that were annealed for 10 minutes at different annealing temperatures as indicated; values obtained from 24 individual devices per temperature. b) Short-circuit current of solar cells assembled with $Cs_2AgBiBr_6$ films that were annealed for 10 minutes at different annealing temperatures as indicated; values obtained from 24 individual devices per temperature. c) Open-circuit voltage of solar cells assembled with $Cs_2AgBiBr_6$ films that were annealed for 10 minutes at different annealing temperatures as indicated; values obtained from 24 individual devices per temperature. d) Fill factor of solar cells assembled with $Cs_2AgBiBr_6$ films that were annealed for 10 minutes at different annealing temperatures as indicated; values obtained from 24 individual devices per temperature.

The values in Figure 6-10a clearly show that the device performance increases with increasing annealing temperature up to 300 °C. Regarding the characteristic values of the current-voltage (J-V) curves, the increase of the device performance is mainly attributed to an increase of the short-circuit current (J_{sc}), which points to an improved charge extraction from the double perovskite films. This matches well with the results regarding the PL intensity and the lifetimes of the photoexcited species discussed above. However, the performance of the solar cells comprising $Cs_2AgBiBr_6$ that were annealed at 325 °C seems to contradict the optoelectronic results because the films which were annealed at 325 °C show the longest decay times τ_3. As a long decay time is typically associated with well performing solar cells, the best working devices could be expected for the double perovskite films which were annealed at 325 °C. As indicated by the PXRD patterns shown in Figure 6-8, a small degree of degradation proceeds with increasing annealing temperature, suggesting that an annealing temperature of 300 °C represents an optimum. Furthermore, the $Cs_2AgBiBr_6$ films slowly start to delaminate off the substrate at 325 °C, leading to a loss of the light absorption properties (see Figure 6-11), which results in a decreased device performance as shown in Figure 6-10a-d.

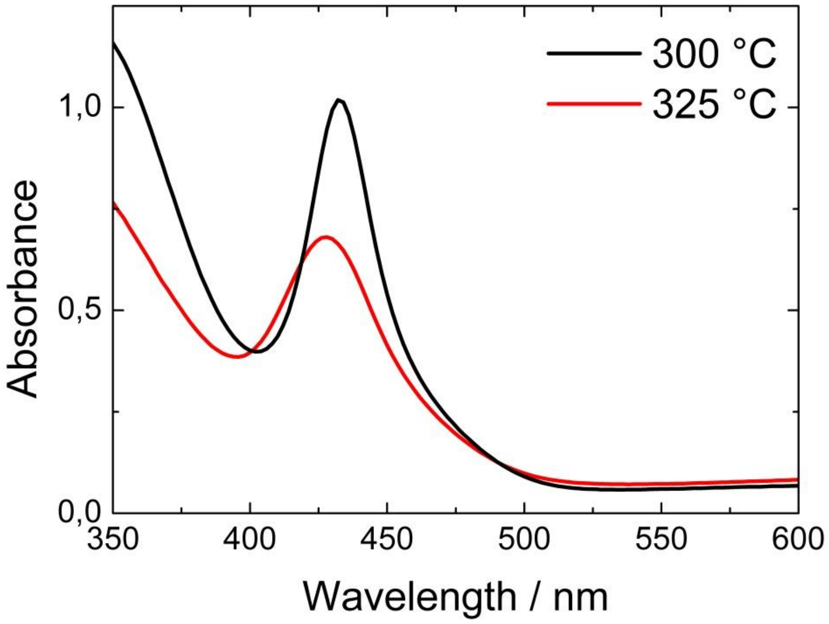

Figure 6-11: Absorbance spectra of $Cs_2AgBiBr_6$ films annealed at either 300 °C or 325 °C for 10 minutes. As the absorption charactersitics do not differ significantly for annealing tempartures up to 300 °C, the graph 300 °C represents also the films which were annealed at lower temperatures.

We note that solar cells comprising double perovskite films that appear phase pure according to the PXRD pattern in Figure 6-8a, do not show the best performance. This is most likely caused by the less optimal optoelectronic properties of these films. On the other hand, this indicates that possible negative effects on the device performance caused by the formation of side phases upon hot annealing can be, at least partially, compensated by the strongly improved optoelectronic properties induced by hot annealing.

In the next step, the influence of the annealing time on the performance of the solar cells was studied. Accordingly, the statistics of 120 individual devices comprising double perovskite films that were annealed at 300 °C for different time spans are given in Figure 6-12a-d.

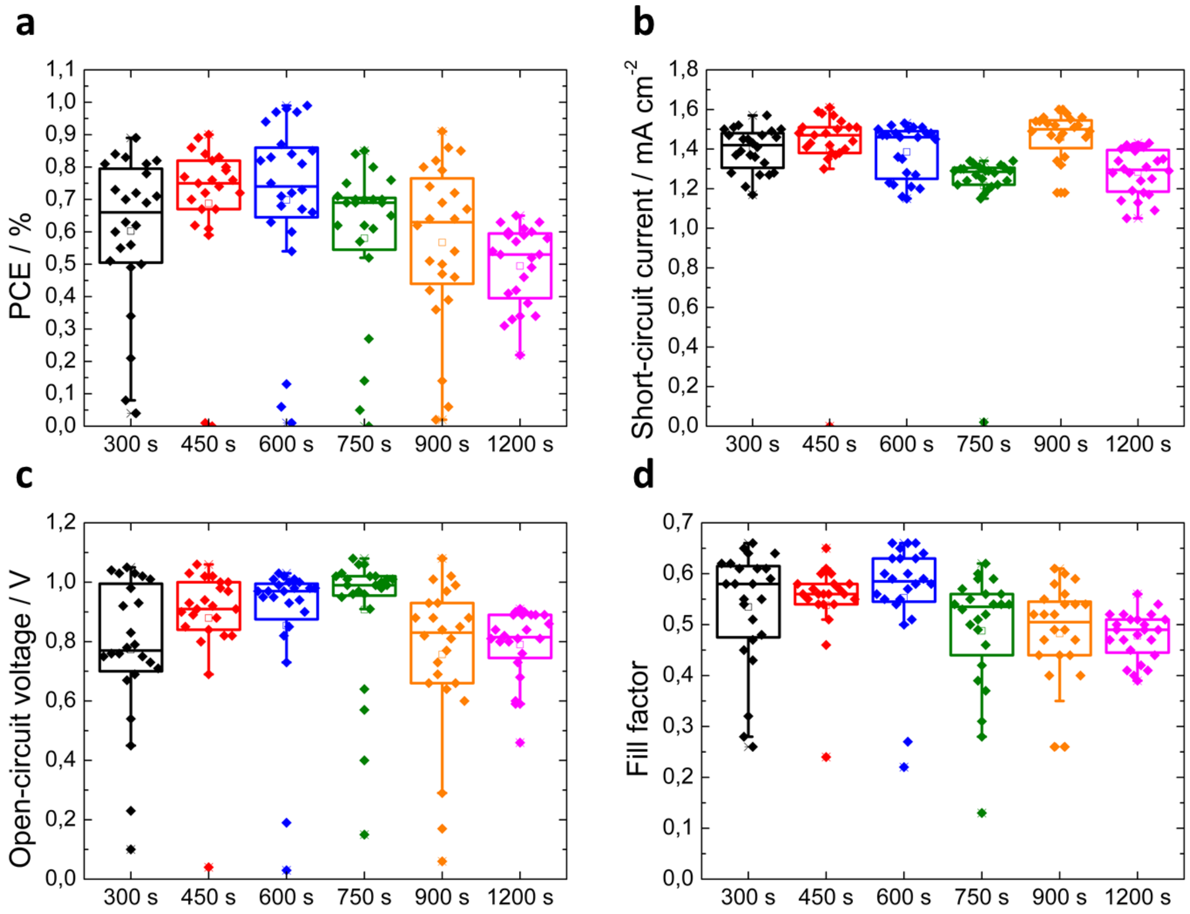

Figure 6-12: a) Device performance as a function of annealing time of solar cells assembled with $Cs_2AgBiBr_6$ films that were annealed at 300 °C, values obtained from 24 individual devices per temperature. b) Short-circuit current as a function of annealing time of solar cells assembled with $Cs_2AgBiBr_6$ films that were annealed at 300 °C, values obtained from 24 individual devices per temperature. c) Open-circuit voltage as a function of annealing time of solar cells assembled with $Cs_2AgBiBr_6$ films that were annealed at 300 °C, values obtained from 24 individual devices per temperature. d) Fill factor as a function of annealing time of solar cells assembled with $Cs_2AgBiBr_6$ films that were annealed at 300 °C, values obtained from 24 individual devices per temperature.

As already indicated by the lifetimes of the photoexcited species, the effect of the annealing time on the device performance is less pronounced than that of the annealing temperature. Nevertheless, there is an observable trend in device performance, in particular for annealing times longer than 600 s. The specific values obtained from the corresponding *J-V* curves show that the decrease of the PCEs at longer annealing times is not caused by a decrease of a specific device parameter. In particular, the J_{sc} of the measured devices is very similar for all tested annealing times, which again shows that the major impact on the device performance is given by the annealing temperature. However, annealing for at least 600 s seems to make the device performance more robust, leading to a slightly improved device performance. The decrease of the device performance at longer annealing times, which was not expected by the data obtained from the optoelectronic investigations, is most likely due to the slow disintegration of the double perovskite films over time, leading to a partial shunting of the devices and resulting in slightly decreased V_{oc}´s and fill factors (*FF*), see Figure 6-12c &d.[52]

According to the results obtained from the investigations of the annealing conditions, the optimized synthesis protocol featuring an annealing step at 300 °C for 10 minutes resulted in a champion solar cell exhibiting a PCE of about 1 % with a V_{oc} of more than one volt and a J_{sc} of about 1.5 mA/cm^2, see Figure 6-13.

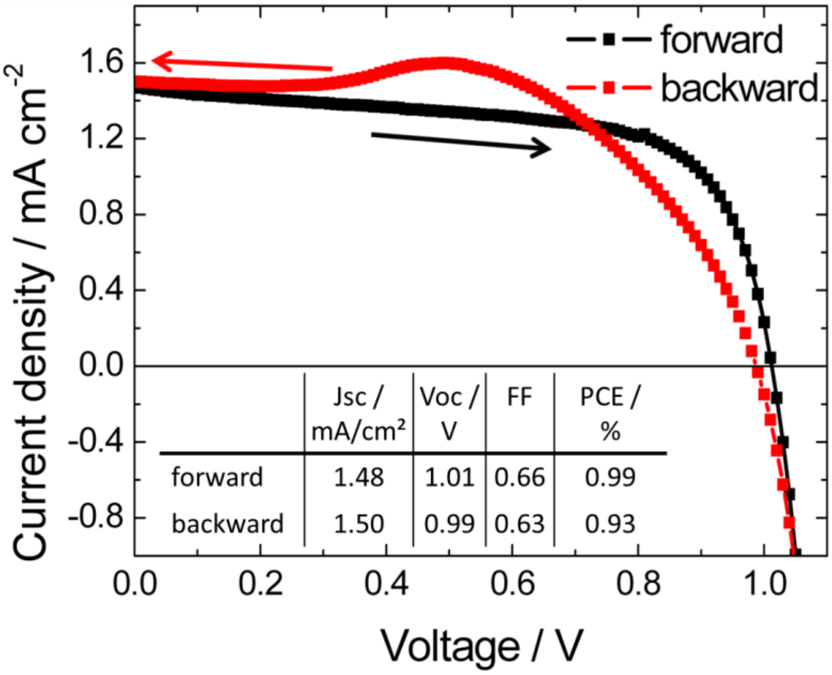

	Jsc / mA/cm²	Voc / V	FF	PCE / %
forward	1.48	1.01	0.66	0.99
backward	1.50	0.99	0.63	0.93

Figure 6-13: a) *J*-*V* curves of the forward and backward scan of the best performing device based on fully solution processed high quality $Cs_2AgBiBr_6$ films. The characteristic values for the different scan directions are given in the table underneath the *J*-*V* curves.

Similar to previously reported *J*-*V* curves of $Cs_2AgBiBr_6$ based photovoltaics, the *J*-*V* curves of devices presented in this work also show a relatively strong hysteresis.[36] Since hysteresis is a very common feature of lead halide perovskite based photovoltaics,[53–56] many studies, experimental and computational, on the origin of the hysteresis in metal halide perovskite solar cells have been published. They revealed that several effects such as ion migration and trapping/de-trapping of charge carriers are likely to contribute to the hysteresis.[53,57,58] According to the crystal structure of $Cs_2AgBiBr_6$, which is similar to that of lead halide perovskites, related effects causing the hysteresis in double perovskite based photovoltaics might be expected. However, since the characteristic photovoltaic parameters of the assembled devices, in particular J_{sc} and V_{oc}, are close to those reported by Wu *et al.*, our newly developed $Cs_2AgBiBr_6$ film processing methods constitute an attractive alternative approach for the generation of lead-free planar heterojunction perovskite solar cells.

6.3 Conclusions

We have demonstrated the preparation of high quality, fully solution processed $Cs_2AgBiBr_6$ films based on an antisolvent drip without the need for an additional low pressure step. The extensive investigation of many different organic solvents revealed that *iso*-propyl ether features physical properties making it an excellent antisolvent for the reproducible production of homogeneous and pin-hole free double perovskite films. Studies of the annealing conditions showed that the optoelectronic properties can be drastically enhanced with increasing annealing temperature, indicating the possibility to tune the optoelectronic properties of $Cs_2AgBiBr_6$ films after film formation. The manufactured high quality films were incorporated into planar heterojunction solar cells, resulting in a PCE of the best performing device of about one percent. Furthermore, the characteristic values of the solar cells presented in this work are close to previously published values obtained for solar cells comprising double perovskite films made with an additional low pressure step. Since our newly developed $Cs_2AgBiBr_6$ films were manufactured under ambient conditions without the need for any costly additional step, we believe that this work paves the way for the efficient preparation of environmentally friendly high quality double perovskite films for diverse optoelectronic applications.

6.4 Experimental section

All chemicals were used as received without any further purification. All synthesis and annealing steps were conducted under ambient conditions except the application of the hole transporting layer (HTL) which was performed in a nitrogen-filled glove box.

Substrate preparation

Fluorine-doped tin oxide (FTO)-coated glass sheets (7 Ωsq^{-1}, Pilkington, USA, 12 cm x 12 cm in size) were patterned by etching with zinc powder and 3 M HCl. They were subsequently cleaned with a 2% Hellmanex solution and rinsed with deionized water and ethanol. Afterwards the (FTO)-coated glass sheets were cut down to substrates of 3 cm x 3 cm in size. Directly before applying the blocking layer, remaining organic residues were removed by an oxygen plasma treatment for 5 min. A compact titanium dioxide (TiO_2) layer was deposited by spin-coating a sol-gel precursor solution at 2000 rpm for 45 s followed by subsequent annealing at 500 °C for 45 min. For preparing the sol-gel solution, a 27.2 mM (70 µL) solution of HCl in 2-propanol (5 mL) was added dropwise to a vigorously stirred 0.43 mM (735 µL) solution of titanium isopropoxide (99.999%, Sigma–Aldrich) in 2-propanol (5 mL).

Perovskite film preparation

The precursor solution was prepared by dissolving 224 mg $BiBr_3$ (0.5 mmol, ≥ 98%, Sigma Aldrich), 94 mg of AgBr (0.5 mmol, 99.5%, Alfa Aesar) and 212 mg CsBr (1.0 mmol, 99 %, Alfa Aesar) in dimethylsulfoxide (1 mL, DMSO, anhydrous, 99.9%, Sigma-Aldrich). The precursor solution was heated to about 150 °C to ensure complete dissolution of the precursors. Afterwards, the clear, yellow solution was allowed to cool down to room temperature. 100 µL of the precursor solution was spin-coated onto the TiO_2-covered substrate employing a two-step spinning procedure. In the first step, the substrate was spun with 1000 rpm for 10 s followed by a spinning step at 4000 rpm for 30 s. After approximately 3s after starting the spinning process, the precursor solution was added. The antisolvent was added 10 s before the end of the second, fast spinning step. The substrates were subsequently *annealed* at 300 °C for 10 min under ambient conditions by putting the substrates, which are coated with the double perovskite films, on a temperature-controlled hot plate placed in a fume hood to improve the optoelectronic properties of the prepared films. The temperature for this step was also varied to identify the optimal conditions.

Solar cell fabrication

After film formation, the films were covered with a HTL of 2,2',7,7'-tetrakis-(*N*,*N*-di-4-methoxyphenylamino)-9,9'-spirobifluorene (spiro-OMeTAD, Borun Chemicals, 99.5% purity). The HTL solution was prepared by dissolving 73 mg of spiro-OMeTAD in chlorobenzene (1 mL, 99.8%, Sigma–Aldrich). The solution was filtered and mixed with 4-*tert*-butylpyridine (10 µL, TBP, 96% Sigma Aldrich) and a 173 mg mL^{-1} bis(trifluoromethane)sulfonamide lithium salt (LiTFSI, 99.95%, Sigma–Aldrich) solution in acetonitrile (30 µL). This solution was spin-coated dynamically at 1500 rpm for 45 s. In a second step the sample rotation was accelerated to 2000 rpm for 5 s to allow the solvent to dry completely. Finally, 40 nm thick gold electrodes were thermally deposited under a high vacuum on top of the device.

Characterization

PXRD measurements were performed in transmission mode on a STOE Stadi MP diffractometer with a Cu Kα1 radiation source (λ = 1.54060 Å) operating at 40 kV and 40 mA. The diffractometer was equipped with a DECTRIS MYTHEN 1K solid-state strip detector. Scanning electron microscopy (SEM) images were acquired on a FEI Helios NanoLab G3 UC microscope. The sample was fixed by silver paste. For the optical characterization, precursor solutions were prepared similar to those used for the devices. Similar deposition conditions were also chosen. For UV-Vis, PL and TCSPC measurements the films were prepared on glass substrates. Steady-state absorption spectra were acquired with a Lambda 1050 UV-Vis spectrophotometer (Perkin Elmer) using an integrating sphere. Steady state and time resolved PL measurements were conducted with a Fluotime 300 Spectrofluorometer (Picoquant GmbH). The excitation wavelength was fixed at 405 nm. The emission for time-resolved measurements was monitored at 630 nm, being the wavelength of the maximum intensity of the steady state photoemission. *J-V* curves were recorded with a Keithley 2400 sourcemeter under simulated AM 1.5 sunlight, calibrated to 100 mW cm^{-2} with a Fraunhofer ISE certified silicon cell. The active area of the solar cells was defined with a square metal aperture mask of 0.0831 cm^2.

6.5 Literature

[1] H. Zhu, Y. Fu, F.Meng, X. Wu, Z. Gong, Q. Ding, M. V. Gustafsson, M. T. Trinh, S. Jin, X.-Y. Zhu, *Nat. Mater.* **2015,** *14*, 636.

[2] Z.-K. Tan, R. S. Moghaddam, M. L. Lai, P. Docampo, R. Higler, F. Deschler, M. Price, A. Sadhanala, L. M. Pazos, D. Credgington, F. Hanusch, T. Bein, H. J. Snaith, R. H. Friend, *Nat. Nanotechnol.* **2014,** *9*, 687.

[3] A. Kojima, K. Teshima, Y. Shirai, T. Miyasaka, *J. Am. Chem. Soc.* **2009,** *131*, 6050.

[4] J. M. Ball, M. M. Lee, A. Hey, H. J. Snaith, *Energy Environ. Sci.* **2013,** *6*, 1739.

[5] NREL chart, http://www.nrel.gov/ncpv/images/efficiency_chart.jpg, (accessed July 2017).

[6] Y.-Y Zhang, S. Chen, P. Xu, H. Xiang, X.-G. Gong, A. Walsh and S.-H. Wei, *arXiv:1506.01301*, **2015**.

[7] G. P. Nagabhushana, R. Shivaramaiah, A. Navrotsky, *Proc. Natl. Acad. Sci. U. S. A.* **2016,** *113*, 7717.

[8] N. Aristidou, I. Sanchez-Molina, T. Chotchuangchutchaval, M. Brown, L. Martinez, T. Rath, S. A. Haque, *Angew. Chem., Int. Ed.* **2015,** *54*, 8208.

[9] A. Babayigit, A. Ethirajan, M. Muller,B. Conings, *Nat. Mater.* **2016,** *15*, 247.

[10] S. Shao, J. Liu, G. Portale, H.-H. Fang, G. R. Blake, G. H. ten Brink, L. J. A. Koster, M. A. Loi, *Adv. Energy Mater.* **2018,** *8*, 1702019.

[11] F. Hao, C. C. Stoumpos, D. H. Cao, R. P. H. Chang and M. G. Kanatzidis, *Nat. Photonics* **2014,** *8*, 489.

[12] N. K. Noel, S. D. Stranks, A. Abate, C. Wehrenfennig, S. Guarnera, A. A. Haghighirad, A. Sadhanala, G. E. Eperon, S. K. Pathak, M. B. Johnston, A. Petrozza, L. M. Herz and H. J. Snaith, *Energy Environ. Sci.* **2014,** *7*, 3061.

[13] T. Krishnamoorthy, H. Ding, C. Yan, W. L. Leong, T. Baikie, L. Zhang, M. Sherburne, S. Li, M. Asta, N. Mathews, et al., *J. Mater. Chem. A* **2015,** *3*, 23829.

[14] B. Saparov, F. Hong, J. P. Sun, H. S. Duan, W. Meng, S. Cameron, I. G. Hill, Y. Yan, D. B. Mitzi, *Chem. Mater*. **2015,** *27*, 5622.

[15] X. P. Cui, K. J. Jiang, J. H. Huang, Q. Q. Zhang, M. J. Su, L. M. Yang, Y. L. Song, X. Q. Zhou, *Synth. Met*. **2015,** *209*, 247.

[16] M. Lyu, J. H. Yun, M. Cai, Y. Jiao, P. V. Bernhardt, M. Zhang, Q. Wang, A. Du, H. Wang, G. Liu, L. Wang, *Nano Res.* **2016,** *9*, 692.

[17] R. Jakubas, J. Zaleski, L. Sobczyk, *Ferroelectrics* **1990,** *108*, 109.

[18] S. Sun, S. Tominaka, J-H. Lee, F. Xie, P. D. Bristowe, A. K. Cheetham, *APL Mater*. **2016,** *4*, 031101.

[19] B. Chabot, E. Parthé, *Acta Cryst.* **1978,** *B34*, 645.

[20] A. J. Lehner, D. H. Fabini, H. A. Evans, C. A. Hébert, S. R. Smock, J. Hu, H. Wang, J. W. Zwanziger, M. I. Chabinyc, R. Seshadri, R. *Chem. Mater*. **2015,** 27, 7137.

[21] E. T. McClure, M. R. Ball, W. Windl, P. M. Woodward, *Chem. Mater*. 2016, **28,** 1348.

[22] L. R. Morrs, W. R. Robinson, *Acta Crystallogr., Sect. B: Struct. Crystallogr. Cryst. Chem.* **1972,** *28*, 653.

[23] F. Pelle, B. Jacquier, J. Denis, B. J. Blanzat, *Lumin*. **1978,** *17*, 61.

[24] W. Smit, G. Dirksen, D. Stufkens, *J. Phys. Chem. Solids.* **1990**, *51*, 189.

[25] Z. Deng, F. Wei, S. Sun, G. Kieslich, A. K. Cheetham, P. D. Bristowe, *J. Mater. Chem. A* **2016,** *4*, 12025.

[26] A. Tressaud, S. Khaïroun, J. P. Chaminade, M. Couzi, *Phys. Status Solidi A* **1986,** *98*, 417.

[27] F. Wei, Z. Deng, S. Sun, F. Xie, G. Kieslich, D.M. Evans, M. A. Carpenter, P. D. Bristowe, A. K. Cheetham, *Mater. Horiz*. **2016,** *3*, 328.

[28] A. H. Slavney, T. Hu, A. M. Lindenberg, H. I. Karunadasa, *J. Am. Chem. Soc.* **2016,** *138*, 2138.

[29] G. Volonakis, M. R. Filip, A. A. Haghighirad, N. Sakai, B. Wenger, H. J. Snaith, F. Giustino, *J. Phys. Chem. Lett.* **2016,** *7*, 1254.

[30] F. Wei, Z. Deng, S. Sun, F. Zhang, D. M. Evans, K. Kieslich, S. Tominaka, M. A. Carpenter, J. Zhang, P. D. Bristowe, A. K. Cheetham, *Chem. Mat*. **2017,** *29*, 1089.

[31] M. R. Filip, S. Hillman, A. A. Haghighirad, H. J. Snaith, F. Giustino, *J. Phys.Chem.Lett*. **2016,** *7*, 2579.

[32] M. R. Filip, C. Verdi, F. Giustino, *J. Phys. Chem. C* **2015,** *119*, 25209.

[33] Y. Kim, Z. Yang, A. Jain, O. Voznyy, G.-H. Kim, M. Liu, L. N. Quan, F. p. García de Arquer, R. Comin, J. Z. Fan, E. H. Sargent, *Angew. Chem., Int. Ed.* **2016,** *55*, 9586.

[34] B.-W. Park, B. Philippe, X. Zhang, H. Rensmo, G. Boschloo, E. M. Johansson, *J. Adv. Mater.* **2015,** *27*, 6806.

[35] I. Turkevych, S. Kazaoui, E. Ito, T. Urano, K. Yamada, H. Tomiyasu, H. Yamagishi, M. Kondo, S. Aramaki, *ChemSusChem* **2017,** *10,* 1–7.

[36] E. Greul, M. L. Petrus, A. Binek, P. Docampo, T. Bein, *J. Mater. Chem. A* **2017,** *5*, 19972.

[37] R. Sheng, A. W. Y. Ho-Baillie, S. Huang, M. Keevers, X. Hao, L. Jiang, Y.-B Cheng, and M. A. Green, *J. Phys. Chem. Lett.*, **2015,** *6*, 3931.

[38] T. B. Song, Q. Chen, Zhou, C. Jiang, H. H. Wang, Y. M. Yang, Y. Liu, J. You, Y. Yang, *J. Mater. Chem. A* **2015,** *3*, 9032.

[39] C. Wu, Q. Zhang, Y. Liu, W. Luo, X. Guo, Z. Huang, H. Ting, W. Sun, X. Zhong, S. Wei, S. Wang, Z. Chen, L. Xiao, *Adv. Sci.* **2018,** 5, 1700759.

[40] M. L. Petrus, Y. Hu, D. Moia, P. Calado, A. M. A. Leguy, P. R. F. Barnes, P. Docampo, *ChemSusChem* **2016**, *9*, 2699.

[41] M. Xiao, F. Huang, W. Huang, Y. Dkhissi, Y. Zhu, J. Etheridge, A. Gray-Weale, U. Bach, Y.-B. Cheng, L. Spiccia, *Angew. Chem.***2014,** *126*, 10056.

[42] L.-Y. Wang, L.-L. Deng, X. Wang, T. Wang, H.-R. Liu, S-M. Dai, Z. Xing, S.-Y. Xie, R.-B. Huang, L.-S. Zheng, *Nanoscale* **2017,** *9*, 17893.

[43] N. Ahn, D.-Y. Son, I.-H. Jang, S. M. Kang, M. Choi, N.-G. Park, *J. Am. Chem. Soc.* **2015,** *137*, 8696.

[44] Diethyl ether; MSDS Version 5.6 [online]; Sigma-Aldrich, Steinheim, Germany, September 27, 2017. https://www.sigmaaldrich.com/MSDS/MSDS/DisplayMSDSPage.do?country=DE&language=EN-generic&productNumber=296082&brand=SIAL&PageToGoToURL=https%3A%2F%2Fwww.sigmaaldrich.com%2Fcatalog%2Fsearch%3Fterm%3Ddiethyl%2Bether%26interface%3DAll%26N%3D0%26mode%3Dmatch%2520partialmax%26lang%3Dde%26region%3DDE%26focus%3Dproduct (accessed April 11, 2018).

[45] Dipropyl ether; MSDS Version 5.2 [online]; Sigma-Aldrich, Steinheim, Germany, April 04, 2017. https://www.sigmaaldrich.com/MSDS/MSDS/DisplayMSDSPage.do?country=DE&language=EN-generic&productNumber=111333&brand=ALDRICH&PageToGoToURL=https%3A%2F%2Fwww.sigmaaldrich.com%2Fcatalog%2Fproduct%2Faldrich%2F111333%3Flang%3Dde (accessed April 15, 2018).

[46] Diisopropyl ether; MSDS Version 7.2 [online]; Sigma-Aldrich, Steinheim, Germany, September 29, 2017. https://www.sigmaaldrich.com/MSDS/MSDS/DisplayMSDSPage.do?country=DE&language=EN-generic&productNumber=296856&brand=SIAL&PageToGoToURL=https%3A%2F%2Fwww.sigmaaldrich.com%2Fcatalog%2Fproduct%2Fsial%2F296856%3Flang%3Dde (accessed April 15, 2018).

[47] D. W. deQuilettes, S. M. Vorpahl, S. D. Stranks, H. Nagaoka, G. E. Eperon, M. E. Ziffer, H. J. Snaith, D. S. Ginger, *Science* **2015,** aaa5333.

[48] Z. Xiao, W. Meng, J. Wang,Y. Yan, *ChemSusChem* **2016,** *9*, 2628.

[49] Bismuth(III) bromide; MSDS Version 5.0 [online]; Sigma-Aldrich, Steinheim, Germany, October 12, 2012. https://www.sigmaaldrich.com/MSDS/MSDS/DisplayMSDSPage.do?country=DE&language=EN-generic&productNumber=401072&brand=ALDRICH&PageToGoToURL=https%3A%2F%2Fwww.sigmaaldrich.com%2Fcatalog%2Fproduct%2Faldrich%2F401072%3Flang%3Dde (accessed 16, 2018).

[50] Z. Song, S. C. Watthage, A. B. Phillips, M. J. Heben, *J. of Photonics for Energy* **2016,** *6*(2), 022001.

[51] H. Zhang, M. Tao, B. Gao, W. Chen, Q. Li, Q. Xu, S. Dong, *Sci. Rep.* **2017,** *7*, 8458.

[52] A. R.Jeong, S. B.Choi, W. M. Kim, J.-K. Park, J. Choi, I. Kim, J.-h. Jeong, *Sci. Rep.* **2017,** *7*, 15723.

[53] H .J. Snaith, A. Abate, J. M. Ball, G. E. Eperon, T. Leijtens, N. K. Noel, S. D. Stranks, J. T. W. Wang, K. Wojciechowski, W. Zhang, *J. Phys. Chem. Lett.* **2014,** *5*, 1511.

[54] E. L. Unger, E. T. Hoke, C. D. Bailie, W. H. Nguyen, A. R. Bowring, T. Heumüller, M. G. Christoforo, M. D. McGehee, *Energy Environ. Sci*. **2014,** *7*, 3690.

[55] H. S. Kim, N. G. Park, *J. Phys. Chem. Lett*. **2014,** *5*, 2927.

[56] R. S. Sanchez, V. Gonzalez-Pedro, J. W. Lee, N. G. Park, Y. S. Kang, I. Mora-Sero, J. Bisquert, *J. Phys. Chem. Lett.* **2014,** *5*, 2357.

[57] C. Eames, J. M. Frost, P. R. F. Barnes, B. C. O´Regan, A. Walsh, M. S. Islam, *Nat. Commun.* **2015,** 7497.

[58] A. Dualeh, T. Moehl, N. Tétreault, J. Teuscher, P. Gao, M. K. Nazeeruddin, M. Grätzel, *ACS Nano* **2013**, *8*, 362.

7 Conclusions

This thesis focused on the investigation and processing of lead-free perovskite related materials for applications in optoelectronic devices. In the first part, the tin based hybrid perovskites $(BuA)_2SnI_4$ and $(PEA)_2SnI_4$ comprising the large ammonium cations BuA and PEA were investigated for their viability to perform in optoelectronics and for their moisture stability. It turned out that the investigated compounds feature optoelectronic properties that are different from their lead-based counterparts, making them suitable for applications as top cell in a tandem solar cell assembly and in light emitting devices such as LEDs. Moisture stability studies revealed that ammonium cations featuring large hydrophobic cations can strongly enhance the stability of tin-based perovskites, similar to their lead-based counterparts. However, in contrast to their lead-based relatives, the choice of the organic residue of the ammonium cation in order to improve the moisture stability is much more critical for the tin containing compounds.

Besides the toxicity of the lead-based perovskite, the toxicity of the solvents utilized for the preparation of perovskite thin films was also addressed. Accordingly, a mixture of two new solvents, namely MeOH and 1-4-dioxane, which are less hazardous than the commonly utilized solvents DMF and DMSO, was employed for the formation of lead-free $MASnI_3$ films. The ratio of the two solvents in the mixture was shown to be essential to enhance the solubility of SnI_2 without simultaneously precipitating the perovskite. Films prepared from solutions comprising the optimal solvent ratio feature an excellent morphology with a surface coverage of 100 %. Solar cells assembled with films made by the newly developed route outperformed devices made by conventional one step deposition routes based on DMF or DMSO precursor solution, which can mainly be attributed to the high quality of the films prepared by the less hazardous route.

Due to the high sensitivity of tin(II) halide-based hybrid perovskites towards oxidation, an alternative stable lead-free material, which features a double perovskite structure with the composition $Cs_2AgBiBr_6$, was investigated for its viability to perform in optoelectronic devices. Accordingly, a synthesis route for the deposition of double perovskite films via the spin-coating method was developed. Considering the low solubility of $Cs_2AgBiBr_6$, it was shown that the optical absorption properties of the prepared films, which are important for efficient light harvesting of the resulting solar cells, can be enhanced by preheating the substrate and the precursor solution prior the spin-coating. Furthermore, it turned out that hot annealing at temperatures higher than 250 °C was necessary to obtain phase-pure $Cs_2AgBiBr_6$ films. The viability of $Cs_2AgBiBr_6$ for optoelectronic applications was demonstrated by incorporating the double perovskite films into photovoltaic devices. Devices comprising $Cs_2AgBiBr_6$ films made by the optimized synthesis protocol exhibited encouraging power conversion efficiencies close to 2.5 % with a high open-circuit voltage of more than 1 V, which is so far the highest voltage obtained with a lead-free perovskite-based solar cell. Furthermore, stability tests revealed an excellent stability of the assembled devices under working conditions, even surpassing the stability of lead halide perovskite-based photovoltaics.

Since the performance of a photovoltaic device strongly depends on the quality of the photoactive layer, a new route for the synthesis of high quality $Cs_2AgBiBr_6$ films based on the addition of an antisolvent to precipitate the double perovskite crystals was developed. Extensive studies with many different organic solvents revealed that *iso*-propyl ether is a proper antisolvent for the preparation of smooth, homogeneous and pin-hole free double perovskite thin films. We showed that trap states being introduced by the rapid film formation can be efficiently removed by hot annealing at 300 °C, leading to drastically increased lifetimes of the photo-excited species within the double perovskite film. Accordingly, films that were integrated in planar heterojunction solar cells showed an increase of the performance with increasing annealing temperature, resulting in promising power conversion efficiencies of about one percent.

In view of the still relatively low performance of lead-free perovskite based photovoltaics compared to their lead-based counterparts, there is still much research needed to make the efficiencies of lead-free perovskite-based solar cells competitive with commonly used devices such as silicon-based technologies. However, considering that the investigation of lead-free perovskites for photovoltaic applications is just at the very beginning and regarding the rapid development of lead halide-based solar cells during the last six years, which resulted in perovskite-based solar cells with efficiencies similar to silicon solar cells, a significant improvement of lead-free perovskite based photovoltaics can be expected in the near future.

8 Publications and Presentations

8.1 Journals

1. “Synthesis of hybrid tin halide perovskite solar cells with less hazardous solvents: methanol and 1,4-dioxane”

   E. Greul, P. Docampo, T. Bein, *Zeitschrift für anorganische und allgemeine Chemie* **2017,** *643*, 1704–1711.

2. “Highly stable, phase pure $Cs_2AgBiBr_6$ double perovskite thin films for optoelectronic applications”

   E. Greul, M. L. Petrus, A. Binek, P. Docampo, T. Bein, *Journal of Materials Chemistry A* **2017,** *5*, 19972–19981.

3. “Fully solution processed $Cs_2AgBiBr_2$ high quality films for photovoltaic applications”

   E. Greul, M. Sirtl, M. L. Petrus, P. Docampo, Thomas Bein, *manuscript in preparation*

8.2 Poster presentations

1. “Influence of the organic cation on the properties of hybrid organic inorganic perovskites”

   Enrico Greul, Pablo Docampo, Thomas Bein

   International Conference Solution Processed Semiconductor Solar Cells (SSSC), 2014, Oxford, United Kingdom.

2. “Influence of the organic cation on the properties of hybrid organic inorganic perovskites”

   Enrico Greul, Pablo Docampo, Thomas Bein

Soltech Workshop, **2015**, Kloster Banz, Germany.

3. “Homogeneous thin films of tin based hybrid organic inorganic perovskites”

   Enrico Greul, Pablo Docampo Thomas Bein

   Soltech Workshop, **2016**, Munich, Germany.

4. “Highly stable, phase pure $Cs_2AgBiBr_6$ double perovskite thin films for optoelectronic applications”

   Enrico Greul, Michiel L. Petrus, Andreas Binek, Pablo Docampo, Thomas Bein

   Soltech Workshop, **2017**, Munich, Germany.